Electron Beam Manipulation in Terahertz Frequency Radiation-Driven Structures

Oliver Finlay

A Thesis submitted to the University of Lancaster for the Degree of Doctor of Philosophy in the Faculty of Science and Technology

Department of Physics
University of Lancaster
United Kingdom

March 2022

Abstract

Electron beam manipulation using THz frequency radiation has been considered in two regimes, fully relativistic and sub-relativistic. For the fully relativistic regime, experiments were undertaken at 35 MeV, while the sub-relativistic experiments were undertaken with 100 keV electron bunches. Acceleration of relativistic electron beams in a THz-driven rectangular dielectric-lined waveguide was demonstrated at the Compact Linear Accelerator for Research and Applications (CLARA) facility. To the author's knowledge, this experiment was the first demonstration of THz-driven linear acceleration of a fully relativistic beam. Here, factors effecting efficiency of acceleration, including THz transport, mode-conversion, THz dispersion, and THz-beam velocity matching, are examined. Experimental verification of THz phase velocity to particle velocity matching is provided through the frequency response of the interaction strength and the observed modulation period. Velocity matching is key to achieving long interaction lengths between particle bunches and laser fields. This is the first conclusive demonstration of its achievement in a THz-driven linear accelerator.

The sub-relativistic regime was explored by THz-driven deflection and compression of 100 keV electrons. Deflection has been performed experimentally to diagnose the electron bunch duration with two different structures: a dielectric-lined waveguide for extending the interaction length by velocity matching, and a sub-wavelength aperture in a metal foil for breaking the free-space propagation symmetry. The streaking speed achieved with the dielectric-lined waveguide compares favourably with previously reported experiments, which is indicative of a bunch duration diagnostic with high temporal resolution. Finite difference and semi-analytical calculations have been performed with these two structures to characterise the compression interaction. Simulation results show that the THz-driven dielectric waveguide is capable of achieving bunch compression within the interaction vacuum chamber using only a fraction of the available THz pulse energy. The results bode well for future experimentation where compression and deflection of sub-relativistic electrons will be performed in conjunction.

Declaration

I hereby declare that I am the sole author of this thesis and that this work has not been submitted in substantially the same form for the award of a higher degree elsewhere.

Chapter 4 contains work previously published by ourselves in [1].

The research underpinning this thesis was undertaken with the help and guidance of my supervisor Professor Steven Jamison. Our research was conducted with the Terahertz Acceleration Group at the Cockcroft Institute.

I grant the institutional repository any permissions and conditions that are necessary with respect to the online access to my work. Where subsidiary material owned by third party copyright holders has been included permission has been sought.

Acknowledgements

I'd first like to thank Professor Steven Jamison for his guidance and support throughout my PhD. Thank you to the whole THz acceleration group for your help, with a special thanks to Dan for being my laser lab tutor and bearing the brunt of my incessant questioning. Thanks also Matt and the rest of the Daresbury laser-plasma group for looking after me in my first year and supporting my career since.

The last few years would have been a lot less fun without friends at Daresbury and in Manchester. Thanks for the good times.

Thank you Lucy for always being there for me, and for being unwaveringly calm when I'm stressed. Thanks to my parents and to my family for everything.

Contents

List of Figures

List of Tables

1 Introduction

1.1 Particle Accelerators

Particle accelerators have been integral to the expansion of our understanding of the universe since the earliest iterations in the 1930s. The Large Hadron Collider (LHC) [2], for example, has been credited with the discovery of a number of never before observed particles, most famously the Higgs Boson [3, 4]. In the scientific effort to push the boundaries of the standard model, advancements in other technologies have been facilitated. Particle accelerators are capable of generating the high energy photons required for penetrative imaging, which allows inspection of the internal structure of an object. Non-destructive x-ray imaging is used most notably in a medical context [5], but is implemented in security applications [6, 7] and in many other sectors [8–11]. High energy photon beams are also fundamental to radiotherapy, where x-rays or gamma rays are used to destroy cancer cells. Proton beams are used as well in this context as they have different properties with regards to radiation dose deposition in healthy tissue [12].

Conventional accelerators, such as the LHC, use radio-frequency (RF) radiation to accelerate particles. These machines have a fundamental limit to the achievable acceleration gradient due to RF breakdown at the cavity walls [13]. State of the art cavities are capable of achieving 100 MV/m acceleration gradients [14] but currently operational facilities operate at lower gradients than this [15]. Hence, in order to achieve particle energies on the order of 100 GeV-1 TeV, many kilometres worth of real estate is required. Adding to the cost of this length of accelerating cavities are the high-field magnets permeating the beamline and the hundreds of gigawatt per year power requirement. Clearly, these multi-billion pound facilities cannot easily be replicated around the world and scaling up the energy only increases the economical and environmental footprint. It is paramount for this reason to explore alternatives to RF acceleration in order to reduce the size of future particle accelerators. An additional reason to explore novel accelerator concepts is that many applications, such as ultra-fast electron diffraction [16], require femtosecond-scale bunch durations. These bunches are challenging to generate in conventional accelerators due to the large mismatch between the RF field period and these small bunch durations.

The acceleration gradient limit due to cavity breakdown is dependent on the frequency of the accelerating field: the greater the frequency, the greater the potential accelerating gradient. Extremely high electric fields are accessible via lasers.

Klystrons generate fields for most conventional accelerators that have GHz frequencies, whereas laser frequencies tend to be on the order of 100s THz. The immediate issue with working at this frequency is the strict constraint it places on the bunch duration. For full bunch acceleration, the duration needs to be shorter than the accelerating field period, which is typical a few femtoseconds. Assuming a bunch can be injected into the accelerating phase, there is further difficulty in keeping the particles in this region over a significant acceleration length due to the super-luminal phase velocity of a focusing laser pulse in vacuum. The highest electric fields are accessible at the focus, but the phase velocity of a radially polarised laser pulse means the acceleration length when interacting with relativistic particles is limited to the Rayleigh length [17, 18]. Injecting and extracting electrons from the accelerating field close to the focus leads to optic damage thresholds becoming a hard limitation on the achievable gain [17]. The dielectric laser accelerator (DLA) is one proposal suggested to overcome the issue with phase-matching between particle bunch and laser field [19]. These structures are still subject to material damage threshold limitations and place challenging constraints on the electron beam transverse size as well as duration.

Another way to utilise high-power for large acceleration gradients is the laser-plasma wakefield accelerator (LWFA) [20]. As a high-power laser propagates through an underdense plasma, a plasma wave is established in its wake. This THz frequency wave is capable of supporting longitudinal field gradients on the order of 100 GV/m [21]. LWFAs have been demonstrated to provide quasi-monoenergic electron beams in the GeV energy range [22–26]. Previously these accelerators were limited to very low repetition rates due to the intense lasers required, but advancement of laser technology has led to 10 Hz, Joule class laser facilities. Despite recent progress in the stability of LWFAs and in the generated beam quality, the achievable electron beam transverse emittance is still orders of magnitude higher than in conventional machines [27, 28]. Externally injected electron beams from an RF linear accelerator (LINAC) have shown promise in preservation of emittance but timing jitter between the bunch and the drive laser provides a significant challenge [29, 30].

1.2 THz Radiation

Terahertz radiation (THz) is typically defined as radiation of frequency between 0.1 THz and 10 THz. Until recently this has been a relatively unexplored region of the electro-magnetic spectrum. This is due to the difficulty in the generation, collection and the detection of such waves. Optical generation of far-infrared ra-

diation was first observed in the 1970s [31] but it was not until the 80s, with the discovery of THz time-domain spectroscopy (TDS) [32], that the electric field of the radiation could be measured. Developments in the generation and measurement of intense THz frequency radiation has opened up many application possibilities [33, 34] in terahertz spectroscopy [35], biomedical science [36] and communication [37].

THz can be generated in a number of different ways, including from photoconductive antennas [38, 39], spintronics sources [40, 41] and coherent transition radiation from electron bunches [42, 43]. Optical rectification of intense laser pulses in non-linear materials [44] is the most frequently used method to generate high-field THz pulses with frequency below 1 THz. Lithium niobate ($LiNbO_3$) is often favoured as the source material due to its high non-linear susceptibility [45, 46], but the difference in refractive index between the optical laser and the generated THz in the medium leads to the radiation being emitted in a Cherenkov cone [47] in a collinear pumping geometry. This is not desirable for most applications as it is difficult to collect the radiation. In 2004, Hebling et al [48] proposed a method involving the tilting of the optical laser pulse front capable of producing coherent THz radiation as a pulse, which is more convenient practically and allows more efficient generation. The highest peak electric field reported to date from a tilted pulse front pumped $LiNbO_3$ crystal is $\sim 400\,\mathrm{MV/m}$ [49]. Source development is an ongoing field of research, but this already exceeds acceleration gradients achievable in state of the art RF-based facilities.

1.3 THz Radiation in Particle Accelerators

The frequency of THz radiation is desirable for the next generation of particle accelerators as the pulsed cavity breakdown-limited peak accelerating field is higher than in conventional RF machines. The period of the accelerating field though is larger than in optical frequency fields which loosens the constraints on the bunch duration and timing of an injected particle bunch. THz sources which emit radiation below 1 THz are generally preferred in the context of particle manipulation as they allow full bunch acceleration of bunches with duration on the order of 100 fs. Optically generated THz sources are favoured since lasers are often used in other contexts in the accelerator; whether this is for the generation of electron bunch at a photocathode [50, 51], for pump-probe measurements or for inverse Compton scattering-based x-ray/gamma-ray sources [52, 53]. If the same laser is used for two or more of these methods, timing jitter between them is greatly reduced compared to RF-laser synchronisation. Current state of the art limits RF-laser

synchronisation to the $\sim$ 10 - 100 fs level [54], whereas lasers can be synchronised to the sub fs level [55, 56].

A significant challenge in the implementation of THz frequency particle accelerators is the mismatch in phase velocity between a focusing laser pulse and an electron beam. A number of schemes have been suggested to circumvent this issue. Dielectric-lined waveguides are the most commonly used structures for THz-driven particle acceleration. These structures modify the dispersion of light passing through in a known way, such that electron velocity to laser pulse phase velocity matching can be achieved. Acceleration in dielectric-lined waveguides was numerically evaluated [57] before the first experimental demonstration of THz-driven acceleration in a dielectric-lined waveguide [58]. Recently, demonstration of multistage acceleration has been performed with these structures, paving the way for THz-driven accelerators with larger particle energy gains [59–61].

The laser-electron velocity mismatch can also be overcome by use of evanescent waves. Particle acceleration by optical frequency evanescent waves was suggested in [62] and the idea was later extended to the THz regime [63]. Demonstration of the sub-luminal THz pulse propagation facilitated by this interaction geometry was demonstrated in [64]. Other notable work in the field of THz-driven particle acceleration include acceleration in an inverse free-electron laser [65] and with a segmented terahertz electron accelerator and manipulator (STEAM) device [66].

Particle beam interaction with THz frequency radiation can be exploited for more accelerator applications than simply the replacement of RF accelerating cavities. Velocity bunching, or ballistic bunching, is a technique for achieving particle bunches with a short duration [67]. It involves giving a sub-relativistic bunch a negative energy chirp. Since the tail of the bunch will be travelling at a greater velocity than the head, at some later point in the beamline, a longitudinal focus will be achieved. As well as being useful for injection into a particle accelerator, velocity bunching is commonly used to provide a source for ultra-fast electron diffraction [16]. RF-driven bunch compressors are an established method for generating ultrashort duration bunches [68–70]. THz-driven bunch compressors possess both the synchronisation and the peak field advantages discussed earlier for acceleration. They also benefit from an intrinsically sharper field gradient at the zero-crossing due to the higher frequency. The sharper field gradient means a greater chirp can be imposed on the bunch, so the longitudinal focus is reached closer to the compression interaction. Reducing this distance not only reduces the footprint of the compressor in the beamline, but also means shorter bunch durations can

be reached, so greater temporal resolution can be achieved in electron diffraction experiments. Given a sufficiently sub-relativistic initial bunch, relatively low particle energy gain is needed for compression, which means phase-matching is not necessarily required in the interaction. Several demonstrations of THz-driven velocity bunching have been performed using structures which simply limit the region over which the laser pulse and particle bunch interact [66, 71–73]. Dielectric-lined waveguides have also been studied numerically [57] and experimentally [59, 74] for this purpose. Electron bunch durations on the order of 10 fs are consistently reported.

The accelerator applications of THz radiation discussed above take advantage of an interaction in which an energy gain is achieved in the particle direction of motion. THz radiation can also be implemented to deflect a particle bunch for diagnostic purposes. RF transverse deflecting cavities are commonly used in accelerator beamlines to measure the particle bunch length [75–77]. The time dependent transverse kick allows longitudinal bunch properties to be inferred from an image in the transverse plane. Implementing a THz-driven interaction to achieve this kick is advantageous due to the greater field gradient available which means less space is required for the diagnostic and greater temporal resolution can be achieved in the measurement. Again, precise synchronisation can be achieved between the optically generated THz driving the transverse interaction and other laser-based diagnostics or beamline features. A number of structures have successfully demonstrated bunch duration measurements with femtosecond-scale temporal resolution using THz-driven streaking of electron beams. Sub-wavelength apertures on a metallic substrate are the most commonly used in the literature, which limit the interaction to a small region in the vicinity of the interaction mediator. These structures can be separated into resonant structures, which enhance the electric field at a particle frequency [78, 79], and non-resonant structures, which simply provide a phase shift between electric and magnetic field components. Both of these types of slit have been implemented experimentally to diagnose electron bunch durations [71, 74, 80, 81], often in conjunction with THz-driven bunch compression. THz-driven streaking has also been performed with dielectric-lined tubes [74] and rectangular dielectric-lined waveguides have been numerically studied [82] for this purpose.

1.4 Thesis Outline

My contribution to the ongoing work at the Cockcroft Institute to develop THz-driven particle accelerator technology will be described in this thesis. Chapter

2 gives an outline of the required knowledge for the THz-driven interactions discussed later on. It first describes how high-field THz radiation is generated from $LiNbO_3$ when pumped by an optical laser with a tilted-pulse-front. It then discusses the difficulties of facilitating energy gain between a Gaussian laser pulse and an electron bunch. This section also deals with the application of a THz-driven interaction to perform electron beam phase-space manipulation, in the forms of velocity bunching and streaking. In the final section of this chapter, details are given of numerical methods used in this thesis for electron beam and laser pulse propagation.

Chapter 3 reviews the equipment required for the work in this thesis. The laser systems, the electron sources and the THz detection apparatus will be summarised here.

Chapter 4 describes results of an experimental campaign to accelerate 35 MeV electrons in a dielectric-lined waveguide at the CLARA linear accelerator [83]. THz-driven acceleration of the relativistic electron beam was achieved. This chapter focuses predominantly on the physics behind the interaction in a dielectric-lined waveguide and provides confirmation that phase-matched acceleration was observed. Work on the diagnosis of the electron beam longitudinal phase space from the electron spectra post-interaction is also detailed.

Another set of experimental results, described in chapter 5, revolve around the interaction of THz radiation with a sub-relativistic electron beam. The goal of these activities was to deflect the 100 keV electron beam with THz radiation. A secondary goal was to establish potential for velocity bunching driven by a THz frequency field. The design of the THz source and the electron beam is discussed first. The electron energy diagnostic design which will be used at a later date to characterise the success of the electron bunch compression is then detailed. Deflection of the electron bunch facilitated by two different interaction structures has been performed experimentally. Simulation results of the acceleration interaction with these two structures has been simulated using the numerical methods detailed in chapter 2.

Chapter 6 summarises the results presented in chapters 4 and 5 and will give an outlook with respect to these research areas within the THz acceleration group at the Cockcroft Institute.

2 Theory

2.1 Generation and Detection of Terahertz Radiation

This section details the relevant information for the optical generation of terahertz frequency radiation. In this thesis, both single-cycle and multi-cycle terahertz radiation is generated experimentally by pumping a lithium niobate crystal with an ultrashort pulse laser.

2.1.1 The Non-Linear Wave Equation

The behaviour of electromagnetic fields is governed by Maxwell's equations

$$\nabla \cdot \mathbf{D} = \rho_\mathrm{f} \,, \tag{1}$$

$$\nabla \cdot \mathbf{B} = 0 \,, \tag{2}$$

$$\nabla \times \mathbf{E} = -\frac{\partial \mathbf{B}}{\partial \mathrm{t}} \,, \tag{3}$$

$$\nabla \times \mathbf{H} = \mathbf{J}_\mathrm{f} + \frac{\partial \mathbf{D}}{\partial \mathrm{t}} \,, \tag{4}$$

where ρ_f is the charge density and $\mathbf{J}_\mathrm{f}$ is the free current density. The macroscopic fields, $\mathbf{D}$ and $\mathbf{H}$, are defined in terms of the fundamental fields, $\mathbf{E}$ and $\mathbf{B}$, such that

$$\mathbf{D} = \epsilon_0 \mathbf{E} + \mathbf{P} \,, \tag{5}$$

$$\mathbf{H} = \frac{1}{\mu_0} \mathbf{B} - \mathbf{M} \,, \tag{6}$$

where $\mathbf{P}$ is the polarisation and $\mathbf{M}$ is the magnetisation. The wave equation is derived here in a medium with no free charges, $\rho_\mathrm{f} = 0$, and no free current, $\mathbf{J}_\mathrm{f} = 0$. Taking the curl of equation 3 gives

$$\nabla \times \nabla \times \mathbf{E} = -\nabla \times \frac{\partial \mathbf{B}}{\partial \mathrm{t}} = -\mu_0 \frac{\partial^2 \mathbf{D}}{\partial \mathrm{t}^2} \,, \tag{7}$$

where the final result is found by substituting in equation 4 with $\mathbf{M} = 0$. This can be simplified using the vector identity

$$\nabla \times \nabla \times \mathbf{A} = \nabla (\nabla \cdot \mathbf{A}) - \nabla^2 \mathbf{A} \,. \tag{8}$$

Given that $\rho_\mathrm{f} = 0$, the divergence of $\mathbf{E}$ equals 0. Equation 7 can then be written as

$$\nabla^2 \mathbf{E} = \mu_0 \frac{\partial^2 \mathbf{D}}{\partial \mathrm{t}^2} \,. \tag{9}$$

In free space, the polarisation term is equal to 0 and the linear wave equation can be retrieved using $\mu_0 \epsilon_0 = 1/\mathrm{c}^2$

$$\nabla^2 \mathbf{E} - \frac{1}{c^2} \frac{\partial^2 \mathbf{E}}{\partial \, \mathrm{t}^2} = 0 \, . \tag{10}$$

If instead, $\mathbf{D}$ in equation 7 is written in terms of equation 5, the non-linear wave equation can be retrieved

$$\nabla^2 \mathbf{E} - \frac{1}{\mathrm{c}^2} \frac{\partial^2 \mathbf{E}}{\partial \, \mathrm{t}^2} = \mu_0 \frac{\partial^2 \mathbf{P}}{\partial \, \mathrm{t}^2} \, . \tag{11}$$

By taking the Fourier transform of equation 11, it can be written in the frequency domain as

$$\nabla^2 \widetilde{\mathbf{E}} + \frac{\omega^2}{\mathrm{c}^2} \widetilde{\mathbf{E}} = -\omega^2 \, \mu_0 \, \widetilde{\mathbf{P}} \, , \tag{12}$$

The polarisation term can be written in the time domain as a sum of the different order contributions,

$$\mathbf{P} = \epsilon_0 \, \left(\chi^{(1)} \, \mathbf{E} + \chi^{(2)} \, \mathbf{E}^2 + \, ... \right) \, , \tag{13}$$

where χ denotes the susceptibility of the medium that the electromagnetic wave is travelling through [84]. By exploiting the convolution theorem, the polarisation can be written in the Fourier domain as

$$\widetilde{\mathbf{P}} = \epsilon_0 \, \left(\chi^{(1)} \, \widetilde{\mathbf{E}} + \chi^{(2)} \, \widetilde{\mathbf{E}} * \widetilde{\mathbf{E}} + \, ... \right) \, , \tag{14}$$

In the linear regime, only the first term is considered. At higher intensities and in non-linear materials, the higher order terms are not negligible. Considering the first order polarisation term separately to the higher orders, $\mathbf{P}^{\mathrm{NL}}$, the frequency domain wave equation can be written as

$$\nabla^2 \widetilde{\mathbf{E}} + \frac{\omega^2}{\mathrm{c}^2} \, \left(1 + \chi^{(1)} \right) \, \widetilde{\mathbf{E}} = -\omega^2 \, \mu_0 \, \widetilde{\mathbf{P}}^{\mathrm{NL}} \, . \tag{15}$$

From the definition of the first order susceptibility, $\chi^{(1)} = (\epsilon_{\mathrm{r}} - 1)$, where ϵ_{r} is the relative permittivity of the propagation medium. The electric field coefficient in the wave equation can be written as the wavenumber, $\mathrm{k} = \sqrt{\epsilon_{\mathrm{r}}} \, \omega / \mathrm{c}$

$$\nabla^2 \widetilde{\mathbf{E}} + \mathrm{k}^2 \, \widetilde{\mathbf{E}} = -\omega^2 \, \mu_0 \, \widetilde{\mathbf{P}}^{\mathrm{NL}} \, . \tag{16}$$

Equation 16 describes the electric field generated from a non-linear polarisation source.

2.1.2 Optical Terahertz Emission

The intensity of the generated radiation from pumping a non-linear crystal can be derived by using the second order non-linear polarisation term as the source to the wave equation. The induced non-linear polarisation from the mixing of two

electric fields, $\widetilde{\mathrm{E}}_1$ and $\widetilde{\mathrm{E}}_2$, propagating in the z direction in the frequency domain is

$$\widetilde{\mathrm{P}}^{(2)}(\mathrm{z},\,\omega) = \epsilon_0\,\chi^{(2)}\,\widetilde{\mathrm{E}}_1(\mathrm{z},\,\omega)\;*\;\widetilde{\mathrm{E}}_2(\mathrm{z},\,\omega) = \epsilon_0\,\chi^{(2)}\int_{-\infty}^{\infty}\widetilde{\mathrm{E}}_1(\mathrm{z},\,\Omega)\,\widetilde{\mathrm{E}}_2(\mathrm{z},\,\omega-\Omega)\,\mathrm{d}\Omega\;. \tag{17}$$

The integral can be split into positive and negative frequencies

$$\begin{aligned}\widetilde{\mathrm{P}}^{(2)}(\mathrm{z},\,\omega) = \epsilon_0\,\chi^{(2)}\int_{-\infty}^{0}\widetilde{\mathrm{E}}_1(\mathrm{z},\,\Omega)\,\widetilde{\mathrm{E}}_2(\mathrm{z},\,\omega-\Omega)\,\mathrm{d}\Omega \\ +\,\epsilon_0\,\chi^{(2)}\int_{0}^{\infty}\widetilde{\mathrm{E}}_1(\mathrm{z},\,\Omega)\,\widetilde{\mathrm{E}}_2(\mathrm{z},\,\omega-\Omega)\,\mathrm{d}\Omega\;.\end{aligned} \tag{18}$$

By switching the integral bounds for the negative frequencies, changing the sign of the bounds and using the identity $\mathrm{E}(\text{-}\omega) = \mathrm{E}^*(\omega)$, the negative integral can be written as

$$\begin{aligned}\widetilde{\mathrm{P}}^{(2)}(\mathrm{z},\,\omega) = \epsilon_0\,\chi^{(2)}\int_{0}^{\infty}\widetilde{\mathrm{E}}_1^*(\mathrm{z},\,\Omega)\,\widetilde{\mathrm{E}}_2(\mathrm{z},\,\omega+\Omega)\,\mathrm{d}\Omega \\ +\,\epsilon_0\,\chi^{(2)}\int_{0}^{\infty}\widetilde{\mathrm{E}}_1(\mathrm{z},\,\Omega)\,\widetilde{\mathrm{E}}_2(\mathrm{z},\,\omega-\Omega)\,\mathrm{d}\Omega\;.\end{aligned} \tag{19}$$

Equation 19 describes both sum and difference frequency terms. Sum frequency generation (SFG) is exploited for electro-optic (EO) field measurements. Ultrashort near-infrared laser pulses have bandwidths on the order of THz frequency so lend themselves to THz emission by difference frequency generation (DFG).

To perform the convolution integral in equation 19, an electric field is assumed in the form

$$\widetilde{\mathrm{E}}_\mathrm{i}(\mathrm{z},\,\omega) = \widetilde{\mathrm{A}}_\mathrm{i}\,(\mathrm{z},\,\omega)\,\mathrm{e}^{\mathrm{i}\,\mathrm{k}_\mathrm{i}(\omega)\,\mathrm{z}}\;, \tag{20}$$

where the generated electric field from the induced polarisation and its wavenumber are denoted by E_3 and k_3, respectively. Substituting the induced electric field in equation 20 into the Fourier domain wave equation (equation 16), gives on the left-hand side

$$\mathrm{LHS} = \left(\frac{\partial^2\widetilde{\mathrm{A}}_3}{\partial\,\mathrm{z}^2} + 2\,\mathrm{i}\,\mathrm{k}_3\,\frac{\partial\widetilde{\mathrm{A}}_3}{\partial\,\mathrm{z}} - \mathrm{k}_3^2\,\widetilde{\mathrm{A}}_3 + \mathrm{k}_3^2\,\widetilde{\mathrm{A}}_3\right)\mathrm{e}^{\mathrm{i}\,\mathrm{k}_3\,\mathrm{z}} \approxeq 2\,\mathrm{i}\,\mathrm{k}_3\,\frac{\partial\widetilde{\mathrm{A}}_3}{\partial\,\mathrm{z}}\,\mathrm{e}^{\mathrm{i}\,\mathrm{k}_3\,\mathrm{z}}\;. \tag{21}$$

The terms with the factor of k_3^2 cancel. The term containing the second order derivative can be omitted with the approximation that envelope is slowly varying, which is valid when the pulse envelope duration is much larger than the period of the oscillation of the electric field. Because of this, the higher order the derivative, the smaller the term. Equation 21 is equal to the right-hand side of the wave equation which contains the polarisation term from equation 19 so

$$\frac{\partial \widetilde{A}_3}{\partial z} = \frac{i\,\omega^2\,\mu_0\,\epsilon_0\,\chi^{(2)}\,e^{-i\,k_3\,z}}{2\,k_3}\left(\int_0^\infty \widetilde{A}_1^*(z,\,\Omega)\,\widetilde{A}_2(z,\,\omega+\Omega)\,e^{-i\,k_\Omega\,z}\,e^{i\,k_{\omega+\Omega}\,z}\,d\Omega + \int_0^\infty \widetilde{A}_1(z,\,\Omega)\,\widetilde{A}_2(z,\,\omega-\Omega)\,e^{i\,k_\Omega\,z}\,e^{i\,k_{\omega-\Omega}\,z}\,d\Omega\right) . \quad (22)$$

Given that the spectral shape terms A_1 and A_2 are only significant around a central frequency, ω_0, which is in the optical frequency range, the wavenumber can be written as a Taylor expansion around ω_0. Taking up to the second order,

$$k_\Omega = k(\omega_0) + \left.\frac{dk}{d\Omega}\right|_{\omega_0}(\Omega-\omega_0) = k(\omega_0) + \frac{n_g}{c}(\Omega-\omega_0)\,, \quad (23)$$

$$k_{\omega+\Omega} = k(\omega_0) + \left.\frac{dk}{d(\omega+\Omega)}\right|_{\omega_0}(\omega+\Omega-\omega_0) = k(\omega_0) + \frac{n_g}{c}(\omega+\Omega-\omega_0)\,, \quad (24)$$

$$k_{\omega-\Omega} = k(\omega_0) + \left.\frac{dk}{d(\omega-\Omega)}\right|_{\omega_0}(\omega-\Omega-\omega_0) = k(\omega_0) + \frac{n_g}{c}(\omega-\Omega-\omega_0)\,, \quad (25)$$

where n_g is the group refractive index of the optical pulse. Given $k(\omega_0) = n_\phi\,\omega_0/c$ where n_ϕ is phase refractive index, the combination of wavenumbers in equation 22 becomes

$$k_{\omega+\Omega} - k_\Omega = \frac{n_g\,\omega}{c}\,, \quad (26)$$

$$k_{\omega-\Omega} + k_\Omega = \frac{n_g\,\omega}{c} + \frac{2\,\omega_0\,(n_\phi - n_g)}{c} \approx \frac{n_g\,\omega}{c}\,, \quad (27)$$

where in the last equation the difference in group and phase refractive index is assumed to be small for simplicity of calculation. With this form for the wavenumbers, equation 22 can be expressed

$$\frac{\partial \widetilde{A}_3}{\partial z} = \frac{i\,\omega^2\,\mu_0\,\epsilon_0\,\chi^{(2)}\,e^{-i\,k_3\,z}}{2\,k_3}\left(\int_0^\infty \widetilde{A}_1^*(z,\,\Omega)\,\widetilde{A}_2(z,\,\omega+\Omega)\,e^{i\,n_g\,\omega\,z/c}\,d\Omega + \int_0^\infty \widetilde{A}_1(z,\,\Omega)\,\widetilde{A}_2(z,\,\omega-\Omega)\,e^{i\,n_g\,\omega\,z/c}\,d\Omega\right) . \quad (28)$$

A Gaussian spectrum is assumed such that

$$\widetilde{A}_1(\omega) = \widetilde{A}_2(\omega) = E_0\exp\left(-\frac{(\omega-\omega_0)^2}{\sigma_f^2}\right)\,, \quad (29)$$

which means equation 28 can be expressed

$$\frac{\partial \widetilde{A}_3}{\partial z} = \frac{i\,\omega^2\,E_0^2\,\mu_0\,\epsilon_0\,\chi^{(2)}\exp\left(\frac{i\,\Delta n\,\omega\,z}{c}\right)}{2\,k_3} \times \int_0^\infty \exp\left(-\frac{(\Omega-\omega_0)^2}{\sigma_f^2}\right)\left[\exp\left(-\frac{(\omega+\Omega-\omega_0)^2}{\sigma_f^2}\right) + \exp\left(-\frac{(\omega-\Omega-\omega_0)^2}{\sigma_f^2}\right)\right] d\Omega\,, \quad (30)$$

where $\Delta n = n_g$ - n_3 describes the wave vector mismatch. Calculating this integral gives

$$\frac{\partial \widetilde{\mathrm{A}}_3}{\partial\, \mathrm{z}} = \frac{\mathrm{i}\,\omega^2\,\mathrm{E}_0^2\,\mu_0\,\epsilon_0\,\chi^{(2)}\exp\left(\frac{\mathrm{i}\,\Delta \mathrm{n}\,\omega\,\mathrm{z}}{\mathrm{c}}\right)}{2\,\mathrm{k}_3} \times \frac{1}{2}\sqrt{\frac{\pi}{2}}\,\sigma_\mathrm{f} \times \left\{\exp\left(-\frac{\omega^2}{2\,\sigma_\mathrm{f}^2}\right)\left(1-\mathrm{erf}\left[\frac{\omega-2\,\omega_0}{\sqrt{2}\,\sigma_\mathrm{f}}\right]\right)+ \exp\left(-\frac{(\omega-2\,\omega_0)^2}{2\,\sigma_\mathrm{f}^2}\right)\left(1-\mathrm{erf}\left[\frac{-\omega}{\sqrt{2}\,\sigma_\mathrm{f}}\right]\right)\right\}\,. \tag{31}$$

The first term is responsible for DFG of THz frequency radiation where $\omega_{\mathrm{THz}} \ll \omega_0$. Since $\omega_0 \gg \sigma_\mathrm{f}$, the first error function can be assumed to be equal to minus 1. The second term is responsible for SFG. The second error function can also be assumed to be equal to minus 1 as $\omega_{\mathrm{SFG}} \gg \sigma_\mathrm{f}$. This gives

$$\frac{\partial \widetilde{\mathrm{A}}_3}{\partial\, \mathrm{z}} = \frac{\mathrm{i}\,\omega^2\,\mathrm{E}_0^2\,\mu_0\,\epsilon_0\,\chi^{(2)}\exp\left(\frac{\mathrm{i}\,\Delta \mathrm{n}\,\omega\,\mathrm{z}}{\mathrm{c}}\right)}{2\,\mathrm{k}_3} \times \sqrt{\frac{\pi}{2}}\,\sigma_\mathrm{f} \times \left\{\exp\left(-\frac{\omega^2}{2\,\sigma_\mathrm{f}^2}\right)+\exp\left(-\frac{(\omega-2\,\omega_0)^2}{2\,\sigma_\mathrm{f}^2}\right)\right\}\,. \tag{32}$$

Taking the DFG term so only THz generation is considered and integrating between z = 0 and L, the length of the non-linear medium,

$$\widetilde{\mathrm{A}}_{\mathrm{THz}} = \frac{\mathrm{i}\,\omega^2\,\mathrm{E}_0^2\,\mu_0\,\epsilon_0\,\chi^{(2)}\,\sigma_\mathrm{f}}{2\,\mathrm{k}_{\mathrm{THz}}}\sqrt{\frac{\pi}{2}}\exp\left(-\frac{\omega^2}{2\,\sigma_\mathrm{f}^2}\right)\left(\frac{\exp\left(\frac{\mathrm{i}\,\Delta \mathrm{n}\,\omega\,\mathrm{L}}{\mathrm{c}}\right)-1}{\mathrm{i}\,\Delta \mathrm{n}\,\omega/\mathrm{c}}\right)\,, \tag{33}$$

which can be simplified to

$$\widetilde{\mathrm{A}}_{\mathrm{THz}} = \frac{\mathrm{i}\,\omega\,\mathrm{E}_0^2\,\chi^{(2)}\,\sigma_\mathrm{f}}{2\,\mathrm{n}_{\mathrm{THz}}\,\mathrm{c}}\sqrt{\frac{\pi}{2}}\exp\left(-\frac{\omega^2}{2\,\sigma_\mathrm{f}^2}\right)\left(\frac{\exp\left(\frac{\mathrm{i}\,\Delta \mathrm{n}\,\omega\,\mathrm{L}}{\mathrm{c}}\right)-1}{\mathrm{i}\,\Delta \mathrm{n}\,\omega/\mathrm{c}}\right)\,. \tag{34}$$

The $\mathrm{i}\,\omega$ multiplied by the frequency domain envelope term, when an inverse Fourier transform is applied, is equal to the time derivative of the temporal envelope. The intensity can be found using the time-averaged Poynting vector

$$\widetilde{\mathrm{I}}_\mathrm{i} = \frac{\mathrm{n_i}\,\epsilon_0\,\mathrm{c}}{2}\,|\widetilde{\mathrm{A}}_\mathrm{i}|^2\,. \tag{35}$$

Replacing the A terms with intensity in equation 34 and simplifying leads to

$$\widetilde{\mathrm{I}}_{\mathrm{THz}} = \frac{\pi\,\epsilon_0\,\omega^2\,\mathrm{E}_0^4\,{\chi^{(2)}}^2\,\sigma_\mathrm{f}^2}{16\,\mathrm{n}_{\mathrm{THz}}\,\mathrm{c}}\exp\left(-\frac{\omega^2}{\sigma_\mathrm{f}^2}\right)\,\mathrm{sinc}^2\left(\frac{\Delta \mathrm{n}\,\omega\,\mathrm{L}}{2\,\mathrm{c}}\right)\,. \tag{36}$$

The bandwidth of the generated intensity profile is equal to the pump field bandwidth if phase-matching and absorption are neglected. In the time domain, assuming a transform limited input and output, the THz intensity pulse duration is a factor of $\sqrt{2}$ multiplied by the pump intensity duration, which is equivalent to the THz field pulse duration being equal to the pump intensity duration. The spectral dependence on phase-matching comes from the sinc term, which has a

maximum at $n_{THz} \approx n_g$, where phase matching occurs. Phase matching is unlikely to occur over the full pump bandwidth so the frequencies which form the output spectrum will be the ones that are generated most efficiently. The spectral dependence on the absorption in the non-linear medium also plays a part in the spectrum of the measured THz pulse. For some commonly used non-linear crystals such as zinc telluride, phase-matching occurs naturally in the THz range with co-linearly propagating pump and THz pulses. If in the generation crystal, there is a large discrepancy between the refractive index of the pump laser and the refractive index of the desired THz frequency components, the pumping scheme needs to be modified to achieve efficient generation.

2.1.3 Narrow-Bandwidth Optical Terahertz Generation

Broadband quasi-single-cycle THz radiation can be generated by pumping a non-linear crystal with a near-infrared, transform limited Gaussian pulse, as detailed in the previous section. Narrow-bandwidth radiation can be generated by pumping the same crystal with two, time delayed pulses with a more complex relationship between time and frequency. The time profile of the electric field of a pulse such as this can be expressed in the time domain as

$$\mathrm{E(t)} = \mathrm{A(t)}\cos(\omega_0 \mathrm{t} + \phi(\mathrm{t}))\ , \tag{37}$$

where ϕ(t) is the phase of the pulse given by

$$\phi(t) = \phi_0 + \phi_1\, t + \phi_2\, t^2 + \phi_3\, t^3 + \ldots\ . \tag{38}$$

Taking the Fourier transform of the electric field gives the spectral characteristics of the pulse. The electric field in the frequency domain can be written as

$$\widetilde{\mathrm{E}}(\omega) = \widetilde{\mathrm{A}}\,(\omega)\,\mathrm{e}^{\mathrm{i}\,\varphi\,(\omega)}\ , \tag{39}$$

where $\widetilde{\mathrm{A}}\,(\omega)$ is the spectral field envelope and $\varphi(\omega)$ is the spectral phase. This definition refers to the electric field for positive frequencies; the electric field for negatives frequencies is the complex conjugate of the electric field for positive frequencies. The spectral phase can be expressed as a Taylor series:

$$\varphi(\omega) = \varphi_0 + (\omega - \omega_0)\,\varphi_1 + \frac{1}{2}\,(\omega - \omega_0)^2\,\varphi_2 + \frac{1}{6}\,(\omega - \omega_0)^3\,\varphi_3 + \ldots\ . \tag{40}$$

The zeroth order term corresponds to the absolute phase, or the phase of the carrier oscillation with respect to the envelope term. First order spectral phase gives a time delay to a pulse. Second order spectral phase gives a linear frequency chirp to a pulse i.e a linear time dependence to the carrier wave frequency. This stretches the laser pulse to a 1/e field half width duration, σ_t, by

$$\sigma_{\mathrm{t}} = \sqrt{\sigma_0^2 + \frac{4\,\varphi_2^2}{\sigma_0^2}}\,, \tag{41}$$

where σ_0 is the pulse transform limited 1/e field half width duration. Third order spectral phase gives a quadratic chirp to a pulse. In the time domain, a positive φ_3 can be seen as beating after the main pulse arrives [85]. Figure 1 shows how second and third order spectral phase affect an ultra-short, Gaussian laser pulse in the time domain. The frequency domain electric definition is most useful in propagation calculations, since field at a later time is easily accessible given a medium's propagation function, $\mathrm{k}(\omega)$.

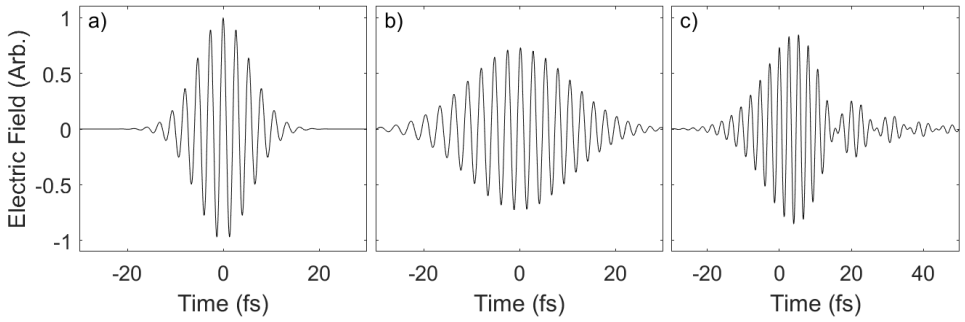

Figure 1: Temporal electric field profile of **a)** a pulse with no higher order spectral phase, **b)** a pulse with positive second order spectral phase and **c)** a pulse with positive third order spectral phase.

Narrow-bandwidth THz generation requires two pulses with a linear chirp, or a significant φ_2 component, and a time delay, τ. It is useful to use the frequency domain pulse definition here because, in the time domain, the chirp component, ϕ_2, is a function of both chirp and the pulse bandwidth. Experimentally, φ_2 is the component which is modified in a grating pulse compressor, not ϕ_2. Starting at equation 28 with assumed spectra

$$\widetilde{\mathrm{A}}_1(\mathrm{z},\,\Omega) = \mathrm{E}_0 \exp\left(-\frac{(\Omega-\omega_0)^2}{\sigma_{\mathrm{f}}^2}\right) \exp\left(\frac{\mathrm{i}\,\varphi_2}{2}\,(\Omega-\omega_0)^2\right) \exp\left(\mathrm{i}\,\Omega\,\tau\right)\,, \tag{42}$$

$$\widetilde{\mathrm{A}}_2(\mathrm{z},\,\Omega) = \mathrm{E}_0 \exp\left(-\frac{(\Omega-\omega_0)^2}{\sigma_{\mathrm{f}}^2}\right) \exp\left(\frac{\mathrm{i}\,\varphi_2}{2}\,(\Omega-\omega_0)^2\right)\,, \tag{43}$$

equation 31, when only considering DFG, becomes

$$\frac{\partial \widetilde{\mathrm{A}}_{\mathrm{THz}}}{\partial\, \mathrm{z}} = \frac{\mathrm{i}\,\omega^2\,\mathrm{E}_0^2\,\mu_0\,\epsilon_0\,\chi^{(2)}\exp\left(\frac{\mathrm{i}\,\Delta \mathrm{n}\,\omega\,\mathrm{z}}{\mathrm{c}}\right)}{2\,\mathrm{k}_{\mathrm{THz}}} \times \tag{44}$$
$$\int_0^\infty \exp\left(-(\Omega-\omega_0)^2\left[\frac{1}{\sigma_f^2}+\frac{i\varphi_2}{2}\right]\right)\times$$
$$\exp\left(-(\omega+\Omega-\omega_0)^2\left[\frac{1}{\sigma_f^2}-\frac{i\varphi_2}{2}\right]\right)\exp\left(-\mathrm{i}\,\Omega\,\tau\right)\,\mathrm{d}\Omega\;.$$

Integrating with respect to Ω gives

$$\frac{\partial \widetilde{\mathrm{A}}_{\mathrm{THz}}}{\partial\, \mathrm{z}} = \frac{\mathrm{i}\,\omega^2\,\mathrm{E}_0^2\,\mu_0\,\epsilon_0\,\chi^{(2)}\exp\left(\frac{\mathrm{i}\,\Delta \mathrm{n}\,\omega\,\mathrm{z}}{\mathrm{c}}\right)}{2\,\mathrm{k}_{\mathrm{THz}}} \times\sqrt{\frac{\pi}{2}}\,\sigma_{\mathrm{f}}\times \tag{45}$$
$$\left\{\exp\left(-\frac{\omega^2}{2\,\sigma_{\mathrm{f}}^2}-\frac{\sigma_{\mathrm{f}}^2}{8}\left[\tau-\omega\varphi_2\right]^2+\frac{\mathrm{i}\,\omega\,\tau}{2}-\mathrm{i}\,\omega_0\,\tau\right)\right\}\;.$$

Integrating with respect to z over the length of the crystal and simplifying gives the generated field spectrum

$$\widetilde{\mathrm{A}}_{\mathrm{THz}} = \frac{\mathrm{i}\,\omega\,\mathrm{E}_0^2\,\chi^{(2)}}{2\,\mathrm{n}_{\mathrm{THz}}\,\mathrm{c}}\times\sqrt{\frac{\pi}{2}}\,\sigma_{\mathrm{f}}\times\left(\frac{\exp\left(\frac{\mathrm{i}\,\Delta \mathrm{n}\,\omega\,\mathrm{L}}{\mathrm{c}}\right)-1}{\mathrm{i}\,\Delta \mathrm{n}\,\omega/\mathrm{c}}\right)\times \tag{46}$$
$$\exp\left(-\frac{\omega^2}{2\,\sigma_{\mathrm{f}}^2}-\frac{\sigma_{\mathrm{f}}^2\,\varphi_2^2}{8}\left[\omega-\frac{\tau}{\varphi_2}\right]^2+\frac{\mathrm{i}\,\omega\,\tau}{2}-\mathrm{i}\,\omega_0\,\tau\right)\;. \tag{47}$$

The final exponential term describes the spectral shape of the generated radiation. The first term defines DFG over the full bandwidth of the pulse. It dictates that THz frequencies outside of the pump pulse spectrum can not be generated efficiently. The second term in the exponential defines the narrow bandwidth generation due to a fixed frequency difference between the two pulses at a given point in time. The central frequency of the generated THz is at the beat frequency of the two pulses

$$\mathrm{f}_{\mathrm{b}} = \frac{\tau}{2\,\pi\,\varphi_2}\;. \tag{48}$$

The 1/e field frequency bandwidth is then given by

$$\sigma_{\mathrm{b}} = \frac{1}{2\,\pi}\sqrt{\frac{8}{\sigma_{\mathrm{f}}^2\,\varphi_2^2}} = \frac{\sqrt{2}}{\pi\,\sigma_{\mathrm{f}}\,\varphi_2}\;. \tag{49}$$

The third term is a $\tau/2$ time delay as the centre of the THz is in between the two pump pulse centroids. The final term describes a constant phase in the THz. This is important because a π phase change can occur with a time delay difference of half the pump laser period. For a 800 nm pump laser, as used in the experimental work in this thesis, this corresponds to time delay difference of 1.3 fs. A π phase change in the generated THz leads to a half THz period time shift in the peak, which is on the order of picoseconds. Ensuring a stable time delay is key for purposes where the stability of the THz peak timing is important.

2.1.4 Optical Terahertz Generation in Lithium Niobate

Lithium niobate ($LiNbO_3$) is commonly used for high field terahertz applications because of its large non-linear susceptibility [46]. Due to the crystalline lattice structure of crystals such as $LiNbO_3$, $\chi^{(2)}$ is not uniform throughout the structure. The susceptibility is defined in cartesian coordinates over the crystal dimensions as $\chi^{(2)}_{ijk}$. The second order polarisation in the time domain at a difference frequency $\omega_3 = \omega_2$ - ω_1 can be written as a sum over the crystal axis

$$\mathbf{P}^{(2)}_{i}(\omega_3) = \sum_{j,\,k} \chi^{(2)}_{ijk}(\omega_3, \omega_1, \omega_2)\, \mathbf{E}_j(\omega_1)\, \mathbf{E}_k(\omega_2)\ , \tag{50}$$

The notation for the susceptibility indices can be contracted such that j and k are combined into a single index, l. Table 1 shows the j and k values that values of l refer to.

jk	11	22	33	23, 32	13, 31	12, 21
l	1	2	3	4	5	6

Table 1: The relationship between indices of the crystal axes, j and k, and the contracted notation, l.

The new susceptibility matrix, $d_{il} = \frac{1}{2}\chi^{(2)}_{ijk}$, is now 3×6 rather than $3 \times 3 \times 3$. The polarisation can be calculated as

$$\mathbf{P}^{(2)}_{i} = 2\,\epsilon_0 \sum_{l} d_{il}\, \mathbf{E}^2\ . \tag{51}$$

The polarisation in terms of the contracted susceptibility matrix of $LiNbO_3$ can be expressed

$$\begin{pmatrix} P_x \\ P_y \\ P_z \end{pmatrix} = 2\,\epsilon_0 \begin{pmatrix} 0 & 0 & 0 & 0 & d_{31} & d_{21} \\ d_{21} & -d_{21} & 0 & d_{31} & 0 & 0 \\ d_{31} & d_{31} & d_{33} & 0 & 0 & 0 \end{pmatrix} \begin{pmatrix} E_x\, E_x \\ E_y\, E_y \\ E_z\, E_z \\ 2\,E_y\, E_z \\ 2\,E_z\, E_x \\ 2\,E_x\, E_y \end{pmatrix}\ . \tag{52}$$

Non-zero values of the d_{il} have been experimentally measured. The d_{33} component is significantly larger than the other components, so the the d_{31} and d_{21} terms are set to zero. The polarisation is then induced in the crystal z axis by the input field in that dimension

$$\mathbf{P}^{(2)}_{z} = 2\,\epsilon_0\, d_{33}\, E^2_z\ . \tag{53}$$

For efficient generation, the crystal z axis needs to be oriented in the direction of the pump laser polarisation.

Another consideration for efficient THz generation is phase matching. There is a large difference between the refractive index of optical frequencies and the refractive index of THz frequencies within $LiNbO_3$ so radiation is emitted in a Cherenkov cone. If a pencil beam illuminates the crystal, THz is emitted as in figure 2a), where the Cherenkov angle is given by

$$\theta = \cos^{-1}\left(\frac{n_g}{n_{THz}}\right). \tag{54}$$

If a pump beam of significant transverse size is used, each horizontal spatial position within the beam emits light in this fashion, so the THz emission from different points within the pump beam will not be in phase. If the pump laser has a pulse front tilt (PFT) in the non-linear crystal that matches the Cherenkov cone angle, as in figure 2b), the effective delay between generated radiation from different transverse positions leads to constructive interference and phase-matching can be achieved over a significant transverse beam size [48]. For stoichiometric MgO-doped $LiNbO_3$, with an extraordinary refractive index at 0.5 THz of $n_{THz} = 4.91$ [86] and optical group refractive index at $\lambda = 800\,\text{nm}$ of $n_g = 2.25$, the pulse front should be tilted to an angle of $\approx 63°$.

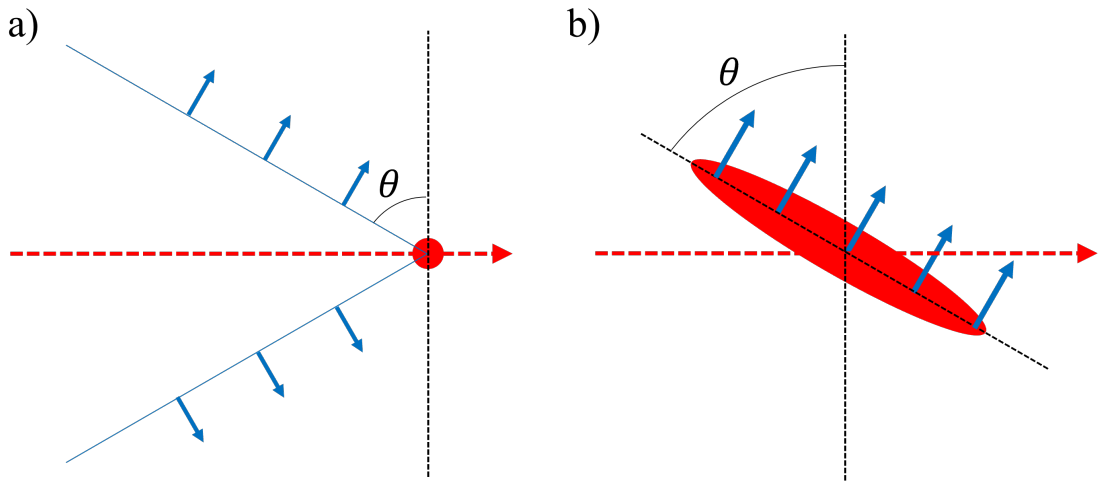

Figure 2: THz generation from a narrow pump beam in a Cherenkov cone is plotted in **a)**. The pulse front tilt scheme for THz generation over a large area pump beam is depicted in **b)**.

A PFT can be generated by using a diffraction grating [87]. The grating disperses

the pulse, meaning components with different wavelengths leave the grating travelling in slightly different directions. The diffracted angle at which light leaves a grating, ϕ_{d}, is given by

$$\sin(\phi_{\mathrm{d}}) = \frac{\mathrm{m}\,\lambda}{\mathrm{d}} - \sin(\phi_{\mathrm{i}}) \;, \tag{55}$$

where m is the diffraction order, d is the line spacing in the grating and ϕ_{i} is the incident angle. The angular chirp imposed upon the laser pulse by the grating is

$$\mathrm{C_a} = \left(\frac{\mathrm{d}\,\phi_{\mathrm{d}}}{\mathrm{d}\,\lambda}\right)_{\lambda_0} = \frac{\mathrm{m}}{\mathrm{d}\cos(\phi_{\mathrm{d}})} \;. \tag{56}$$

The effect of the grating can also be expressed in terms of a shift in the phase fronts of the pulse with respect to the transverse position

$$\Delta\varphi = \frac{2\pi}{\lambda_0}\,\Delta\phi_{\mathrm{d}}(\lambda)\,\Delta\mathrm{x} \;, \tag{57}$$

where x is the axis perpendicular to both the propagation of the laser and the grating lines. Taking the derivative of the spectral phase with respect to the angular frequency shift gives a group delay, $\Delta\mathrm{t_g}$, along the x axis

$$\Delta\mathrm{t_g} = \left(\frac{\mathrm{d}\,\varphi}{\mathrm{d}\,\omega}\right)_{\omega_0} = -\frac{\lambda_0^2}{2\,\pi\,\mathrm{c}}\left(\frac{\mathrm{d}\,\varphi}{\mathrm{d}\,\lambda}\right)_{\lambda_0} = \frac{\lambda_0\,\mathrm{C_a}}{\mathrm{c}}\,\Delta\mathrm{x} \;. \tag{58}$$

The group delay multiplied by c and divided by the difference in transverse position gives $\frac{\Delta\mathrm{z}}{\Delta\mathrm{x}}$, so the tangent of the tilt angle, α, can be expressed

$$\tan(\alpha) = \lambda_0\,\mathrm{C_a} = \frac{\mathrm{m}\,\lambda_0}{\mathrm{d}\cos(\phi_{\mathrm{d}})} \;. \tag{59}$$

The generation of a PFT from a diffraction grating is illustrated in figure 3. A number of sinusoidal waves which have an x dependent phase shift are initialised, e.g. figures 3a and 3b, with a phase shift magnitude related to the wavelength. Taking the sum over these components multiplied by the amplitude of the spectral component, $\widetilde{\mathrm{A}}(\lambda)$, gives

$$\mathrm{E_{PFT}} = \mathrm{Re}\left(\sum_{\lambda=0}^{\infty}\widetilde{\mathrm{A}}(\lambda)\,\mathrm{e}^{\mathrm{i}\,\mathrm{k}\,\mathrm{z}}\,\mathrm{e}^{\mathrm{i}\,\Delta\varphi}\right) , \tag{60}$$

which is plotted in figure 3c. The pulse still travels in the z direction but has a PFT in the direction perpendicular to the diffraction grating lines. The desired pulse is generated soon after the diffraction grating but it quickly disperses as it propagates.

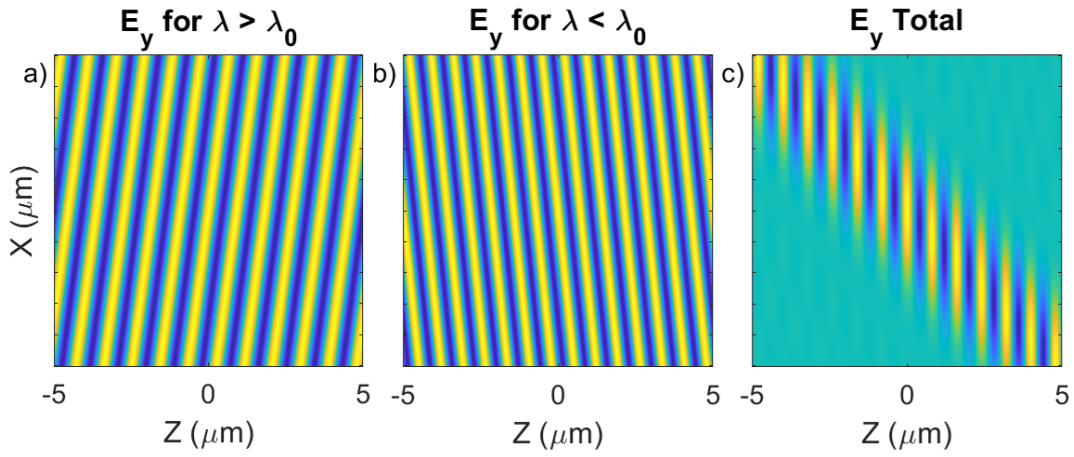

Figure 3: Illustration of the generation of a pulse front tilt at a grating surface. Plane waves with different wavelengths, as in **a)** and **b)**, interfere to generate a tilted pulse front, as in **c)**.

An imaging system is required to project the tilted pulse at the grating surface onto the $LiNbO_3$ exit surface. Imaging is only needed in the grating dispersion axis where the PFT is formed. The magnification of the imaging system, M, and the difference in group refractive index between air and $LiNbO_3$ affects the setup required to achieve the Cherenkov angle by

$$\theta = \tan^{-1}\left(\frac{1}{n_g\,M}\left(\frac{m\,\lambda_0}{d\cos(\phi_d)}\right)\right) = \cos^{-1}\left(\frac{n_g}{n_{THz}}\right). \tag{61}$$

The imaging places another constraint on the system. Since the pulse at the grating, the object plane, is at an angle, the image plane will also be tilted. The image plane tilt (IPT) angle is given by

$$\tan(\theta) = n_g\,M\tan(\phi_d)\,. \tag{62}$$

For most efficient generation, the PFT angle and the IPT angle should be equal to each other. Setting θ to the Cherenkov angle, figure 4a plots the magnification with the diffracted angle for the PFT with a number of grating spacings (equation 61) and for the IPT (equation 62). There are infinite combinations of M and ϕ_d that satisfy the criteria individually but, with a given grating, only one that satisfies both simultaneously. The consequence of an angle mismatch is that at a transverse position, x, away from the centre of the pump pulse, there is a distance, Δz, between the pulse front and the image plane. In the plane of the pulse front, the pulse duration will be a function of Δz, and therefore x, due to the accumulated group velocity dispersion in the distance between the PFT plane and the image

plane. A larger pulse duration leads to a smaller peak intensity of the pump and lower intensity of THz radiation generated. Assuming that the image plane and the pulse front overlap at x = 0, the increased 1/e half width field pulse duration off-axis can be calculated by [88]

$$\sigma_t = \sigma_0 \sqrt{1 + \frac{\Delta z \, \Psi^4 \, \lambda_0^6}{\pi^2 \, c^4 \, \sigma_0^4}} \, , \tag{63}$$

where $\Psi = \tan(\theta)/\lambda_0$. Using $\Delta z = x(\tan(\theta_{PFT}) - \tan(\theta_{IPT}))$ where $\theta_{PFT} = \theta$ and $\theta_{IPT} = \theta - 2°$, figure 4b plots the FWHM intensity pulse duration as a function of transverse position for a number of transform limited pulse durations. Higher bandwidth pulses are most sensitive to the effects of this angle mismatch.

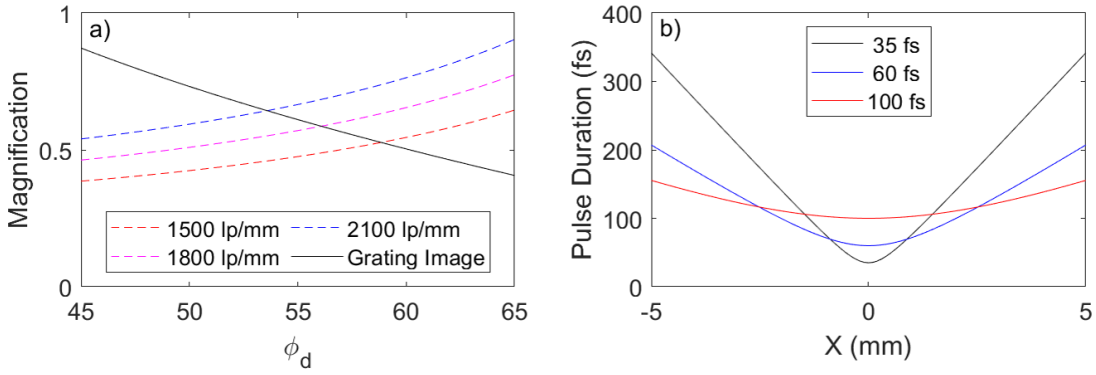

Figure 4: **a)** Magnification against diffracted angle with θ equal to the Cherenkov angle. Dotted lines refer to equation 61 with different grating line spacings and the solid line shows equation 62. **b)** FWHM pulse duration as a function of transverse position for different transform limited pulse durations, given a mismatch in PFT angle and IPT angle of 2°.

2.1.5 Electro-Optic Detection

Electro-optic (EO) sampling is a common technique for measuring the time-resolved electric field of a THz pulse [89–91]. It takes advantage of the Pockels electro-optic effect, which describes the induced birefringence in a material due to an electric field. The physics behind the Pockels effect is the same as THz generation [92], so a material with high second order susceptibility is used to increase the efficiency of the process: most commonly zinc telluride (ZnTe) or gallium phosphide (GaP) crystals. A THz electric field induces a birefringence in the material so the refractive index is dependent on the polarisation. Assuming spatial and temporal overlap between the THz field and an optical probe pulse, the change in the probe

pulse's polarisation state can be used to calculate the THz electric field. The induced polarisation leads to refractive indices in orthogonal directions given by:

$$n_1 = n_0 + \frac{n_0^3 \, r_{41} \, E_{THz}}{2} \, , \tag{64}$$

$$n_2 = n_0 - \frac{n_0^3 \, r_{41} \, E_{THz}}{2} \, , \tag{65}$$

where r_{41} is the relevant EO coefficient and n_0 is the ordinary refractive index at the probe frequency. Equations 64 and 65 assume that the THz polarisation is at 45° to the axes 1 and 2. If the probe beam is much shorter in duration than the THz period, E_{THz} can be assumed to be a single point within the THz pulse time profile. The probe pulse traversing the crystal experiences a phase shift, Γ, which is dependent on the refractive indices in the transverse planes

$$\Gamma = \frac{\omega_0 L}{c}(n_1 - n_2) \, , \tag{66}$$

where L is the length of the crystal. Substituting in the two orthogonal refractive indices, the phase shift can be written as

$$\Gamma = \frac{\omega_0 \, L \, n_0^3 \, r_{41} \, E_{THz}}{c} \, . \tag{67}$$

Balanced detection is often used to infer the terahertz field from the phase shift in the probe beam. A quarter waveplate after the detection crystal changes the probe pulse polarisation from linear to circular given zero THz field. The probe pulse is then passed through a polarising cube which splits it into two, orthogonal, linearly polarised pulses. Two photodiodes are then used to measure the intensity of the pulses in each polarisation state, which are equal without a THz induced birefringence. An example balanced detection setup is depicted in figure 5. The signal, S, which is defined as the difference in the photodiode signal divided by the sum of the photodiode signal, can be written as a function of the phase rotation

$$S = \frac{\Delta I}{I_1 + I_2} = \sin(\Gamma) \approx \Gamma \, , \tag{68}$$

where a small angle is assumed in the final term. Equation 67 can now be rewritten to give the THz field in the detection crystal in terms of known parameters

$$E_{THz} = \frac{\lambda}{2 \, \pi \, L \, n_0^3 \, r_{41}} \, S \, . \tag{69}$$

The THz field in free space is modified from this result by a factor of the Fresnel transmission coefficient at normal incidence, $T = \frac{2}{1+n_{THz}}$, into the detection crystal

$$E_{THz}^{air} = \frac{\lambda}{4 \, \pi \, L \, n_0^3 \, r_{41}} \, (1 + n_{THz}) \, S \, . \tag{70}$$

The terahertz field can be sampled across the pulse time profile by changing the timing between the probe and the terahertz pulse to give a full temporal characterisation of the pulse electric field.

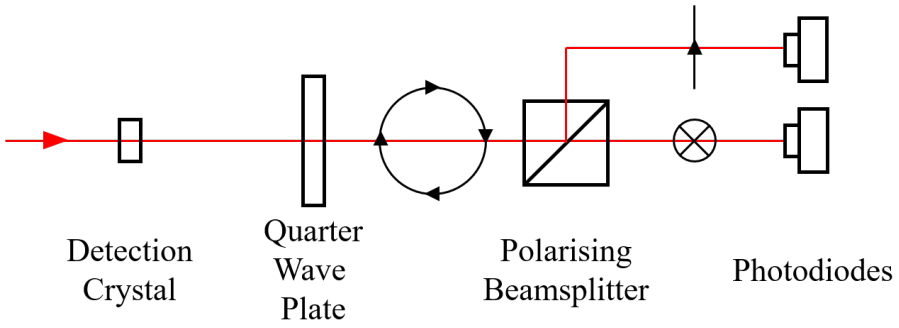

Figure 5: An example electro-optic detection layout showing the probe pulse path. The probe pulse passes through a detection crystal where it overlaps in time with a co-propagating THz electric field. The probe and THz are initially linearly polarised as they pass through the detection crystal, which has orthogonal crystal axes oriented at 45° to the probe and the THz polarisation. The photodiodes measure a change in the probe polarisation state due to the THz-induced birefringence in the crystal.

2.2 Electron Beam Manipulation Using Terahertz Radiation

Understanding how energy can efficiently be transferred from a THz frequency field to an electron first requires knowledge of the behaviour of a charged particle in an electromagnetic field, which is described in section 2.2.1. Section 2.2.2 gives details of the transverse electric field profile of a real laser pulse and section 2.2.3 covers the difficulties that that field definition brings with regards to electron acceleration. For matching of the electron velocity and the THz field phase velocity, dielectric-lined waveguides can be used, which is the topic of section 2.2.4. Performing time-dependent acceleration and deflection are useful applications of THz radiation. These will be discuss in 2.2.5 and 2.2.6 respectively.

2.2.1 Charged Particles in an Electromagnetic Field

A charged particle in an electromagnetic field experiences a force given by

$$\mathbf{F} = \mathrm{q}\ (\mathbf{E} + \mathbf{v} \times \mathbf{B})\ , \tag{71}$$

where q is the particle's charge and $\mathbf{v}$ is its velocity. This states the force exerted on a particle by the electric field is parallel to the electric field direction and that force exerted on a particle by the magnetic field is perpendicular to both the field and the direction of travel. Given that the energy gain over a distance, $\mathbf{d}$, is

$$\Delta\mathbf{U} = \mathbf{F} \cdot \mathbf{d}\ , \tag{72}$$

only interaction with the electric field can lead to particle energy gain. The magnetic field provides a deflecting force but can not do work on a particle.

The relativistic Lorentz force is the same on the right-hand side but the force is instead expressed in terms of the relativistic momentum

$$\mathbf{F} = \frac{\mathrm{d}\mathbf{p}}{\mathrm{dt}} = \frac{\mathrm{d}}{\mathrm{dt}} \left(\mathrm{m}\, \gamma\, \boldsymbol{\beta}\, \mathrm{c} \right) \ . \tag{73}$$

Equation 71 can be rewritten

$$\mathrm{m}\, \boldsymbol{\beta}\, \mathrm{c} \frac{\mathrm{d}\gamma}{\mathrm{dt}} + \mathrm{m}\, \gamma\, \mathrm{c} \frac{\mathrm{d}\boldsymbol{\beta}}{\mathrm{dt}} = \mathrm{q}\, \left(\mathbf{E} + \mathbf{v} \times \mathbf{B} \right) \ . \tag{74}$$

The total particle energy, $\mathbf{U} = \mathrm{m}\gamma\mathrm{c}^2$. Taking the time derivative of equation 72 and noting that forces perpendicular to the velocity will not count towards the energy, gives

$$\frac{\mathrm{d}\mathbf{U}}{\mathrm{dt}} = \mathrm{q}\, \mathbf{E} \cdot \boldsymbol{\beta}\, \mathrm{c} = \mathrm{m}\, \mathrm{c}^2 \frac{\mathrm{d}\gamma}{\mathrm{dt}} \ . \tag{75}$$

This form for the differential of γ can be substituted in equation 74 to give the change in particle velocity with time

$$\frac{\mathrm{d}\boldsymbol{\beta}}{\mathrm{dt}} = \frac{\mathrm{q}}{\mathrm{m}\gamma\mathrm{c}} \left[\mathbf{E} + c \left(\boldsymbol{\beta} \times \mathbf{B} \right) - \boldsymbol{\beta} \left(\mathbf{E} \cdot \boldsymbol{\beta} \right) \right] \ . \tag{76}$$

2.2.2 Gaussian Laser Pulses

So far, one dimensional waves have been considered. For acceleration of electrons, a full picture of the pulse field profile is required. The linear wave equation (10) needs to be satisfied for any field definition chosen. The wave equation can be reduced to the paraxial wave equation under the condition that the minimum beam waist is larger than the wavelength, $\mathrm{w}_0 \gg \lambda$. In this case, an electric field travelling in the z direction of the form

$$\mathbf{E} = \boldsymbol{\varepsilon}\, \mathrm{e}^{\mathrm{i}\, \mathrm{k}\, \mathrm{z}} \ , \tag{77}$$

must satisfy the paraxial wave equation [93]

$$\frac{\partial^2 \boldsymbol{\varepsilon}}{\partial\, \mathrm{x}^2} + \frac{\partial^2 \boldsymbol{\varepsilon}}{\partial\, \mathrm{y}^2} + 2\, \mathrm{k}\, \mathrm{i} \frac{\partial\, \boldsymbol{\varepsilon}}{\partial\, \mathrm{z}} = 0 \ . \tag{78}$$

Gaussian-Hermite transverse electromagnetic modes ($\mathrm{TEM}_{\mathrm{mn}}$) describe a set of solutions to the paraxial wave equation in a Cartesian coordinate system. The electric field for a single frequency mode polarised in the y direction can be expressed

$$\widetilde{E}_y(x,y,z,\omega) = E_0 \frac{w_0}{w(z)} H_m\left(\frac{\sqrt{2}\,x}{w(z)}\right) H_n\left(\frac{\sqrt{2}\,y}{w(z)}\right) e^{-(x^2+y^2)/w^2(z)}\, e^{i\,\varphi}\ , \tag{79}$$

with

$$\varphi = kz + \frac{k(x^2+y^2)}{2R(z)} - (m+n+1)\tan^{-1}\left(\frac{z}{z_R}\right) + \varphi_0\ , \tag{80}$$

where $w(z)$ is the $1/e$ waist radius, $R(z)$ is wavefront radius of curvature, z_R is the Rayleigh length [93]. These can be calculated by

$$w(z) = w_0\sqrt{1+\left(\frac{z}{z_R}\right)^2}\ , \tag{81}$$

$$R(z) = z + \frac{z_R^2}{z}\ , \tag{82}$$

$$z_R = \frac{\pi\, w_0^2}{\lambda}\ , \tag{83}$$

where the beam focus is at $z = 0$. H_m and H_n denote the m^{th} and n^{th} order hermite polynomial respectively and φ_0 is a constant phase term. The $\tan^{-1}$ term describes the Gouy phase which is responsible for a phase shift as a laser pulse passes through a focus and for an effective greater than speed of light phase velocity of a laser pulse on-axis. A fundamental Gaussian beam is described by $m = n = 0$ and its transverse electric field is depicted in figures 6a and 6b. The transverse field of the TEM_{01} mode is plotted in figures 6d and 6e.

For laser acceleration of electrons in a co-linear geometry, two features in the pulse field are required. Firstly, there must be an electric field component in the particle's direction of motion. Given a Gaussian transverse profile, the longitudinal field will be strongest if it has a maxima on-axis. The second desirable feature is a minima in the transverse field on-axis. This is to minimise deflection of the electron as it is accelerated. The existence of a longitudinal electric field is predicted by Gauss's law, which states that the divergence of the electric field is 0 in free space. Considering a field polarised in the y direction, the condition

$$\frac{\partial E_y}{\partial y} = -\frac{\partial E_z}{\partial z} \tag{84}$$

needs to be satisfied. Under the paraxial approximation, the longitudinal field of a y polarised Gaussian-Hermite beam on-axis can be expressed as [94]

$$\widetilde{E}_z(x,y,z,\omega) \approx \frac{i}{k}\frac{\partial\widetilde{E_y}}{\partial y}\ . \tag{85}$$

Hence, the longitudinal field given a fundamental Gaussian is

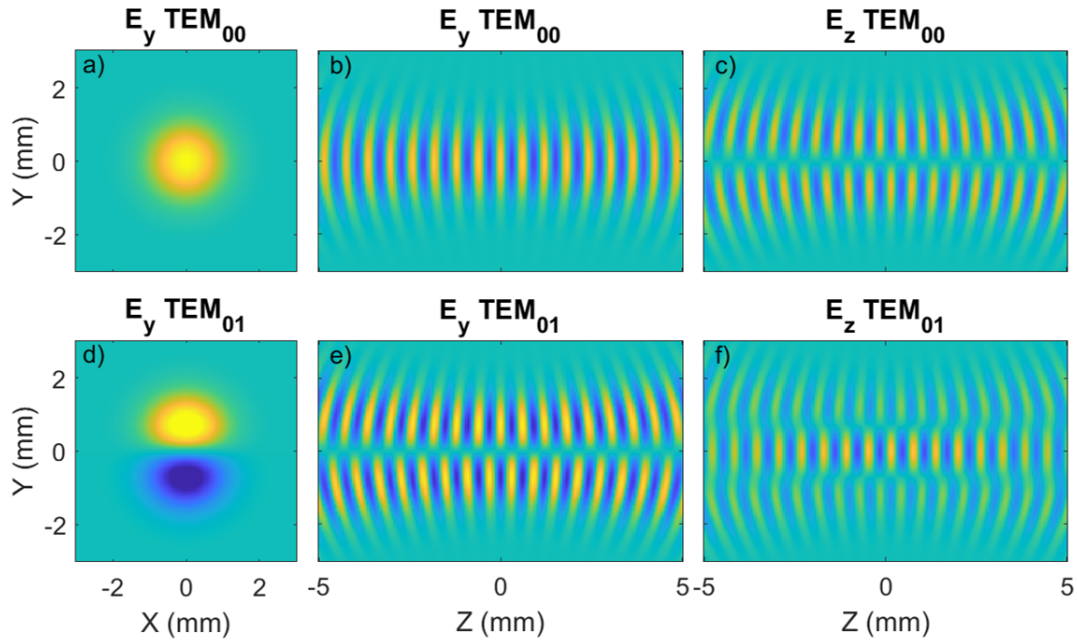

Figure 6: Transverse electric field in the X-Y plane is plotted in **a)** and **d)** for the TEM_{00} and TEM_{01} modes respectively. Transverse electric field in the Z-Y plane is plotted in **b)** and **e)** and longitudinal electric field in the Z-Y plane is plotted in **c)** and **f)**.

$$\widetilde{\mathrm{E}}_{\mathrm{z},00}(\mathrm{x},\mathrm{y},\mathrm{z},\omega) = -\frac{\mathrm{E}_0\,\mathrm{w}_0}{\mathrm{k}\,\mathrm{w}(\mathrm{z})}\,\mathrm{e}^{-(\mathrm{x}^2+\mathrm{y}^2)/\mathrm{w}^2(\mathrm{z})}\left(\frac{2\,\mathrm{y}\,\mathrm{i}}{\mathrm{w}^2(\mathrm{z})}+\frac{\mathrm{k}\,\mathrm{y}}{\mathrm{R}(\mathrm{z})}\right)\mathrm{e}^{\mathrm{i}\,\varphi}\ . \tag{86}$$

The axial transverse field is at a maximum for this Gaussian mode and the longitudinal field is zero on-axis, as plotted in figure 6c. A TEM_{01} mode pulse has a longitudinal field that is expressed by

$$\widetilde{\mathrm{E}}_{\mathrm{z},01}(\mathrm{x},\mathrm{y},\mathrm{z},\omega) = \frac{\mathrm{E}_0\,\mathrm{w}_0}{\mathrm{k}\,\mathrm{w}^2(\mathrm{z})}\,\mathrm{e}^{-(\mathrm{x}^2+\mathrm{y}^2)/\mathrm{w}^2(\mathrm{z})}\left(\mathrm{i}-\frac{2\,\mathrm{y}^2\,\mathrm{i}}{\mathrm{w}^2(\mathrm{z})}-\frac{\mathrm{k}\,\mathrm{y}^2}{\mathrm{R}(\mathrm{z})}\right)\mathrm{e}^{\mathrm{i}\,\varphi}\ . \tag{87}$$

A laser pulse in this Gaussian-Hermite mode has a maxima in the longitudinal field on-axis and has $\mathrm{E}_\mathrm{y} = 0$ at $\mathrm{y} = 0$, as plotted in figure 6f, so is suitable for particle acceleration.

The definition above assumes a single frequency laser. A pulse with a finite bandwidth can be defined in the frequency domain as the product of a spectral shape term, $\widetilde{\mathrm{A}}(\omega)$, and the single frequency electric field definition, $\widetilde{\mathrm{E}}_\mathrm{y}(\mathrm{x},\mathrm{y},\mathrm{z},\omega)$. The time domain field is given by the inverse Fourier transform

$$\mathrm{E}_\mathrm{y}(\mathrm{x},\mathrm{y},\mathrm{z},\mathrm{t}) = \int_{-\infty}^{\infty}\widetilde{\mathrm{A}}(\omega)\,\widetilde{\mathrm{E}}_\mathrm{y}(\mathrm{x},\mathrm{y},\mathrm{z},\omega)\,\mathrm{e}^{\mathrm{i}\,\omega\,\mathrm{t}}\,\mathrm{d}\omega\ \ , \tag{88}$$

which gives a laser pulse of finite duration.

2.2.3 Electron Acceleration

In order to estimate the energy gain from a laser pulse interacting with an electron, the average field over an interaction length, d, is required. To calculate both of these, the electron velocity and the laser phase and group velocity are needed. The on-axis phase velocity of a focusing electro-magnetic pulse in free-space is larger than the speed of light due to the Gouy phase shift. At the focus, the phase and group velocities can be approximated for a fundamental Gaussian as [95]

$$\mathrm{v_p/c} = 1 + \frac{2}{\mathrm{k^2\, w_0^2}} \,, \tag{89}$$

$$\mathrm{v_g/c} = 1 - \frac{2}{\mathrm{k^2\, w_0^2}} \,. \tag{90}$$

For tighter focusing, the phase velocity is higher, hence the velocity mismatch between the pulse phase and an electron is greater. Assuming a free-space interaction between a relativistic charged particle and an electromagnetic field, due to this mismatch, if the interaction is allowed to continue to infinity, it will yield a net energy gain of zero. This is the Lawson-Woodward theorem [17] which essentially states that an electron will experience the same magnitude of positive and negative electric field in this scenario. To achieve significant acceleration of a particle in an electro-magnetic field, the interaction needs to violate assumptions within the Lawson-Woodward theorem which can be summarised as:

1. The electron velocity does not change due to the interaction.
2. The interaction continues to infinity.
3. The interaction occurs in free-space.

The first case in which acceleration can occur is interaction with a sub-relativistic electron. As an electron passes through a focusing laser pulse field, it is accelerated by positive components and decelerated by negative components. In the sub-relativistic regime, this corresponds to a changing velocity, hence variable phase velocity mismatch. A net energy change can be achieved because of this, but it is not an energy efficient method of particle acceleration since both positive and negative accelerating phases contribute. In free-space, acceleration can be achieved by only allowing the particle to interact with a finite region of the accelerating field. Experimentally, there are significant challenges in implementing this, but in [17], a mathematical description of electron acceleration by a radially symmetric higher order Gaussian mode is given nonetheless. This mode is chosen to maximise the longitudinal field on-axis. A particle travelling at a velocity close to the speed of light will slip with respect to the accelerating field phase due to the Guoy

phase shift. As depicted in figure 7 by the black line, the field experienced by this particle will fall to zero at $z = \pm z_R$. It concludes in [17] that for a highly relativistic particle, assuming the particle is injected and extracted at the ideal positions as illustrated in figure 7, the maximum energy gain is approximately

$$\Delta W_{max} = e\, E_0\, w_0 \ , \tag{91}$$

where the maximum longitudinal field in this mode is given by $E_z = 2E_0/kw_0$. For a calculation of the best case scenario of acceleration with laser generated THz radiation, parameters given in [96] for a high field THz source are used ($E_0 = 120\,\mathrm{MV/m}$, $w_0 = 250\,\mu\mathrm{m}$) with 100 % efficiency of coupling into the higher order Gaussian mode assumed. This would yield an energy gain of $\approx 30\,\mathrm{keV}$. The inefficiency of this interaction stems from the fact that it only interacts over twice the Rayleigh length, which in this case corresponds to $\approx 680\,\mu\mathrm{m}$ at 1 THz, and that it samples through π phase of the accelerating field over that distance. The interaction length can be increased by using a larger spot size, but the corresponding decrease in the field amplitude cancels any efficiency gain. The interaction length is even shorter for an interaction in free-space with a sub-relativistic particle since the pulse phase velocity to electron velocity mismatch is greater, which means the interaction in free-space is less efficient, as depicted in figure 7.

For optimal efficiency, the phase velocity of the THz pulse should match the electron velocity so that the interaction length can be extended and the electron always interacts with the peak THz field. This is not the case in free space but can be achieved in specially designed structures.

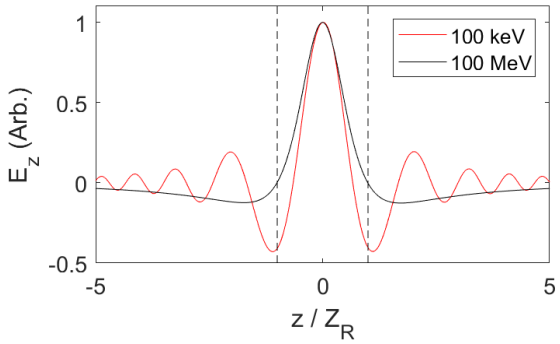

Figure 7: The longitudinal electric field experienced by particles with energies of 100 keV and 100 MeV. Propagation distance is in terms of the Rayleigh length, Z_R.

2.2.4 Dielectric-Lined Waveguides

Waveguides are used to modify how an electro-magnetic pulse propagates. It was shown in [97] that freely propagating THz pulses can couple into metal waveguides of suitable size for spectroscopy applications. Several waveguide geometries have been explored for this application such as parallel plate waveguides [98, 99], metal wire waveguides [100, 101] and metallic slot waveguides [102]. In the simplest case, a waveguide can be a hollow conducting structure with a uniform cross-section [103]. For a guide such as this, the phase and group velocity of a given mode are

$$v_p = \frac{c}{\sqrt{1 - \left(\frac{f_c}{f}\right)^2}} , \quad \text{for } f_c > 0 , \tag{92}$$

$$v_g = \frac{c^2}{v_p} , \tag{93}$$

where f_c is the cutoff frequency of the mode. Below this frequency, the propagation constant is imaginary, so the wave is evanescent and decays in amplitude exponentially. The phase velocity for a wave propagating within a waveguide governed by this relation is always greater than the speed of light in vacuum and is unsuitable for acceleration of particles, which always have a velocity lower than c. If the metallic walls are lined with a dielectric material [104], lower phase velocities can be achieved, opening up the opportunity for phase-matched particle acceleration [57, 105]. Here we discuss a dielectric-lined waveguide (DLW) with a rectangular cross-section.

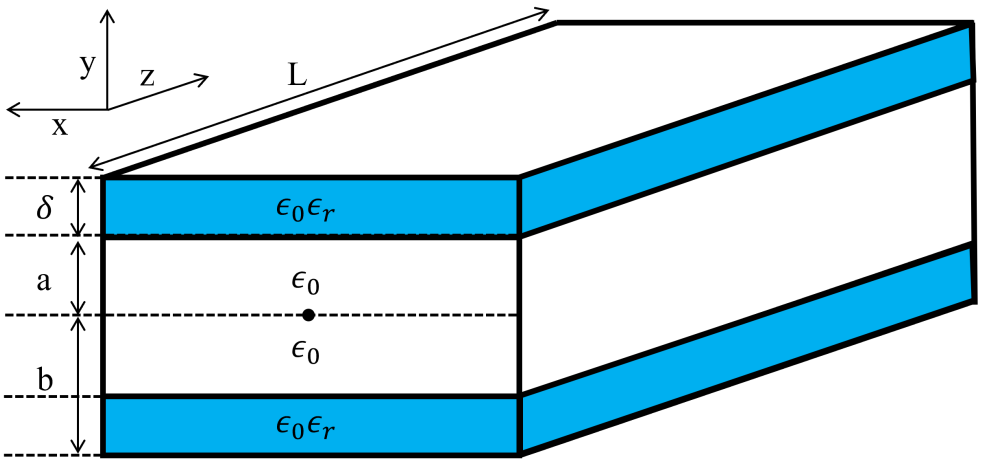

Figure 8: Typical geometry of a dielectric-lined waveguide (DLW). The origin is at the centre of the cross-section.

A rectangular DLW as depicted in figure 8 is considered here. The field within this can be written as a superposition of modes which satisfy the boundary condition that the parallel electric fields at the perfectly conducting metal walls are zero [106]. For a rectangular DLW, these modes are termed longitudinal section electric (LSE) and longitudinal section magnetic (LSM) modes, where $\mathrm{LSE_{mn}}$ modes are derived by setting one of the transverse electric components to zero and $\mathrm{LSM_{mn}}$ modes have a transverse magnetic component set to zero. The subscript m can take any positive integer whilst n can be any positive integer or 0. The set of modes, $\mathrm{LSM_{mn}}$, can be split into odd and even modes, depending on the parity of n. The field components in the LSM modes can be derived by defining Hertz scalar potentials which satisfy the boundary condition at the metal walls, as well as the wave equation [107]. The field is symmetrical around $\mathrm{y} = 0$. Fields here are defined for the top half of the DLW. The scalar potentials for the odd modes are given by

$$\psi_{mn} = \begin{cases} \mathrm{A_{mn}} \sin\left(\frac{\mathrm{m}\,\pi}{\mathrm{w}}\left(\mathrm{x} + \frac{\mathrm{w}}{2}\right)\right) \sin\left(\mathrm{k_y^{(0)}\,y}\right), & \text{if } 0 \leq \mathrm{y} \leq \mathrm{a}\,, \\ \mathrm{B_{mn}} \sin\left(\frac{\mathrm{m}\,\pi}{\mathrm{w}}\left(\mathrm{x} + \frac{\mathrm{w}}{2}\right)\right) \cos\left(\mathrm{k_y^{(1)}}\,(\mathrm{b} - \mathrm{y})\right), & \text{if } \mathrm{a} < \mathrm{y} \leq \mathrm{b}\,, \end{cases} \tag{94}$$

where b is the vacuum half aperture, a, plus the dielectric thickness, δ, and w is the width of the waveguide. Superscripts 0 and 1 denote vacuum and dielectric regions, respectively, $\mathrm{A_{mn}}$ and $\mathrm{B_{mn}}$ are constants and the transverse wavenumbers are

$$\mathrm{k_{y,\,mn}^{(0)}} = \sqrt{\mathrm{k_0^2} - \left(\frac{\mathrm{m}\pi}{\mathrm{w}}\right)^2 - \beta_{\mathrm{mn}}^2}\,, \tag{95}$$

$$\mathrm{k_{y,\,mn}^{(1)}} = \sqrt{\epsilon_{\mathrm{r}}\,\mathrm{k_0^2} - \left(\frac{\mathrm{m}\pi}{\mathrm{w}}\right)^2 - \beta_{\mathrm{mn}}^2}\,, \tag{96}$$

where β_{mn} is the longitudinal wavenumber. For even modes the scalar potential is given by

$$\psi_{mn} = \begin{cases} \mathrm{A_{mn}} \sin\left(\frac{\mathrm{m}\,\pi}{\mathrm{w}}\left(\mathrm{x} + \frac{\mathrm{w}}{2}\right)\right) \cos\left(\mathrm{k_y^{(0)}\,y}\right), & \text{if } 0 \leq \mathrm{y} \leq \mathrm{a}\,, \\ \mathrm{B_{mn}} \sin\left(\frac{\mathrm{m}\,\pi}{\mathrm{w}}\left(\mathrm{x} + \frac{\mathrm{w}}{2}\right)\right) \cos\left(\mathrm{k_y^{(1)}}\,(\mathrm{b} - \mathrm{y})\right), & \text{if } \mathrm{a} < \mathrm{y} \leq \mathrm{b}\,. \end{cases} \tag{97}$$

Field components can be expressed in terms of this scalar potential by rewriting the wave equation in terms of the Hertz potential, which leads to

$$\mathrm{E_{x,mn}} = \frac{\partial \psi_{\mathrm{mn}}}{\partial \mathrm{x} \partial \mathrm{y}} \ , \tag{98}$$

$$\mathrm{E_{y,mn}} = \frac{\partial^2 \psi_{mn}}{\partial \mathrm{y}^2} + \epsilon_{\mathrm{r}}\, \mathrm{k}_0^2\, \psi_{\mathrm{mn}} \ , \tag{99}$$

$$\mathrm{E_{z,mn}} = -\mathrm{i}\, \beta_{\mathrm{mn}}\, \frac{\partial \psi_{\mathrm{mn}}}{\partial \mathrm{y}} \ , \tag{100}$$

$$\mathrm{H_{x,mn}} = -\omega\, \epsilon_0\, \beta_{\mathrm{mn}}\, \psi_{\mathrm{mn}} \ , \tag{101}$$

$$\mathrm{H_{y,mn}} = 0 \ , \tag{102}$$

$$\mathrm{H_{z,mn}} = -\mathrm{i}\, \omega\, \epsilon_0\, \frac{\partial \psi_{\mathrm{mn}}}{\partial \mathrm{x}} \ . \tag{103}$$

These equations can be expanded to express the field components for the vacuum and dielectric regions for odd modes

$$\mathrm{E_{x,mn}}(\mathrm{x},\mathrm{y},0,\omega) = \begin{cases} \mathrm{A_{mn}}\, \frac{\mathrm{m}\pi}{\mathrm{w}}\, \mathrm{k_y^{(0)}} \cos\left(\frac{\mathrm{m}\pi}{\mathrm{w}}(\mathrm{x}+\frac{\mathrm{w}}{2})\right) \cos(\mathrm{k_y^{(0)}}\, \mathrm{y}) \ , & \text{if } 0 \le \mathrm{y} \le \mathrm{a} \ , \\ \mathrm{B_{mn}}\, \frac{\mathrm{m}\pi}{\mathrm{w}}\, \mathrm{k_y^{(1)}} \cos\left(\frac{\mathrm{m}\pi}{\mathrm{w}}(\mathrm{x}+\frac{\mathrm{w}}{2})\right) \sin\left(\mathrm{k_y^{(1)}}\, (\mathrm{b}-\mathrm{y})\right) \ , & \text{if } \mathrm{a} < \mathrm{y} \le \mathrm{b} \ , \end{cases} \tag{104}$$

$$\mathrm{E_{y,mn}}(\mathrm{x},\mathrm{y},0,\omega) = \begin{cases} \mathrm{A_{mn}}\, \mathrm{k_c^2} \sin\left(\frac{\mathrm{m}\pi}{\mathrm{w}}(\mathrm{x}+\frac{\mathrm{w}}{2})\right) \sin(\mathrm{k_y^{(0)}}\, \mathrm{y}) \ , & \text{if } 0 \le \mathrm{y} \le \mathrm{a} \ , \\ \mathrm{B_{mn}}\, \mathrm{k_c^2} \sin\left(\frac{\mathrm{m}\pi}{\mathrm{w}}(\mathrm{x}+\frac{\mathrm{w}}{2})\right) \cos\left(\mathrm{k_y^{(1)}}\, (\mathrm{b}-\mathrm{y})\right) \ , & \text{if } \mathrm{a} < \mathrm{y} \le \mathrm{b} \ , \end{cases} \tag{105}$$

$$\mathrm{E_{z,mn}}(\mathrm{x},\mathrm{y},0,\omega) = \begin{cases} \mathrm{A_{mn}}\, (-\mathrm{i}\beta_{\mathrm{mn}})\, \mathrm{k_y^{(0)}} \sin\left(\frac{\mathrm{m}\pi}{\mathrm{w}}(\mathrm{x}+\frac{\mathrm{w}}{2})\right) \cos(\mathrm{k_y^{(0)}}\, \mathrm{y}) \ , & \text{if } 0 \le \mathrm{y} \le \mathrm{a} \ , \\ \mathrm{B_{mn}}\, (-\mathrm{i}\beta_{\mathrm{mn}})\, \mathrm{k_y^{(1)}} \sin\left(\frac{\mathrm{m}\pi}{\mathrm{w}}(\mathrm{x}+\frac{\mathrm{w}}{2})\right) \sin\left(\mathrm{k_y^{(1)}}\, (\mathrm{b}-\mathrm{y})\right) \ , & \text{if } \mathrm{a} < \mathrm{y} \le \mathrm{b} \ , \end{cases} \tag{106}$$

$$\mathrm{H_{x,mn}}(\mathrm{x},\mathrm{y},0,\omega) = \begin{cases} -\mathrm{A_{mn}}\, \omega\, \epsilon_0\, \beta_{\mathrm{mn}} \sin\left(\frac{\mathrm{m}\pi}{\mathrm{w}}(\mathrm{x}+\frac{\mathrm{w}}{2})\right) \sin(\mathrm{k_y^{(0)}}\, \mathrm{y}) \ , & \text{if } 0 \le \mathrm{y} \le \mathrm{a} \ , \\ -\mathrm{B_{mn}}\, \omega\, \epsilon\, \beta_{\mathrm{mn}} \sin\left(\frac{\mathrm{m}\pi}{\mathrm{w}}(\mathrm{x}+\frac{\mathrm{w}}{2})\right) \cos\left(\mathrm{k_y^{(1)}}\, (\mathrm{b}-\mathrm{y})\right) \ , & \text{if } \mathrm{a} < \mathrm{y} \le \mathrm{b} \ , \end{cases} \tag{107}$$

$$\mathrm{H_{z,mn}}(\mathrm{x},\mathrm{y},0,\omega) = \begin{cases} \mathrm{A_{mn}}\, \mathrm{i}\, \omega\, \epsilon_0\, \frac{\mathrm{m}\pi}{\mathrm{w}} \cos\left(\frac{\mathrm{m}\pi}{\mathrm{w}}(\mathrm{x}+\frac{\mathrm{w}}{2})\right) \sin(\mathrm{k_y^{(0)}}\, \mathrm{y}) \ , & \text{if } 0 \le \mathrm{y} \le \mathrm{a} \ , \\ -\mathrm{B_{mn}}\, \mathrm{i}\, \omega\, \epsilon\, \frac{\mathrm{m}\pi}{\mathrm{w}} \cos\left(\frac{\mathrm{m}\pi}{\mathrm{w}}(\mathrm{x}+\frac{\mathrm{w}}{2})\right) \cos\left(\mathrm{k_y^{(1)}}\, (\mathrm{b}-\mathrm{y})\right) \ , & \text{if } \mathrm{a} < \mathrm{y} \le \mathrm{b} \ , \end{cases} \tag{108}$$

where $\mathrm{k_c} = \sqrt{(\mathrm{m}\pi/\mathrm{w})^2 + \beta_{\mathrm{mn}}^2}$. The relation between the $\mathrm{A_{mn}}$ and $\mathrm{B_{mn}}$ coefficients can be found by equating tangential electric and magnetic field components on the vacuum-dielectric boundary, y = a, leading to the conditions

$$\begin{aligned} \mathrm{A_{mn}}\, \mathrm{k_y^{(0)}} \cos(\mathrm{k_y^{(0)}}\, \mathrm{a}) &= \mathrm{B_{mn}}\, \mathrm{k_y^{(1)}} \sin\left(\mathrm{k_y^{(1)}}\, (\mathrm{b}-\mathrm{a})\right) \ , \\ \mathrm{A_{mn}} \sin(\mathrm{k_y^{(0)}}\, \mathrm{a}) &= \mathrm{B_{mn}}\, \epsilon_{\mathrm{r}} \cos\left(\mathrm{k_y^{(1)}}\, (\mathrm{b}-\mathrm{a})\right) \ . \end{aligned} \tag{109}$$

To give the field dependence in the z direction, equations 104-108 need to be multiplied by a factor of exp(-iβ_{mn}z). The field components for even modes are given by

$$E_{x,mn}(x,y,0,\omega) = \begin{cases} A_{mn}\,\frac{m\pi}{w}\,k_y^{(0)}\cos\left(\frac{m\pi}{w}(x+\frac{w}{2})\right)\,\sin(k_y^{(0)}\,y)\,, & \text{if } 0 \le y \le a\,, \\ B_{mn}\,\frac{m\pi}{w}\,k_y^{(1)}\cos\left(\frac{m\pi}{w}(x+\frac{w}{2})\right)\,\sin\left(k_y^{(1)}\,(b-y)\right)\,, & \text{if } a < y \le b\,, \end{cases} \tag{110}$$

$$E_{y,mn}(x,y,0,\omega) = \begin{cases} A_{mn}\,k_c^2\sin\left(\frac{m\pi}{w}(x+\frac{w}{2})\right)\,\cos(k_y^{(0)}\,y)\,, & \text{if } 0 \le y \le a\,, \\ B_{mn}\,k_c^2\sin\left(\frac{m\pi}{w}(x+\frac{w}{2})\right)\,\cos\left(k_y^{(1)}\,(b-y)\right)\,, & \text{if } a < y \le b\,, \end{cases} \tag{111}$$

$$E_{z,mn}(x,y,0,\omega) = \begin{cases} A_{mn}\,(-i\beta_{mn})\,k_y^{(0)}\sin\left(\frac{m\pi}{w}(x+\frac{w}{2})\right)\,\sin(k_y^{(0)}\,y)\,, & \text{if } 0 \le y \le a\,, \\ B_{mn}\,(-i\beta_{mn})\,k_y^{(1)}\sin\left(\frac{m\pi}{w}(x+\frac{w}{2})\right)\,\sin\left(k_y^{(1)}\,(b-y)\right)\,, & \text{if } a < y \le b\,, \end{cases} \tag{112}$$

$$H_{x,mn}(x,y,0,\omega) = \begin{cases} -A_{mn}\,\omega\,\epsilon_0\,\beta_{mn}\sin\left(\frac{m\pi}{w}(x+\frac{w}{2})\right)\,\cos(k_y^{(0)}\,y)\,, & \text{if } 0 \le y \le a\,, \\ -B_{mn}\,\omega\,\epsilon\,\beta_{mn}\sin\left(\frac{m\pi}{w}(x+\frac{w}{2})\right)\,\cos\left(k_y^{(1)}\,(b-y)\right)\,, & \text{if } a < y \le b\,, \end{cases} \tag{113}$$

$$H_{z,mn}(x,y,0,\omega) = \begin{cases} A_{mn}\,i\,\omega\,\epsilon_0\,\frac{m\pi}{w}\cos\left(\frac{m\pi}{w}(x+\frac{w}{2})\right)\,\cos(k_y^{(0)}\,y)\,, & \text{if } 0 \le y \le a\,, \\ -B_{mn}\,i\,\omega\,\epsilon\,\frac{m\pi}{w}\cos\left(\frac{m\pi}{w}(x+\frac{w}{2})\right)\,\cos\left(k_y^{(1)}\,(b-y)\right)\,, & \text{if } a < y \le b\,. \end{cases} \tag{114}$$

The conditions on the A_{mn} and B_{mn} coefficients for even modes are then

$$\begin{aligned} A_{mn}\,k_y^{(0)}\sin(k_y^{(0)}\,a) &= B_{mn}\,k_y^{(1)}\sin\left(k_y^{(1)}\,(b-a)\right)\,, \\ A_{mn}\cos(k_y^{(0)}\,a) &= B_{mn}\,\epsilon_r\cos\left(k_y^{(1)}\,(b-a)\right)\,. \end{aligned} \tag{115}$$

The dispersion relation for LSM_{mn} modes can be found by solving the two pairs of simultaneous equations in 109 and 115 to cancel the coefficients A_{mn} and B_{mn}. The dispersion relation for odd LSM modes is governed by [106]

$$k_{y,mn}^{(1)}\tan(k_{y,mn}^{(1)}\,\delta) = \epsilon_r\,k_{y,mn}^{(0)}\cot(k_{y,mn}^{(0)}\,a)\,. \tag{116}$$

Equation 116 has an infinite number of solutions which are labelled n = 1, 3, 5, etc in order of ascending cutoff frequency. The dispersion relation for a given even LSM mode can be derived from [107]

$$k_{y,mn}^{(1)}\tan(k_{y,mn}^{(1)}\,\delta) = -\epsilon_r\,k_{y,mn}^{(0)}\tan(k_{y,mn}^{(0)}\,a)\,, \tag{117}$$

where solutions are labelled n = 2, 4, 6, etc in order of ascending cutoff frequency. These transcendental dispersion equations must be solved numerically to find the dispersion relation for a certain mode.

Even modes have zero longitudinal electric field on-axis but have a non-zero transverse field. This feature makes these modes applicable for electron beam deflection. Exploitation of odd modes is more appropriate for accelerating structures. A maxima in the longitudinal electric field can be found on-axis for LSM_{mn} modes where n and m are odd. These modes also have zero transverse field on-axis. With correct choice of the waveguide dimensions, the phase velocity of an accelerating mode can be chosen to match a certain electron velocity. The limiting factor to the interaction length then becomes the THz group velocity to electron velocity mismatch, which leads to slippage between the accelerating field envelope and the particle bunch. The interaction length can still be increased to millimetre scale in DLWs though whilst keeping the spot size small.

2.2.5 Velocity Bunching

For low energy beams where the velocity remains affected by the electron energy, bunch compression can be achieved by applying a time dependent acceleration to a bunch. Deceleration of the front of the electron bunch and acceleration of the back of the bunch can lead to a significant velocity difference between the front and the back of the bunch in the sub-relativistic regime. The drift length required between the application of a bunch energy chirp and the longitudinal focus of the beam can be found by equating the time taken for the bunch, travelling at an average velocity, v, to travel this distance, f_d, and the time taken for two electrons in the bunch, separated by a distance Δz with velocity difference Δv, to reach the same z position [108]

$$\frac{f_d}{v} = \frac{\Delta z}{\Delta v} \, . \tag{118}$$

In order to express this velocity in terms of energy, the velocity is replaced with $\beta = v/c$, and the longitudinal focal distance is written in terms of distance between electrons and the fractional difference in their β

$$f_d = \frac{\Delta z}{(\Delta\beta/\beta)} \, . \tag{119}$$

The Taylor expansion of the $\Delta\beta/\beta$ term can be expressed in terms of γ and, only taking the first order, can be written as

$$\frac{\Delta\beta}{\beta} = \frac{\Delta\gamma}{\beta}\frac{\partial\beta}{\partial\gamma} = \frac{\Delta\gamma}{\beta^2\,\gamma^3} \, . \tag{120}$$

Substituting this into the equation for the focal distance, and assuming the energy chirp is the constant along the bunch gives

$$f_d = \frac{\beta^2\,\gamma^3}{(\frac{d\gamma}{dz})} \, . \tag{121}$$

Replacing γ with the bunch kinetic energy, the focal distance can be written in terms of the bunch chirp [71]

$$f_d = \frac{m_e c^2 \beta^2 \gamma^3}{\left(\frac{dE_k}{dz}\right)} = \frac{m_e \beta^2 (c\gamma)^3}{\left(\frac{dE_k}{dt}\right)} . \tag{122}$$

The assumptions implied here are that space charge is not significant, that the bunch has no initial correlated energy spread and that the acceleration is linear along the bunch length. In practice, space charge and uncorrelated energy spread limit the achievable bunch length. The initial correlated energy spread is something that the accelerating field has to overcome so equation 122 alone may lead to an underestimate of the required peak field.

The effect of the bunch duration being significant compared to the THz period is shown in figure 9. A picosecond scale duration bunch longitudinal phase space is initialised in 9a and is then modulated at 0.5 THz with a sinusoidal field, as shown in 9b. Due to the velocity difference along the bunch, at some drift length the longitudinal phase space looks like 9c. Towards the centre of the bunch, where a linear field gradient is experienced by the bunch, bunching occurs as described above. Further from the centre, when the sinusoidal nature of the modulation can be seen, the electrons do not reach the longitudinal focus at the same point as the central electrons. If the electron bunch duration extended over multiple THz periods, charge spikes would be seen, after a drift length, at time periods within the bunch where a negative chirp had been gained.

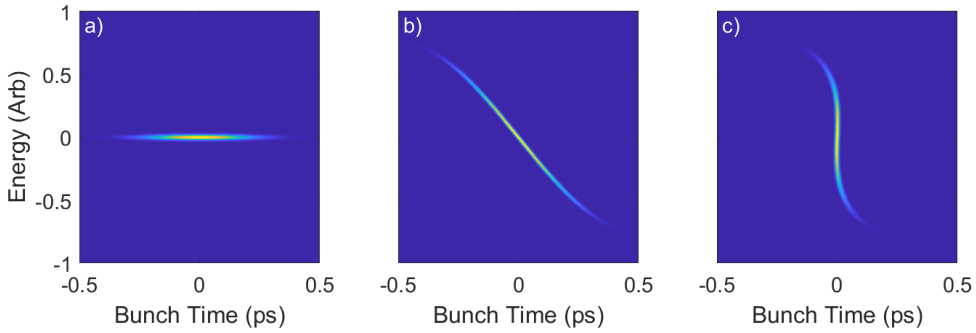

Figure 9: Demonstration of velocity bunching with a sinusoidal field. The initial beam longitudinal phase space is plotted in **a)** and the modulated phase space is plotted in **b)**. In **c)**, the bunch longitudinal phase space is shown after some drift length.

2.2.6 THz-Driven Streaking

Both transverse electric and magnetic fields need to be considered for electron deflection since the desired electron motion is perpendicular to its initial direction of travel. From equation 76, velocity gain in the y direction for a particle travelling the z direction is governed, for small velocity, gains by

$$\frac{\mathrm{d}\beta_\mathrm{y}}{\mathrm{dt}} = \frac{\mathrm{q}}{\mathrm{m}\gamma\mathrm{c}} \left(\mathrm{E_y} + \mathrm{c}\,\beta_\mathrm{z}\,\mathrm{B_x} - \beta_\mathrm{y}\left(\mathbf{E}\cdot\boldsymbol{\beta}\right)\right) . \tag{123}$$

Free-space plane waves travelling in the z direction have $\left|\frac{\mathrm{B_x}}{\mathrm{E_y}}\right| = \frac{1}{\mathrm{c}}$, so the forces on a highly relativistic electron due to transverse electric and magnetic fields cancel. An electron with velocity significantly less than c will experience a net force from the electric field. The same principles behind achieving efficient acceleration, as described in 2.2.3, still apply. Where we have real, non-plane waves, deflection is possible around the Rayleigh length focal region. In the sub-relativistic case though, phase velocity mismatch in free-space still limits interaction efficiency. Even modes in a dielectric-lined waveguide can allow propagation of on-axis transverse fields at phase velocities matched with electron velocities.

THz-driven streaking is an electron bunch duration diagnostic which utilises THz-driven deflection. If a time-dependent transverse kick is given to an electron bunch, the measured transverse profile at a later point will contain information about the longitudinal bunch profile. The transverse position of an electron at a screen, $\mathrm{y_s}$ placed $\mathrm{L_d}$ from an interaction where a transverse velocity it gained is

$$\mathrm{y_s} = \mathrm{L_d}\tan^{-1}\left(\frac{\beta_\mathrm{y}}{\beta_\mathrm{z}}\right) \approx \mathrm{L_d}\,\frac{\beta_\mathrm{y}}{\beta_\mathrm{z}} . \tag{124}$$

In the ideal case of an electron bunch with zero initial transverse size and β_y is a sinusoidal function of bunch time at a known frequency, the transverse position at the screen position becomes

$$\mathrm{y_s} = \mathrm{L_d}\,\frac{\sin(\omega\,\mathrm{t})}{\beta_\mathrm{z}} . \tag{125}$$

Assuming the centre of the bunch overlaps with the highest gradient portion of the sinusoid, a certain position on the screen can be attributed to a unique time within the bunch as long as the bunch duration is less than half the period of the modulation. This is demonstrated in figure 10. Experimentally, this procedure is performed the opposite way around to retrieve the bunch length given a known deflecting field and measured difference in transverse size on the screen due to the deflection [109].

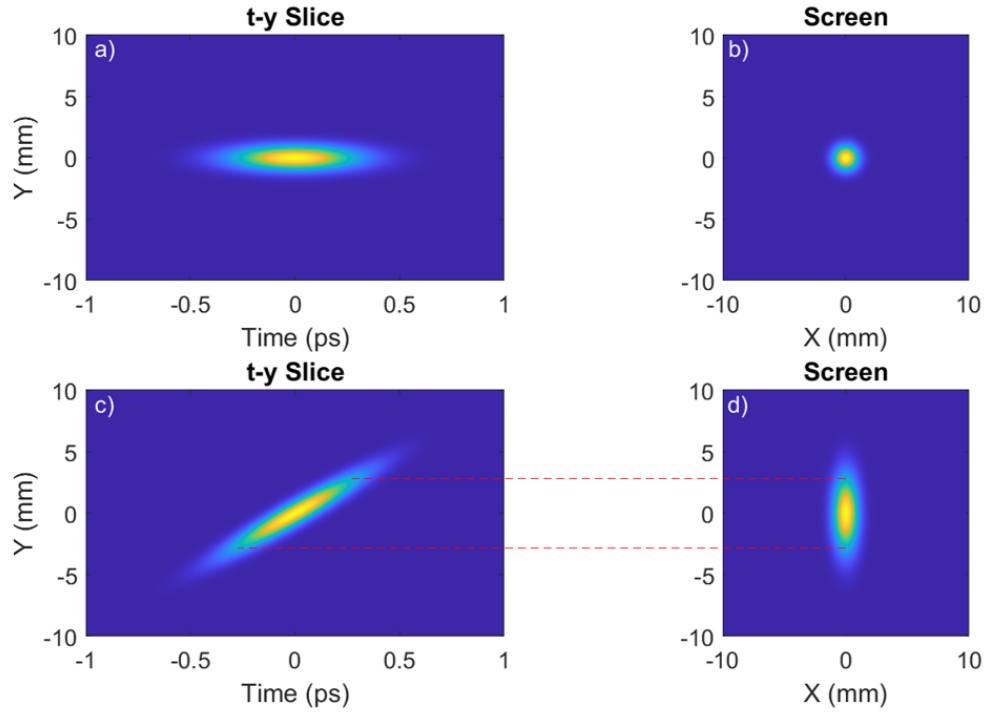

Figure 10: **a)** and **b)** depict an electron bunch time profile and transverse profile, respectively. If the electron bunch is given a time dependent transverse kick, the time profile in **a)** becomes **c)** and the transverse profile in **b)** becomes **d)**. Information about the bunch duration is now projected onto the transverse plane.

2.3 Numerical Methods for Electromagnetic Field and Particle Propagation

The laser waist of a Gaussian pulse as a function of position within an optical system is often required for designing an imaging system. Gaussian propagation is a helpful tool for free space pulse propagation and will be discussed in section 2.3.1. The field profile of Gaussian pulse in a medium with a known dispersion relation can be estimated at a later point in time in the frequency domain with a shift in the first order spectral phase. For propagation of complex, non-Gaussian fields in free space over significant distances (centimetre-scale and beyond), Kirchoff diffraction theory can be applied to calculate the field as a function of position and time. This method is detailed in section 2.3.2. In the case of fields propagation over short distances (typically millimetre-scale) through dispersive structures, the Finite-Difference Time-Domain (FDTD) method, discussed in section 2.3.3, can be implemented.

Given known electro-magnetic fields over a simulation region, a particle's posi-

tion at discrete time steps can be calculated by solving the particle's equations of motion. Runge-Kutta methods, as described in section 2.3.4, are a class of iterative methods which can be implemented to numerically solve differential equations and are commonly used in particle tracking simulations.

2.3.1 Gaussian Beam Propagation

Gaussian beam parameters can be tracked throughout an optical system with the use of ABCD matrices [93]. The complex q parameter is defined as a function of the properties of a Gaussian beam shape which vary with z

$$\frac{1}{\mathrm{q(z)}} = \frac{1}{\mathrm{R(z)}} + \frac{\mathrm{i}\,\lambda}{\pi\,\mathrm{w(z)}^2}\ . \tag{126}$$

If this parameter is known at an initial point, $\mathrm{q}(\mathrm{z}_0)$, the parameter at a point later in the optical system can be calculated using ABCD matrices. These 2×2 matrices are defined for a particular beam optic, such as a drift or a lens, and applied to $\mathrm{q}(\mathrm{z}_0)$ to calculate q at a later point by

$$\mathrm{q(z)} = \frac{\mathrm{A\,q}(\mathrm{z}_0) + \mathrm{B}}{\mathrm{C\,q}(\mathrm{z}_0) + \mathrm{D}}\ . \tag{127}$$

By calculating q(z), the beam waist and curvature can be calculated throughout an optical system with focusing elements. For a drift length, L, in vacuum, the ABCD matrix is

$$\begin{pmatrix} \mathrm{A} & \mathrm{B} \\ \mathrm{C} & \mathrm{D} \end{pmatrix} = \begin{pmatrix} 1 & \mathrm{L} \\ 0 & 1 \end{pmatrix}\ . \tag{128}$$

For a thin lens with focal length f, the ABCD matrix is given by

$$\begin{pmatrix} \mathrm{A} & \mathrm{B} \\ \mathrm{C} & \mathrm{D} \end{pmatrix} = \begin{pmatrix} 1 & 0 \\ -1/\mathrm{f} & 1 \end{pmatrix}\ . \tag{129}$$

Gaussian beam propagation has been implemented in MATLAB for tracking of the beam waist through focusing systems. Firstly, the focal lengths of optics are defined, along with the drift length between them. For each wavelength to be considered, the complex q parameter is calculated given an initial beam waist and radius of curvature (infinite for a collimated beam). Drift lengths are broken up so that the waist can be calculated throughout the system by applying the drift matrix (equation 128). After each drift, the thin lens matrix (equation 129) is applied to q. Figure 11 shows an example of the code output at 800 nm using two lenses with f = 200 mm and f = 100 mm respectively.

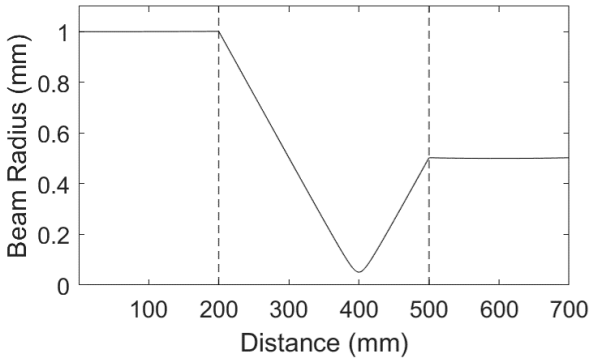

Figure 11: Gaussian propagation code output given an 800 nm laser with an f = 200 mm lens and a f = 100 mm lens. Lens positions are denoted by black dotted lines.

2.3.2 Field Propagation Method based on Kirchhoff Diffraction Theory

The Kirchhoff diffraction integral gives a formalism that can predict the electric field at a point, P, in the image plane, from the electric field at a point, Q, in the source plane [110]. For a monochromatic source, the electric field at a point P, is given by

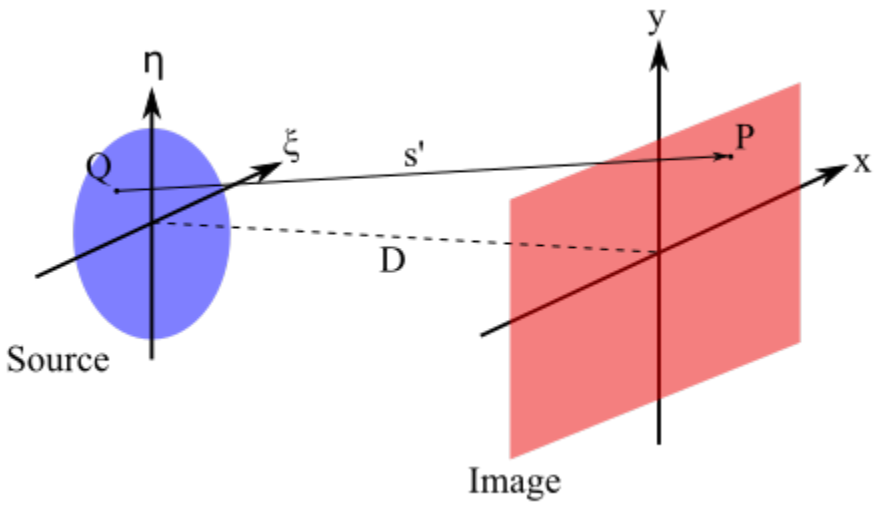

Figure 12: Sketch of the geometry used to define the Kirchhoff diffraction integral for diffraction at a circular aperture. The aperture is labelled as the source plane and the plane at which the electric field is to be calculated is labelled the image plane. Courtesy of Connor Mosley.

$$\mathrm{E(P)} = \frac{1}{4\pi}\int_{\mathrm{S}}\left[\mathrm{E(Q)}\,\frac{\partial}{\partial \mathrm{n}}\left(\frac{\mathrm{e}^{\mathrm{iks}}}{\mathrm{s}}\right) - \left(\frac{\mathrm{e}^{\mathrm{iks}}}{\mathrm{s}}\right)\,\frac{\partial \mathrm{E(Q)}}{\partial \mathrm{n}}\right]\mathrm{dS}\,, \tag{130}$$

where n denotes a derivative normal to the surface, S, and s is the path between Q and P [111, 112]. Diffraction at a circular aperture can be described using equation 130 by assuming a spherical wave source

$$\mathrm{E} = \frac{\mathrm{E}_0}{\mathrm{r}}\,\mathrm{e}^{\mathrm{ikr}}\,, \tag{131}$$

where E_0/r is the amplitude at a distance r from a point source origin. At Q, this is assumed to be incident on an opaque screen with a circular aperture which is much greater than the wavelength, but less than the distance, s. An example geometry is shown in figure 12, for which equation 130 can be rewritten

$$\mathrm{E(P)} = \frac{-\mathrm{ikE}_0}{2\pi}\int_{\mathrm{S}}\frac{\mathrm{e}^{\mathrm{ik(r+s)}}}{\mathrm{rs}}\,\left(\frac{\cos(\theta_{\mathrm{s}}) - \cos(\theta_{\mathrm{r}})}{2}\right)\mathrm{dS}\,, \tag{132}$$

where $1/\mathrm{sr}^2$ and $1/\mathrm{rs}^2$ terms are neglected as they are assumed to be smaller than the $1/\mathrm{rs}$ term. θ_{s} and θ_{r} are angular differences between n, and s and r, respectively. Assuming the point source of the spherical wave is at minus infinity and ensuring $\mathrm{x},\,\mathrm{y} \ll \mathrm{D}$ in figure 12, the cosine terms sum to equal 2 and the influence of r can be neglected. The distance from the centre of the aperture to the point, P, on the image plane is given by $\mathrm{s} = \sqrt{\mathrm{D}^2 + \mathrm{x}^2 + \mathrm{y}^2}$. The field at P is an integral over the full source surface. The distance from an arbitrary point in the source to P is

$$\mathrm{s}' = \sqrt{\mathrm{D}^2 + (\mathrm{x}-\xi)^2 + (\mathrm{y}-\eta)^2} \approx \mathrm{s} - \frac{\mathrm{x}\xi + \mathrm{y}\eta}{\mathrm{s}} + \frac{\xi^2 + \eta^2}{2\mathrm{s}} \tag{133}$$

where a first order binomial expansion is used to simplify the expression. For this case, equation 132 becomes

$$\mathrm{E(P)} = \frac{-\mathrm{ikE}_0}{2\pi}\int_{\mathrm{S}}\frac{\mathrm{e}^{\mathrm{iks}'}}{\mathrm{s}'}\,\mathrm{dS}\,. \tag{134}$$

For a given source field, equation 134 can be written for a given frequency as

$$\widetilde{\mathrm{E}}_{\mathrm{I}}(\mathrm{P},\omega) = \frac{-\mathrm{ik}}{2\pi}\iint\widetilde{\mathrm{E}}_{\mathrm{S}}(\mathrm{Q},\omega)\,\frac{\mathrm{e}^{\mathrm{iks}'}}{\mathrm{s}'}\,\mathrm{d}\xi\mathrm{d}\eta\,. \tag{135}$$

s' in terms of the distance, D, is

$$\mathrm{s}' = \sqrt{\mathrm{D}^2 + (\mathrm{x}-\xi)^2 + (\mathrm{y}-\eta)^2} \approx \mathrm{D} + \frac{\mathrm{x}^2 + \mathrm{y}^2}{2\mathrm{D}} - \frac{\mathrm{x}\xi + \mathrm{y}\eta}{\mathrm{D}} + \frac{\xi^2 + \eta^2}{2\mathrm{D}} \tag{136}$$

Substituting s' into equation 135 gives

$$\begin{aligned}\widetilde{\mathrm{E}}_{\mathrm{I}}(\mathrm{P},\omega) =& \frac{-\mathrm{ik}}{2\pi}\,\frac{\exp(\mathrm{ikD})}{2\mathrm{D}}\exp\left[\frac{\mathrm{ik}(\mathrm{x}^2+\mathrm{y}^2)}{2\mathrm{D}}\right] \\ & \iint\widetilde{\mathrm{E}}_{\mathrm{S}}(\mathrm{Q},\omega)\exp\left[\frac{\mathrm{ik}(\xi^2+\eta^2)}{2\mathrm{D}}\right]\,\exp\left[-\mathrm{i}(\mathrm{k}_{\mathrm{x}}\xi + \mathrm{k}_{\mathrm{y}}\eta)\right]\mathrm{d}\xi\mathrm{d}\eta\,,\end{aligned} \tag{137}$$

where k_x and k_y are termed transverse wavenumbers given by $k_x = kx/D$ and $k_y = ky/D$. For fast calculation of the image plane results, equation 137 can written as a 2D Fourier transform in the form

$$F(k_x, k_y) = \frac{1}{2\pi} \iint G(\xi, \eta) \exp\left[-i(k_x \xi + k_y \eta)\right] \, d\xi d\eta \, , \tag{138}$$

where

$$G(\xi, \eta) = \widetilde{E}_S(Q, \omega) \exp\left[\frac{ik(\xi^2 + \eta^2)}{2D}\right] . \tag{139}$$

The Fourier transform allows computation of the entire image plane in a single calculation whereas if equation 137 was used directly, calculation of every individual point within the image plane would require an integral over the full source plane.

For calculation of the numerical 2D fast Fourier transform (FFT) over a grid, the grid spacing needs to chosen carefully. The spatial frequency in the source plane is related to the grid spacing. In the horizontal direction, $u_x = 1/d\xi$. In the image plane, the spatial frequency can be calculated by $u_x = k_x/(2\pi)$. Using these expressions along with the definition of the transverse wavenumber gives a relation between the image grid size, Δx, and the source grid spacing

$$\Delta x = \frac{2\,\pi\,D}{k\,d\xi} \, . \tag{140}$$

An equivalent expression can be found in y and η. To accurately model the propagation of a given source field, the source and image grid must be sufficiently large so as not to clip the electric field distribution. The grid spacing must be chosen carefully to give sufficient resolution in both time and frequency domains.

Focusing optics can be implemented as transverse position dependent group delays to simulate the change in the pulse radius of curvature due to the optic. For example, the difference in path taken by an off-axis ray compared to an on-axis ray when reflected by a parabolic mirror is given by

$$\Delta z = \frac{\xi^2 + \eta^2}{4f} \, . \tag{141}$$

In the frequency domain, the shift can be applied by multiplying the field by $e^{-ik\Delta z}$.

In order to implement the Kirchhoff method in MATLAB, the optical elements in the system and the drift lengths between them need to be defined, as well as the distance from the source at which the field is to be calculated. The source spectrum, initial radius and transverse profile also need to be defined. For each

wavelength in the spectrum, the field is then projected over the source grid and equation 138 is evaluated, which gives the spatial profile at the image plane for each frequency component. The inverse FFT of the image plane field gives the electric field in terms of transverse coordinates and time at a given position in the propagation direction. In figure 13, the Kirchhoff propagation code was used to calculate the field 100 mm after a Gaussian pulse at 0.5 THz is clipped by a 3 mm radius aperture.

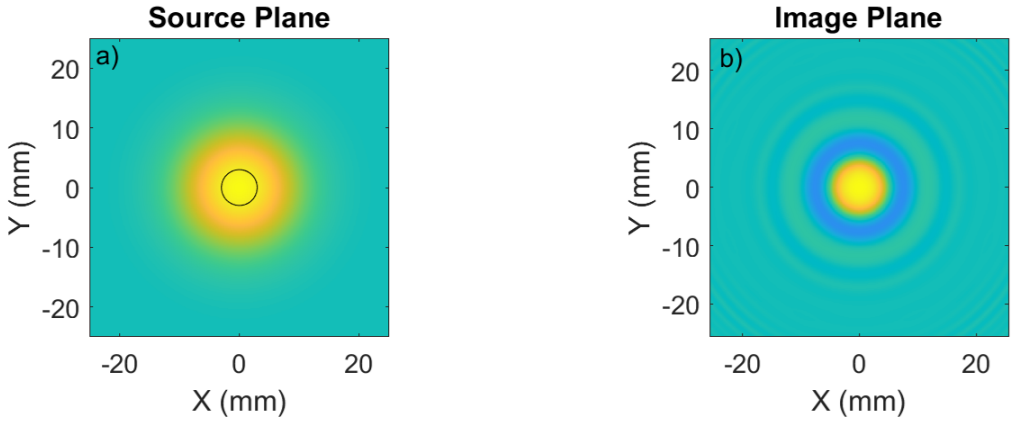

Figure 13: Calculated source plane, **a)**, and image plane, **b)**, electric field from an example usage of a MATLAB-based Kirchhoff propagation code. A Gaussian pulse with a central frequency of 0.5 THz is clipped at the source plane by an aperture with a radius of 3 mm, denoted by the black line in **a)**, and then propagates 100 mm to the image plane.

2.3.3 Finite-Difference Time-Domain Method

A propagation calculation using the FDTD method first requires the mapping of the initial electromagnetic field over a discrete spatial grid. The fields after one discrete time step are calculated by implementing update equations which are discrete solutions to Faraday's Law and Ampere's Law (equations 3 and 4). These equations state that the time dependence of the electric field is related to a spatial differential of the magnetic field, and vice versa. Spatial field differentials can be approximated on a discrete grid by taking the difference between adjacent cells. When performing the differential in this way, the location of the evaluation is actually at a mid point between the cells of the original grid. The mismatch between the location of the differential evaluations and the points at which the fields are defined leads to instability in the field propagation. Stable propagation can be achieved by staggering electric and magnetic field components spatially by half the grid step size in the direction in which differentials are taken. This is known

as the 'Yee Lattice' and is central to FDTD field propagation [113]. The electric and magnetic fields are also staggered temporally by half a time step so that field can be updated sequentially, in a 'leapfrog' manner, rather than simultaneously.

In this thesis calculations are done in 2D models, with non-zero E_x, E_z and H_y fields. These field components are assumed not to vary in the y direction. Faraday's law with a finite magnetic conductivity, σ_m, becomes [114]

$$\nabla \times \mathbf{E} = \left(\frac{\partial E_x}{\partial z} - \frac{\partial E_z}{\partial x} \right) \widehat{j} = - \left(\sigma_m H_y + \mu \frac{\partial H_y}{\partial t} \right) \widehat{j} \,, \tag{142}$$

where $\mu = \mu_{r\mu_0}$. Ampere's Law with a finite electric conductivity, σ_e, is

$$\nabla \times \mathbf{H} = \left(\frac{\partial H_y}{\partial x} \right) \widehat{k} - \left(\frac{\partial H_y}{\partial z} \right) \widehat{i} = \left(\sigma_e \mathbf{E} + \epsilon \frac{\partial \mathbf{E}}{\partial t} \right) \,, \tag{143}$$

where $\epsilon = \epsilon_r \epsilon_0$. These field components are defined over a discrete grid with a spatial step size, δ_s, and temporal step duration, δ_t, such that $\mathbf{E}(x, z, t) = \mathbf{E}(m\delta_s, n\delta_s, q\delta_t) = \mathbf{E}^q[m, n]$ and $\mathbf{H}(x, z, t) = \mathbf{H}(m\delta_s, n\delta_s, q\delta_t) = \mathbf{H}^q[m, n]$, where m, n and q are integers. As can be seen in equations 142 and 143, E_x is related to H_y by a differential in z, so these two components are spatially offset by $\delta_s/2$ is the z direction. The same logic can used to justify a separation in the x direction between the E_z field and the H_y field. Defining the magnetic field at the centre of grid points, i.e. m + 1/2, n + 1/2, an example Yee cell is depicted in figure 14. The differentials with respect to time in equations 142 and 143 mean a temporal stagger between electric and magnetic fields is also necessary. The electric field is chosen to be defined at q and the magnetic field is defined at q + 1/2. Writing equation 143 in a discrete manner and only considering the $\widehat{i}$ direction gives

$$\begin{aligned} &- \left(\frac{H_y^{q+1/2}[m+1/2, n+1/2] - H_y^{q+1/2}[m+1/2, n-1/2]}{\delta_s} \right) = \\ &\sigma_e \frac{E_x^{q+1}[m+1/2, n] + E_x^{q}[m+1/2, n]}{2} + \epsilon \frac{E_x^{q+1}[m+1/2, n] - E_x^{q}[m+1/2, n]}{\delta_t} \,. \end{aligned} \tag{144}$$

Rearranging to write future electric field values (q+1) in terms of past values (q) and the magnetic field gives the update equation for E_x

$$\begin{aligned} E_x^{q+1}[m+1/2, n] = - \left(\frac{1}{\frac{\sigma_e}{2} + \frac{\epsilon}{\delta_t}} \right) \times \Bigg\{ \left(\frac{\sigma_e}{2} - \frac{\epsilon}{\delta_t} \right) E_x^{q}[m+1/2, n] + \\ \left(\frac{H_y^{q+1/2}[m+1/2, n+1/2] - H_y^{q+1/2}[m+1/2, n-1/2]}{\delta_s} \right) \Bigg\} \,, \end{aligned} \tag{145}$$

Similar derivations can be done to retrieve update equations for E_z and H_y

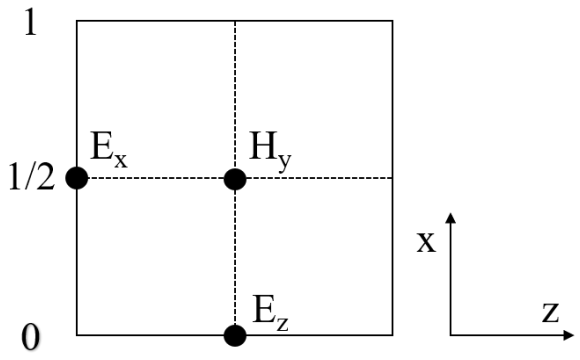

Figure 14: Layout of fields within a grid cell in a two dimensional FDTD calculation.

$$\mathrm{E_z^{q+1}[m,n+1/2]} = -\left(\frac{1}{\frac{\sigma_\mathrm{e}}{2}+\frac{\epsilon}{\delta_\mathrm{t}}}\right) \times \left\{\left(\frac{\sigma_\mathrm{e}}{2}-\frac{\epsilon}{\delta_\mathrm{t}}\right) \mathrm{E_z^q[m,n+1/2]} - \left(\frac{\mathrm{H_y^{q+1/2}[m+1/2,n+1/2]} - \mathrm{H_y^{q+1/2}[m+1/2,n-1/2]}}{\delta_\mathrm{s}}\right)\right\}, \tag{146}$$

$$\mathrm{H_y^{q+1/2}[m+1/2,n+1/2]} = -\left(\frac{1}{\frac{\sigma_\mathrm{m}}{2}+\frac{\mu}{\delta_\mathrm{t}}}\right) \times \left\{\left(\frac{\sigma_\mathrm{m}}{2}-\frac{\mu}{\delta_\mathrm{t}}\right) \mathrm{H_y^{q-1/2}[m+1/2,n+1/2]} - \left(\frac{\mathrm{E_z^q[m+1,n+1/2]} - \mathrm{E_z^q[m,n+1/2]} - \mathrm{E_x^q[m+1/2,n+1]} + \mathrm{E_x^q[m+1/2,n]}}{\delta_\mathrm{s}}\right)\right\}. \tag{147}$$

From the time indices, in a given loop, the magnetic field is always updated first. These equations for the updating of fields can be applied repeatedly in order to calculate the field at a certain time.

The choice of spatial step size and time step duration are not entirely independent of each other. The Courant condition must be satisfied to ensure numerical stability. In 2D, the Courant condition can be written as

$$\delta_\mathrm{t} \leq \frac{\sqrt{2}\,\delta_\mathrm{t}}{\mathrm{c}}\,, \tag{148}$$

The physical interpretation of the Courant condition is that the field energy should not be able to transit through more than one complete mesh cell in one time step because each spatial index only affects its nearest neighbour in the update equations.

The material parameters relating to the electric field, ϵ and σ_e, and the mate-

rial parameters relating to the magnetic field, μ and σ_{m}, are defined on slightly different grids. When FDTD code used in this thesis was written in MATLAB, the material arrays were initially defined on a grid of size [2m, 2n] with spatial step size = $\delta_{\mathrm{s}}/2$. This assisted with ambiguity with regards to positions of material boundary walls. The even coordinates correspond to a grid [m, n] and the odd coordinates correspond to the grid [m + 1/2, n + 1/2]. The finite conductivity assumed here means materials can be lossy, but these parameters are constant at each grid position so do not have any frequency dependence.

As FDTD is a time domain method, the initial electric and magnetic fields must initially be defined in the time domain. Assuming a Gaussian-Hermite pulse in free-space, the time domain field can be written as the Fourier transform of the single frequency definition multiplied by the spectral amplitude, as in equation 88, with t = 0.

2.3.4 Particle Tracking with Runge-Kutta Methods

In numerical field analysis, the electric and magnetic fields are defined over a spatial grid at discrete time intervals. Runge-Kutta methods are a family of iterative methods used to approximate differential equations with discrete temporal steps. For demonstration of a fourth order Runge-Kutta (RK4) solver, a 1D system is assumed where

$$\frac{\mathrm{dz}}{\mathrm{dt}} = \mathrm{f}\left(\mathrm{t}, \mathrm{z}\right) . \tag{149}$$

At an initial time, t_0, the particle is at z_0. The updated particle position is given by

$$\mathrm{z}_{\mathrm{n}+1} = \mathrm{z}_{\mathrm{n}} + \frac{\delta_{\mathrm{t}}}{6}\left(\mathrm{k}_1 + 2\mathrm{k}_2 + 2\mathrm{k}_3 + \mathrm{k}_4\right) , \tag{150}$$

where

$$\begin{aligned}
\mathrm{k}_1 &= \mathrm{f}\left(\mathrm{t}_{\mathrm{n}}, \mathrm{z}_{\mathrm{n}}\right) , \\
\mathrm{k}_2 &= \mathrm{f}\left(\mathrm{t}_{\mathrm{n}} + \frac{\delta_{\mathrm{t}}}{2}, \mathrm{z}_{\mathrm{n}} + \frac{\mathrm{k}_1\delta_{\mathrm{t}}}{2}\right) , \\
\mathrm{k}_3 &= \mathrm{f}\left(\mathrm{t}_{\mathrm{n}} + \frac{\delta_{\mathrm{t}}}{2}, \mathrm{z}_{\mathrm{n}} + \frac{\mathrm{k}_2\delta_{\mathrm{t}}}{2}\right) , \\
\mathrm{k}_4 &= \mathrm{f}\left(\mathrm{t}_{\mathrm{n}} + \delta_{\mathrm{t}}, \mathrm{z}_{\mathrm{n}} + \mathrm{k}_3\delta_{\mathrm{t}}\right) .
\end{aligned} \tag{151}$$

The physical interpretation of these parameters is that k_1 is the gradient at a time, t_{n}. Both k_2 and k_3 are defined at a time which is a mid point in the temporal step, but have adjusted positions based on an underestimate and an overestimate of the

position at this time. The gradient at $t_n + \delta_t$ and $z_n + k_3\delta_t$ is given by k_4. By averaging these four estimates of the gradient, differential equations on a discrete grid can be more accurately approximated.

Particle motion due to an electromagnetic field can be solved implementing an RK4 solver; using equation 76 to update the particle's velocity and then its position. In the MATLAB implementation of an RK4 solver used in this thesis, the magnetic and electric field is first evaluated at a given particle's position, which has a known velocity. Then, equation 76 is calculated to give k_1 from equation 151 in each direction. This k_1 allows calculation of the β in each direction at which k_2 is evaluated. After further iteration, sufficient information is gained to calculate the updated particle β from equation 150. Simultaneously, the particle position is also updated via $\frac{dx,y,z}{dt} = \beta_{x,y,z}\, c$, using the different estimations of β throughout the time step.

3 Experimental Apparatus

3.1 Laser Systems

The laser systems used in this work exploited regenerative amplification to produce mJ level pulse energies. A schematic of a typical regenerative amplifier system is shown in figure 15. The amplifier crystal is first pumped by a laser so that it can accumulate stored energy. Lasers used in this thesis use titanium-sapphire as the gain medium. The regenerative amplifier is seeded by a laser oscillator. The seed laser is chirped to reduce the peak intensity incident on the amplifier crystal [115] and then enters the system in figure 15 via a thin film polariser. The Faraday rotator provides a $\pi/4$ polarisation shift to the laser before a thin film polariser allows the pulse into the resonator. Applying a voltage to the Pockels cell gives a $\pi/2$ polarisation rotation which leads to transmission of the pulse through the thin film polariser. Crucially, the Pockels cell is only switched on for a shorter time than it takes for the laser to complete one round trip of the resonator. The pulse passes through the gain medium many times until it has achieved the desired level of amplification and is then extracted from the cavity by once again applying a voltage to the Pockels cell. The polarisation rotation means the thin film polariser now reflects the pulse back towards the Faraday rotator. The Faraday rotator gives a $\pi/4$ polarisation shift in the same direction as it gave the input pulse, meaning input and output pulses are orthogonally polarised. The output pulse can then be separated from the input and the laser oscillator is then protected from any back reflections after the Faraday rotator. The output from the regenerative amplifier is later recompressed to achieve a femtosecond-scale duration pulse.

The laser used in the CLARA experiment to generate THz radiation in chapter 4 for interaction with the electron beam was a custom titanium:sapphire system. The first amplification stage was a regenerative amplifier and the second amplification stage was a multipass amplifier (MPA), which brought the pulse energy to approximately 500 mJ. Both amplifier types exploit a pumped amplifier crystal, but in an MPA, the beam propagates through the crystal a fixed number of times based on the cavity geometry. An example MPA geometry is shown in figure 16. Instead of an electro-optic switch, the beam travels through a fixed optic path so that it passes through the gain medium a certain number of times before leaving the cavity. The CLARA laser MPA has 5 passes through the titanium:sapphire crystal. After the MPA, the pulse was recompressed to a transform limited duration of approximately 60 fs FWHM at a laser rep rate of 10 Hz.

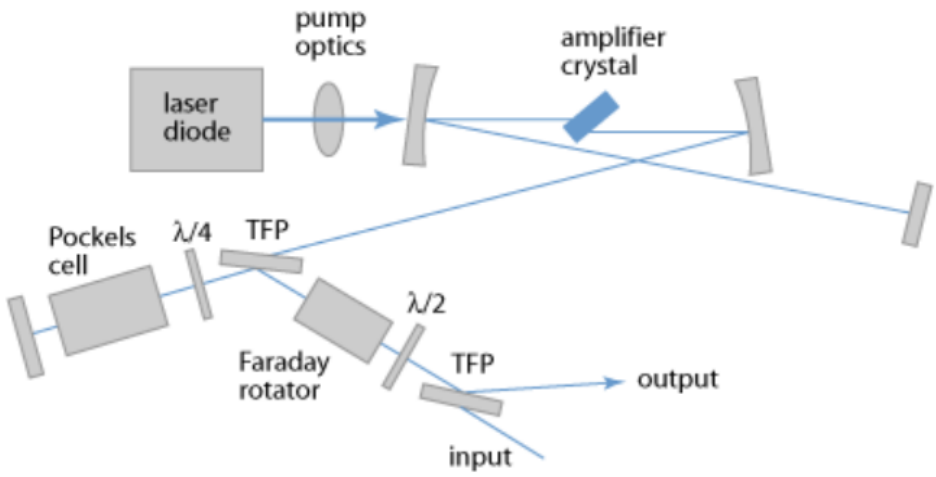

Figure 15: Schematic of a typical regenerative amplifier system. The input is a temporally stretched pulse from the oscillator. Taken from [116].

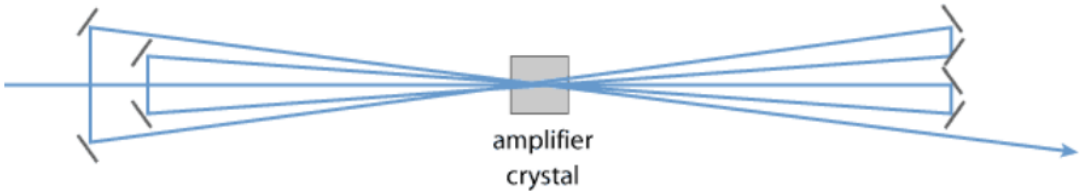

Figure 16: Schematic of a typical multipass amplifier geometry. Taken from [117].

For excitation of the photocathode and generation of THz radiation in chapter 5, a Spectra Physics Spitfire Ace PA laser [118] was used. The laser was designed to generate 13 mJ pulses at a rep rate of 1 kHz, with a pulse duration of 40 fs. The first regenerative amplification stage was seeded by a Spectra-Physics Synergy oscillator [119]. The titanium:sapphire amplifier crystal was pumped by a Spectra-Physics Ascend laser [120]. A second, single-pass amplification stage, again pumped by an Ascend laser, brought the laser pulse up to full energy.

A Spectra Physics Spitfire Ace laser [118] was used in chapter 5 to test relevant concepts for the electron gun work. The laser was designed to generate 7 mJ pulses at a rep rate of 1 kHz, with a pulse duration of 40 fs. The regenerative amplifier was seeded by a Mai-Tai SP oscillator [121] and pumped by an Ascend laser.

3.2 Electron Generation and Measurement

3.2.1 100 keV Electron Gun

Electron bunches were generated by a Kimball Physics EGH-8121A electron gun for the experimental work performed in chapter 5. A schematic of the gun is shown in figure 17. Electrons are generated at the cathode surface by either heating of the material, giving rise to thermally excited electrons, or by exciting the cathode with 400 nm light. The cathode consists of a square lanthanum hexaboride (LaB_6) crystal with a side length of 200 μm. The variable grid, drawn in orange in figure 17, was a Wehnelt cylinder, which was used to control the number of electrons which were allowed to leave the firing unit. The variable grid voltage could be pulsed so electrons were only emitted in 2 μs windows in which the laser excited the cathode. Electrons were initially accelerated by the first anode which was biased to 5 kV, and then to a grounded second anode. After this, electrons were accelerated by a DC electric field to a maximum energy of 100 keV. A solenoid magnet allowed effective focusing of the electron beam anywhere between 50 mm and 1 m from the exit flange. Focusing of the electron beam in this way means electrons far from the bunch centre transversely have the same energy as central electrons, but have an extra component of their velocity in a direction transverse to their direction of propagation. As the bunch propagates from the solenoid, the bunch forms a bowl shape because of this, with outer electrons behind the central electrons. At the focus, all electrons reach the same transverse position but at different longitudinal positions, leading to longer effective bunch duration. Horizontal and vertical deflecting coils gave control of the electron bunch steering.

3.2.2 Microchannel Plate Detector

Microchannel Plate (MCP) detectors are often used to detect single electrons or low charge electron beams. Incident electrons collide with the plate material which leads to the generation of many more, lower energy electrons. These electrons are then accelerated across a potential difference to a fluorescent screen and the emitted photons are detected by a CCD camera. The amplification of the electron signal by the MCP means single electrons can be measured. The plate is split into many channels, which allows the transverse profile of an incident electron bunch to be measured.

The MCP used in chapter 5 was supplied by Torr Scientific Ltd [123]. The plate was circular with diameter 30 mm and a channel size of 15 μm. The MCP itself was biased to a potential difference of 1 kV and the fluorescent screen was biased

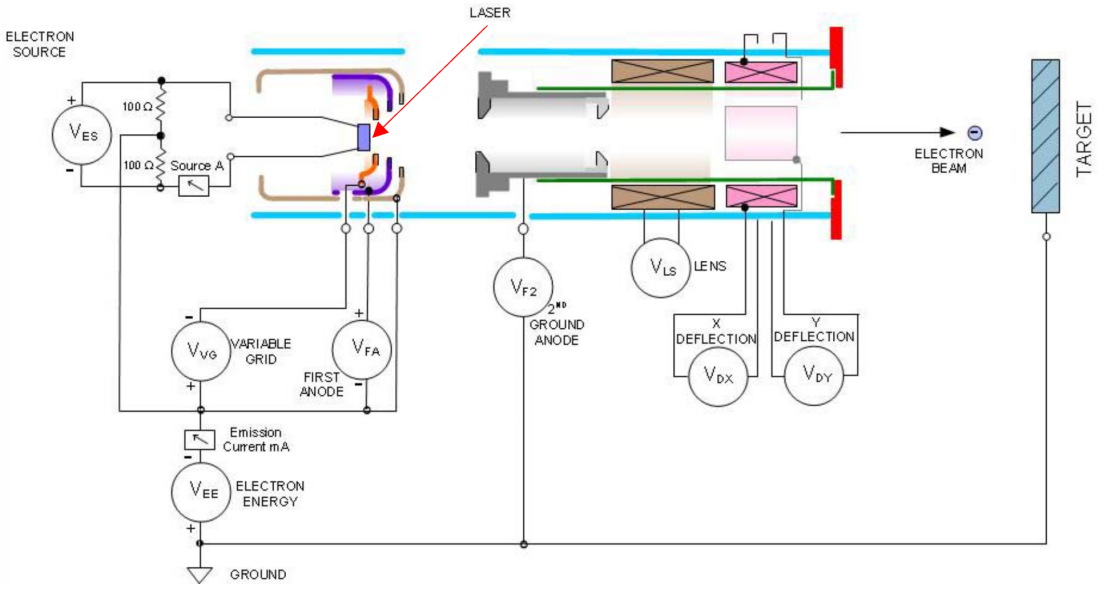

Figure 17: Schematic of the Kimball Physics electron gun used in chapter 5. Taken from [122].

to 5 kV. A phosphor was screen used to convert the amplified electron signal to photons.

3.3 THz Detection

3.3.1 Lock-in Amplifier

Lock-in amplifiers are used to aid detection of small signals compared to the noise which occur at a specific frequency. They have been used for detection of the difference signal between two photodiodes in electro-optic THz measurements in this thesis. The principle of operation requires a signal to be measured, $V_s = A_s \sin(\omega_s t + \theta_s)$, and a reference signal, $V_r = A_r \sin(\omega_r t + \theta_r)$. These are detected by a phase sensitive detector (PSD), which gives an output that is the product of these two signals

$$V_{PSD} = \frac{A_s A_r}{2} \{\cos[(\omega_r - \omega_s) t + \theta_s - \theta_r] - \cos[(\omega_r + \omega_s) t + \theta_s + \theta_r]\} . \quad (152)$$

A low pass filter is implemented to block the higher, sum frequency term. The difference frequency is sinusoidal with time unless $\omega_s = \omega_r$. In this case, the signal is DC. A DC amplifier is used on the filtered PSD output to further increase the signal at the reference frequency [124].

For EO measurements in this thesis, an optical chopper is used to block the pump pulse so that only every other pulse measured by the lock-in amplifier has a THz

induced polarisation rotation. When the pump signal is blocked, only the probe signal is measured. A lock-in reference that has a frequency of half of the laser rep rate will then only amplify the change in signal due to the THz, rather than the full probe signal. Using this technique alongside balanced detection gives the ability to detect THz induced EO signals which are significantly below the noise on the photodiodes.

3.3.2 Thermal Detectors

Thermal detectors are a class of devices which utilise the response of a detector material to heat to measure THz energy. In this work, a GenTec pyroelectric detector, similar to [125] was used for initial source alignment. It was later used for day to day measurements of THz energy where the spatial profile was not needed. This particular device had a 2 mm × 2 mm sensor area and was capable of measuring radiation in the frequency range 0.1 THz - 30 THz. Detectors such as this consist of a pyroelectric crystal placed between two electrodes of opposite polarity. The THz radiation incident on the absorber electrode raises the temperature in the crystal, which reduces the crystal surface charge. A measurable current flows between the electrodes to compensate for the change in surface charge [126]. This current is proportional to THz power incident on the absorber material.

Measurements of the pulse energy profile were taken using the INO MICROXCAM-384i terahertz camera [127]. This comprised a 384 × 288 pixel micro-bolometer array, with a pixel pitch of 35 μm. In a bolometer, the THz radiation is first absorbed on a substrate. A thermometer, whose resistance is temperature dependent, lies behind the substrate in a circuit with a constant current. The voltage in this circuit is proportional to the thermometer resistance and hence the THz power [126].

Signals measured by the pyroelectric detector and the THz camera were calibrated to pulse energy using a Thomas Keating THz power meter, which compares the electrical heating of a thin film to a known signal [128]. The known signal provided by a signal generator is a square wave, which has a duration that is significantly longer than the THz pulse duration but is short enough that it only measures one pulse. The signal generator is connected to the power meter and the amplitude of its output is tuned so that the measured signal is equivalent to the signal measured due to an incident THz pulse. Since only 50 % of the THz energy is absorbed by the film, the total incident THz energy is twice the electric energy in the signal generator pulse. Given the absolute pulse energy, the signal measured by another

detector can be calibrated to energy by assuming the detector has a linear response to THz energy, which is the case for pyroelectric detectors and micro-bolometer arrays.

4 Acceleration of Relativistic Electron Bunches in a Dielectric-Lined Waveguide

The THz acceleration group at the Cockcroft Institute carried out experiments at the CLARA electron linac in January 2019 [83] in order to accelerate the relativistic beam with a rectangular THz-driven dielectric-lined waveguide. The DLW was designed to enable a phase-matched interaction between the accelerating field and the electron bunch over an extended region. In these proof-of-principle results, acceleration of up to 10 keV was seen with modest THz accelerating fields. Here I describe the experiments and data analysis that prove the velocity matching concept in DLWs (4.3). The use of THz interaction to characterise the phase space of electron bunches with durations much greater than the THz period is also demonstrated (4.4).

Previous demonstrations of THz-driven electron acceleration operated in the subrelativistic regime [58, 66] or used an undulator to mediate the interaction [129] which requires significant infrastructure and has fundamental issues with scalability. This experiment was the first demonstration of acceleration of a fully relativistic electron beam in a linear THz-driven accelerator [1].

4.1 Electron Acceleration in a THz-Driven Dielectric-Lined Waveguide

4.1.1 Properties of a Dielectric Waveguide

The geometry of the fused-quartz-lined waveguide used experimentally is given in table 2, with notation demonstrated in figure 18. The waveguide was designed so that the lowest order accelerating mode, LSM_{11}, propagates with a phase velocity that is matched to the velocity of the CLARA electron beam at roughly 0.4 THz. The procedure for designing this waveguide is detailed in [107]. To find the dispersion relation for odd modes in the DLW, equation 116 was solved numerically in MATLAB. The minimisation function, F, was defined as

$$\mathrm{F}\left(\mathrm{m},\, \beta_{\mathrm{mn}}\right) = \left|\mathrm{k}_{\mathrm{y,\,mn}}^{(1)} \tan(\mathrm{k}_{\mathrm{y,\,mn}}^{(1)}\, \delta) - \epsilon_{\mathrm{r}}\, \mathrm{k}_{\mathrm{y,\,mn}}^{(0)} \cot(\mathrm{k}_{\mathrm{y,\,mn}}^{(0)}\, \mathrm{a})\right| , \tag{153}$$

and for each frequency and mode, mn, a longitudinal propagation constant, β_{mn}, was found that minimised F. The minimisation was performed with the 'islocalmin' function which returned the local minima to the dispersion relation in order of ascending frequency. Solutions with imaginary β_{mn} were found by reversing the sign in front of the propagation constant in the transverse wavenumber definitions in

Parameter	Value
2a	575 μm
2b	695 μm
δ	60 μm
w	1.2 mm
L	30 mm
ϵ_r	3.81 [130]

Table 2: Properties of the dielectric-lined waveguide used during exploitation of the CLARA facility.

equations 210 and 96. This process can be performed with even modes by modifying the minimisation function, F, to reflect the even mode dispersion relation. The minimisation process is shown for several frequencies in figure 19a. The lower frequencies have only one real solution whilst at 0.6 THz there are two solutions. There are an infinite number of imaginary solutions to equation 116. The dispersion relation for the LSM_{11} mode in this waveguide is shown in figure 19b. The phase velocity, $v_p = \omega/k$, and the group velocity, $v_g = d\omega/dk$, are shown in figures 19c and 19d respectively. The phase velocity is equal to the speed of light in vacuum at a frequency of 0.41 THz. The group velocity at this frequency is 0.60 c.

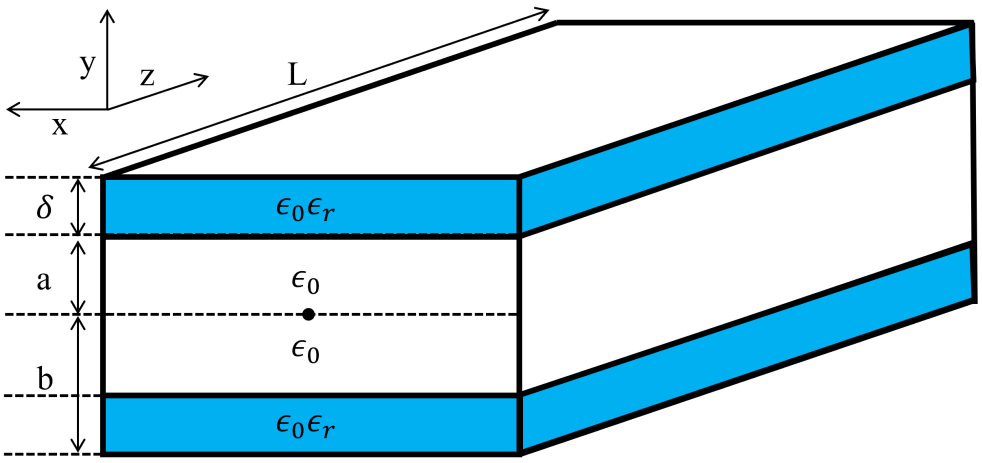

Figure 18: Dielectric-lined waveguide (DLW) with dimensions labelled using standard notation.

Having determined the propagation constants, the field profile at each frequency can be determined according to equations 104-108. Figure 20 plots the transverse electric and magnetic fields for three different modes at 0.4 THz with the waveg-

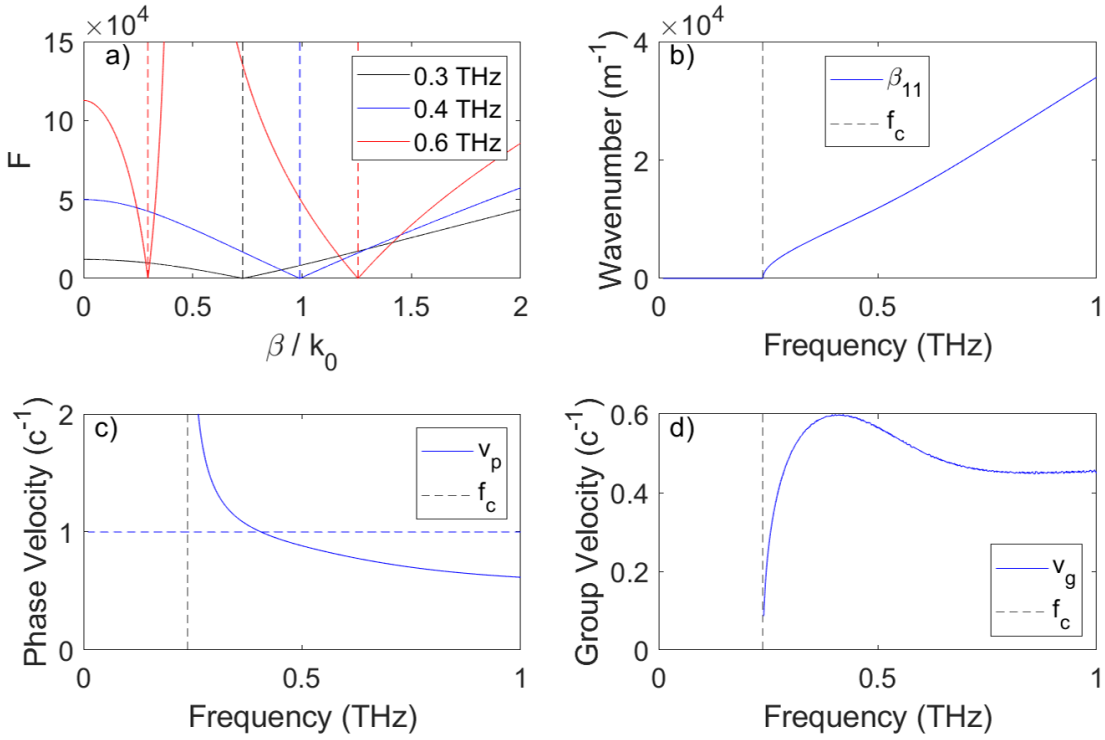

Figure 19: The dispersion relation was found numerically by finding the β value which minimised F (equation 153) for each frequency, as illustrated in **a)**. The propagation constant is given in **b)** and from this, the phase group velocity have been calculated and shown in **c)** and **d)** respectively.

uide dimensions given in table 2. The subscript, m, that defines the number of half periods in the horizontal axis of the cross section of the mode E_y field profile. The subscript, n, defines the number of half periods in the vertical axis of the cross section of the E_y profile.

For the LSM mode of interest for acceleration, at the frequency where the phase velocity is equal to the speed of light, $\beta_{11} = k_0$ and $k^0_{y,11} = i\pi/w$. The longitudinal field in this mode in the vacuum region can then be written as

$$\widetilde{E}_z(x, y, z, \omega) = A_{11} \frac{k_0 \pi}{w} \sin\left(\frac{\pi}{w}(x + w/2)\right) \cosh\left(\frac{\pi y}{w}\right) e^{-ik_0 z} . \qquad (154)$$

The field amplitude is inversely proportional to the width. A higher width also leads to a more uniform field profile in the horizontal (x) and vertical (y) directions. For electron acceleration, the choice of width is a compromise between peak accelerating field and the quality of the accelerated bunch. At the phase-matched frequency for this waveguide, the field components in the LSM_{11} mode in

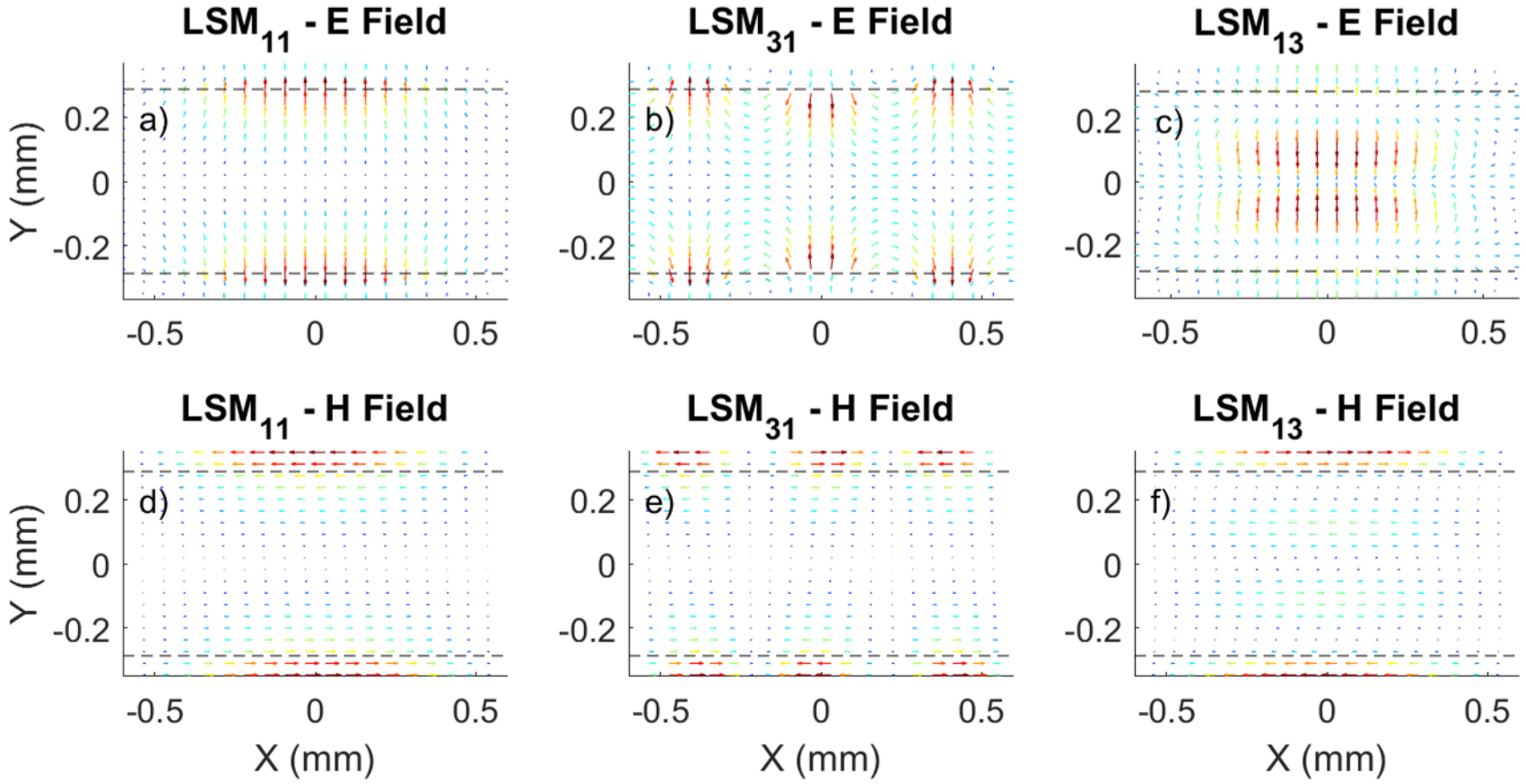

Figure 20: The transverse field for different modes over the cross-section of a DLW, with dimensions given in table 2. In **a)** and **d)**, the LSM_{11} electric and magnetic fields are shown, respectively. **b)** and **e)** show electric and magnetic fields for the LSM_{31} mode and **c)** and **f)** show electric and magnetic fields for the LSM_{13} mode. These field profiles are used for the coupling calculations in section 4.1.2.

the DLW cross-section, given by equations 104-108, are plotted in figure 21. The electric field in these plots is normalised to the maximum E_y and the magnetic field is normalised to the maximum H_x value.

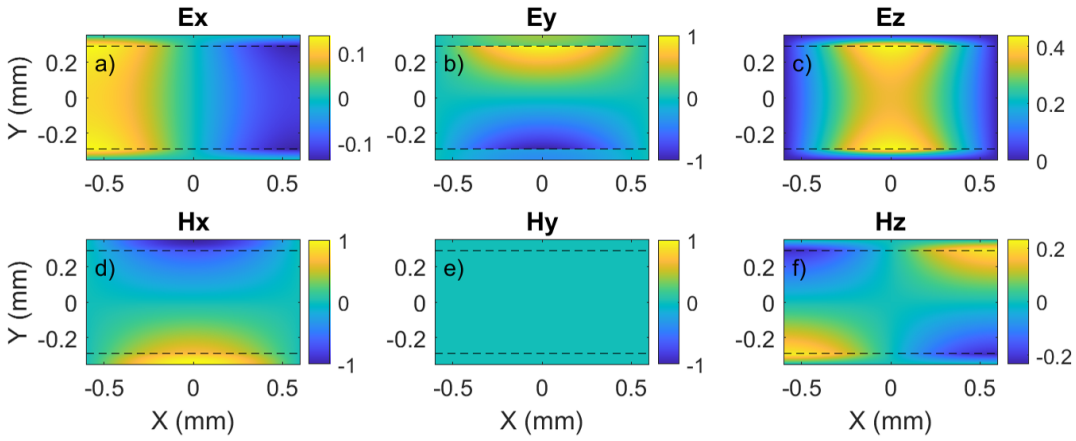

Figure 21: The field components in the LSM_{11} mode over the cross-section of a DLW, with dimensions given in table 2 at the phase-matched frequency. In **a)**, E_x is plotted, in **b)** E_y, in **c)** E_z, in **d)** H_x, in **e)** H_y and in **f)** H_z. The electric fields are normalised to the maximum E_y and the magnetic fields to the maximum H_x.

4.1.2 Coupling into the Longitudinal Mode

In order to excite the accelerating mode in the waveguide efficiently and not excite other modes which may be detrimental to the accelerator's performance, the free-space transverse profile of the input THz needs to modified from a fundamental Gaussian pulse profile. In an ideal case, the transverse profile of the input THz field at the entrance to the DLW should match the transverse profile of the excited mode in both the vacuum region and the dielectric region. As can be seen in figure 21b, a key feature in the field in the y direction is the polarity change between the top and the bottom of the structure. This is a feature which is also found in a Gaussian-Hermite TEM_{01} pulse. The frequency domain field of a Gaussian-Hermite TEM_{01} pulse linearly polarised in the y direction can be expressed as

$$\widetilde{E}_y(x, y, z, \omega) = E_0 \frac{w_0\, x}{w^2(z)} e^{(x^2+y^2)/w^2(z)} \sin(\varphi) \ , \tag{155}$$

with

$$\varphi = kz - \omega t + \frac{k(x^2 + y^2)}{2R(z)} - 2\tan^{-1}\left(\frac{z}{z_R}\right) + \varphi_0 \ , \tag{156}$$

as presented in 2.2.2. This is plotted in figure 22, where in 22a a Gaussian time profile was considered with a 8 ps FWHM pulse duration. The magnetic field, $\widetilde{H}_x$= -$\widetilde{E}_y/(\mu_0 c)$. The profile plotted here has similarities to the LSM_{11} mode in figure 21b.

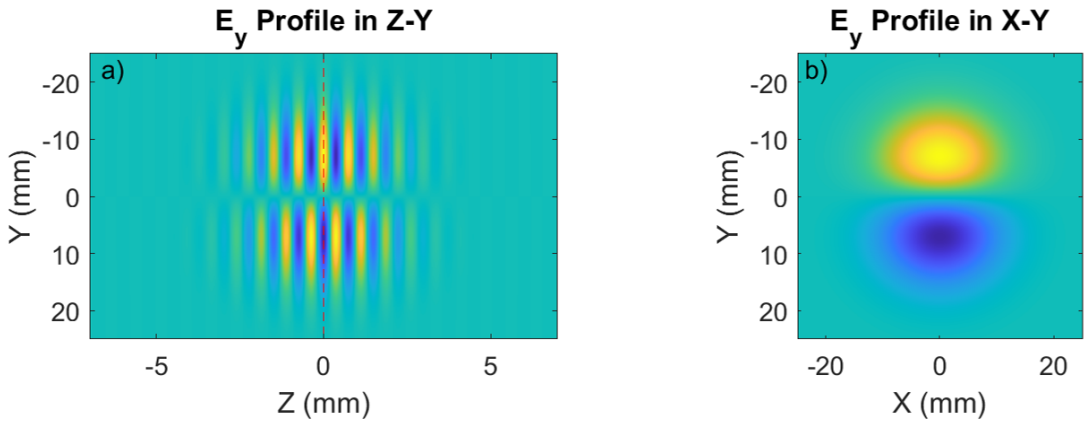

Figure 22: E_y in a Gaussian-Hermite TEM_{01} pulse. Figure **a)** shows the propagation direction and a transverse axis, whilst **b)** shows the field in the axis transverse to the pulse propagation at a z position given by the red line in **a)**.

The coupling efficiency of this higher order Gaussian pulse was quantitatively assessed by rewriting the input transverse field as a sum of LSM modes

$$\widetilde{\mathbf{E}}^{(\mathrm{in})} = \sum_{\mathrm{mn}} \alpha_{\mathrm{mn}} \, \widetilde{\mathbf{E}}^{\mathrm{mn}} \, , \tag{157}$$

$$\widetilde{\mathbf{H}}^{(\mathrm{in})} = \sum_{\mathrm{mn}} \delta_{\mathrm{mn}} \, \widetilde{\mathbf{H}}^{\mathrm{mn}} \, , \tag{158}$$

where α_{mn} and δ_{mn} are mode dependent coupling coefficients. A unique set of solutions for the coupling coefficients can be found due to the fact that LSM modes are orthogonal to each other [131]. The orthogonality condition for the dielectric waveguide mode transverse fields means

$$\int_{\mathrm{X}} \int_{\mathrm{Y}} \widetilde{\mathrm{H}}_{\mathrm{x}}^{\mathrm{mn}*} \, \widetilde{\mathrm{E}}_{\mathrm{y}}^{\mathrm{pq}} - \widetilde{\mathrm{H}}_{\mathrm{y}}^{\mathrm{mn}*} \, \widetilde{\mathrm{E}}_{\mathrm{x}}^{\mathrm{pq}} \, \mathrm{dxdy} = 0 \, , \tag{159}$$

for pq $\neq$ mn. By definition, $\widetilde{\mathrm{H}}_{\mathrm{y}} = 0$ for LSM modes, leaving the term with $\widetilde{\mathrm{H}}_{\mathrm{x}}$ and $\widetilde{\mathrm{E}}_{\mathrm{y}}$. For decomposition of an input electric field into electric field waveguide modes, it is helpful to write equation 159 entirely in terms of electric field. From the LSM mode definitions, $\widetilde{\mathrm{H}}_{\mathrm{x}} = \text{constant} \times \widetilde{\mathrm{E}}_{\mathrm{y}}$ in the vacuum region of the DLW and $\widetilde{\mathrm{H}}_{\mathrm{x}} = \text{constant} \times \epsilon_{\mathrm{r}} \times \widetilde{\mathrm{E}}_{\mathrm{y}}$ in the dielectric region. Substituting this form for the H field into equation 159 and dividing through by the constant term gives

$$\left(\int_{\mathrm{X}} \int_{-\mathrm{a}}^{\mathrm{a}} \widetilde{\mathrm{E}}_{\mathrm{y}}^{\mathrm{mn}*} \, \widetilde{\mathrm{E}}_{\mathrm{y}}^{\mathrm{pq}} \, \mathrm{dxdy} + \int_{\mathrm{X}} \int_{\mathrm{a}}^{\mathrm{b}} \epsilon_{\mathrm{r}} \, \widetilde{\mathrm{E}}_{\mathrm{y}}^{\mathrm{mn}*} \, \widetilde{\mathrm{E}}_{\mathrm{y}}^{\mathrm{pq}} \, \mathrm{dxdy} + \int_{\mathrm{X}} \int_{-\mathrm{b}}^{-\mathrm{a}} \epsilon_{\mathrm{r}} \, \widetilde{\mathrm{E}}_{\mathrm{y}}^{\mathrm{mn}*} \, \widetilde{\mathrm{E}}_{\mathrm{y}}^{\mathrm{pq}} \, \mathrm{dxdy} \right) = 0 \, . \tag{160}$$

An equivalent process can be performed in terms of $\widetilde{\mathrm{H}}_{\mathrm{x}}$ for the magnetic field decomposition, where the only difference is a factor of $1/\epsilon_{\mathrm{r}}$ replaces the factors of ϵ_{r} in equation 160. Since equation 160 has no $\widetilde{\mathrm{E}}_{\mathrm{x}}$ dependence, unique solutions can only be found for equation 157 when considering $\widetilde{\mathrm{E}}_{\mathrm{y}}$ components. With the information given by equation 160, and the knowledge that the integrals over the dielectric region are equal to each other when mn = pq, a solution for the calculation of α_{mn} can be suggested of the form

$$\begin{aligned} &\frac{1}{\eta_1 + 2\epsilon_{\mathrm{r}}\eta_2} \left(\int_{\mathrm{X}} \int_{-\mathrm{a}}^{\mathrm{a}} \widetilde{\mathrm{E}}_{\mathrm{y}}^{(\mathrm{in})} \, \widetilde{\mathrm{E}}_{\mathrm{y}}^{\mathrm{mn}*} \, \mathrm{dxdy} + \right. \\ &\left. \int_{\mathrm{X}} \int_{\mathrm{a}}^{\mathrm{b}} \epsilon_{\mathrm{r}} \, \widetilde{\mathrm{E}}_{\mathrm{y}}^{(\mathrm{in})} \, \widetilde{\mathrm{E}}_{\mathrm{y}}^{\mathrm{mn}*} \, \mathrm{dxdy} + \int_{\mathrm{X}} \int_{-\mathrm{b}}^{-\mathrm{a}} \epsilon_{\mathrm{r}} \, \widetilde{\mathrm{E}}_{\mathrm{y}}^{(\mathrm{in})} \, \widetilde{\mathrm{E}}_{\mathrm{y}}^{\mathrm{mn}*} \, \mathrm{dxdy} \right) \, , \end{aligned} \tag{161}$$

where η_1 and η_2 are constants dependent on the field normalisation. Substituting $\widetilde{\mathrm{E}}_{\mathrm{y}}^{(\mathrm{in})}$ from equation 157 into this gives

$$\begin{aligned} &\frac{1}{\eta_1 + 2\epsilon_{\mathrm{r}}\eta_2} \left(\int_{\mathrm{X}} \int_{-\mathrm{a}}^{\mathrm{a}} \left(\sum_{\mathrm{pq}} \alpha_{\mathrm{pq}} \widetilde{\mathrm{E}}^{\mathrm{pq}} \right) \, \widetilde{\mathrm{E}}_{\mathrm{y}}^{\mathrm{mn}*} \, \mathrm{dxdy} + \right. \\ &\left. \int_{\mathrm{X}} \int_{\mathrm{a}}^{\mathrm{b}} \epsilon_{\mathrm{r}} \left(\sum_{\mathrm{pq}} \alpha_{\mathrm{pq}} \widetilde{\mathrm{E}}^{\mathrm{pq}} \right) \, \widetilde{\mathrm{E}}_{\mathrm{y}}^{\mathrm{mn}*} \, \mathrm{dxdy} \, + \int_{\mathrm{X}} \int_{-\mathrm{b}}^{-\mathrm{a}} \epsilon_{\mathrm{r}} \left(\sum_{\mathrm{pq}} \alpha_{\mathrm{pq}} \widetilde{\mathrm{E}}^{\mathrm{pq}} \right) \, \widetilde{\mathrm{E}}_{\mathrm{y}}^{\mathrm{mn}*} \, \mathrm{dxdy} \right) \, . \end{aligned} \tag{162}$$

Due to the orthogonality condition in equation 160, the sum of these integrals equals 0 for pq $\neq$ mn. When pq = mn, the second and third integral terms are equal to each other, which leaves

$$\frac{1}{\eta_1 + 2\epsilon_r \eta_2} \left(\int_X \int_{-a}^{a} \alpha_{mn} \, \widetilde{E}_y^{mn} \, \widetilde{E}_y^{(mn)*} \, dxdy + \int_X \int_{a}^{b} 2\,\epsilon_r \, \alpha_{mn} \, \widetilde{E}_y^{mn} \, \widetilde{E}_y^{(mn)*} \, dxdy \right) . \tag{163}$$

if the constants η_1 and η_2 are defined as

$$\eta_1 = \int_X \int_{-a}^{a} \left\| \widetilde{E}_y^{mn} \right\|^2 , \tag{164}$$

$$\eta_2 = \int_X \int_{a}^{b} \left\| \widetilde{E}_y^{mn} \right\|^2 , \tag{165}$$

equation 163 simplifies to α_{mn}. Hence the solution for α_{mn} is

$$\begin{aligned} \alpha_{mn} = \frac{1}{\eta_1 + 2\epsilon_r \eta_2} \left(\int_X \int_{-a}^{a} \widetilde{E}_y^{(in)} \, \widetilde{E}_y^{(mn)*} \, dxdy + \right. \\ \left. \int_X \int_{a}^{b} \epsilon_r \, \widetilde{E}_y^{(in)} \, \widetilde{E}_y^{(mn)*} \, dxdy \; + \int_X \int_{-b}^{-a} \epsilon_r \, \widetilde{E}_y^{(in)} \, \widetilde{E}_y^{(mn)*} \, dxdy \right) , \end{aligned} \tag{166}$$

with constants η_1 and η_2 defined as in equations 164 and 165. The δ_{mn} coefficient can be found using a similar ansatz where the factors of ϵ_r are replaced by $1/\epsilon_r$. The solution for δ_{mn} is

$$\begin{aligned} \delta_{mn} = \frac{1}{\eta_{H1} + \frac{2\eta_{H2}}{\epsilon_r}} \left(\int_X \int_{-a}^{a} \widetilde{H}_x^{(in)} \, \widetilde{H}_x^{(mn)*} \, dxdy + \right. \\ \left. \int_X \int_{a}^{b} \frac{1}{\epsilon_r} \, \widetilde{H}_x^{(in)} \, \widetilde{H}_x^{(mn)*} \, dxdy \; + \int_X \int_{-b}^{-a} \frac{1}{\epsilon_r} \, \widetilde{H}_x^{(in)} \, \widetilde{H}_x^{(mn)*} \, dxdy \right) , \end{aligned} \tag{167}$$

where η_{H1} and η_{H2} are defined as

$$\eta_{H1} = \int_X \int_{-a}^{a} \widetilde{H}_x^{mn} \, \widetilde{H}_x^{(mn)*} , \tag{168}$$

$$\eta_{H2} = \int_X \int_{a}^{b} \widetilde{H}_x^{mn} \, \widetilde{H}_x^{(mn)*} . \tag{169}$$

The coefficients α_{mn} and δ_{mn} describe the matching of the tranverse field profile at the free-space-DLW interface but do not specify the direction of propagation of the modes. They can be written as superpositions of the forward, A_{mn}, and backward, B_{mn}, travelling wave coefficients

$$\alpha_{mn} = A_{mn} + B_{mn} , \tag{170}$$

$$\delta_{mn} = A_{mn} - B_{mn} . \tag{171}$$

The sign difference in the coefficient for the reflected wave, B_{mn}, in equations 170 and 171, is because a wave travelling backwards will be defined on the same

vertical (y) axis but will have a flipped horizontal (x) axis, so $\widetilde{H}_x$ changes sign. For a given input field, A_{mn} quantifies the relative coupling strength into the mn waveguide mode. The calculation of this coefficient for an input Gaussian-Hermite TEM_{01} pulse was performed in MATLAB. First, the mode field profiles were calculated over the waveguide cross-section using the dimensions in table 2 and a given frequency. The field of the input was normalised so that the energy flux within the total pulse transverse profile was constant for any given laser waist. The integral of the Poynting vector over the pulse cross section gives the energy flux,

$$\frac{dU}{dt} = -\oint_A \overrightarrow{\mathbf{S}} \cdot dA = \oint_A \widetilde{E}_y \widetilde{H}_x - \widetilde{E}_x \widetilde{H}_y \, dA \, , \tag{172}$$

which is inversely proportional to the waist squared if the pulse is focused at the waveguide entrance. Both $\widetilde{E}_y$ and $\widetilde{H}_x$ have been multiplied by a factor of one over the waist when conducting parameter scans to ensure a THz pulse of constant energy is being considered. Once the input was defined, α_{mn} and δ_{mn} could be calculated individually for each mode for a given frequency and the A_{11} factor could be found by subtracting δ_{mn} from α_{mn} and dividing by 2. Figure 23 shows the absolute value of A_{mn} for m = 1...9 and n = 0...9, with a TEM_{01} mode Gaussian input of 1/e waist radius 0.5 mm at 0.4 THz. The plot is normalised so that $|A_{11}|$ = 1. This calculation is done in the frequency domain, so an imaginary value for A_{mn} corresponds to the input signal coupling to the mode $\pi/2$ out of phase with the one defined in the calculation. A negative value for A_{mn} corresponds to the input signal coupling to the mode π out of phase with the one defined in the calculation. The LSM_{11} mode has by far the strongest coupling. Of the other modes with a non-zero coupling factor, only the LSM_{31} has a real β_{mn} at 0.4 THz; the remainder being below cutoff with imaginary β_{mn}. The propagation constant for this mode though is considerably smaller than the propagation constant for the LSM_{11} at 0.4 THz, meaning a relativistic electron beam and the LSM_{31} mode field would have a significant phase velocity mismatch. The velocity mismatch leads to an almost zero energy gain due to the LSM_{31} mode at the LSM_{11} operating frequency. When considering frequencies near but not at the waveguide operating frequency, the disparity between the amplitude coefficients leads to a negligible interaction with the LSM_{31} mode.

The coupled longitudinal field into the LSM_{11} mode on axis, $\widetilde{E}_{z,wg}$, is equal to the coupling factor, A_{11}, multiplied by the longitudinal field in the mode $\widetilde{E}_{z,11}$. The coupling factor has a frequency dependence because it is related to the transverse field profile of the LSM modes, which are frequency dependent. Changing the

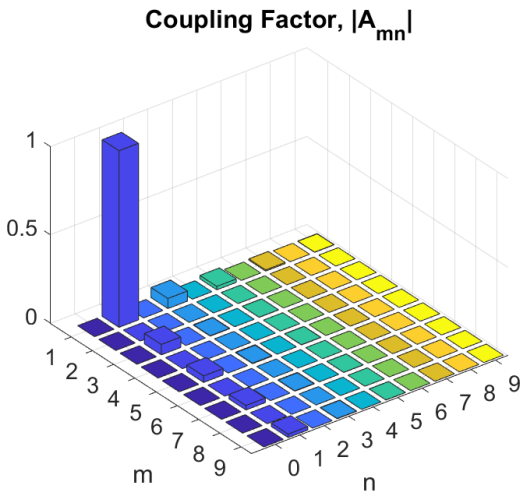

Figure 23: Coupling factor, $|A_{mn}|$, into the DLW described in table 2 for a TEM_{01} Gaussian pulse input with a waist radius of 0.5 mm at 0.4 THz. $|A_{mn}|$ is normalised to the largest calculated coupling factor.

input laser waist changes the input transverse field profile so also has an effect on the coupling factor. In order to see the effect these parameters have on the coupled longitudinal field on axis, the coupling factor for the LSM_{11} mode was calculated for a range of frequencies and laser waist sizes. The absolute value of $\widetilde{E}_{z,wg}$ is plotted in figure 24a as a function of frequency and laser waist size. Figure 24b shows the coupled longitudinal field with a frequency of 0.4 THz. This field is normalised to the largest calculated coupling which occurs at a frequency of 0.26 THz and a waist of 0.29 mm. The LSM_{11} mode $\widetilde{E}_y$ profile at this frequency is plotted in figure 25a and the laser E_y profile with this waist is depicted in figure 25b. A waist of 0.29 mm is too small to practically achieve with mm-scale wavelengths. For a given focusing optic, the diffraction limited focal spot of a Gaussian beam scales as

$$w_0 = \left(\frac{2\lambda}{\pi}\right)\left(\frac{F}{D}\right), \tag{173}$$

where F and D are the focal length and diameter of the focusing optic respectively and the THz is an ideal Gaussian beam. For a focal length of 50 mm and a 2" diameter parabolic mirror, a 0.4 THz pulse will have a diffraction limited 1/e field waist radius of $w_0 \approx 0.5$ mm. This is already larger than the ideal focusing condition but, in practice, achieving this minimum beam waist is incredibly difficult due to the beam quality of the generated THz radiation. In order to maximise the coupling into the DLW, a rectangular tapered coupling horn was used. The entrance aperture for this coupler was 3.25 mm by 3.18 mm and had a length of 23 mm.

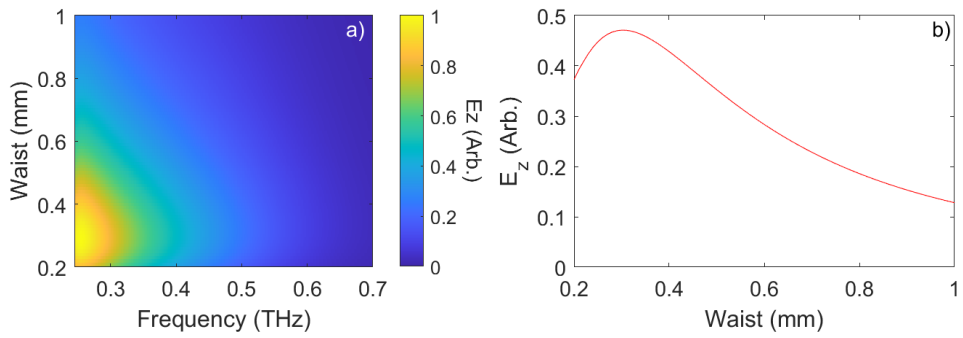

Figure 24: The coupled longitudinal field into the waveguide in table 2 as a function of input laser waist radius and frequency is plotted in **a)**. In **b)**, the coupled field at a frequency of 0.4 THz is plotted. Plots are normalised to the coupled field at the waist and frequency at which the highest coupled field is calculated.

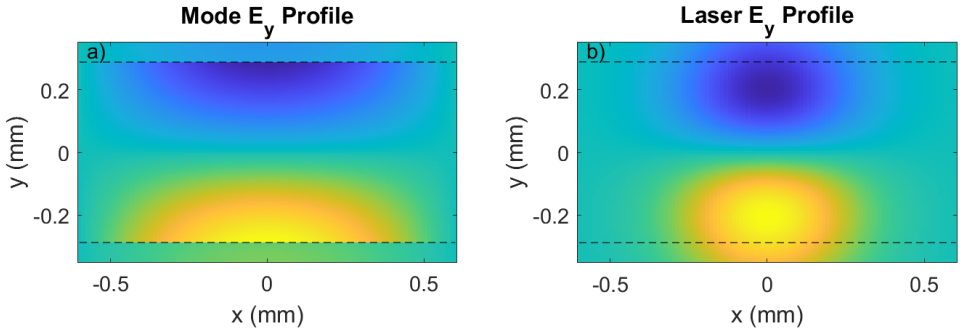

Figure 25: The LSM_{11} mode $\widetilde{E}_y$ profile, **a)**, and the free-space laser $\widetilde{E}_y$ profile, **b)**, at the frequency and waist at which the largest coupling factor is observed in figure 24a ($f = 0.26\,THz$, $w_0 = 0.29\,mm$).

The coupler can be crudely modelled as a rectangular metallic waveguide with decreasing dimensions along its length. The lowest order mode with longitudinal field on-axis, the TM_{11} (transverse magnetic), has been considered here. The propagation constant of the TM_{11} mode is given by $\beta_{TM} = \sqrt{k_0^2 - k_c^2}$, where $k_c = \sqrt{(\pi/w)^2 + (\pi/h)^2}$ is the cutoff wavenumber, and w and h are the width and height at a given longitudinal position. The phase velocity in a metallic waveguide is always greater than the speed of light, but the larger the dimensions of the waveguide, the closer to c the phase velocity is. This means that at the entrance to the coupler, the accelerating field will be close to phase velocity matched to relativistic electrons, and at the exit, there will be a greater velocity mismatch.

The integrated effect of the coupler on the pulse can be calculated by assuming the coupler to be constructed from a series of rectangular metallic waveguides of length dz with gradually decreasing cross sections, as depicted in figure 26a. The effective propagation constant, β_{eff}, was calculated by

$$\beta_{\text{eff}} = \frac{\int_0^{L_c} \beta_{\text{TM}}\, dz}{L_c}\,, \tag{174}$$

where L_c is the coupler length. The effective propagation constant is plotted as a blue line in figure 26b. This is an integrated effect of the coupler which can be used to give an estimate of the pulse dispersion after passing through. It would be incorrect to assume this relation to estimate the field at an intermediate point within the coupler. Looking at the dispersion relation of a metallic waveguide with dimensions of the coupler exit illustrates this, as depicted by the red line in figure 26b. At the taper exit, the guide is at its most dispersive, so the majority of the chirp imparted onto the incident radiation by the coupler is due to the region near the coupler exit.

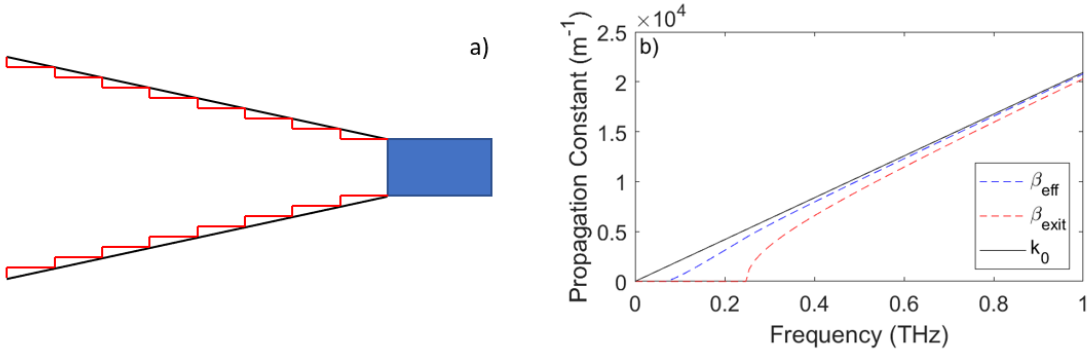

Figure 26: In **a)**, the assumption that the coupler consists of a number of rectangular metallic waveguides with decreasing dimensions is illustrated. The integrated propagation constant, β_{eff}, and the propagation constant at the exit of the coupler, β_{exit}, are plotted against the free-space wavenumber in **b)**.

.

When considering the dimensions of the coupler exit, higher order TM modes with on-axis longitudinal field have cutoff frequencies greater than 0.4 THz so are not useful for phase-matched acceleration with the LSM_{11} mode in this DLW. The transverse field components of the TM_{11} mode are given by

$$\widetilde{\mathrm{E}}_{\mathrm{x}}(\mathrm{x},\mathrm{y},0,\omega) = \frac{\beta_{\mathrm{TM}}\,\pi}{\mathrm{w}\,\mathrm{k}_{\mathrm{c}}^2}\cos\left[\frac{\pi}{\mathrm{w}}\,(\mathrm{x}+\frac{\mathrm{w}}{2})\right]\,\sin\left[\frac{\pi}{\mathrm{h}}\,(\mathrm{y}+\frac{\mathrm{h}}{2})\right], \tag{175}$$

$$\widetilde{\mathrm{E}}_{\mathrm{y}}(\mathrm{x},\mathrm{y},0,\omega) = \frac{\beta_{\mathrm{TM}}\,\pi}{\mathrm{h}\,\mathrm{k}_{\mathrm{c}}^2}\sin\left[\frac{\pi}{\mathrm{w}}\,(\mathrm{x}+\frac{\mathrm{w}}{2})\right]\,\cos\left[\frac{\pi}{\mathrm{h}}\,(\mathrm{y}+\frac{\mathrm{h}}{2})\right], \tag{176}$$

$$\widetilde{\mathrm{H}}_{\mathrm{x}}(\mathrm{x},\mathrm{y},0,\omega) = -\frac{\mathrm{k}\,\pi}{\mathrm{h}\,\mathrm{k}_{\mathrm{c}}^2}\sin\left[\frac{\pi}{\mathrm{w}}\,(\mathrm{x}+\frac{\mathrm{w}}{2})\right]\,\cos\left[\frac{\pi}{\mathrm{h}}\,(\mathrm{y}+\frac{\mathrm{h}}{2})\right], \tag{177}$$

$$\widetilde{\mathrm{H}}_{\mathrm{y}}(\mathrm{x},\mathrm{y},0,\omega) = \frac{\mathrm{k}\,\pi}{\mathrm{w}\,\mathrm{k}_{\mathrm{c}}^2}\cos\left[\frac{\pi}{\mathrm{w}}\,(\mathrm{x}+\frac{\mathrm{w}}{2})\right]\,\sin\left[\frac{\pi}{\mathrm{h}}\,(\mathrm{y}+\frac{\mathrm{h}}{2})\right]. \tag{178}$$

Using these field components as the input field profile, the coupling factors, $|\mathrm{A}_{\mathrm{mn}}|$, into the $\mathrm{LSM}_{\mathrm{mn}}$ modes in the DLW were evaluated at 0.4 THz. It can be seen in figure 27 that the coupling is primarily into the LSM_{11} DLW mode since they both have very similar transverse field profiles. Figure 27 is normalised so that the mode with the largest coupling factor has $|\mathrm{A}_{\mathrm{mn}}| = 1$. The coupling efficiency from the free-space TEM_{01} mode laser input to the TM_{11} mode at the entrance to the coupler can be calculated by setting $\epsilon_{\mathrm{r}} = 1$ in equations 166 and 167. The orthogonality of the TM modes and the fact that input E_x and H_y are equal to 0 make this assumption valid. The input field was again normalised so the energy flux in the pulse was constant with laser waist. As seen in figure 28a, smaller frequencies are still favoured for coupling, but the optimal laser waist is now w_0 = 1.2 mm, which is an achievable spot size for THz experiments. Figure 28b plots the scaling of the coupling factor with laser waist at 0.4 THz. These plots are normalised to the most efficient parameter set. The relative coupling efficiency with and without the coupler can be compared by first ensuring the same input TEM_{01} mode laser input, with $\mathrm{w}_0 = 1.2$ mm and $\mathrm{f} = 0.4$ THz. The efficiency of the free-space coupling is defined only by the A parameter from free-space to the DLW LSM_{11} mode. To consider the coupler, the free-space to TM_{11} mode A parameter was calculated at the coupler entrance. The energy flux over the coupler cross-section in the TM_{11} at the exit, as calculated by equation 172, was set to be the same as at the entrance, which is equivalent to the assumption of a lossless coupler. The coupling factor was then calculated between the TM_{11} mode at the coupler exit and the LSM_{11} mode. Comparing the two overall coupling coefficients, the coupler leads to 5 times larger field in the LSM_{11} mode compared to the case with no coupler. Approximately 87 % of the energy flux in the pulse incident on the coupler couples to the LSM_{11}. Most of this is lost at the coupler entrance due to clipping of the pulse.

4.1.3 Acceleration in a Dieletric-Lined Waveguide

The phase velocity of the accelerating mode in the DLW at 0.4 THz is approximately matched to the velocity of a relativistic electron, but the group velocity of

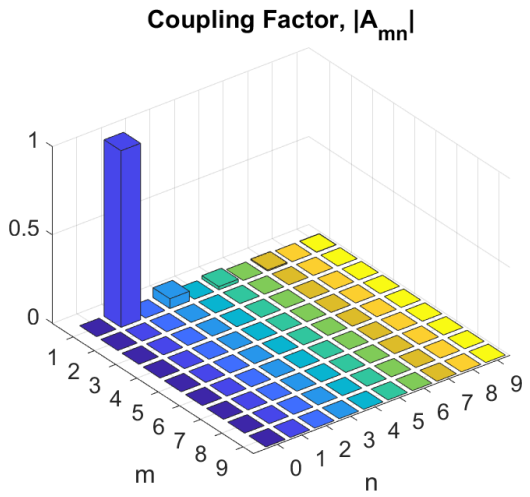

Figure 27: Field coupling factor, $|A_{mn}|$, into the DLW described in table 2 for a rectangular waveguide TM_{11} mode input at 0.4 THz. $|A_{mn}|$ is normalised to the largest coupling factor.

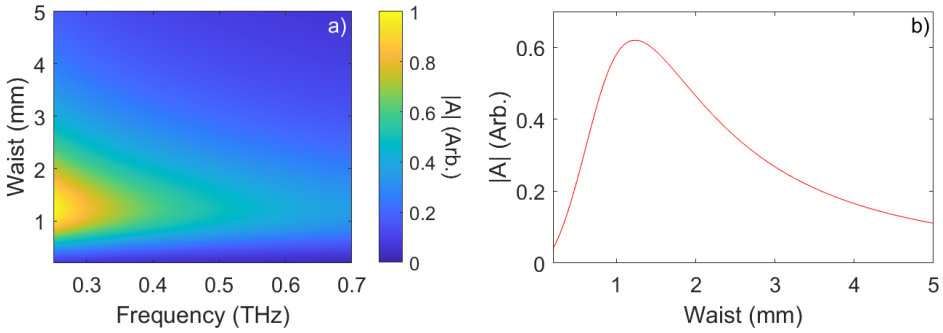

Figure 28: The field coupling factor, |A|, from the free-space TEM_{01} mode laser input to the rectangular waveguide TM_{11} mode as a function of input laser waist radius and frequency is plotted in **a)**. In **b)**, the coupled field at a frequency of 0.4 THz is plotted. Plots are normalised to the coupling factor at the waist and frequency at which the highest coupling factor is calculated.

the mode is only 0.6 c. The mismatch between the group velocity and the electron velocity leads to slippage between the pulse envelope and the accelerated electrons. The group velocity limited FWHM interaction length can be found by equating the FWHM pulse field duration, $\sqrt{2} \times \tau$, to the difference in time taken for the electron and the pulse to travel a certain distance, L_{int}. This can be rearranged in terms of the interaction length

$$L_{int} = \frac{\sqrt{2}\, v_g\, \beta_e\, c\, \tau}{|\beta_e\, c - v_g|} \,. \tag{179}$$

For a bandwidth limited pulse, $\tau = 0.44/\sigma$, where σ is the FWHM intensity band-

width and the pulse has a Gaussian shape. The interaction length can be increased by using a THz pulse with a longer duration. Equation 179 assumes no dispersion in the waveguide which is not the case for a THz pulse of finite bandwidth.

Equation 179 was applied to predict the interaction length when using pulses of different spectral widths. Separately, the interaction within a waveguide with dimensions given in table 2 was modelled in MATLAB using the calculated dispersion relation for the LSM_{11} mode, presented in figure 19. Only the field experienced by the electron inside the waveguide has been included in the evaluation of the energy gain. At the exit of the waveguide, diffraction at the exit surface leaving negligible field strengths. At the entrance to the waveguide, it is assumed that the non-phase-matched interaction in the coupler is insignificant compared to the phase-matched interaction in the waveguide. The field was initiated in the frequency domain as a Gaussian spectrum with a time delay, t_0 and a linear chirp, φ_2,

$$\widetilde{\mathrm{E}}_\mathrm{z}(\omega, \mathrm{z}_0) = \mathrm{e}^{-(\frac{\omega-\omega_0}{\sigma})^2}\, \mathrm{e}^{-\mathrm{i}\,\omega\,\mathrm{t}_0}\, \mathrm{e}^{\mathrm{i}\,\frac{\varphi_2}{2}\,(\omega-\omega_0)^2}\ , \qquad \text{for } \omega > 0\ . \tag{180}$$

The field within the waveguide was then given by

$$\widetilde{\mathrm{E}}_\mathrm{z}(\omega, \mathrm{z}) = \widetilde{\mathrm{E}}_\mathrm{z}(\omega, \mathrm{z}_0)\, \mathrm{e}^{\mathrm{i}\,(\beta_{11}-\mathrm{k}/\beta_\mathrm{e})\,\mathrm{z}}\ , \qquad \text{for } \omega > 0\ , \tag{181}$$

where β_{11} is the propagation constant for the accelerating mode in the dielectric waveguide and β_e is the electron velocity divided by c. The inverse Fourier transform of equation 181 gives the time domain field, $\mathrm{E}_\mathrm{z}(\mathrm{t},\ \mathrm{z})$, in the rest frame of an electron travelling at a velocity, $\mathrm{v}_\mathrm{e} = \beta_\mathrm{e}\mathrm{c}$. The electric field interacting with a 35.5 MeV electron, travelling at $\mathrm{v}_\mathrm{e} = 0.9999\,c$, can be calculated by tracking the time domain field at a stationary point in this frame, $\mathrm{E}_\mathrm{z}(\mathrm{t}_\mathrm{e},\ \mathrm{z})$. Assuming zero initial chirp and a central THz frequency of 0.4 THz, figure 29a shows $\mathrm{E}_\mathrm{z}(\mathrm{t}_\mathrm{e},\ \mathrm{z})$ when interacting with pulses of different spectral width, σ. When an electron interacts with a pulse with a bandwidth of 50 GHz, the pulse is not dispersed significantly so the electron sees a field which is Gaussian in time as it passes through the THz envelope. When the bandwidth is larger, the pulse is more strongly dispersed and quickly becomes chirped. The interaction is not initially phase-matched due to the phase velocity of the local frequency components, so the electron sees both positive and negative contributions to the accelerating field. The interaction with phase-matched components of the pulse then follows. A larger bandwidth also means a higher peak field when the pulse energy is kept constant. The calculated FWHM interaction length as a function of bandwidth from the simulation is plotted in

29b where the fit line is given by equation 179. For larger bandwidths, the analytical results fail to predict the simulation results that show how the interaction length plateaus. The dispersion in the DLW increases the pulse duration which leads to an interaction length greater than the one predicted by equation 179 for higher bandwidth pulses. The point at which the accelerating radiation and the electrons overlap within the waveguide also affects the interaction length, as it defines the pulse duration through the interaction. Equation 179 best describes the behaviour when the interaction occurs at the beginning of the DLW and with narrow-bandwidth pulses.

Taking the integral of the time domain field over the DLW length at a time, t_e, gives the energy gain, W, at that electron injection time

$$W = \int_0^{L_{wg}} E(t_e, z)\, dz \ . \tag{182}$$

For the bandwidths considered in 29b, the interaction efficiency is effectively constant with bandwidth when the input THz pulse has a central frequency matched to the operating frequency of the waveguide and the injection time is constant. This can be attributed to the trade off between peak field and interaction length for smaller bandwidths. For larger bandwidths, where the interaction length is approximately constant, the higher peak field of larger bandwidths is cancelled by the detrimental effect of non phase-matched frequencies interacting with the electron.

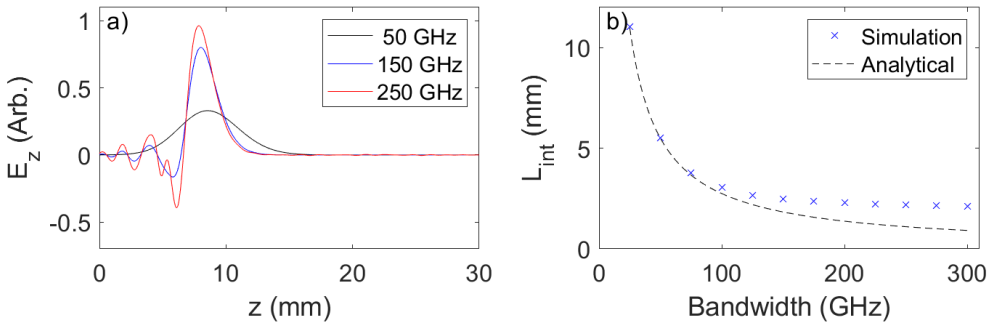

Figure 29: The accelerating field interacting with an electron as a function of waveguide position is shown for a range of bandwidths in **a)**. In **b)**, the FWHM interaction length as a function of bandwidth is plotted.

Another way to increase the interaction length would be to add a linear chirp, φ_2, in equation 180. Figure 30a shows the interaction at the start of the waveguide

between an electron and a number of pulses with different chirped durations given a transform limited duration of 6 ps. A positive chirp is used here as that is the chirp polarity that is gained in the coupler. Chirp on the THz pulse lengthens the interaction but also leads to the particle seeing negative fields before and after the phase-matched interaction, where the interacting frequencies are not phase-matched. The interaction length against chirped pulse duration is plotted in 30b, where the dotted line comes from equation 179. For smaller linear chirp components, the simulation, from equation 181, and the analytical results, from equation 179, are similar. The discrepancy between these two calculations for higher chirps comes from the extreme frequencies at the beginning and end of the pulse not being phase-matched. If the interaction occurs at the beginning of the DLW as it has here, the polarity of the input chirp is not too important. If the interaction occurs later in waveguide, further chirp is accrued due to propagation in the dispersive DLW. The pulse duration at the point where it interacts with the electron is then dependent on a combination of the initial chirp and the waveguide dispersion. Since the dispersion in the DLW occurs in a fixed direction, opposite initial chirp polarities lead to different pulse durations at the interaction point. The interaction efficiency at the injection time shown in the plots is constant with chirped pulse length which suggests the increased interaction length is cancelled by the reduced field strength. The results from figures 29 and 30 show that the dispersion-free approximation assumed in equation 179 is accurate for small bandwidths and linear chirp components, when the interaction occurs at the beginning of the waveguide. For higher bandwidths and chirps, the lack of information with regards to pulse dispersion in this equation leads to a significant discrepancy between the modelled and calculated interaction lengths. Although the constant interaction efficiency observed with pulse duration and chirp is consistent with intuition, modelling is required to fully understand the underlying physical process.

4.1.4 Truncated Interaction by a Finite Waveguide

When the central frequency of the THz does not match the operating frequency of the waveguide, the interaction efficiency drops significantly. Energy can be gained from a non-phase-matched interaction if it is truncated such that the electron does not experience travel through the full pulse field. The interaction can effectively be truncated at the waveguide entrance, where a sharp change in the phase velocity occurs as the field passes from coupler to DLW. To investigate this potential non-phase-matched interaction mechanism, electrons were allowed to be injected into a region of significant field at the waveguide entrance. Only the waveguide fields though contributed to the electron acceleration. Figure 31a plots the in-

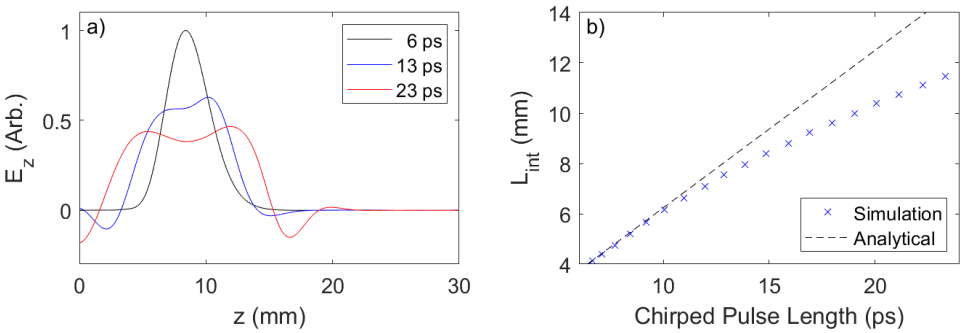

Figure 30: The accelerating field interacting with an electron as a function of waveguide position is shown for a range of chirped pulse durations in **a)**. In **b)**, the FWHM interaction length as a function of chirped pulse duration is plotted.

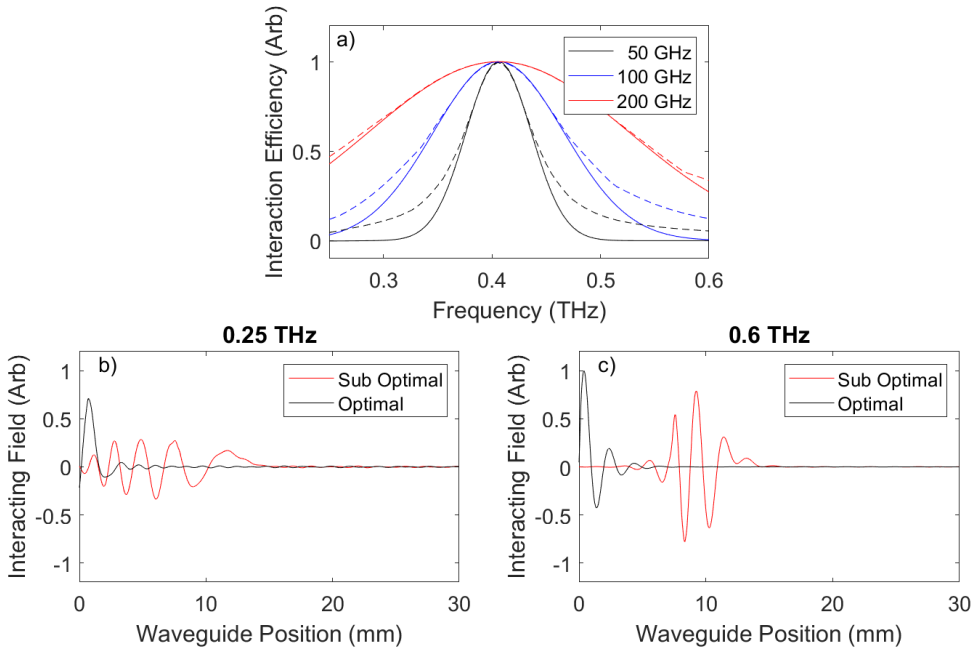

Figure 31: Interaction efficiency as a function of frequency at 3 different bandwidths is plotted in **a)**. The solid line represents the interaction efficiency at a fixed injection time at which the phase-matched interaction is optimised, whereas the dashed line plots the efficiency at the optimal injection time for a given frequency. **b)** and **c)** show the field experienced by an electron with an accelerating field of central frequency 0.25 THz and 0.6 THz respectively, at two different injection times.

teraction efficiency as a function of central frequency of the input THz radiation for a number of spectral widths. The solid line depicts the interaction where the injection time is fixed. The injection time was chosen so that the interaction

efficiency was maximised when the driving frequency matched the waveguide operating frequency and is where an electron would pass through the full THz pulse envelope. The dashed line is found by considering only the DLW fields as discussed and varying the electron injection time until the maximum energy gain is achieved. The two calculations overlap close to the phase-matched frequency of 0.4 THz, as the injection time for the fixed injection simulation is set such that it maximises the energy gain at 0.4 THz. For central frequencies far from the operating frequency, a broader frequency response can be seen in the scenario where the injection time is varied. When the pulse only contains a very small amplitude of the phase-matched frequency, the interaction is more efficient when the electron is injected into a region of significant THz field at the waveguide entrance. The comparison between these two injection times is illustrated in figures 31b and 31c where the field interacting with an electron when the pulse central frequency is 0.25 THz and 0.6 THz respectively is shown. Both plots depict an accelerating field with a bandwidth of 0.05 THz at two different injection times, with the field normalised to the highest field in figure 31c. The black line is the injection time which is optimal for energy gain at these frequencies and the red line is optimal for energy gain at the waveguide operating frequency. Since these interactions are not phase-matched, particles at the injection time depicted by red lines see equal positive and negative phase of the THz pulse and zero net energy gain occurs. Energy gain can occur at the injection times denoted by the black lines because the electron sees more of the positive phase of the accelerating field than it sees of the negative. At 0.25 THz, as in figure 31b, the interacting field amplitude is smaller than in figure 31c, at 0.6 THz. A large portion of the pulse is below the waveguide cutoff frequency so does not propagate into the waveguide and the steeper gradient of the dispersion curve at this frequency leads to stronger dispersion of the pulse. The interaction efficiency of the lower than waveguide operating frequency interaction is still very similar to the higher than waveguide operating frequency interaction since the larger wavelength leads to an increased effective interaction length. The frequency at which the truncated interaction becomes more efficient than interacting with the whole pulse is bandwidth dependent, as it is related to the phase-matched component of the THz spectra.

Previously, the field experienced by a single electron at given injection times has been considered. When considering an electron bunch, if the duration is on the order of or larger than the accelerating field period, energy modulations are seen; some electrons will be accelerated and some decelerated. Given a phase-matched interaction between THz and electrons, the energy modulation imparted onto the

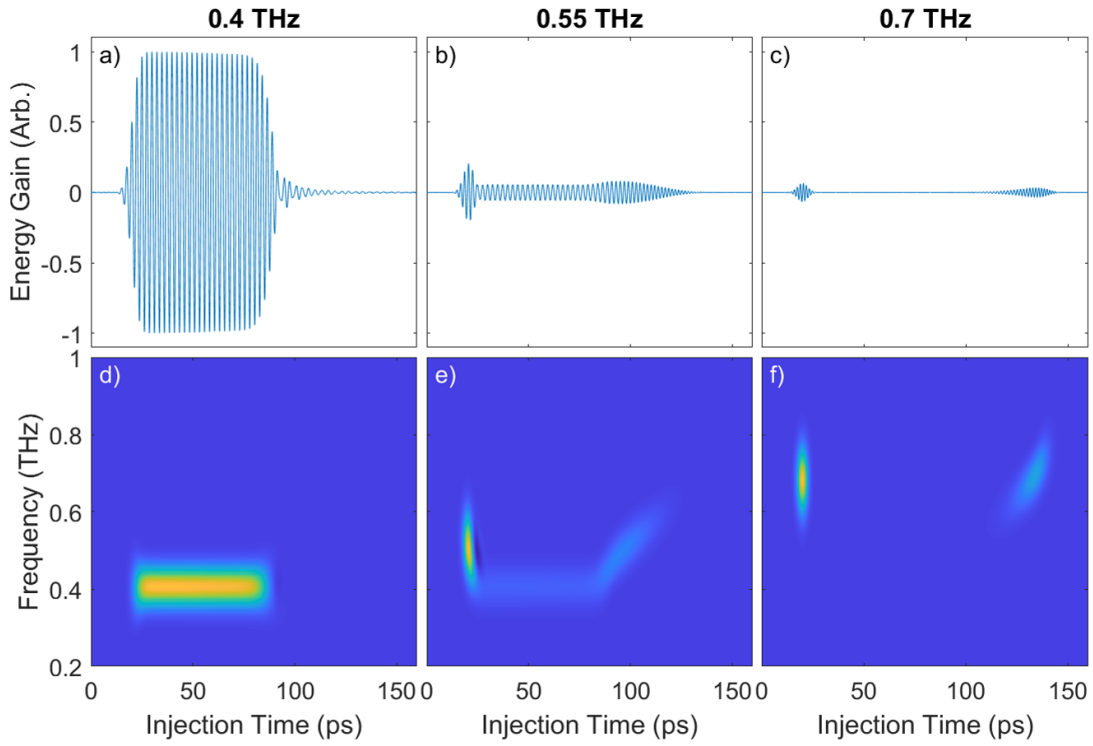

Figure 32: **a)**, **b)** and **c)** plot energy gain as a function of injection time for THz central frequencies of 0.4 THz, 0.55 THz and 0.7 THz, respectively. Time-frequency analysis was performed on these plots to give the energy modulation frequency as a function of injection time shown in **d)**, **e)** and **f)**.

electron bunch will be sinusoidal in time with an approximately constant amplitude and frequency, as long as the electrons pass through the full THz pulse. For the truncated interaction, the energy modulation will be the same shape as the accelerating field and energy gain only occurs at either the waveguide entrance or exit. A pulse with a finite bandwidth with a frequency different to the operating frequency will exhibit contributions from both of these mechanisms. To illustrate this, the interaction between a THz pulse of bandwidth 100 GHz and an electron bunch was simulated at a number of different central frequencies. The energy gain as a function of electron injection time for central frequencies of 0.4 THz, 0.55 THz and 0.7 THz are plotted in figures 32a, 32b and 32c respectively. The interaction at 0.4 THz field is phase-matched. At 0.7 THz, there is almost no phase-matched component within the THz spectrum so the truncated, non-phase-matched interaction dominates. The strongest interaction at 0.7 THz occurs at the beginning of the waveguide, since, by the end of the waveguide, the THz pulse has significantly dispersed and the field strength is reduced. When the central frequency is set to 0.55 THz, as in 32b, phase-matched and non-phase-

matched mechanisms are enabled. Interaction between electrons and the THz in figure 32 occurs over a larger range of injection times at off-resonant frequencies because at these frequencies, the pulse group velocity is lower, so the pulse takes longer to traverse the DLW length. The frequency of the energy modulation is injection time dependent. To confirm that the frequency of the interaction is reliant on the injection time in the expected way, time-frequency analysis of the energy gain versus injection time signal was performed using the Wigner-Ville distribution (WVD). For a continuous signal, S(t), the WVD gives the frequency of the signal as a function of time by first taking the autocorrelation of the signal at two times separated by a small time difference, τ. The Fourier transform of the autocorrelation gives the Wigner function. Given a distribution with zero mean, the Wigner function can be written as [132]

$$\mathrm{WVD_S}\,(\mathrm{t},\mathrm{f}) = \int_{\infty}^{-\infty} \mathrm{S}(\mathrm{t}-\tau/2)\,\mathrm{S}^{*}(\mathrm{t}+\tau/2)\,\mathrm{e}^{\mathrm{i}\,2\,\pi\,\mathrm{f}\,\tau}\,\mathrm{d}\tau\ . \tag{183}$$

Equation 183 can be calculated for a discrete signal by summing over the available samples. The MATLAB 'wvd' function which was used for this analysis has the option to provide a smoothed-pseudo WVD, which uses low-pass windows in frequency and in time to filter out unhelpful interference terms. The smoothed-pseudo WVDs in figures 32d-f give the energy modulation frequency as a function of injection time. If an electron is allowed to pass through the full THz pulse, energy gain can only occur due to the phase-matched component of the pulse. Where the interaction is truncated at the entrance, the energy modulation frequency is set by the driving THz frequency. The truncation at the exit behaves in a similar manner but the electron is interacting with a chirped pulse rather than a transform limited pulse.

4.2 Experimental Setup

A diagram of the experimental layout outside the interaction chamber is shown in figure 33a. The setup was built on 4 separate breadboards which were pre-aligned prior to the allotted beam time. The modular approached meant that it could easily be transported to the beam area and quickly re-aligned via the two iris' at the start of the setup. Two delay stages were used to vary the THz to electron timing and the THz to probe pulse timing. The setup inside vacuum is drawn in figure 33b along with a photograph of the waveguide and final mirror assembly. The EO detection setup inside the chamber was placed on a separate breadboard on a translation stage so it could be moved into the beamline when THz field measurements were required and then out of the beamline to allow the electron beam to pass. For a course measurement of the temporal overlap between the THz and electron beam, a coherent transition radiation target was placed at the waveguide position in the electron beam path. The THz frequency emission from this target and the optically generated THz were measured using a Schottky diode and the signal from the two sources was overlapped to achieve approximate synchronisation.

4.2.1 THz Generation and Transport

The THz source was powered by the CLARA laser system described in 3.1. The transform limited FWHM pulse duration of 60 fs was stretched to approximately 12 ps in order to produce narrowband THz via chirped pulse beating (CPB) [133, 134]. A Michelson interferometer, as in figure 34a, was used to split the pulse in two and then recombine with one half time delayed, which forms a beat wave pattern as shown in figure 34b. Half of the pulse energy is lost in this process. The THz generation process is described in 2.1.3. Stability of the time delay introduced by the interferometer is a very important factor in the synchronisation of the timing of the electron beam and THz pulse. A change in the delay, $\Delta\tau$, of $0.5/f_0$, or 1.3 fs in this case, leads to a pi change in the initial phase of the beat wave, which is approximately a one picosecond shift in the THz peak position. This is illustrated in figure 34b as the difference between the two beat wave intensity outputs. Isolation of the interferometer from vibrations and making sure that the optics are mounted securely is crucial to ensure stable electron-THz timing. Given $\tau \ll \sigma_t$, the beat wave intensity profile occurs over a duration approximately equal to the chirped pulse duration. To match the DLW design frequency of 0.4 THz, a delay of approximately 650 fs was given to one arm of the Michelson interferometer. The central frequency could be tuned by adjusting the delay via a mechanical stage.

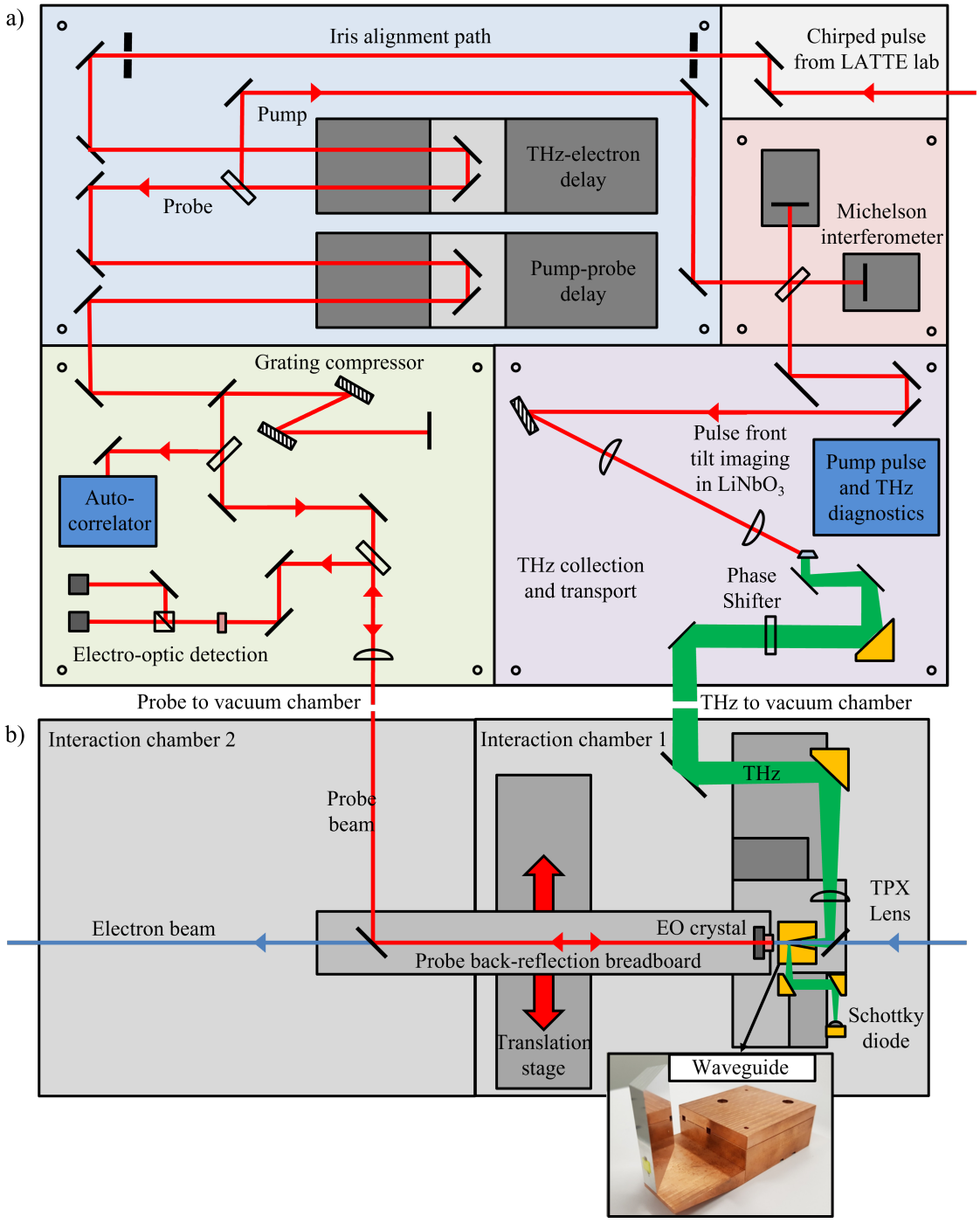

Figure 33: **a)** shows the THz source setup outside the interaction chamber. An approximately 12 ps terawatt class laser pulse is transported from the LATTE lab where it is split into a pump and probe. Chirped pulse beating of the pump pulse generates narrowband THz radiation. The probe pulse is compressed to 60 fs and used for electro-optic detection of the THz. The setup inside the interaction chamber is shown in **b)** along with a photograph of the waveguide and final mirror assembly. Courtesy of Morgan Hibberd.

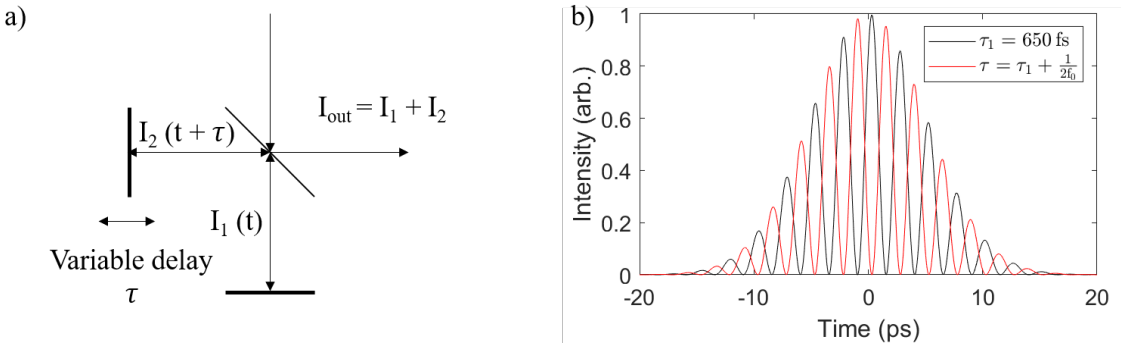

Figure 34: **a)** A schematic of the Michelson interferometer. **b)** Output intensity envelopes with a time delay difference, τ, in the Michelson interferometer of half of the laser period. The laser in this calculation had a central frequency of 800 nm, a transform limited FWHM duration of 60 fs and a chirped duration of 12 ps.

THz radiation was generated by tilted pulse front pumping of a stoichoimetric lithium niobate crystal. A 4f imaging system consisting of an f = 130 mm cylindrical lens and an f = 75 mm cylindrical lens imaged the pulse at the grating surface to the exit surface of the lithium niobate crystal with a magnification of 0.577. The lenses were chosen to minimise the mismatch between the grating image angle and the pulse front tilt of the pump beam. The incident angle of the pump onto the grating was 31.2 ° and the diffracted angle was 57.5 °. This arrangement lead to a pulse front tilt in the crystal of 62.9 ° and a grating image angle of 63.8 °. Due to the 50 % efficiency of the interferometer and losses at the grating, a pulse of energy 18 mJ reached the non-linear crystal.

The pump $1/e^2$ intensity radius on the lithium niobate was 2.5 mm × 5 mm, giving an estimated THz beam size at the exit surface of ≈ 3.5 mm × 3.5 mm assuming a factor of $1/\sqrt{2}$ for intensity to field conversion and a factor of tan(62.9 °) in the horizontal. The THz radiation was collected and collimated by an off-axis parabolic mirror (OAP) with a reflected focal length of 152.4 mm, which was placed ≈ 150 mm away from the lithium niobate crystal. A second OAP of focal length 228.6 mm was placed a focal length away from the coupler of the waveguide for gentle focusing of the THz. When it was found that the THz focal spot at the coupler was too large, a TPX lens of focal length 100 mm was placed close to the coupler entrance in order to focus the THz more tightly. The THz radiation was aligned to the electron beam by using a visible alignment laser which roughly followed the electron beam path. Assuming the generated THz has no initial divergence, the beam waist could be tracked through the transport using ray transfer matrices

to predict the focal spot size at the coupler and to ensure that the THz beam would not be clipped severely by optics along the way. For a Gaussian beam this involves tracking the evolution of the complex beam parameter, q, through drift and through focusing optics using matrix operators, as described in section 2.3.1. The thin lens approximation was used here. Figure 35 shows the $1/e^2$ waist radius of the THz intensity profile through the transport system for 0.35 THz, 0.40 THz and 0.45 THz, from the generation crystal to the waveguide coupler entrance. The $1/e^2$ radius at the coupler entrance is approximately 2 mm, which is larger than the ideal beam size for energy efficient coupling into the accelerating waveguide mode.

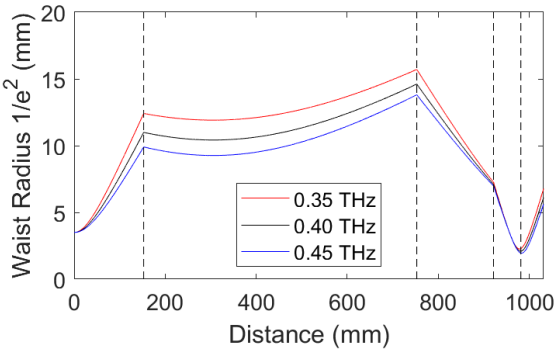

Figure 35: The $1/e^2$ waist radius of the THz intensity profile through the THz transport to the coupler entrance. The first 3 black dotted lines denote focusing optics and the final one is the position of the coupler entrance.

A probe pulse was picked off from the pump pulse before the Michelson interferometer using a 95/5 beamsplitter for electro-optic measurements of the THz field at the interaction point. The probe passed through a grating compressor which re-compressed the chirped pulse back to its transform limited duration of approximately 60 fs FWHM intensity duration. This was significantly shorter than the THz period so the temporal profile of the THz pulse could be measured precisely. The compressed probe was split into two parts; one was deflected to a GRENOUILLE [135] which measured the probe pulse duration and the other was transported into the interaction chamber for the EO measurement of the THz field strength at the interaction point with a ZnTe crystal in a back-reflection geometry. The probe pulse duration measurement was also a diagnostic of the chirped pulse duration. The grating compressor setup was known to compress a 12 ps pulse to a 60 fs transform limited pulse, so a change in the chirped pulse length would affect the probe pulse duration in known manner.

Temporal overlap between the main pulse and its reflections inside the detection crystal caused the measured signal to appear longer than the pulse truly was. Post-processing was required to retrieve the true waveform. In the time domain, the measured signal, S, can be written as a sum of the pulse and its reflections which are attenuated by a factor, r, and delayed by a time, τ,

$$\mathrm{S(t)} = \sum_{\mathrm{m}=0}^{\infty} \mathrm{r^m\, E(t - m\tau)}\ . \tag{184}$$

Assuming that each subsequent reflection gains an extra attention factor, r, and that the time delay between each reflection is constant, a Fourier transform of this yields a result that can be written as a geometric series

$$\widetilde{\mathrm{S}}(\omega) = \widetilde{\mathrm{E}}(\omega)\ \left(\sum_{\mathrm{m}=0}^{\infty} \mathrm{r^m\, e^{i\,\omega\, m\,\tau}}\right) = \frac{\widetilde{\mathrm{E}}(\omega)}{1 - \mathrm{r\, e^{i\,\omega\,\tau}}}\ . \tag{185}$$

Rearranging this in terms of $\widetilde{\mathrm{E}}(\omega)$ and performing the inverse Fourier transform gives the reflection subtracted electric field waveform. As the reflections originate from the ZnTe detection crystal, the time delay can be calculated using $\tau = 2\mathrm{dn}_\phi/\mathrm{c}$, where d is the thickness of the detection crystal, 0.5 mm in this case, and n_ϕ is the phase velocity refractive index of ZnTe, which is approximately 3.17 at 0.4 THz [136]. The reflection coefficient given this refractive index was calculated to be 0.52 from the Fresnel equations. Removal of the first reflection was all that was needed to suppress distortions in the signal.

To generate a quasi-TEM_{01} mode Gaussian THz pulse, a thin piece of PTFE was used to time delay one transverse half of the pulse by half of the THz period. The required thickness differential between the two sides of the PTFE plate, ΔL, was calculated by equating the time taken for the radiation with a central wavelength, λ_0, to travel half a wavelength further in air compared to in a material with refractive index, n. This gives $\Delta\mathrm{L} = \frac{\lambda_0}{2\,(\mathrm{n}-1)}$. For a PFTE refractive index of 1.43 [137] at a THz frequency of 0.4 THz, the difference in thickness between the top and bottom of the mode converter needs to be approximately 900 μm. The transverse electric field profile at the focus was explored using the Kirchhoff diffraction-based propagation method described in section 2.3.2. The experimental transport system for the THz from the phase shifter position onwards was mimicked in simulation, with the mode converting plate placed 100 mm from the first parabola. The central frequency of the THz pulse polarised linearly in the y direction was 0.4 THz and the intensity FWHM bandwidth was 70 GHz. The source was initialised as a pulse with a group delay of 1.25 ps on one side, as plotted in figure 36a, with the corresponding cross-section profile in figure 36b. After propagation, energy is lost in

the centre of the pulse due to diffraction where there is sharp change in the electric field. At the focus, the transverse electric field time profile is plotted in figure 36c. The corresponding field cross-section in figure 36d is very similar to an analytical TEM_{01} Gaussian mode which validates that assumption in the calculation of coupling into the coupler and the DLW. Confirmation of the understanding of how the phase shifter worked was gained from EO scans of the transverse field above and below the central region. Figure 37 shows the reflection suppressed transverse field induced signal through each half of the mode converting plate. There is a time delay between the measured fields of approximately half the period of the pulse and the peak field on each side was similar, which gave evidence that the plate was performing as expecting.

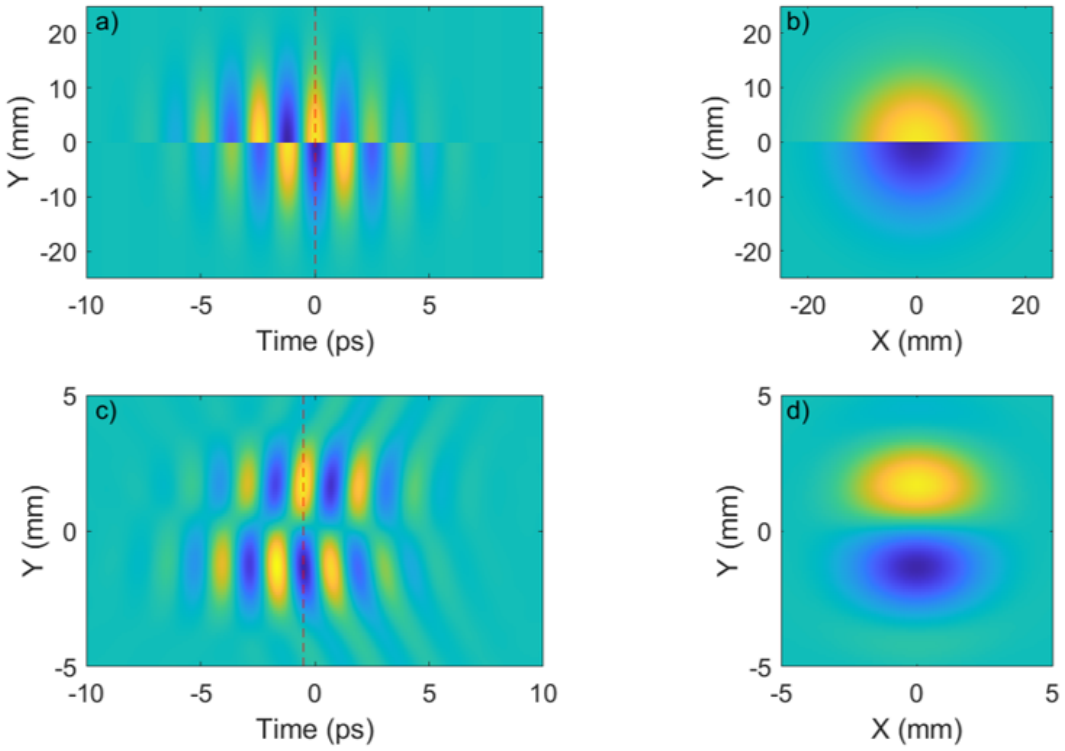

Figure 36: The time profile of the assumed electric field at the phase shifter exit surface, **a)**, and the field cross section at the position of the dotted red line, **b)**. The simulated time profile of the electric field at the interaction point and the field cross section at the position of the dotted red line are shown in **c)** and **d)**, respectively.

Figure 38a shows an EO time domain measurement of the longitudinal field of the

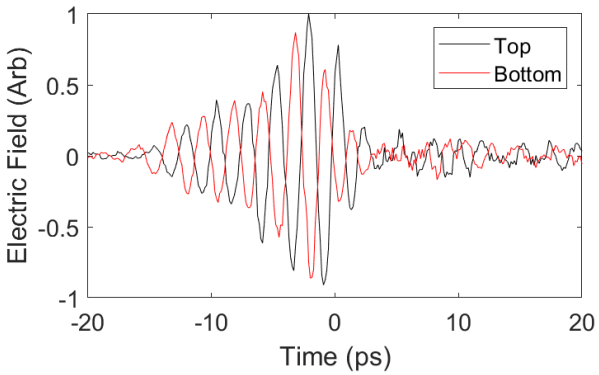

Figure 37: Electro-optic signal as a function of time. The measurements show the field passing through the top and the bottom of the phase shifter plate.

generated THz, with and without reflection suppression, retrieved from balanced detection, as described in section 2.1.5. The central frequency of 0.4 THz was found to be optimal for the waveguide and the FWHM intensity bandwidth was 70 GHz. The peak electric field at the entrance to the waveguide coupler was measured by EO detection to be 340 kV/m. The EO field was calibrated from the lock-in amplifier signal using equation 70 in section 2.1.5, where $r_{41} = 4$ pm/V and a (110)-cut ZnTe crystal of thickness 0.5 mm was used. The pulse energy was measured by a calibrated pyro-electric detector to be 2.1 μJ at the generation crystal surface.

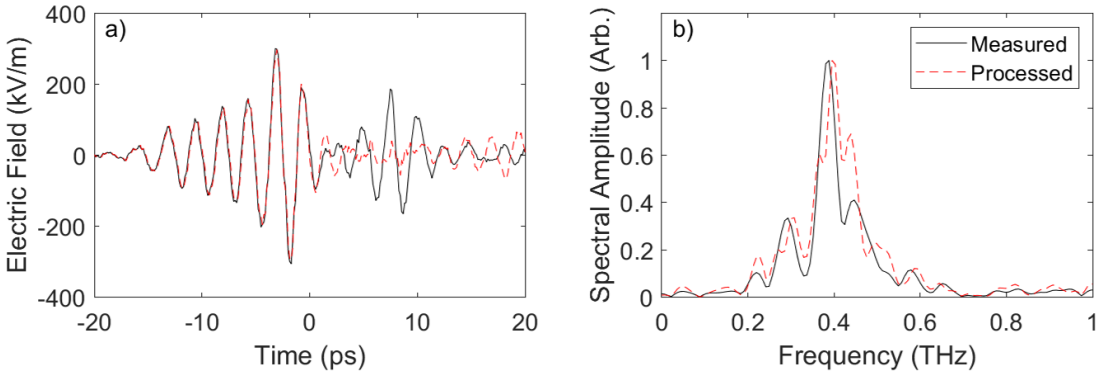

Figure 38: Electro-optic scan taken at the entrance to the waveguide, **a)**, before and after removal of reflections. The Fourier transform is illustrated in **b)**.

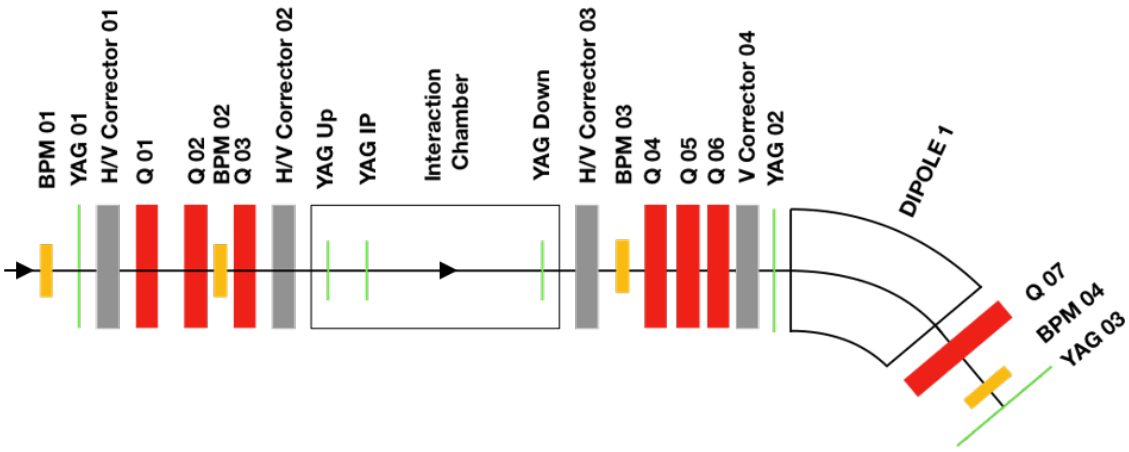

Figure 39: The electron beam-line in Beam Area 1 at the CLARA facility. BPMs are beam position monitors, H/V correctors are horizontal and vertical correctors, Q stands for quadrupole magnet, IP is the interaction point and the YAGs are scintillating screens which measure the transverse beam profile. The electron beam enters the area from the left and is steered and focused towards the interaction point, using two H/V correctors and a quadrupole triplet, where it then passes through the waveguide. After the waveguide, the beam is focused towards the spectrometer which consists of a dipole, a quadrupole and a YAG screen.

4.2.2 Electron Beamline

The components in the electron beamline in the experimental area are shown in figure 39. Upstream of the interaction chamber, two horizontal and vertical correctors give control of the position and the angle of the electron beam going into the chamber. A quadrupole triplet was used to focus the beam onto a YAG(Ce) scintillation screen mounted on the waveguide, adjacent to the electron aperture. Once the optimal focusing for electrons was found by looking at the scintillation screen, the DLW could be moved so that the electron beam passed through the waveguide aperture. The waveguide was mounted on a 5-axis stage and pre-aligned using a helium neon alignment laser which was positioned so that it followed the electron beam path. A YAG screen at the back of the interaction chamber, after the waveguide, could be used to check the electron beam transverse profile after the waveguide, to see if it was being clipped. Downstream, a pair of transverse steering correctors were used to steer the beam through the centre of the quads. The quadrupole triplet, Q4 - Q6, were tuned to give the best quality focus on the final YAG screen. The dispersion introduced by the dipole could be tuned by the final quadrupole, Q7. This meant the field of view and the energy resolution of the energy spectrometer could be varied. The energy spectrometer was calibrated by first assuming that the horizontal position on the screen was linearly related

to the energy. With the known central energy of 35.5 MeV, the axis could be ascertained by measuring the spatial separation between two calibration reticles and the difference in magnet current required to move the beam from one reticle to the other [138]. A schematic of the beam area at the CLARA facility is given in figure 40.

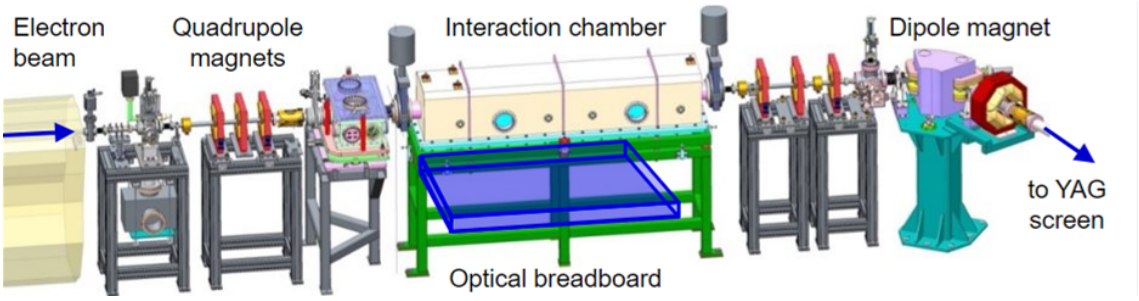

Figure 40: A schematic of the experimental area at the CLARA facility. Courtesy of Morgan Hibberd.

The electron beam charge was varied by adjusting the attenuation on the photoinjector laser. The bunch charge used in this experiment varied between 10 pC and 70 pC - the lower limit being the threshold for seeing the beam on the scintillator screens. Another import parameter was the linac phase, Φ. By accelerating off-crest at different phases, a specified chirp could be applied to the electron beam. The accelerating phases at which data was taken in this experiment are illustrated in figure 41. The bunches at $\Phi = +15°$ and $\Phi = +10°$ had a duration of order of 10 ps, had a linear chirp and gave smaller energy jitter on the spectrometer screen than shorter bunch modes. These were used to see THz-induced modulations in the beam and gave a starting point from which to optimise. These datasets will be focused on in sections 4.3 and 4.4. The $\Phi = +4°$ bunch had a duration on the order of the THz period and had minimal energy spread, whereas the Φ = -10° accelerating phase produced the shortest bunch.

4.3 Energy Modulation Analysis

4.3.1 THz Frequency Calibration

To validate our understanding of the THz-electron beam interaction, electron energy measurements were performed at several different THz driving frequencies. The THz central frequency could be tuned by varying the delay between the arms of the Michelson interferometer. Electro-optic scans were taken at two different

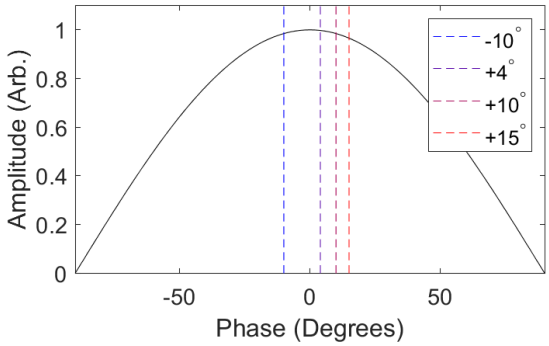

Figure 41: Sinusoidal RF accelerating field with key phases used in the experiment labelled.

micrometer positions to calibrate the micrometer position on the delay arm stage to a THz frequency. Given the measurement of the central frequency at these two positions and that, as shown in equation 48, the central frequency of the THz is proportional to the time delay, the calibration between micrometer position and frequency could be calculated. The calibration along with measured data points from electro-optic scans is plotted in figure 42.

The error on the micrometer position at the point where this EO data was taken was estimated to be $\pm$ 2 μm. The micrometer uncertainty gave rise to an uncertainty in the THz central frequency calibration, that was calculated by looking at the minimum and maximum frequencies that a given micrometer position could correspond to whilst still adhering to a fit line which passed through the error bars of the measured data. Using equation 48 with a transform limited pump pulse duration of approximately 60 fs FWHM and a chirped pulse duration of 12 ps FWHM gives a consistent scaling between micrometer position and THz frequency. This calibration allowed exploration of the frequency dependence on the THz-electron interaction in the DLW.

4.3.2 Modulation Depth

The linac phase for the data taken for optimisation of the THz frequency was $\Phi = +15°$, which produced an electron bunch with an approximate duration of 10 ps and a linear chirp. A spectrometer scintillation screen image with this linac phase and the chosen beam optic strengths is shown in figure 43a. The asymmetrical nature of this profile was due to clipping of the electron beam in the waveguide structure. To retrieve the energy spectra, a constant dark field was first subtracted from the spectrometer images. The subtracted images were then summed over the

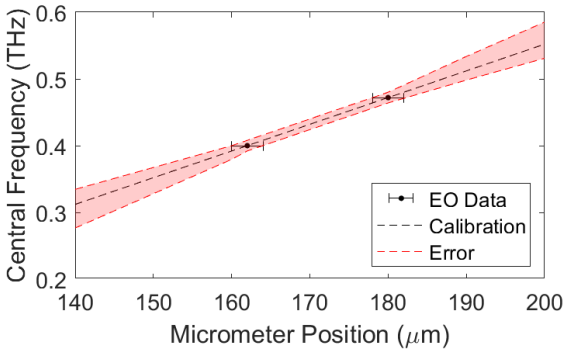

Figure 42: The calibration between the delay stage position in the Michelson interferometer to THz central frequency.

axis orthogonal to the dispersive plane to give the screen signal versus electron energy, as shown in figures 43b and 43c. Since the energy measurement is not an absolute measurement, the axis is centred on zero, with energy relative to that point plotted on the x axis. The average depth of the modulation was calculated for several THz frequencies to quantify the interaction efficiency. At each frequency, the THz-electron timing was varied to find the strongest interaction. The modulation depth here was calculated from the background subtracted signal. The jitter in the amplitude of the electron energy spectrometer signal and in the spectral shape was significant, so a mean of the background images did not give a representative background for each THz on spectra. Instead, background spectra were individually selected to best match each modulated spectra. It was assumed that the charge accelerated was roughly equal to the charge decelerated. Hence, it was expected that the sum of the positive regions of the subtracted signal would be roughly equal to the sum of the negative regions. The background spectrum which minimised the sum of positive and negative components in the subtracted spectrum was selected to be the best fitting one. Every background spectra was iterated over for every individual THz on spectra. Once the background was chosen, it was subtracted from the image, and the subtracted image was divided by the peak of the background spectra for normalisation. The modulation depth was then defined as the average height between the peak of the modulated signal and its adjacent troughs, as demonstrated in figure 43d. Plotted in figure 44b is the modulation depth against THz frequency. Each frequency point is the mean of the modulation depth calculated from 100 images, with the error being the standard deviation of these measurements. It can be seen that the peak modulation depth is at a frequency of 0.4 THz.

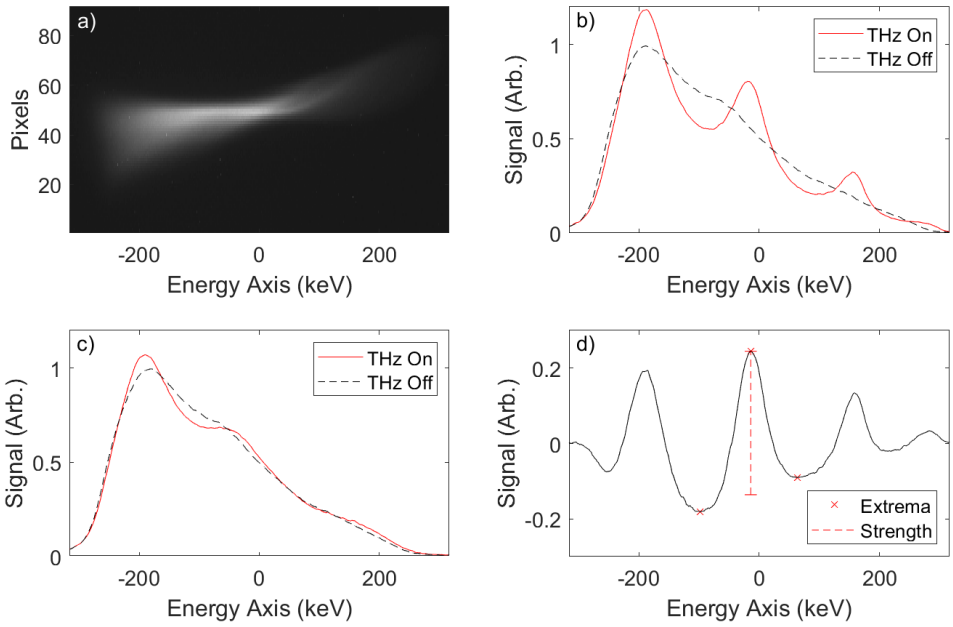

Figure 43: **a)** A typical spectrometer image with no THz in the $\Phi = +15°$ dataset. Corresponding electron spectra are shown with a THz induced modulation for an optimised central frequency and a sub-optimal frequency in **b)** and **c)**, respectively. **d)** A background subtracted spectrum.

In the background spectra in figures 43b and 43c, there is a hint of a periodic structure. The self-interaction of the electron bunch and its wakefield in the DLW could be the cause of this structure in the spectra [139]. The frequency of the modulation from the self-interaction should be equal to the phase-matched frequency of the accelerating mode in the waveguide. It can be seen though in figure 43b that the THz-driven interaction is significantly larger.

The interaction in the waveguide was modelled as described earlier to retrieve the frequency scaling of the efficiency. This assumes that the electron energy gain is linear to the modulation depth, which is the case for small energy gains with respect to the bunch chirp. The height of the fit was modified to give the best representation of the experiment data. A Lorentzian distribution was used to model the THz spectrum, as this better represented the measured EO signal than a Gaussian distribution. The calculation was repeated for a range of spectral widths, as shown in figure 44a, to account for errors in the EO measurement and for any changes in the spectrum as the central frequency changed. The frequency domain field within the waveguide in the electron rest frame could then be written as

$$\widetilde{E_z}(\omega, z) = \frac{\gamma^2}{(\omega - \omega_0)^2 + \gamma^2} \, e^{-i\,\omega\,t_0} \, e^{i\,(\beta_{11} - k/\beta_e)\,z} \, . \tag{186}$$

where γ defines the spectral width and is between 0.25 THz and 0.5 THz. The blue shaded region in figure 44b shows the result of this calculation where the injection time is optimised for the central frequency and kept constant throughout the frequency range. The red shaded region is where the best possible injection time is chosen with each central frequency. Both curves show a trend consistent with the experimental data. These fits overlap near the waveguide operating frequency where the interaction with the phase-matched component of the pulse is most efficient. The FWHM interaction length with the most efficient THz central frequency of 0.406 THz was calculated with this model to be between 2.8 mm and 3.8 mm in this range of spectral widths, where the larger bandwidth corresponds to the shorter interaction length. By comparing the modelled modulation to the experimental results, a maximum electron energy gain of 10 keV was estimated. The lower and upper limits on the calculated average accelerating gradient over the FWHM interaction length were 2.6 MV/m and 3.5 MV/m, respectively. The corresponding peak accelerating gradient was between 3.3 MV/m and 4.4 MV/m.

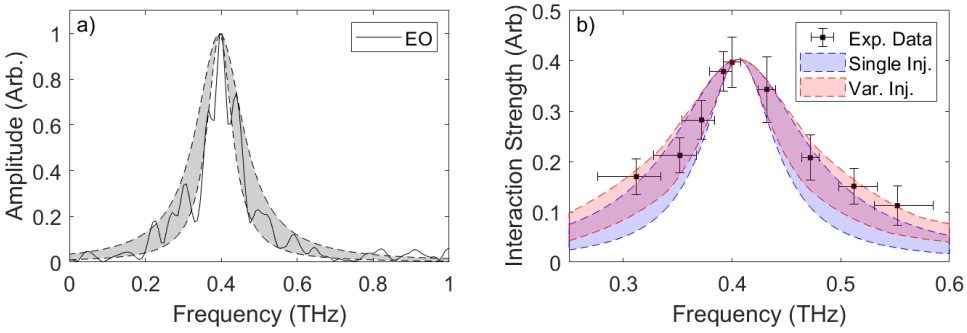

Figure 44: In **a)**, the assumed spectral widths in the fit to the experimental data are plotted with the measured electro-optic signal. The interaction efficiency as a function of frequency is plotted in **b)**, where the blue region depicts the efficiency within the spectral range for a single injection point and the red region trials various injection times and chooses the one with the greatest efficiency.

When a truncated interaction is more efficient than the interaction with the phase-matched component of the pulse, the two fits in figure 44b separate. The red region seems to better fit the data which gives credence to the hypothesis that for certain frequencies, the most efficient interaction is not phase-matched. This does not necessarily prove that the interaction is due to electrons entering the waveguide

in a region of significant THz field since the fields in the coupler and before the coupler have not been considered here.

Small differences in the waveguide properties, especially the dielectric thickness and the relative permittivity, can lead to significant changes in the waveguide operating frequency. For example, if the dielectric constant was 4 instead of 3.81, the operating frequency would be 0.4 THz rather than 0.406 THz. If the dielectric thickness was 57 μm instead of 60 μm, the operating frequency would be 0.418 THz. Within manufacturing tolerances there can be significant differences in the waveguide dispersion that would lead to a slightly adjusted frequency scaling for the interaction efficiency. Characterisation of the manufactured waveguide before it is used for acceleration is very important for this reason.

4.3.3 Modulation Frequency

For an electron bunch with a linear chirp, the period of the energy modulation across the bunch is proportional the THz period inducing the modulation. If only the phase-matched component of the pulse interacts with the electron bunch, the frequency of the modulation will be dictated by the waveguide operating frequency. If an interaction which is not phase-matched is enhancing the interaction efficiency for a certain driving frequency, the modulation frequency will differ slightly from the waveguide operating frequency. The average modulation period was found by first subtracting a suitable background spectrum from each THz-on spectrum. The extrema were found for all subtracted spectra using a peak finder in MATLAB. A minimum distance was set in this to stop peaks being represented by multiple points. The energy difference between the extrema was calculated. When this energy difference was greater than a set threshold, that measurement was discounted as it was assumed that a point had been missed by the peak finder. This led to a number of measurements of the half period per image within the 100 image dataset. A mean of all of these measurements for each frequency was taken and multiplied by 2 to give the energy modulation period. The standard deviations of the measurements on each image were added in quadrature and divided by the number of images to quantify the error. Assuming a linear chirp, C, the energy modulation period, ΔE, could be converted to a frequency by $f = \Delta E/C$. The linear chirp was estimated by assuming that the modulation period at 0.4 THz corresponded to a frequency equal to the waveguide operating frequency, which gave $C \approx 66\,\mathrm{keV/ps}$. The longitudinal phase space of the beam will be discussed in more detail in section 4.4. The modulation frequency as a function of THz driving frequency is plotted in figure 45a. The point at 0.47 THz was calculated from only

11 images which is why the uncertainty is higher. The modulation frequency for all driving frequencies is close to the waveguide operating frequency, which is proof of a phase-matched interaction occurring. At the two highest driving frequencies measured here though, the measured modulation frequency is higher than the waveguide operating frequency. As discussed in the section 4.1.4, the truncated interaction at the entrance leads to region in which the modulation frequency is dictated by the driving frequency. The extent of this injection time window is less than the electron bunch length, as can be seen in the WVD of the simulated energy gain as a function of injection time using the highest driving frequency measured experimentally, plotted in figure 45b. The spectral width of $\gamma = 0.35\,\mathrm{THz}$ was chosen to be approximately in the middle of the values used to model the interaction efficiency in the previous section. An average modulation frequency over a 10 ps window, as we are effectively measuring with the long electron bunch, would have contributions from the region over which the interaction is truncated and from the phase-matched region. With this in mind, it is expected that the modulation frequency would increase with higher driving frequencies but would still be lower than the driving frequency, as observed here. This effect is only seen at the higher driving frequencies because the lower than 0.4 THz frequency data measured experimentally are not far enough away from the waveguide operating frequency. An accurate model of the data would require knowledge of the exact injection time within the WVD plot that measurements were taking place and a quantification of the timing jitter and the THz phase jitter. Although the higher modulation frequency of these data points indicates a truncated interaction at the waveguide entrance, it should be noted that the modulation strength at these points was low which gives a greater likelihood of measurement error. Repeating these results with a higher THz frequency would give greater confidence in the interpretation described above.

4.4 Longitudinal Phase Space Diagnosis of Electron Bunches

Measurement of the longitudinal energy profile of an electron bunch would usually be performed using an RF deflecting cavity [75–77]. This requires significant, costly infrastructure and metres of space within the beamline dedicated to the diagnostic. The method of measuring the chirp of a bunch described here uses THz radiation to provide energy modulations to the electron bunch. Figure 46 shows an example of a linearly chirped bunch with a sinusoidal energy modulation and the resulting spectra. For the figure, a bunch was initialised with a Gaussian energy distribution and longitudinal profile, and a linear correlation between the time and energy. A time dependent energy modulation was then added to

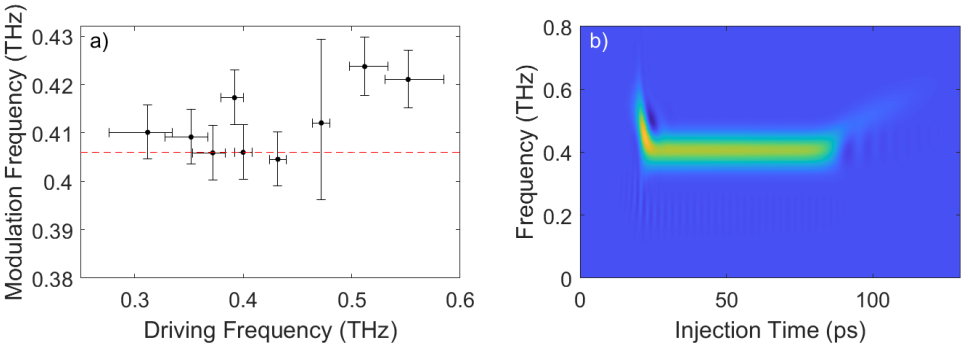

Figure 45: **a)** The measured modulation period as a function of driving frequency. **b)** a WVD, as in section 4.1.4, showing the modulation frequency as a function of injection time with a driving frequency of 0.55 THz.

mimic the THz induced modulation. The energy modulation period in the projected electron energy spectrum is dependent on the bunch chirp and the time period of the THz induced modulation. The chirp can be retrieved by measuring the energy difference between peaks on the spectrometer image, as shown in the energy projection in figure 46, and then dividing by the known THz period. The energy difference between each peak gives a local measurement of the gradient, $\frac{\Delta E}{\Delta t}$, allowing the bunch longitudinal phase space to be probed at a number of points per spectrometer image. Varying the phase of the THz with respect to the bunch allows probing of different parts of the bunch to create a full picture of the chirp along the bunch. The assumptions made here are that the bunch energy is a monotonically increasing or decreasing function with time and that the period of the induced modulation is at the waveguide operating frequency.

The chirp measurement method described above was trialled with data from the CLARA experiment for two different linac phases. Both were expected to give a bunch with a duration stretching over multiple THz pulse cycles and a chirp that was roughly linear. Firstly, a suitable background spectrum was chosen for each THz on spectrum and was subtracted, as described earlier. The energy axis was centred at the mean electron position in the background spectrum, so $E = 0\,\text{keV}$ here corresponds to the central beam energy of 35.5 MeV. The re-centring was justified by the fact that the jitter at this phase was primarily due to RF amplitude jitter rather than phase jitter. The consequence of this was that the shape of the longitudinal phase space should not have been changing significantly shot to shot. Local maxima were found in the image using a MATLAB function, with a minimum distance between peaks to stop multiple points representing a single peak

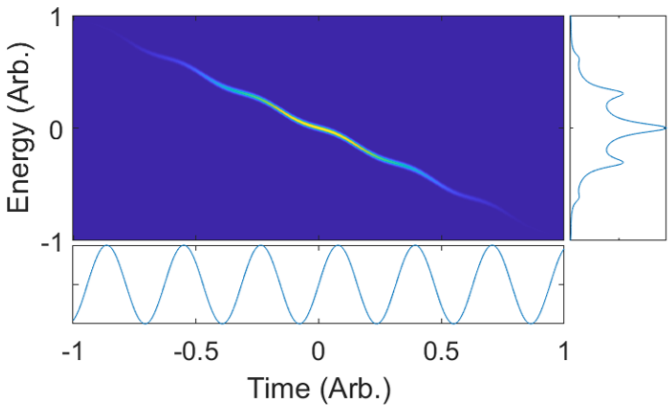

Figure 46: Longitudinal phase space of a linearly chirped electron bunch that has been modulated with a sinusoidal field. The corresponding energy spectrum is shown on the right.

and a minimum prominence set to avoid the function identifying noise peaks. The energy difference between peaks, ΔE, was then calculated and the mean position between peaks, E, was noted to track where the energy difference measurement was taken, as illustrated in figure 47a for $\Phi = +10°$. The corresponding bunch length was sufficient for the measurement of 4 or 5 peaks per spectra which allowed 3 or 4 ΔE measurements per image. Multiplying ΔE by the THz frequency gave a local chirp measurement. The chirp as a function of bunch energy for the $+10°$ linac phase is plotted in figure 47b, where the colour denotes which measurement on an image it refers to, with the 1st measurement being taken at the lowest energy. It can be seen that this takes advantage of the large timing jitter between the electron bunch and the accelerating field. If there was no timing jitter, the chirp measurements would always be at the same 4 points. The timing jitter means that the position of the peaks relative to the bunch profile varies from shot to shot so chirp measurements can be taken along the bunch. A high order polynomial fit to the chirp is also shown figure 47b. In order to convert this into the longitudinal phase space, a way to retrieve the bunch time axis is required. Independent particle tracking modelling of the CLARA beamline scientists predicted that the bunch had a linear negative chirp at the linac phase i.e. that the head of the bunch, at negatives times, was lower in energy than the tail of the bunch, at positive times. Assuming that the bunch energy was a monotonically increasing function with time meant that a particular energy on the spectrometer could be attributed to a particular point in relative bunch time. Setting t = 0 at the zero of the energy axis, the bunch time, t, at a given energy, E, could be calculated by dividing E by the mean chirp, $\overline{C} = \frac{E}{t}$, between E = 0 and E = E. The chirp polynomial fit was

used to calculate this mean. In practice, the bunch has a finite slice energy spread so a point in time corresponds to a range of energies. Through independent analysis, the bunch at this phase was calculated to have a Gaussian slice energy spread with a 1/e value of approximately 7.9 keV. It was assumed in the reconstructed longitudinal phase of the beam with no THz modulation, plotted in figure 48, that the time-energy calibration calculated above corresponded to the central energy at each time slice. The longitudinal charge density was chosen to match the mean of the background spectra, as plotted at the right-hand side of figure 48. The red lines in the side plot denote the region of the bunch which is diagnosed here. Due to the fact that the energy at which chirp measurements are taken is the mean of two peaks, the minimum time from the edge of the bunch which a measurement can be taken is half the THz period. This means information can not be inferred about the bunch longitudinal phase space at the very start and end of the bunch. The linear chirp component measured for this linac phase was 48 keV/ps, which was in agreement with predictions from beam dynamics simulations performed by CLARA beamline scientists. The shape of the longitudinal phase space was also consistent with the understanding of the CLARA scientists.

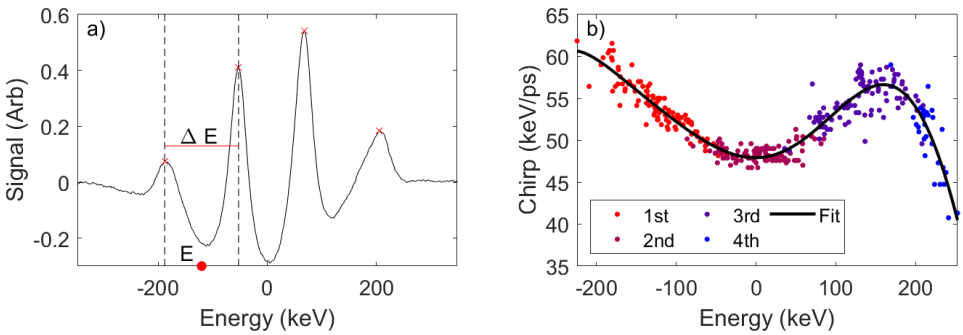

Figure 47: **a)** The measurements taken from each subtracted electron energy spectrum in order to diagnose the longitudinal phase space of the $\Phi = +10°$ bunch. **b)** The chirp as a function of position of the chirp measurement on the spectrometer screen. The colours denote different measurements on each individual spectrum.

The analysis presented above was repeated for $\Phi = +15°$. An example subtracted spectra is shown at this linac phase in 49a. The chirp as a function of average energy at which the measurement was taken is plotted in 49b. From the chirp measurements, the longitudinal phase space of the unmodulated beam was deduced over the central region of the bunch, as can be seen in figure 50. The linear chirp component at this phase was measured to be 72 keV/ps, which again was in line

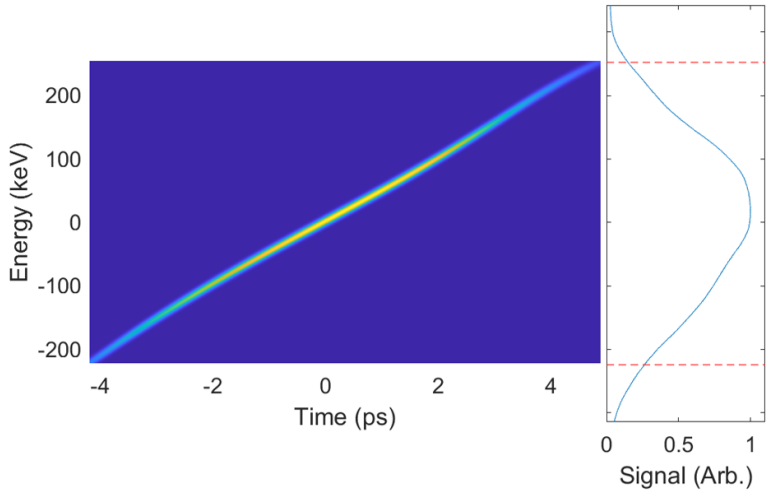

Figure 48: The $\Phi = +10°$ bunch longitudinal phase space is plotted along with the mean background beam energy spectrum.

with predictions from CLARA beamline scientists.

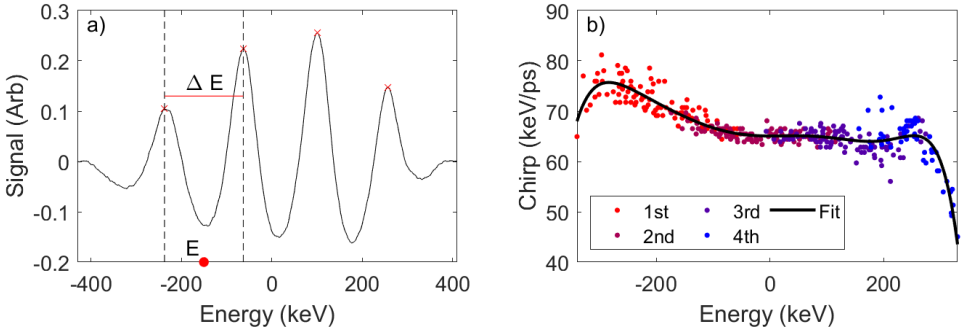

Figure 49: **a)** The measurements taken from each subtracted electron energy spectrum in order to diagnose the longitudinal phase space of the $\Phi = +15°$ bunch. **b)** The chirp as a function of position of the chirp measurement on the spectrometer screen. The colours denote different measurements on each individual spectrum.

4.5 Discussion

The results from a proof of principle experiment at the CLARA facility describe phase-matched acceleration of a relativistic electron beam in a THz-driven dielectric lined waveguide. The maximum energy gain was 10 keV in an interaction length of approximately 3 mm. Proof of the phase-matching was found by observing the effect that changing the frequency of the driving THz radiation had on the THz-electron interaction. The efficiency of acceleration as a function of the

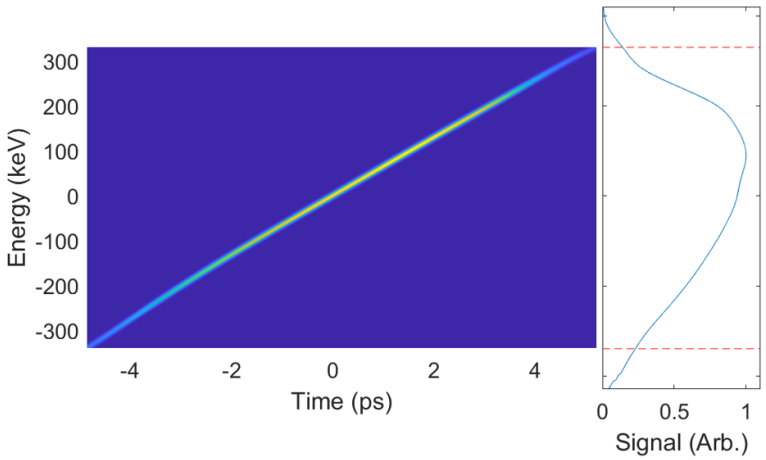

Figure 50: The $\Phi = +15°$ bunch longitudinal phase space is plotted along with the mean background beam energy spectrum.

THz frequency followed an approximate Lorentzian form, and was consistent with that expected from a phase-matched interaction. The scaling of the interaction efficiency with THz driving frequency was also consistent with our understanding of a phase-matched interaction. The modulation frequency at which the bunch was accelerated was equal to the waveguide operating frequency and was constant with THz driving frequency, which was further confirmation that the spectral component of the source at the phase-matched frequency was key to the interaction.

In looking at the electron energy spectrum when the DLW was driven by THz central frequencies far from the waveguide operating frequency, it was found that interaction with the phase-matched component of the pulse did not accurately describe the interaction efficiency or the modulation period. Allowing electrons to be injected into a significant region of the THz field gave a better fit to the experimental results. Including this truncated interaction mechanism led to an increase in the interaction efficiency and a modified modulation frequency when the THz central frequency was off-resonant for the DLW. This observation was important for our understanding of the interaction and gives a better estimate of the gains that can be made with a phase-matched interaction.

A diagnostic for determining the longitudinal phase space of electron bunches with durations spanning multiple THz cycles was trialled. For two different electron beam configurations, each with different linear and higher order chirp components, the longitudinal phase space was deduced.

Achieving phase-matched acceleration is important for scaling up the THz-electron interaction length. In this experiment, the interaction length was limited by the group velocity mismatch to a few millimetres. The interaction length could be increased by using a longer THz pulse duration. Although lengthening the THz pulse without changing the pulse energy would not in itself increase the electron energy gain, it would lead to a lower fluence on the THz generation crystal. Reducing the constraint placed by the crystal damage threshold could allow larger pump laser energies to be used for THz generation, which would increase the THz pulse energy and hence by the same factor, the electron energy gain.

5 Sub-Relativistic THz-Driven Electron Bunch Manipulation

The Terahertz Acceleration Group's experimental activity at the Cockcroft Institute involves performing THz-driven manipulation of the 100 keV electron beam generated from the DC gun described in section 3. Here I report thesis investigations into THz-driven velocity bunching and THz-driven deflection for characterisation of the electron bunch duration. Work on velocity bunching is confined to simulation, while deflection is examined both through modelling and experiment.

Using THz frequency radiation for imparting time dependant velocity changes has advantages over conventional radio frequency methods. Firstly, since the photocathode excitation and the THz generation use the same pump laser, the timing jitter between electron bunches and the field is minimal. Also, moving towards THz frequencies from conventional radio frequencies means the gradient of the field at the zero crossing can be increased. For velocity bunching, this means the longitudinal focus of the beam can be shorter and therefore the bunch duration can be shorter. For deflection applications, a larger gradient can be utilised to give a finer temporal resolution in the bunch length measurement, so few femtosecond scale bunch durations can be diagnosed. Compression and deflection have been reported elsewhere in the literature with a range of interaction structures [66, 71–74]. Deflection has been performed at the Cockcroft Institute with a dielectric waveguide structure, as in chapter 4 but with phase matching of the LSM_{01} mode rather than the LSM_{11} mode. We have also measured deflection with a slit structure, similar to the structure in [140]. To inform our future velocity bunching experiments, sub-relativistic electron interaction with the accelerating mode of a dielectric waveguide has been modelled. Interaction with a sub-wavelength dimension slit as the mediator has also been simulated.

Section 5.1 gives an overview of the optical and electron beam setup used here for electron bunch interaction. The design of an energy spectrometer for measurement of the chirp imparted by a velocity bunching interaction is covered in section 5.2. Simulation and experimental results for THz-driven electron deflection in a DLW along with modelled velocity bunching results are discussed in section 5.3. In section 5.4, simulation and experimental results for THz-driven electron deflection using a slit structure and modelled velocity bunching results are presented. The work is summarised in section 5.5.

5.1 Experiment Overview

An overview of the experimental setup required for THz-driven manipulation of a sub-relativistic electron bunch is given. Section 5.1.1 will give details of the THz generation and section 5.1.2 describes the transport to the interaction point at which DLW and slit structures are placed. The measurement of the THz field is described in section 5.1.3 and the use of a phase plate to generate a longitudinal electric field for electron acceleration will be discussed in section 5.1.4. Section 5.1.5 will describe the electron beam generation at the photocathode and section 5.1.6 describes the apparatus used to compensate for the earth's magnetic field and its role in the electron beam alignment procedure.

5.1.1 THz Source

An experimental goal was to separately achieve deflection and acceleration of the 100 keV electron bunches. For these demonstrations, only one THz source was required. A diagram of the THz source setup outside the chamber is shown in figure 51. Two apertures were used to verify day to day alignment. A motorised stage was used to vary the pump-probe timing for EO detection. A mirror on a magnetic mount was placed before the entrance to the interaction chamber in order to direct the THz to a 'dummy' interaction point where the THz pulse energy was confirmed on a day to day basis by a pyro-electric detector. The setup inside the chamber is depicted in figure 52. The components on the motorised stages will be discussed in section 5.1.5.

A 99 %/1 % beam sampler was used to split off a small portion of the Spitfire Ace PA laser pulse (section 3.1) for the photocathode excitation and the rest pumped a stoichiometric $LiNbO_3$ crystal with a PFT to generate broadband, quasi-single-cycle THz radiation. The tilted pulse front was generated by use of a 1500 line pairs/mm diffraction grating, and an f = 250 mm and an f = 130 mm cylindrical plano-convex lens in a 4f geometry, as shown in figure 53. A waveplate was placed between the two lenses because the pump polarisation required for maximum grating efficiency was perpendicular to the required polarisation onto the $LiNbO_3$ crystal. The angle of incidence onto the grating was -20.4° and the diffracted angle was 58.4°. The grating and imaging setup gave a PFT angle in the crystal of approximately 63°, which matched the Cherenkov angle. The grating image angle was 62.2°, giving an estimated 0.8° mismatch. The lowest achievable mismatch in this imaging geometry was limited by the selection of focal lengths of stock optics. The angular mismatch leads to an increased pulse duration off-axis, as

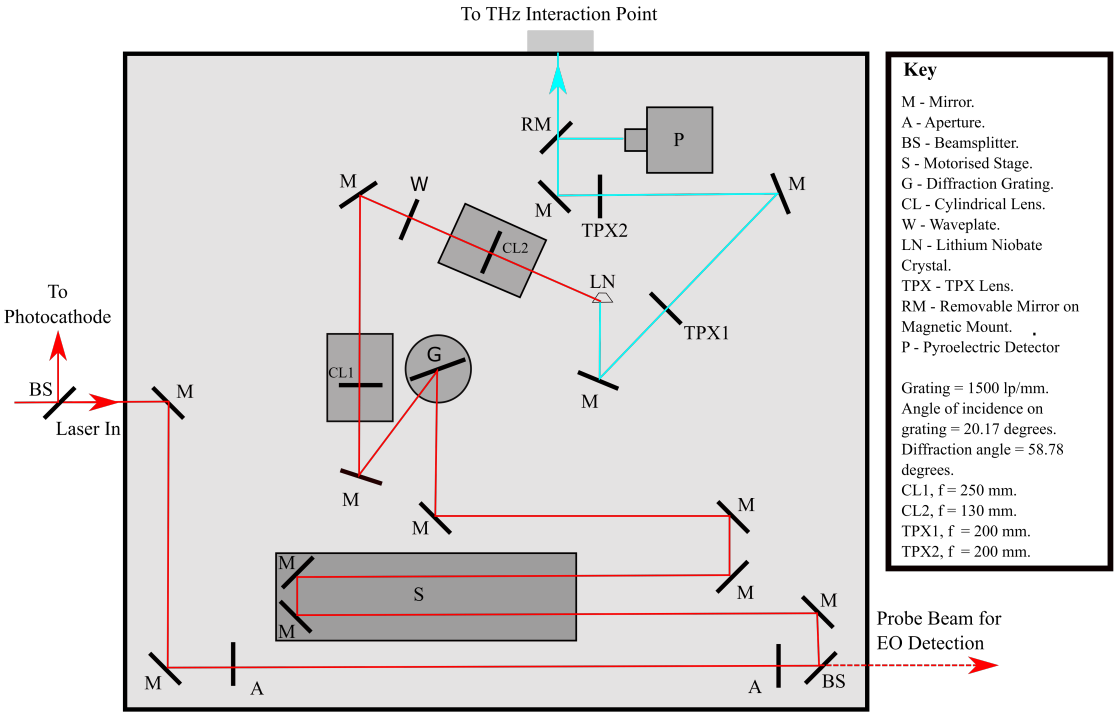

Figure 51: Optical setup for the generation of THz radation. The pump laser enters at the left after passing through a beam sampler which splits off a fraction of the laser energy for generation of electrons at the photocathode. The THz radiation, depicted in blue, exits this section into the interaction chamber. The THz setup within the chamber is depicted in figure 52.

explained in section 2.1.4, and is plotted for a transform limited FWHM intensity pulse duration of 40 fs in figure 54a. The efficiency of the generated THz is proportional to the pump field to the power of 4 (equation 36), and the electric field in a chirped laser pulse is proportional to $\sqrt{\sigma_0/\sigma_t}$. A mismatch in the PFT angle and the IPT angle leads to a reduction in the pump laser pulse field off-axis, hence a lower overall pulse energy of the generated THz. The loss comes from off-centre components of the pump pulse so the width of a THz pulse generated from a mismatched setup is decreased compared to the ideal case. The pump pulse had a $1/e^2$ intensity width of 12 mm on the grating, which was reduced by the angle off the grating and the demagnification of the imaging system. The energy loss for a mismatch of 0.8° in this scenario was estimated by considering two Gaussian pulses with a reduced $1/e^2$ intensity diameter, from 12 mm to 3.5 mm, incident on the generation crystal. Using the scaling $I_{THz} \propto I_{pump}^2$, the efficiency of generation at each transverse position with a transform limited pulse was compared to one with a pulse duration that varied transversely as shown in figure 54a. The sum

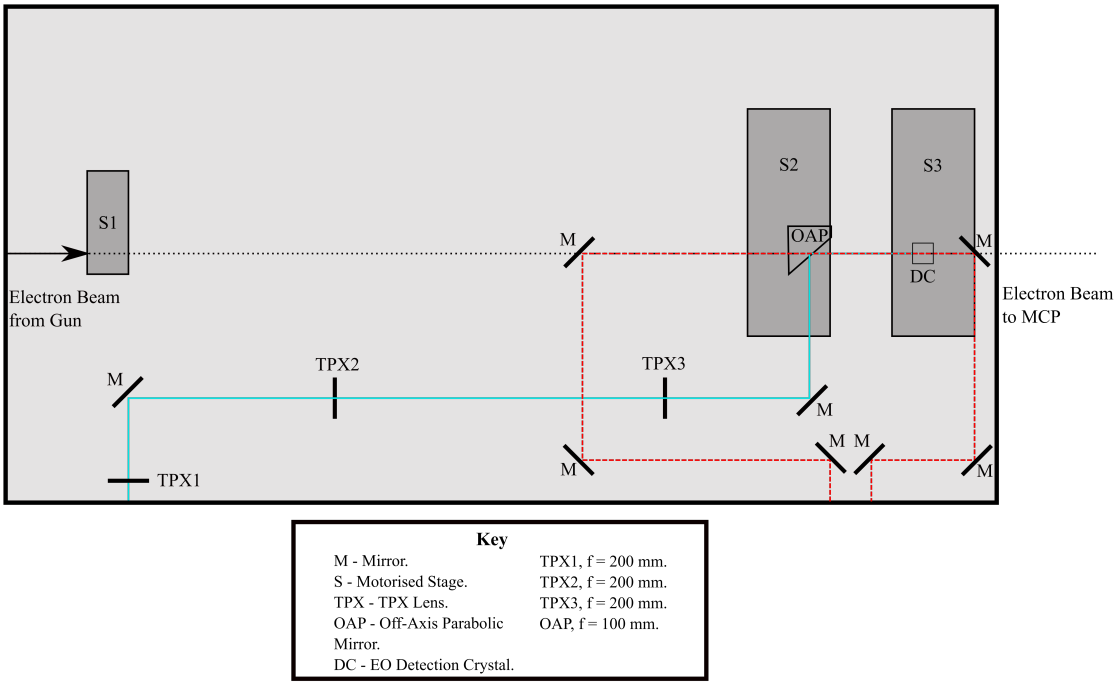

Figure 52: THz and optical setup inside the interaction chamber. The THz beam enters the chamber from the exit of figure 51 and is transported to a final off-axis parabolic mirror, which focuses the THz at the interaction point. A 3 mm diameter hole in the off-axis parabolic mirror allows collinear propagation of THz and electrons.

of THz intensity along the transverse axis is proportional to the THz energy. The angular mismatch of 0.8° led to a decrease in energy generation efficiency of approximately 10 % between these two cases and a decrease in the THz pulse width of approximately 10 %. These losses were deemed acceptable so custom lenses in the imaging system were not used.

The imaging system for the PFT was chosen to have two lenses in a telescope geometry rather than a single lens in order to reduce the distortion in the PFT image due to spherical aberrations [141]. The magnification of a system like this is $M = f_2/f_1$ without misalignment. Misplacement of the lenses in the PFT imaging system leads to a change in the focal spot position and the magnification, hence PFT angle. Small differences in the position of the first and second lens are denoted by δ_1 and δ_2, respectively in figure 53. Given these distances between the optics in the setup, the change in the distance, δ_3, between the final lens and the image plane can be calculated from the lens equation as

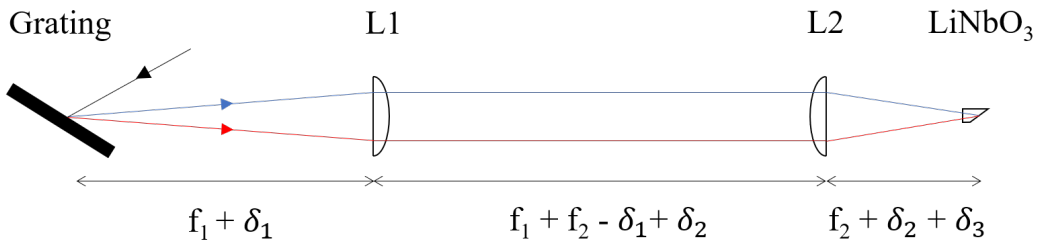

Figure 53: Depiction of the optics used for imaging of the pulse front tilt onto the generation crystal. The crystal is assumed to be located at the image plane. Misalignment from the ideal lens positions are denoted by δ_1 and δ_2.

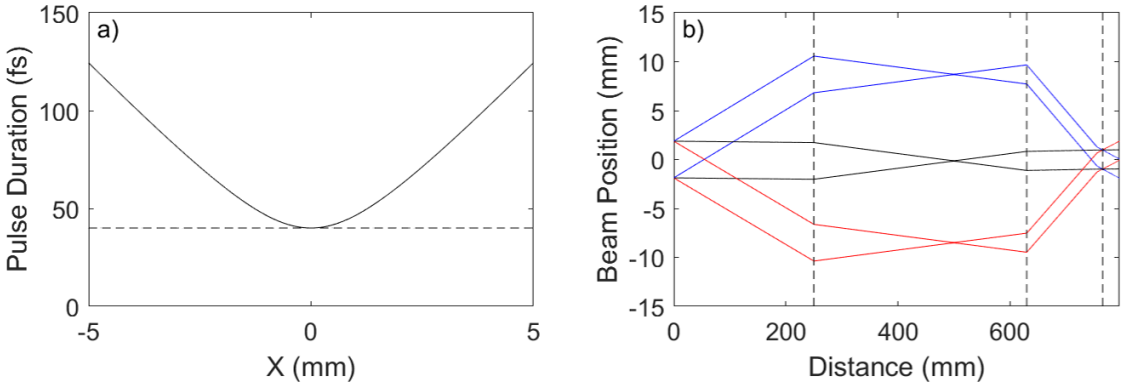

Figure 54: **a)** The pulse duration of a 40 fs transform limited pulse as a function of transverse position at the pulse front tilt plane due to a 0.8° angular mismatch between the PFT and IPT. **b)** The optical ray tracing through the PFT imaging system. The black line denotes light at a wavelength of $\lambda_0 = 800\,\text{nm}$. The blue and red lines denote wavelengths of λ_0 minus half of the FWHM bandwidth and λ_0 plus half of the FWHM bandwidth, respectively. The FWHM bandwidth was 24 nm.

$$\delta_3 = \frac{\delta_1 \, f_2^2}{f_1^2 + \delta_1^2 - \delta_1 \, \delta_2} \, . \tag{187}$$

Although the image position will change through misplacement of the second lens, the distance between the final lens and the image plane is only modified if the first lens is in the wrong position. The magnification of the system can be calculated from the distances between lenses and the object and image planes

$$M = - \frac{f_1 \, (f_2 + \delta_3)}{f_1^2 + \delta_1 \, (\delta_1 - \delta_2 - f_2)} \, . \tag{188}$$

The magnification is once again only modified from its ideal value given misplacement of the first lens, since an ideally placed first lens will have an image plane at

infinity. These results highlight the importance of correct placement of optics in this setup, particularly of the first lens. The benefit of using longer focal length optics can be also be seen, since for a given discrepancy in the ideal positions of optics, the change in the magnification is smaller. The disadvantages of longer focal length optics are the amount of space required and the possibility of clipping the beam, since a pulse will rapidly increase in size after a diffraction grating. The chosen optics were a compromise between these considerations. Figure 54b shows the $1/e^2$ beam position at the central wavelength and at plus and minus the half width half maximum bandwidth of the 40 fs pulse. Given a first lens of width 60 mm and a second lens of width 30 mm, it can be seen that clipping is minimal in this setup.

5.1.2 THz Transport

The optical pump $1/e^2$ intensity spot diameter on the diffraction grating was 12 mm. In the vertical direction, this is the diameter that pumps the crystal, giving a THz intensity beam diameter in the vertical of 8.5 mm at the crystal exit surface. In the horizontal plane, the beam size of the pulse is modified by the tilt angle, the magnification and the diffraction angle. The THz intensity beam diameter in the horizontal dimension was estimated to be 4.8 mm at the generation crystal exit surface. From here it was transported by 5 TPX lenses with f = 200 mm to a final, f = 100 mm off-axis parabolic mirror, with a 3 mm hole in the centre, which focused the beam to the interaction point. Gaussian propagation calculations were used to track the THz beam size from the generation crystal to the interaction point, as shown in figure 55. In the horizontal plane (figure 55a), a smaller initial beam size leads to a larger beam size at the position of the focusing optics. As these optics have a 50.8 mm diameter, some low THz frequency components will be clipped in the transport. The larger beam size at focusing optics also leads to a smaller focal spot size than in the vertical with a $1/e^2$ intensity diameter of 2.4 mm. In the vertical direction, figure 55b, the modelled frequencies have no issue with clipping but the beam spot at the interaction point was larger, at 4.3 mm. To verify the alignment, the transverse beam profile was measured using the INO THz camera detailed in section 3.3.2. An image was taken at the second focal spot in the transport line at a distance of 1.6 m, which is shown in figure 56a. The vertical $1/e^2$ diameter of this beam in the camera image is 9.8 mm as opposed to the 8.5 mm in the model. The horizontal size in the camera image is 6.7 mm rather than the expected 4.8 mm. The discrepancy is likely larger in the horizontal dimension since the beam quality of the THz is affected by the imaging of the PFT; both by the IPT to PFT mismatch leading to different THz spectra

being produced as a function of transverse position and by image distortions due to spherical aberrations. At the interaction point, the camera image in figure 56b displays a height of 8.4 mm and a width of 5.5 mm. These interaction point measurements have a much larger discrepancy than at the previous focal spot which suggests either misalignment of the final parabola or that the camera was not imaging the minimum beam waist.

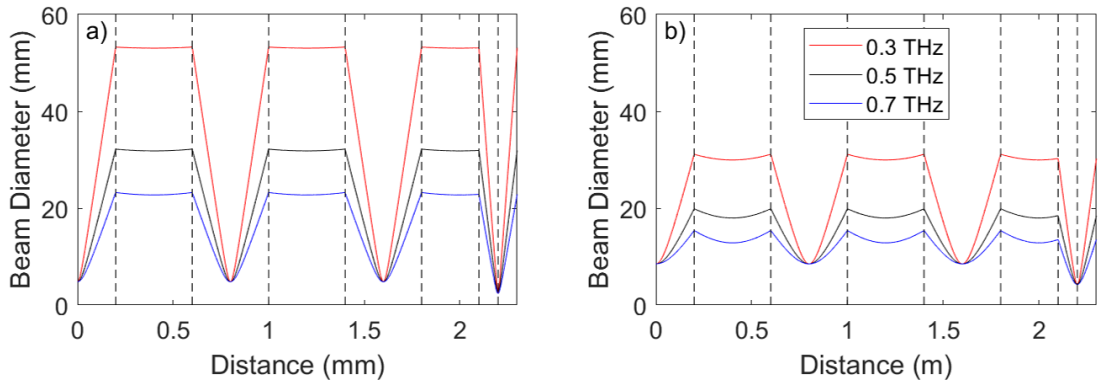

Figure 55: Calculated horizontal beam diameter, **a)**, and vertical beam diameter, **b)**, of the THz radiation from the $LiNbO_3$ crystal to the interaction point, denoted by the final dotted line. Other dotted lines denote focusing optics.

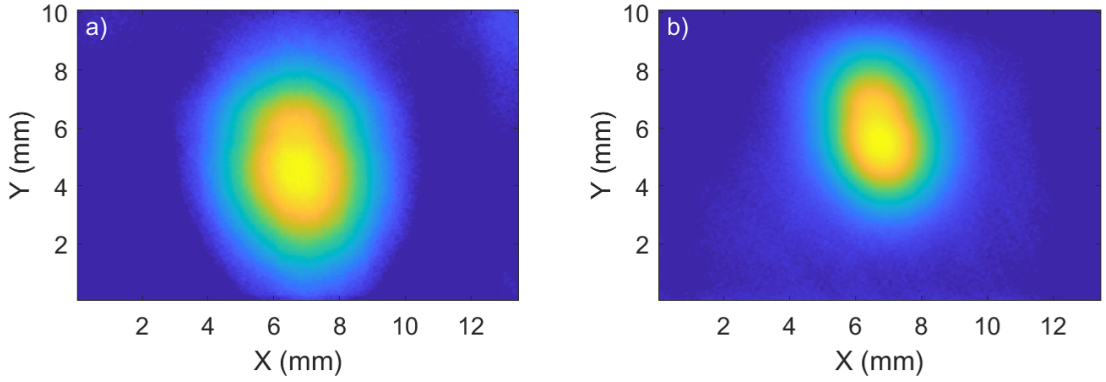

Figure 56: Camera images of the THz transverse profile at the focal position at 1.6 m in figure 55a, **a)**, and at the interaction point, **b)**.

5.1.3 Electro-Optic Detection of THz

The time domain field profile at the interaction point was measured with balanced EO detection. A beamsplitter was used to split off 5 % of the pump laser pulse

which served as the probe beam, as shown in the lower right corner of figure 51. The probe was routed into the chamber where it interacted in a collinear geometry with the THz within a 0.5 mm thick ZnTe crystal placed at the interaction point. The polarisation rotated probe pulse was then directed out of the chamber towards a quarter waveplate, a polarising cube beamsplitter and a pair of photodiodes, as in figure 5 (page 40). The THz-probe time-delay was varied using a motorised stage on the pump line and the photodiode signal was enhanced using a lock-in amplifier. The THz field profile is plotted in figure 57a, with and without the reflection subtraction process described in section 4.2.1. The pulse spectrum is plotted in figure 57b. The pulse energy, W, at the interaction point was measured to be 525 nJ via a THz power meter (section 3.3.2). The peak field was calibrated from this pulse energy and using the known transverse profile and time profile. The square of the envelope of the EO scan gives the temporal intensity profile. In free space, where there is an equal energy content in the magnetic and electric field, with a normalised intensity profile, I, the peak field could be calculated by

$$\mathrm{E}_0 = \sqrt{\frac{\mathrm{W}}{\epsilon_0 \iiint_{-\infty}^{\infty} \mathrm{I}\,\mathrm{dV}}}\,. \tag{189}$$

This calculation gave a peak field of 2.3 MV/m at the interaction point in free space. Each TPX lens had 75 % transmission of the THz energy, and the window to the interaction chamber allowed 66 % transmission. Given these, the THz pulse energy at the crystal surface was inferred to be 3.4 μJ. The corresponding conversion efficiency is 6×10^{-4}, achieved with a pump energy of 5.6 mJ.

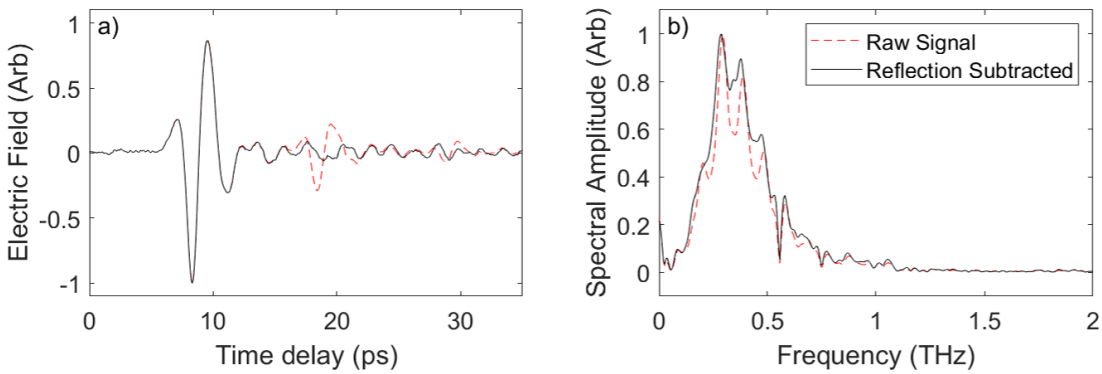

Figure 57: **a)** EO measurement of the time domain transverse electric field at the interaction point. **b)** The corresponding THz field spectra.

5.1.4 Characterisation of Phase Plate for the Generation of Longitudinal Electric Field

As in the relativistic beam experiments described in chapter 4, a Teflon phase plate was used to delay one half of the pulse to generate the quasi-TEM_{01} mode Gaussian-Hermite pulse. The difference in thickness between phase plate regions was 800 μm to give a half-period time delay between the 0.5 THz components of the top and the bottom of the pulse. Testing of the phase plate was performed using the Spitfire Ace laser (section 3.1) with a separate PFT pumped $LiNbO_3$ THz source to the one previously described. The radiation was transported to a focus in a 0.5 mm thick GaP crystal after three off-axis parabolic mirrors, where it interacted in a co-linear fashion with an 800 nm probe beam, as in figure 58a. The EO signal from the THz transverse field without the phase shifter in place is plotted in figure 58b, with a maximum field of 2.1 MV/m inferred from equation 70. The phase shifter was then inserted into the beamline, as depicted in figure 58a. The probe beam was kept at the same height, but the phase shifter was moved up and down so that the centre of the THz beam was either going through the thicker half or the thinner half. The result, plotted in figure 58c, is that the peak is delayed by 1 ps, or half the period of radiation at 0.5 THz, when going through the thicker side of the plastic plate. The longitudinal electric field time profile was then measured with the phase shifter placed centrally in the THz beam. For longitudinal field measurements, the GaP detection crystal was swapped for a 0.5 mm thick (100) cut ZnTe crystal; the crystal axis optimised for detection of field in the direction of the probe beam. The peak longitudinal field was expected to be at a time delay between the two peaks in the transverse field and zero at the peaks. For this reason, the signal was minimised at the time delay of the peak transverse field by adjusting the crystal tilt angle, to ensure the measured field was in fact the E_z [142]. The phase shifter height was then optimised to give the largest longitudinal field. The time scan plotted in figure 58d was then taken. The longitudinal field has a $\pi/2$ phase shift with respect to the transverse field and was measured to have a maximum field strength of 0.8 MV/m.

For modelling of the field in the region of the focus in the presence of the phase plate, the Kirchhoff integral based method described in section 2.3.2 was used. As in section 4.2.1, the source was initialised such that there was a 1 ps time delay between the top and the bottom of the pulse, as in figures 59a and 59b. The pulse had a broadband spectrum similar to the experimental source and the waist was chosen such that the spot size of a simulated fundamental Gaussian pulse was

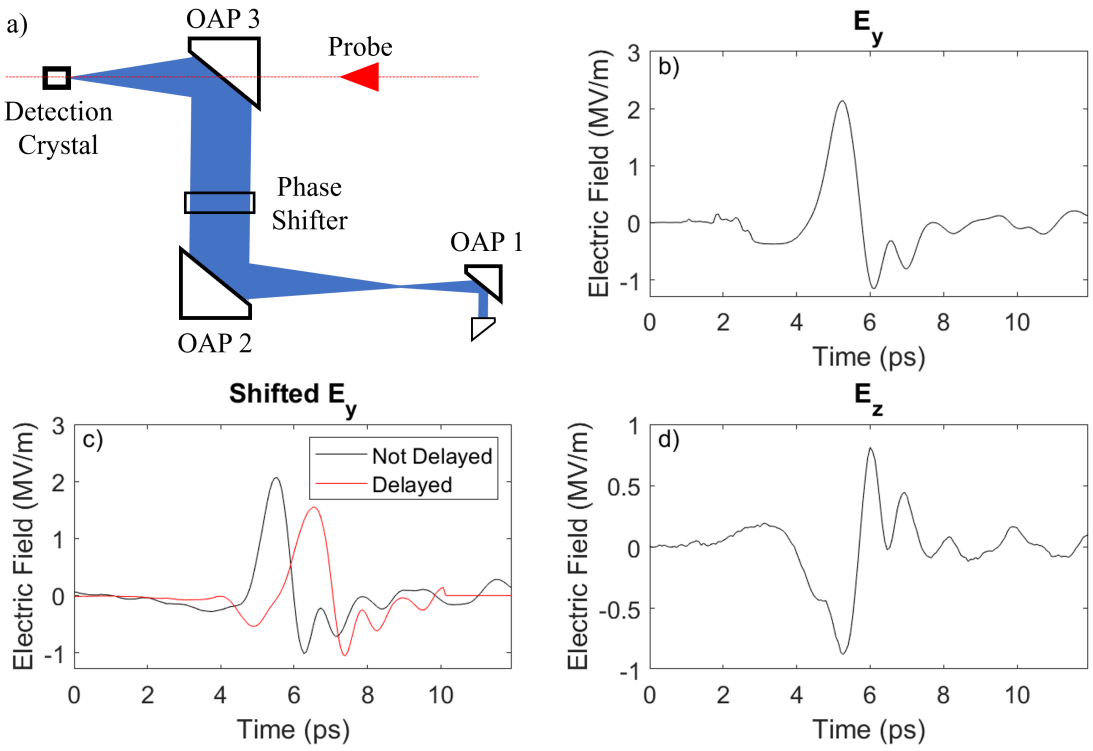

Figure 58: **a)** A diagram of the THz transport from crystal to detection crystal. **b)** The transverse electric field of the source without the phase shifter in place. **c)** The transverse electric field when allowing the THz to travel through each half of the phase shifter. **d)** The measured longitudinal field.

similar to the experiment. The pulse was propagated 50 mm to an f = 50 mm off-axis parabolic mirror and then a further 50 mm to the THz beam focus. The calculated transverse electric field at the focus is shown in figures 59c and 59d. A spatial asymmetry is observed in the transverse field profile at the focus. The root of this phenomena is the single-cycle pulse duration. The amplitude of the pulse envelope is significantly reduced 1 ps before or after the peak. Therefore, at a given time slice, the amplitude of one half of the pulse transversely will differ from the other substantially. Consequences of this were not seen in section 4.2.1 due to the longer pulse duration used there. If the phase plate is used with a single-cycle THz source to couple into a DLW, spatial asymmetry at a given time slice may lead to a lower coupling efficiency into the accelerating mode, and more critically, coupling into deflecting modes. The consequences of this transverse profile on coupling to a waveguide will be explored in section 5.3.7.

Images were taken at several points around the focal plane with the THz camera to

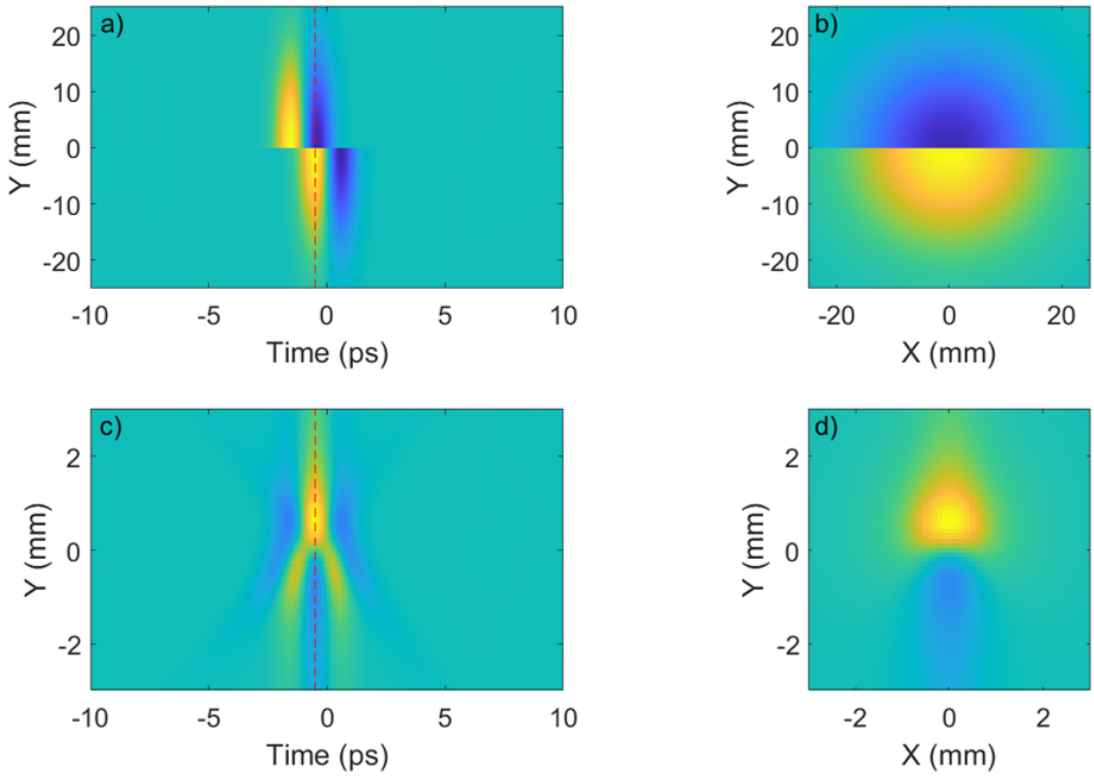

Figure 59: The modelled electric field at the phase shifter position is shown in **a)** at x = 0 and in **b)** at t = -0.5 ps. The modelled electric field at the focal position is shown in **c)** at x = 0 and in **d)** at t = -0.5 ps.

validate prediction made by the model. The Kirchhoff diffraction integral gives the frequency domain transverse profile at a chosen z position. For direct experimental comparison to THz camera images, the square of the time domain profile was summed to give a signal comparable to that measured by the camera. Figures 60a to 60c depict modelled transverse profiles at various measured distances from the focus. The experimental equivalents are shown in figures 60d to 60f. The region of the pulse that receives the greater time delay has a greater intensity in both simulation and experiment, and the evolution in shape is in good agreement.

5.1.5 Electron Photocathode

Electrons are generated by excitation of an LaB_6 photocathode with 400 nm light. Approximately 1 % of the pump beam is picked off by a beam sampler for the generation of this electron beam. A motorised stage after the pick off gives the ability to adjust the THz-electron time delay. A pair of lenses are used to reduce the 800 nm beam size before it passes through a 200 μm thick BBO crystal which generates 400 nm light by second harmonic generation. The second harmonic light

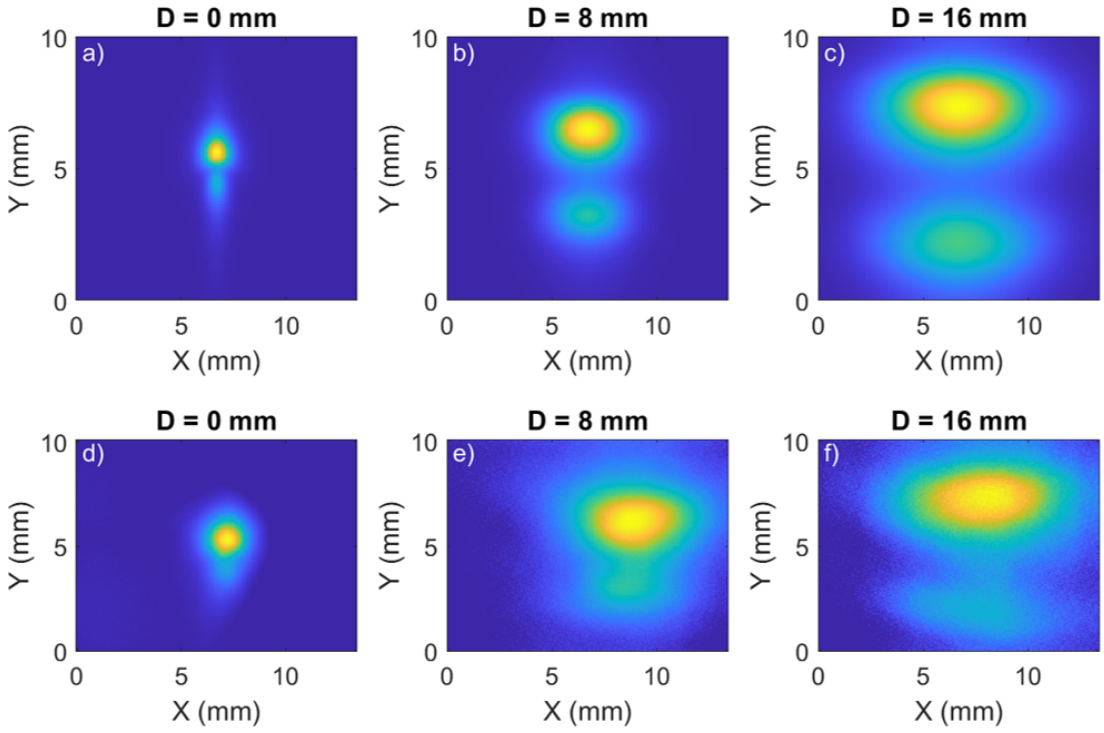

Figure 60: **a)-c)** The simulation expectation for the THz camera measurement at a number of distances with respect to the focus. **d)-f)** The experimentally measured intensity profiles.

is then gently focused with an f = 1 m lens onto the 200 μm × 200 μm photocathode. A schematic of the optical layout is shown in figure 61.

The maximum available 400 nm pulse energy incident on the photocathode was 5.8 μJ. The charge excited was proportional to the energy incident on the photocathode, so the pulse could be attenuated to run at lower bunch charges. An unsuccessful attempt was made to measure the electron bunch charge with a Faraday cup with a minimum detectable charge of 10 fC. Due to the expected sensitivity of the Faraday cup, it was concluded that the bunch charge was less than 10 fC with the maximum 400 nm laser energy incident on the photocathode.

The electron gun could be run with a warm photocathode, which increased the charge excited for a given incident laser pulse energy, but reduced the electron beam quality. The data presented in this thesis was taken with zero source voltage heating the photocathode.

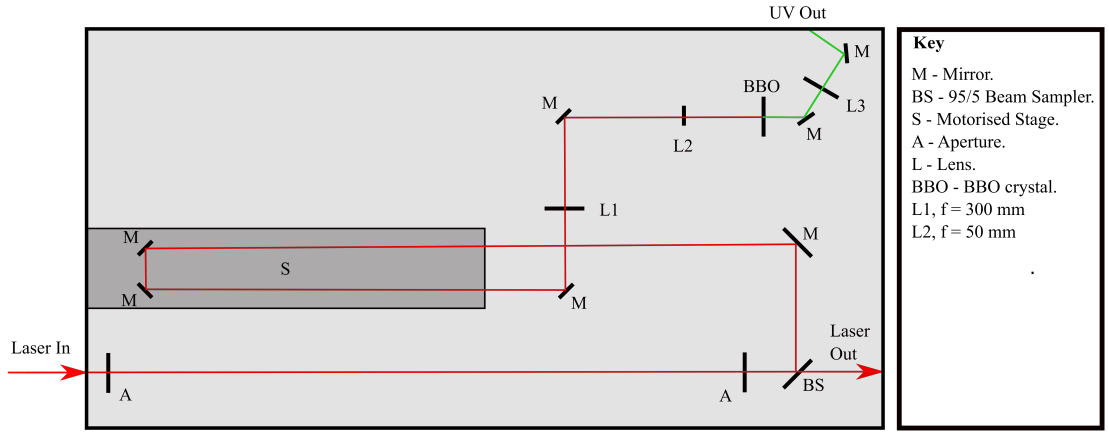

Figure 61: Optical setup for generation of electrons. A BBO crystal generates second harmonic radiation which is focused onto the photocathode by L3.

5.1.6 Compensation for the Earth's Magnetic Field

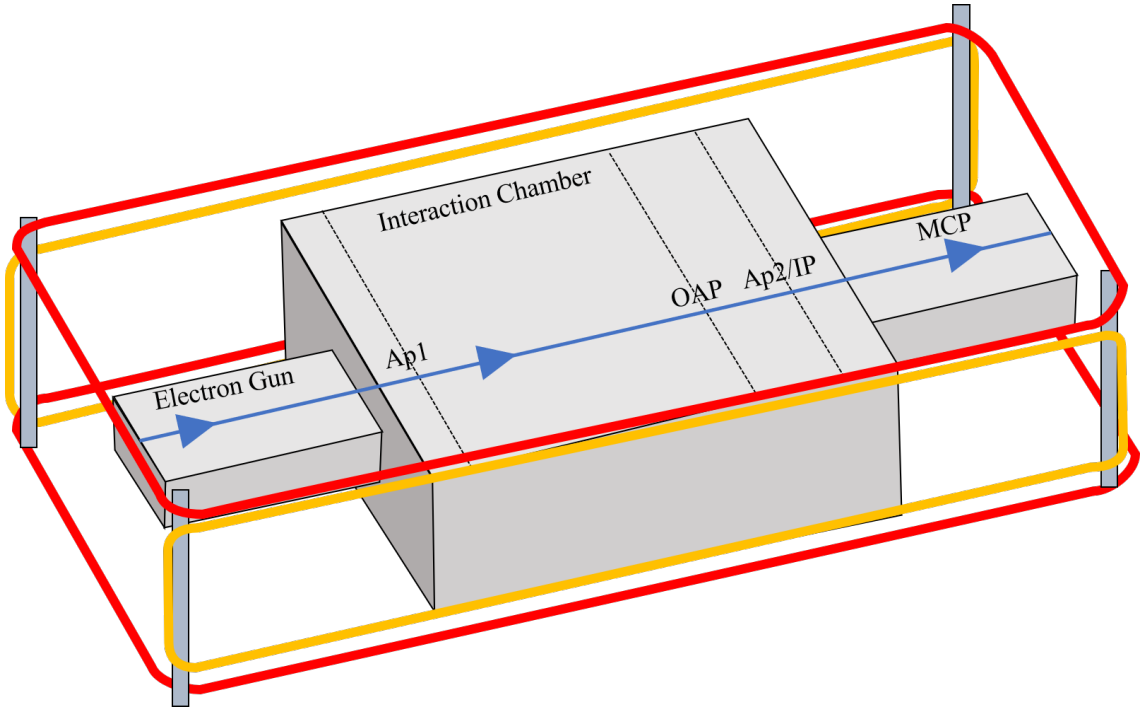

Figure 62: Diagram of the electron beamline. Coils were wrapped around the electron gun, the chamber and the MCP for compensation of the earth's magnetic field. Red lines denote horizontal deflection coils, the orange lines denote vertical deflection coils, and the electron path is drawn in blue. Ap1 and Ap2 are apertures used to aid electron beam alignment. The final off-axis parabola is labelled OAP and the interaction point is labelled IP.

The earth's magnetic field caused centimetre-scale deflection of our 100 keV electrons over meter-scale travel distances. Compensation of this magnetic field along the beamline was achieved using two coil pairs which extended over the electron gun, chamber and MCP, as depicted in figure 62. These two coil pairs provided an approximately uniform field along the beamline to counteract the components of the earth's magnetic field transverse to the beam propagation axis. Ensuring the electron beam travelled in an approximately straight line through the chamber required use of apertures Ap1 and Ap2 in figure 62, placed on translation stages S1 and S3 in figure 52, respectively. The electron beam was first measured on the MCP with no apertures in place and no current on the chamber coils. Ap1 was then brought in and the electron beam was aligned so that it passed through the centre of it using the chamber coils. This aperture was removed from the beamline and Ap2 was brought in. The gun deflecting coils were used for alignment to this aperture. These two apertures were iterated over until the beam passed through both and onto the centre of the MCP. Once this alignment procedure was completed the off-axis parabolic mirror (on stage S2 in figure 52) and the interaction structure at the position of Ap2 were brought into the beamline. The final step in the electron beam alignment was to make fine adjustments to the coil currents to maximise transmission through the parabolic mirror and the interaction structure. A photograph of the interaction point and parabolic mirror motorised stages in situ is shown in figure 63. The horizontal positions of the components in the figure are not representative of their positions in usage.

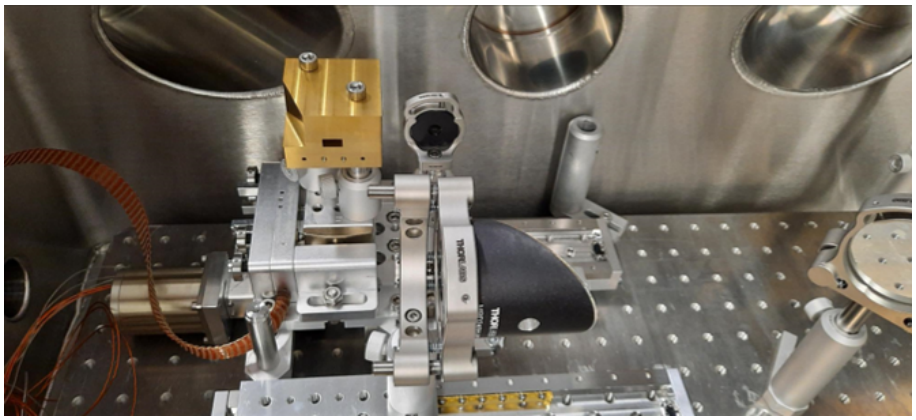

Figure 63: Photograph of the interaction point and parabolic mirror stages in situ in the interaction chamber. Courtesy of Morgan Hibberd.

5.2 Electron Energy Measurement

Previous demonstrations of THz-driven velocity bunching have confirmed the bunching interaction by measurement of the bunch duration at the electron bunch longitudinal focus [66, 71–74]. Here, for measurement of the energy chirp imparted by the interaction through projected energy spread and confirmation of synchronisation, an energy spectrometer setup was designed and manufactured. This diagnostic required an energy resolution on the order of 10 eV in order to confirm the small energy chirp needed for velocity bunching with 100 keV electrons. For maximum visibility of dispersion, it also needed to work alongside the limited beam optics at our disposal to give a focus in the horizontal dimension at the plane where electrons were detected.

5.2.1 Electron Spectrometer

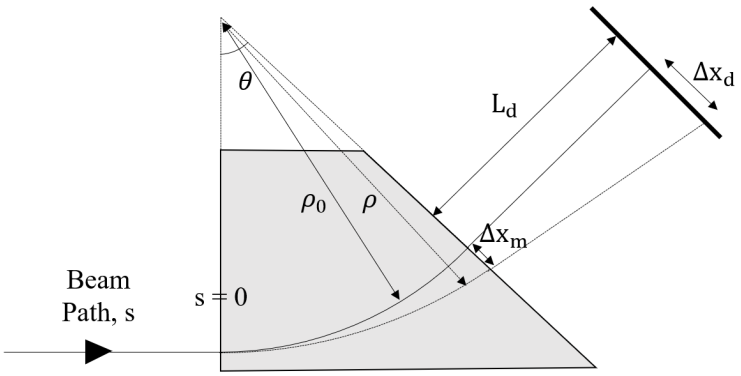

Figure 64: Simple electron energy spectrometer system where an electron travelling at a velocity, v, through a deflecting magnetic field of constant amplitude, B, is deflected towards a detection screen. A second trajectory is shown, denoted by the dashed line, which is taken by an electron with a momentum larger than the design value.

In its simplest form, an energy spectrometer consists of a dipole magnet, which gives energy dependent deflection of the charged particle beam, and a screen, in this case a micro-channel plate (MCP). An example geometry is shown in figure 64 where the electron is travelling through a deflecting magnetic field of constant amplitude, B. At a reference momentum, a beam on the central axis travels through the magnet in a circular path with a radius dependent on the particle's momentum

$$\rho_0 = \frac{\mathrm{p}_0}{\mathrm{q\,B}} \,. \tag{190}$$

The path taken by a particle travelling with a modified momentum, p_1, will have a modified radius of curvature and therefore a different transverse position at the exit of the magnet. The momentum offset is quantified by a fractional change

$$\delta = \frac{\Delta p}{p_0} = \frac{p_1 - p_0}{p_0} \ . \tag{191}$$

Since $\frac{\Delta p}{p_0} = \frac{\Delta \rho}{\rho_0}$, the difference in transverse position at a point, s, along the particle's trajectory can be calculated by assuming that the change in radius is the dominant contributor

$$\Delta x = \Delta\rho \, (1 - \cos \frac{s}{\rho_0}) = \delta \rho_0 \, (1 - \cos\theta) \ . \tag{192}$$

At the end of the magnet s is equal to the length of the arc travelled by an electron within the magnet, so $s/\rho_0 = \theta$, as defined in figure 64. The transverse offset is then

$$\Delta x_m = \delta \rho_0 \, (1 - \cos\theta) \ . \tag{193}$$

The change in angle experienced by electrons with a different momenta at the end of the magnet is given by the differential of this with respect to s

$$\Delta\theta = \delta \sin\theta \ . \tag{194}$$

The total difference in position due an offset in momenta after a drift to the detection plane can be calculated as a sum of the offset in the magnet and in the offset gained over the drift due to the angle offset

$$\Delta x_d = \Delta x_m + L_d \tan \Delta\theta \approx \delta \, \rho_0 \, (1 - \cos\theta) + L_d \, \delta \sin\theta \ , \tag{195}$$

where a small angular deviation is assumed in the final expression.

The geometrically derived result above can be written more compactly in a transfer matrix. In a two dimensional case, a particle can be defined as having an initial position, x_0, which is the transverse offset from the ideal trajectory. It can also be assigned an initial angular offset, x_0', and a fractional momentum offset, δ. Using the transfer matrix for a sector magnet, as in figure 64, the particle's position can be evaluated after the magnet by

$$\begin{pmatrix} x \\ x' \\ \delta \end{pmatrix} = \begin{pmatrix} \cos\theta & \rho\sin\theta & \rho\,(1-\cos\theta) \\ -\frac{1}{\rho}\sin\theta & \cos\theta & \sin\theta \\ 0 & 0 & 1 \end{pmatrix} \begin{pmatrix} x_0 \\ x_0' \\ \delta \end{pmatrix} \ . \tag{196}$$

The results derived earlier for the position and angle of an off-momentum particle at the end of the magnet, equations 193 and 194, can be retrieved by setting $x_0 =$

$x'_0 = 0$. A drift transfer matrix can then give the electron position at the detector plane where

$$R_{\text{drift}} = \begin{pmatrix} 1 & L & 0 \\ 0 & 1 & 0 \\ 0 & 0 & 1 \end{pmatrix} . \tag{197}$$

The beam energy dependent deflection, compared to the central path, quantifies the energy resolution of the spectrometer. Higher resolution leads to a lower energy offset required to deflect a certain distance. Rewriting equation 195 in terms of 3×3 transfer matrix components, R_{mn}, where m denotes the column and n the row, and rearranging gives

$$\frac{\Delta p}{\Delta x_d} = \frac{p_0}{R_{13} + L_d\, R_{23}} . \tag{198}$$

For highly relativistic energies where the electron kinetic energy is much greater than the rest mass, $p \propto E$ so the energy deflected per unit distance can be found trivially using equation 198. For $E = 100\,\text{keV}$, the electron's rest energy can not be neglected. Using the relation $p^2c^2 = E^2 - m_e^2c^4$, the energy difference from the central energy for a given transfer offset at the detector plane, Δx_d, is

$$\Delta E = \left(\sqrt{p_0^2\, c^2 \left(1 + \frac{\Delta x_d}{R_{13} + L_d\, R_{23}} \right)^2 - m_e^2\, c^4} \right) - E_0 , \tag{199}$$

which reduces to the relativistic result when the rest mass energy is negligible compared to the kinetic energy component.

The transfer matrix also gives information about how the magnet effects the divergence of the output beam. The reciprocal of the R_{21} term, in the sector magnet case $\rho/\sin\theta$, gives the focal length of the magnet if the input beam is collimated, i.e. $x'_0 = 0$. The R_{22} then gives information about how the focusing would be adjusted for an initially divergent beam.

5.2.2 Magnet Geometry

In the previous section, the transfer matrix of a sector magnet was discussed. Given a collimated input beam and a deflection angle of 45°, the focal length of such a magnet would be $\sqrt{2} \times \rho$. The magnet length in the axis where the electron beam enters the magnet is given by $L_{\text{mag}} = \rho/\sqrt{2}$. This means the focal length is twice the length of the magnet when deflecting by 45°. High energy resolution

can be achieved with a long drift length, which can be seen when subbing in $\theta = 45°$ and the expression for the magnet length into equation 195 and dividing by δ to give the offset on the screen for a certain momentum offset

$$\frac{\Delta x_d}{\delta} = L_{mag}\,(\frac{\sqrt{2}-1}{2}) + L_d\frac{\sqrt{2}}{2} \approx 0.2\,L_{mag} + 0.7\,L_d\ . \tag{200}$$

Given a certain amount of laboratory space for the spectrometer setup, high energy resolution can be achieved by maximising the drift length and minimising the magnet length. If focusing at the detector plane is not achieved, the energy dispersion will be limited by the transverse beam size. To give greater flexibility in the detector location, magnets with a modified geometry were considered.

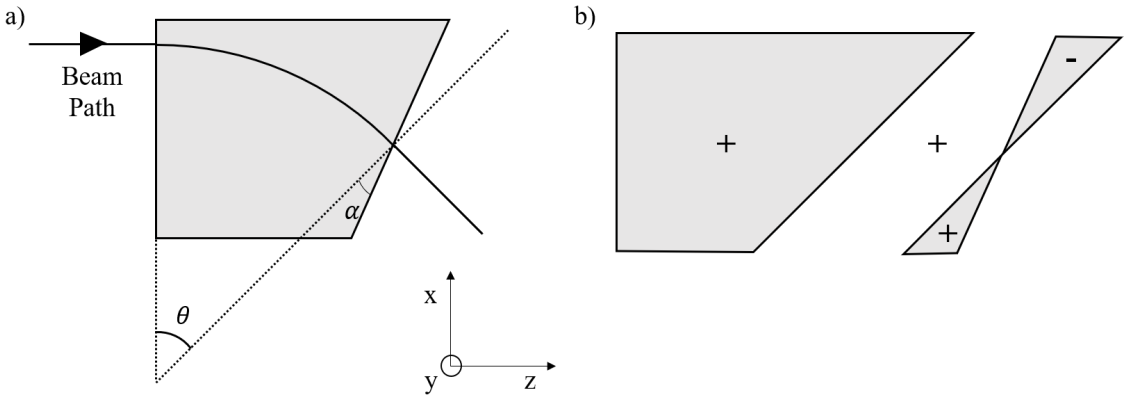

Figure 65: A diagram of a magnet with the exit face angle adjusted by α compared to the sector magnet is given in **a)**. In **b)**, it is shown how this magnet can be decomposed into a sector magnet and a quadrupole-like end piece.

The focusing properties can be modified by changing the angle of the boundary at the magnet's exit, as depicted in figure 65. As can be seen in figure 65a, the trajectory of an on-axis beam does not change with respect to the sector magnet case. However, off-axis particles see different lengths of magnet resulting in modified focusing properties. The transfer matrix for such a magnet can be derived by assuming it to be a sector magnet plus an end piece which acts like a defocusing quadrupole, as depicted in 65b. The length of this end piece that an off-axis electron experiences is given by L = x tan(α). The difference in the angle the electron is travelling in is then L/ρ, which gives an R_{12} component of tan(α)/ρ. Since this piece only has a focusing effect, the full transfer matrix of the end wedge piece can be written as

$$\mathrm{R_{wedge}} = \begin{pmatrix} 1 & 0 & 0 \\ \frac{\tan\alpha}{\rho} & 1 & 0 \\ 0 & 0 & 1 \end{pmatrix} . \tag{201}$$

The total transfer matrix of this magnet is equal to $\mathrm{R_{wedge}}$ multiplied by $\mathrm{R_{sector}}$

$$\mathrm{R_{angled}} = \begin{pmatrix} \cos\theta & \rho\sin\theta & \rho\,(1-\cos\theta) \\ \frac{1}{\rho}\,(\cos\theta\tan\alpha - \sin\theta) & \sin\theta\tan\alpha + \cos\theta & \tan\alpha\,(1-\cos\theta) + \sin\theta \\ 0 & 0 & 1 \end{pmatrix} . \tag{202}$$

In the case of a rectangular magnet, where $\theta = \alpha$, this magnet will have an infinite focal length in the x direction.

These calculations have assumed the magnet has a uniform field that is entirely in the vertical direction, leading to a deflection in the horizontal plane. In reality, towards the edge, the $\mathrm{B_y}$ field of the magnet tapers off slowly and there are a significant $\mathrm{B_x}$ and $\mathrm{B_z}$ components as the field lines curl around the edge of the magnet. To account for the $\mathrm{B_y}$ spatial field profile, an effective length needs to be defined including the fringe fields. A uniform field, with the magnitude of the peak of the real field, assumed over this effective length must have the same overall effect on the electron beam so

$$\mathrm{B_0\,L_{eff}} = \int_0^\infty \mathrm{B_y(s)\,ds} . \tag{203}$$

This is known as the hard-edge approximation and it is important when comparing transfer matrix results to a magnet with a realistic field profile. In a sector magnet, electrons enter and exit the magnet perpendicular to the entrance and exit faces. Because of this, the fringe field components perpendicular to the edges will not lead to any focusing in the vertical direction as that component of v $\times$ B will be zero. Where the magnet exit boundary is not normal to the electron direction of travel, there is focusing in the vertical due to the exit wedge. The focal length in the vertical is -1 multiplied by the focal length of the wedge in the horizontal, so equals $\rho/\tan(\alpha)$. Although the change in vertical beam size at the detector does not affect the dispersion, it is worth considering as it affects the total beam measurability in the presence of a detector noise floor. This is especially important when dealing with fC bunch charges as here.

5.2.3 Electromagnet Field

Given a certain magnet length, the peak field required for a 100 keV electron to be deflected 45° can be calculated from equation 190. The radius of curvature can be

written as $\rho = \mathrm{L_s}/\theta$, where L_s is length of the magnet along the electron trajectory. Given $\mathrm{L}_s = 10\,\mathrm{cm}$, the magnetic field required for 45° deflection of 100 keV electrons is on the order of 10 mT. It was decided for this diagnostic that an electromagnet would be used, primarily due to the difficulty of moving a permanent magnet out of the beamline when not in use, and then realigning whenever spectral measurements were required. One power efficient way of generating a magnet field from a current is wrapping the wire around a former made from a material with a high relative permeability, such as iron. Using two blocks of iron, as drawn in figure 66, with current carrying wire wrapped around, the field in the centre of the gap can be estimated by

$$\mathrm{B_y} = \frac{\mu_0\,\mathrm{N\,I}}{\mathrm{h}}\,, \tag{204}$$

where N is the number of turns, I is the current and h is the gap height. Another way to generated this field is by using two coils on a non-magnetic former. Assuming a geometry like in figure 66 where coils are wrapped around either end of the gap and $\mathrm{L_x} = \mathrm{L_y} = \mathrm{L}$, the field at the centre of the magnet can be approximated by first calculating the field from a single square coil using the Biot-Savart law

$$\mathrm{B(r)} = \frac{\mu_0\,\mathrm{N\,I}}{4\,\pi}\oint_{\mathrm{L}}\frac{\mathrm{d\hat{l}}\times(\mathbf{r}-\mathbf{r}')}{|\mathbf{r}-\mathbf{r}'|^3}\,, \tag{205}$$

where $\mathbf{r}$ is the observation point and $\mathbf{r}'$ is the current path, both in Cartesian coordinates. The coil can be split into 4 straight wire segments with side length L which form a closed loop. With the axis at zero in the centre of the coil, the sum of the $\mathrm{B_y}$ contributions of each wire is given by

$$\begin{aligned}\mathrm{B_y(x,y,z)} = {}& \frac{\mu_0\,\mathrm{N\,I}}{4\,\pi}\int_{-\mathrm{L}/2}^{\mathrm{L}/2}\left(\frac{\mathrm{z}+\frac{\mathrm{L}}{2}}{\left[(\mathrm{z}+\frac{\mathrm{L}}{2})^2+(\mathrm{x}-\mathrm{x}')^2+\mathrm{y}^2\right]^{3/2}}-\frac{\mathrm{z}-\frac{\mathrm{L}}{2}}{\left[(\mathrm{z}-\frac{\mathrm{L}}{2})^2+(\mathrm{x}+\mathrm{x}')^2+\mathrm{y}^2\right]^{3/2}}\right)\mathrm{dx}' \\ & + \frac{\mu_0\,\mathrm{N\,I}}{4\,\pi}\int_{-\mathrm{L}/2}^{\mathrm{L}/2}\left(\frac{\mathrm{x}+\frac{\mathrm{L}}{2}}{\left[(\mathrm{z}-\mathrm{z}')^2+(\mathrm{x}+\frac{\mathrm{L}}{2})^2+\mathrm{y}^2\right]^{3/2}}-\frac{\mathrm{x}-\frac{\mathrm{L}}{2}}{\left[(\mathrm{z}+\mathrm{z}')^2+(\mathrm{x}-\frac{\mathrm{L}}{2})^2+\mathrm{y}^2\right]^{3/2}}\right)\mathrm{dz}'\,.\end{aligned} \tag{206}$$

Assuming two square coils centred at y = 0 and y = h, the field at the centre (y = h/2, x = z = 0) is

$$\mathrm{B_y} = \frac{\mu_0\,\mathrm{N\,I}}{\pi\,\left(\frac{\mathrm{h}^2}{4\,\mathrm{L}^2}+\frac{1}{4}\right)\sqrt{\frac{\mathrm{h}^2}{4}+\frac{\mathrm{L}^2}{2}}}\,. \tag{207}$$

For L = 10 cm, N = 100 and I = 1 A, the magnetic field at the centre of a magnet constructed of an iron core and of one assembled from coils on a non-magnetic core is plotted in figure 67. For small gaps, there is a significant discrepancy between the peak field generated by the two magnets. For larger gaps, the gains

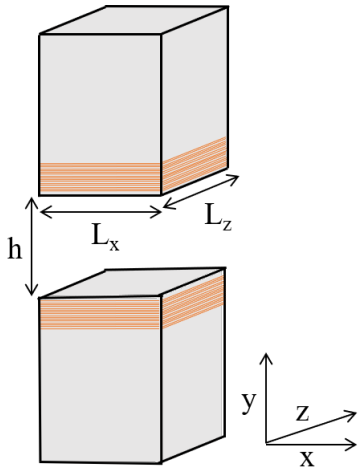

Figure 66: Diagram of a square dipole electromagnet annotated with relevant dimensions.

from using an iron core are smaller. The limitation on the gap size is dependent on the position of the magnet within the setup. If the magnet was to be placed in the interaction chamber under vacuum, the gap size would only be limited by the required electron beam aperture. In vacuum though, electromagnets are susceptible to overheating. It was decided that the dipole would be designed for out of vacuum use due to heating concerns, vacuum quality concerns given the length of wire required, and for ease of access for alignment purposes. In this regime, the limitation on the magnet gap size is imposed by the beam pipe diameter, which is 41.3 mm at the magnet position. Given this, figure 67 shows that the gain in peak magnetic field from using a ferromagnetic core is a factor of approximately 1.5. Considering the lead time and expense of the iron core magnet fabrication, it was decided that an air coil magnet would be manufactured, as it was believed that the reduced power efficiency was manageable.

5.2.4 Particle Tracking Simulations

At this point in the design process the minimum height was been fixed by the beam pipe diameter. The maximum coil side length was approximately 12 cm due to experimental space restrictions in the lab where the magnet was to be placed and a 45° deflection of the central energy was chosen. Due to the finite coil-cross section, a compromise was required between cross-sectional height and width to achieve the necessary field whilst maintaining a feasible power requirement. To find the required power for 45° deflection for different coil diameters and associ-

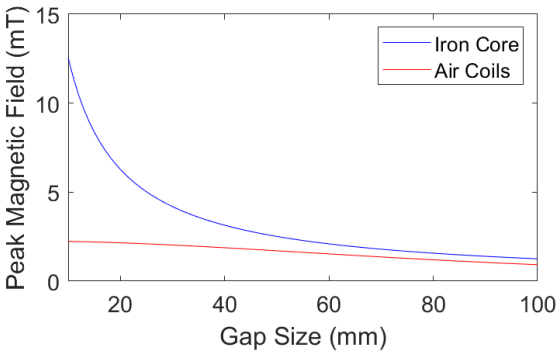

Figure 67: Peak magnetic field in the centre of an iron core magnet and in the centre of two square coils are plotted as a function of gap size. In this calculation, N = 100, I = 1 A and L = 10 cm.

ated fringe fields, the electron beam trajectory was numerically evaluated given the analytical field derived from the Biot-Savart law with two sets of four connected straight lines of current. The numerical calculation propagated electrons with a fourth order Runge-Kutta method implemented in MATLAB, as described in section 2.3.4. The electron trajectory through an example static magnet field is shown in figure 68a as a red line. Here, a grid spacing of 100 μm was used with a temporal step size of 236 fs. In figure 68b, the field experienced by an electron along its trajectory is plotted. The polarity reversed field experienced by the electron before and after the main magnet field reduces the effective magnet length (equation 203). The effective length here is 7.4 cm for a coil side length of 9 cm. A larger current supply is needed to achieve a 45° deflection because of the fringe field.

Using this simulation tool, the required current, and power, for a 45° deflection was first evaluated for square magnets of several side lengths, as plotted in figure 69a. Here, the gap size was fixed at h = 6 cm and the number of turns was kept constant at N = 160, so the coil cross-sectional area was constant throughout. Electrons at y = 0 were propagated through the magnet and the current that led to a 45° deflection was noted. The power was calculated as $P = I^2 R$, where R was evaluated by using the resistivity of copper, a wire diameter of 1.5 mm and the required length of wire to build the coils. The fit line is the result of cubic spline interpolation between the simulation data point to highlight the trend. Figure 69b shows the power required for a number of gap sizes with a fixed edge length, L = 10 cm. From these two plots, a lower power input is required to achieve the deflection of 45° when gap size is small and the side length is large. If the magnet was to be used for focusing in the horizontal direction as well as generating the

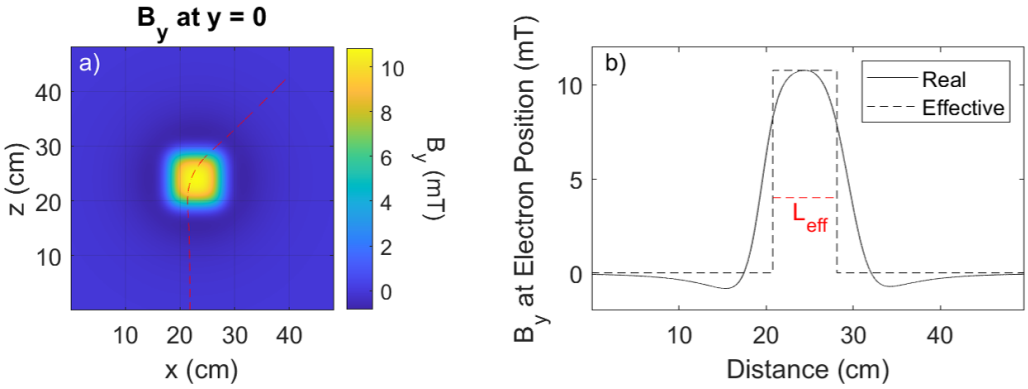

Figure 68: In **a)**, the trajectory of a 100 keV electron is shown as a red line on top of the analytical field from a square coil pair. The field experienced by an electron on this trajectory is plotted in **b)**, along with the assumed field with the hard edge approximation.

dispersion, the angle of the exit face can be modified. Fixing h = 6 cm and L = 10 cm, the power required for 45° deflection is plotted in figure 69c. The angle, α is defined with respect to the sector magnet as in figure 65 and in the transfer matrix 202, and the length through the centre of the magnet is kept constant with α. A square magnet has $\alpha = 45°$. The further the deviation from a square magnet, the higher the power required. This is partly due to the higher resistance as a slightly longer length of wire is needed. There is also a decrease in the effective magnet length experienced by the electron as α is decreased.

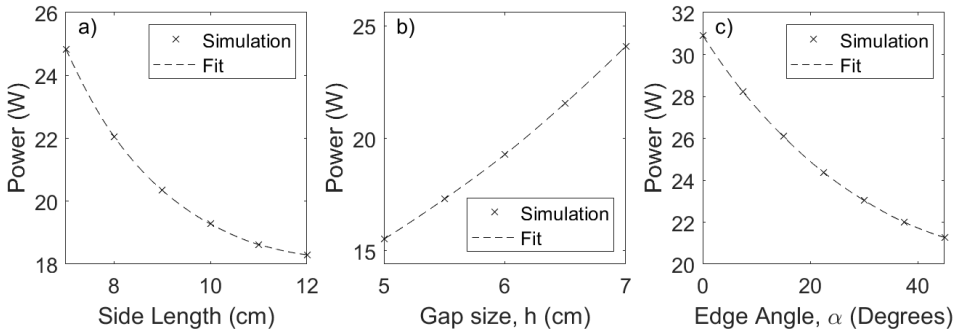

Figure 69: Power required to achieve 45° deflection of a 100 keV electron. The coil side length, L, the gap size, h, and the edge angle, α, are scanned individually in **a)**, **b)** and **c)**, respectively.

It is also essential that an electron beam does not interact with the corners of the magnet and that the field is uniform over a significant central region. In simulations for square magnets, the magnet has been offset in the x direction to avoid electrons travelling through the corners of the magnet. The offset was found for

each magnet size by comparing the deflected angle of electrons, which were initially collimated, with different initial x positions. The chosen offset was the one which minimised the standard deviation of the output angles of electrons. The uniformity of the field in the region of the electron trajectory could also be quantified with the standard deviation of the output angles of electrons. With a square magnet with L = 12 mm and an optimised offset, an electron beam with a width of 10 mm will not have any significant focusing or defocusing of electrons along the transverse dimension. With L = 7 cm, an electron beam of width 2 mm will have issues with electrons at the edge of the beam being deflected at slightly different angles to central electrons. Although the electron beam size is expected to be much less than 10 mm, it is advantageous to have a large area of uniform field for ease of alignment.

The diagram in figure 70 depicts the relevant areas of the experimental setup for this calculation. When the power supply for the dipole is off, the transverse beam profile can be measured at MCP 1. When spectral measurements are required, the dipole can deflect the beam to MCP 2. The beam focusing in the setup is dictated entirely by a solenoid within the electron gun. For maximum detectability of the energy spread, the electron beam needs to be focused on the MCP. There are two potential modes of operation where this can be achieved: gun solenoid focusing at the MCP and gun solenoid focusing at the interaction point with the dipole shaped to provide the additional focusing to the MCP. The edge angle of the dipole required for the second mode of operation is $\alpha = 23.6°$, assuming an effective magnet length of 8 cm (physical length $\approx$ 10 cm). Analytically, the energy deflected per unit distance can be calculated from equation 199 and equation 202. Assuming a drift length of $L_d = 95$ cm, $\theta = 45°$ and that the majority of the energy spreading occurs after the magnet so the R_{13} term can be neglected, a 1 mm difference in transverse position at the MCP plane corresponds to a 190 eV energy difference when using a square magnet. Given the 15 μm channel size of the MCP, this is 2.9 eV/pixel. A magnet with $\alpha < 45°$ will have a reduced resolution due to the reduced R_{23} term. For a magnet with $\alpha = 23.6°$, a 1 mm difference in transverse position at the MCP plane corresponds to 230 eV, which is 3.5 eV/pixel. The MCP diameter is 30 mm so the energy field of view for a square magnet and a focusing magnet assuming a linear dispersion relation is 5.7 keV and 6.9 keV respectively.

Tracking of a realistic electron beam from the gun to the MCP has been done using transfer matrices to quantify the electron beam size on the MCP. N electrons were initiated with a random initial transverse position offset (x_0, y_0), a random initial angular difference from the reference trajectory (x_0', y_0'), z = 0 and a random

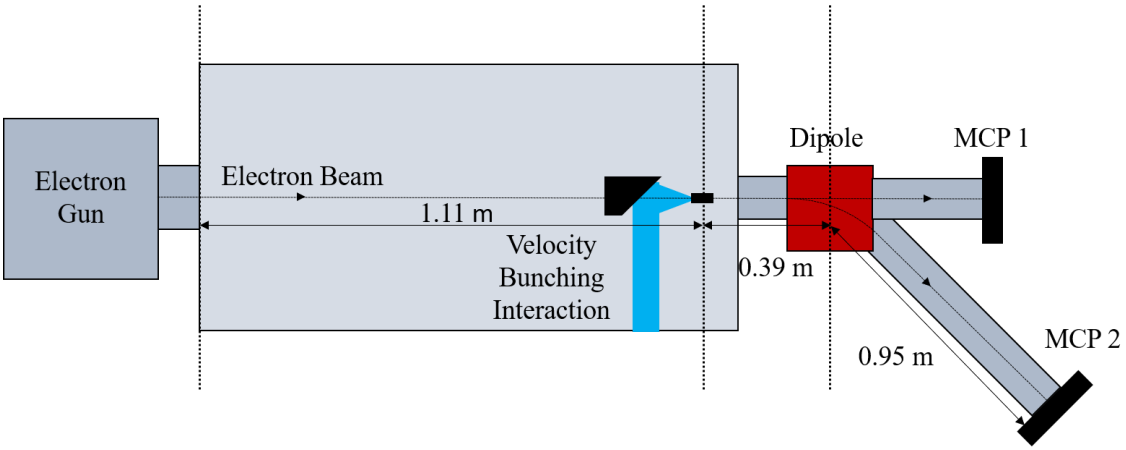

Figure 70: Diagram of the experimental setup for velocity bunching. Electrons are generated at the gun's photocathode and accelerated to 100 keV by a DC field. They then travel into the interaction chamber where a THz-driven accelerator imparts a negative chirp on the bunch. The beam transverse profile can be measured on MCP 1 or the spectrum can be measured on MCP 2.

fractional momentum deviation, δ, at the start of the interaction chamber in figure 70. The random position and angle values were selected from realistic distributions outputted from a model in General Particle Tracer (GPT) of the electron gun with a bunch charge of 0.5 fC[1]. The number of particles in the simulation was one million, which is equivalent to summing approximately 320 images at this charge. Figure 71a plots the transverse profile of the initiated electron beam, which has a FWHM size in the horizontal and the vertical of 2.8 mm. The uncorrelated angular spread was taken from the GPT model but the correlated spread was modified to give focal positions at the MCP plane and the interaction structure, respectively. The horizontal angular distribution is plotted against the horizontal coordinate for MCP and interaction structure focuses in figure 71b. The vertical angular trajectory is chosen from the same distribution in y. This meant a finite emittance was considered, but space charge was not taken into account in this calculation. An uncorrelated energy deviation was added from a Gaussian distribution of FWHM width 100 eV and the central energy was taken to be 99.95 keV, which was the mean of the GPT output. Once the initial 6D phase space was defined, the beam position on the MCP was evaluated using 6D transfer matrices, given in the appendix (7.1). The x dimension of the magnet transfer matrix is given by equation 202 and the focusing in the y direction is given by equation 201. The evolution of the 6D phase

[1]GPT simulations performed by Christopher Shaw.

space is defined by

$$\begin{pmatrix} x_{MCP} \\ x'_{MCP} \\ y_{MCP} \\ y'_{MCP} \\ z_{MCP} \\ \delta_{MCP} \end{pmatrix} = R_{drift}\, R_{angled}\, R_{drift} \begin{pmatrix} x_0 \\ x'_0 \\ y_0 \\ y'_0 \\ z_0 \\ \delta_0 \end{pmatrix} . \tag{208}$$

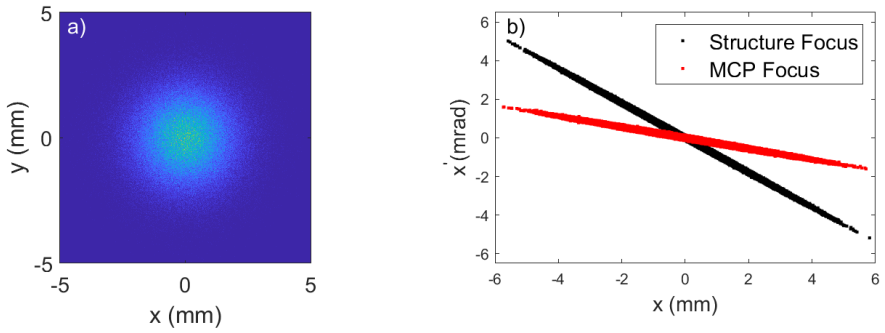

Figure 71: **a)** The initial transverse profile of the electron beam for tracking simulations. **b)** The horizontal angular distribution, x′, of the electrons against the horizontal position coordinate, x, for the structure focus and for the MCP focus setups. The FWHM width of these beams is 2.8 mm.

The horizontal beam size along the beamline for both setups was calculated by outputting the x position through the beam line, taking the standard deviation of the x values, and then converting to FWHM. Figure 72a shows how the horizontal beam size evolves over the beamline for both focusing conditions. Focusing to the MCP with the electron gun solenoid gives a slightly smaller beam size on the MCP in this dimension, which is beneficial for the energy measurement. Although the square magnet does not focus a collimated beam, it does adjust the focusing of an already divergent beam; the effect of which can be calculated using the R_{22} component in equation 202. The R_{11} and R_{12} terms determine the change in horizontal beam position between the entrance and the exit of the magnet. Both of these mean the gun solenoid current needs to adjusted when the magnet is in place. Figure 72b plots the evolution of the vertical beam size. Over-focusing by the square magnet in the y direction for the gun-MCP focus leads to a large vertical beam size on the MCP. The charge throughput will be higher for the structure focus. The difference in the beam clipping is dependent on the structure aperture size but it is expected to significantly clip the gun-MCP focused beam, especially in the vertical dimension.

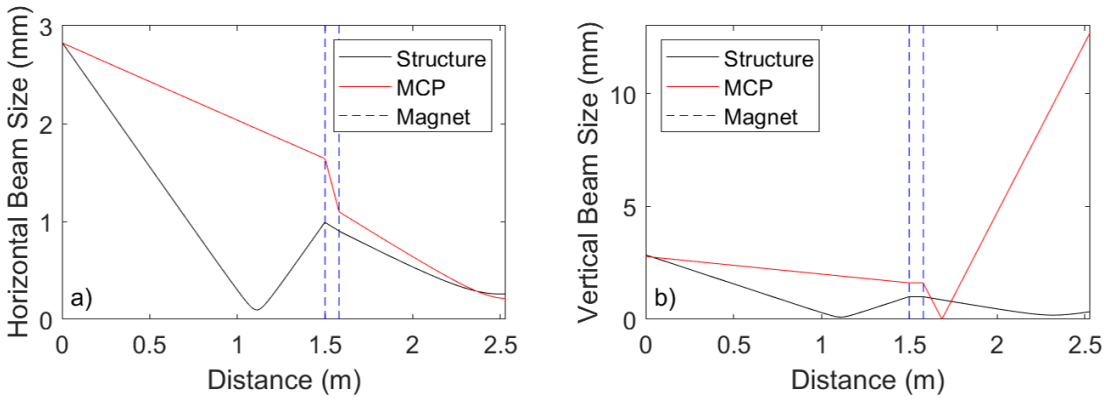

Figure 72: Beam size evolution for structure and MCP focusing in the horizontal, **a)**, and in the vertical, **b)**.

To model the image at the MCP, the output transverse positions are binned in 15 μm pixels. Figures 73a and 73d show the electron beam with zero energy spread, σ, after travelling along the spectrometer beamline given an MCP focus and structure focus, respectively. This is without any structure in place so all of the initial charge reaches the MCP in both setups. A beam with a Gaussian energy spread of FWHM 100 eV is dispersed in the horizontal direction in figures 73b and 73e. All simulated MCP images here are plotted on the same colour scale. Summing over the non-dispersed axis of the MCP images gives 73c and 73f. The combination of the smaller horizontal beam size and the larger dispersion of the gun-MCP focus setup leads to a more significant energy spreading.

The increased resolution from the gun-MCP focus system can be quantified by looking at the energy distribution at the MCP plane. In the ideal case of a point-like electron beam on the screen when it has zero energy spread, a certain position on the screen corresponds to a unique electron energy. When the electron bunch has a finite transverse size it leads to the smearing in the energy measurement. Figures 74a and 74b show the GPT simulated electron energy distribution as a function of horizontal position at the MCP plane for a structure focus and for gun-MCP focusing, respectively. The energy spectra in these two figures are the same. The degradation in resolution in an energy measurement can be estimated by taking the standard deviation of the energy difference from the central energy, ΔE, at a single x position. For a structure focus setup, the resolution limit from finite beam size is $\pm$21 eV and for the gun-MCP focus, it is equal to $\pm$16 eV.

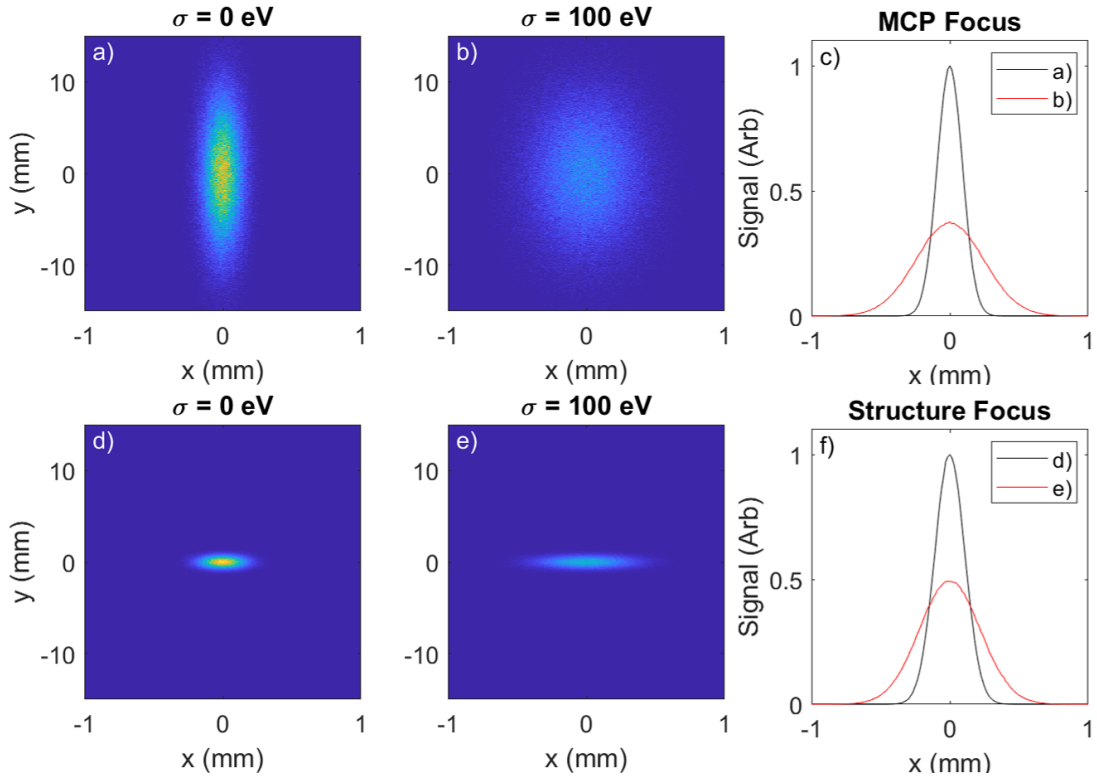

Figure 73: **a)-b)** Simulated MCP images for a gun solenoid to MCP focus with no energy spread and a 100 eV energy spread, respectively. **c)** vertical projection of the images to give the energy spectrum. **d)-e)** Simulated MCP images for a gun solenoid to structure focus with no energy spread and a 100 eV energy spread, respectively. **f)** vertical projection of the images to give the energy spectrum.

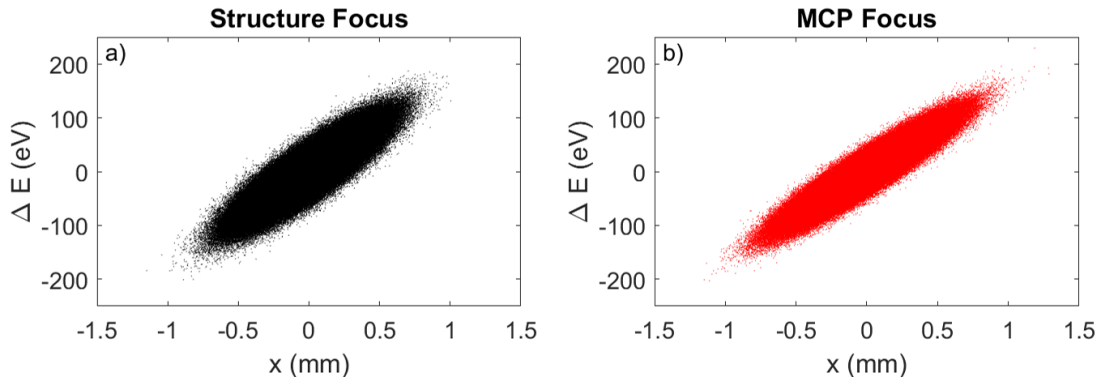

Figure 74: GPT simulated electron energy with respect to the mean energy against horizontal coordinate at the MCP plane for the structure focus, **a)**, and for the MCP focus, **b)**.

5.2.5 Spectrometer Design

The proposed design is a square magnet as it is approximately 10 % more power efficient than the focusing magnet and has an energy measurement error of approximately ±16 eV rather than ±21 eV. The square magnet is also easier to align because with the focusing magnet, the effective length, and therefore focal length, is dependent on the transverse position at which the electron enters the magnet. Whilst the square magnet can be placed in the beamline position by eye and the current can be increased until the beam is seen on the MCP, the focusing magnet would require much more precise positioning until the minimum beam transverse beam size is seen on the MCP. The advantages of the focusing magnet, such as the higher charge throughput and smaller vertical beam size on the MCP, can be recovered with the square magnet if a separate quadrupole is added before the dipole. Separating the magnetic elements providing focusing and dispersion gives flexibility to the position of the interaction point and choice of electron beam focal position from the gun. The proposed design for the dipole coil holder is shown in figures 75a and 75b. The effective coil side length is L = 9 cm and the effect gap is h = 6.3 cm. The required current for 45° deflection of a 100 keV electron beam is 4.4 A. With two 30 m spools of wire with diameter 1.5 mm making each coil, ∼ 160 turns can be wrapped with a cross-sectional diameter of ≈ 4 cm^2. Extra room is built in the grooves for the coils to account for any inefficiency in the winding. The former is made of aluminium and held together with non-magnetic, brass screws. The sections holding the coils are detachable for ease of winding or unwinding and it will be mounted on 4 optical posts.

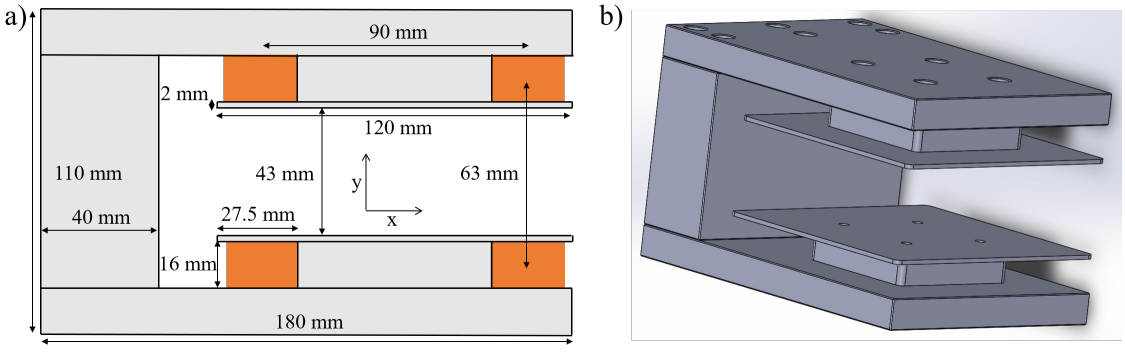

Figure 75: The diagram in **a)** depicts a scale drawing of the dipole in a cutting plane view in the x and y directions. **b)** is a 3D representation of the former.

5.3 Electron Interaction with a THz-Driven Dielectric-Lined Waveguide

A dielectric-lined waveguide was used to provide velocity matching between the 100 keV electron beam and the THz phase. The properties of the dielectric-lined waveguide used for sub-relativistic electron beam manipulation experiments are given in table 3. The procedure for designing this waveguide is detailed in [107]. The geometry allowed either phase matched deflection or acceleration in the THz regime, depending on the field input. The coupler had a length of 44 mm, entrance height and width of 5 mm and 10 mm respectively, and a linear taper in transverse dimensions down to the waveguide size.

Parameter	**Value**
2a	200 μm
2b	680 μm
δ	240 μm
w	1 mm
L	5 mm
ϵ_r	3.81 [130]

Table 3: Properties of the dielectric-lined waveguide used during electron gun experimentation.

5.3.1 Deflecting Mode Dispersion Properties

The LSM_{10} mode was exploited for deflection of 100 keV electron bunches because it has a non-zero transverse electric field on-axis. To find the dispersion relation for even modes in the DLW, equation 117 (page 49) was solved numerically in MATLAB. A minimisation function, F, for even modes was defined as

$$F\,(m,\,\beta_{mn}) = |k_{y,\,mn}^{(1)} \tan(k_{y,\,mn}^{(1)}\,\delta) - \epsilon_r\,k_{y,\,mn}^{(0)} \cot(k_{y,\,mn}^{(0)}\,a)|\;, \tag{209}$$

where, as before,

$$k_{y,\,mn}^{(0)} = \sqrt{k_0^2 - \left(\frac{m\pi}{w}\right)^2 - \beta_{mn}^2}\;, \tag{210}$$

$$k_{y,\,mn}^{(1)} = \sqrt{\epsilon_r\,k_0^2 - \left(\frac{m\pi}{w}\right)^2 - \beta_{mn}^2}\;. \tag{211}$$

For each frequency and mode, mn, a longitudinal wavenumber β_{mn} was found from the constraint that minimised F. The obtained dispersion relation for the LSM_{10} mode is shown in figure 76a. The cutoff frequency of this mode was found to be

0.1 THz. Phase and group velocities are plotted as a function of frequency in figures 76b and 76c respectively. The frequency at which the phase velocity is equal to the 100 keV electron velocity of 0.55 c is 0.47 THz. At this frequency, the group velocity is 0.48 c.

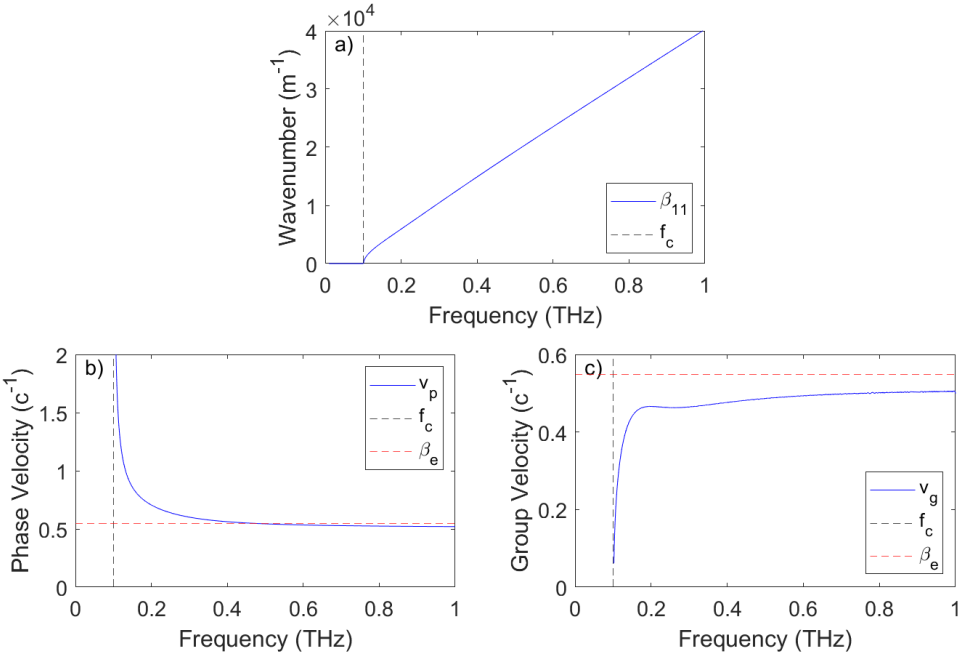

Figure 76: **a)** The propagation constant for the LSM_{10} mode in a DLW with properties given in table 3. **b)** and **c)** The phase and group velocity, respectively, as a function of frequency.

At the phase-matched frequency for this waveguide, the field components in the LSM_{10} mode, given by equations 110-114 (page 49) in the DLW cross-section are shown in figure 77. The electric field in these plots is normalised to the maximum E_y and the magnetic field is normalised to the maximum H_x value. With this DLW geometry, only a small portion of the field energy is contained in the waveguide free-space aperture.

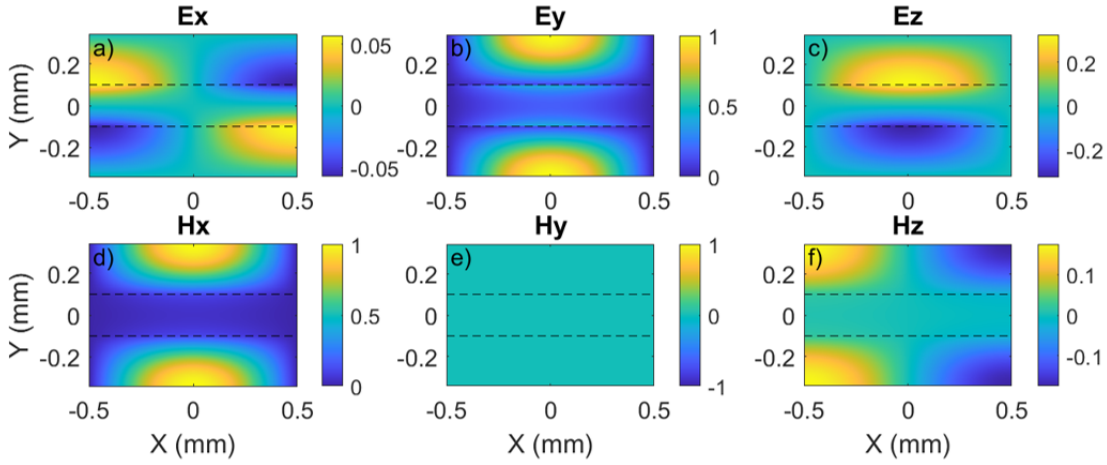

Figure 77: **a)-f)** The transverse profile of the electric and magnetic field components at 0.47 THz in the LSM_{10} mode of the DLW with dimensions given by table 3.

5.3.2 Coupling to the Deflecting Mode

Calculation of the expected deflection required estimation of the coupling into the waveguide from the measured transverse profile at the coupler entrance in figure 56b. The spectrum of the pulse is taken to be the measured spectrum in figure 57. The assumed transverse field profile at the coupler entrance was Gaussian with a height and width a factor $\sqrt{2}$ larger than the measured intensity profile. The coupler entrance dimensions provided the first loss of energy, with 25 % of the 525 nJ in the pulse clipped. The next consideration was the energy coupling from free space to the relevant coupler deflecting mode, which was the TE_{10} mode. The transverse profile matching calculation in section 4.1.2 (page 74) was repeated with the experimentally measured input beam. The TE_{10} mode of the rectangular metallic guide has field components given by

$$\widetilde{E}_x(x,y,0,\omega) = \frac{i\,\omega\,\mu_0\,\pi}{w\,k_c^2}\cos\left[\frac{\pi}{w}\,(x+\frac{w}{2})\right]\sin\left[\frac{\pi}{h}\,(y+\frac{h}{2})\right], \tag{212}$$

$$\widetilde{E}_y(x,y,0,\omega) = \frac{i\,\omega\,\mu_0\,\pi}{h\,k_c^2}\sin\left[\frac{\pi}{w}\,(x+\frac{w}{2})\right]\cos\left[\frac{\pi}{h}\,(y+\frac{h}{2})\right], \tag{213}$$

$$\widetilde{H}_x(x,y,0,\omega) = \frac{i\,\beta_{TE}\,\pi}{h\,k_c^2}\sin\left[\frac{\pi}{w}\,(x+\frac{w}{2})\right]\cos\left[\frac{\pi}{h}\,(y+\frac{h}{2})\right], \tag{214}$$

$$\widetilde{H}_y(x,y,0,\omega) = \frac{i\,\beta_{TE}\,\pi}{w\,k_c^2}\cos\left[\frac{\pi}{w}\,(x+\frac{w}{2})\right]\sin\left[\frac{\pi}{h}\,(y+\frac{h}{2})\right], \tag{215}$$

where $\beta_{TE} = \sqrt{k_0^2 - k_c^2}$ and $k_c = \sqrt{(\pi/w)^2 + (\pi/h)^2}$. At the entrance, $w = 10\,mm$ and $h = 5\,mm$. The result of this mode matching calculation is that effectively all of the energy incident on the coupler aperture couples to the TE_{10} mode. The

transverse profile of the E_y field in free-space and in the TE_{10} mode at the coupler entrance are shown in figures 78a and 78b, respectively.

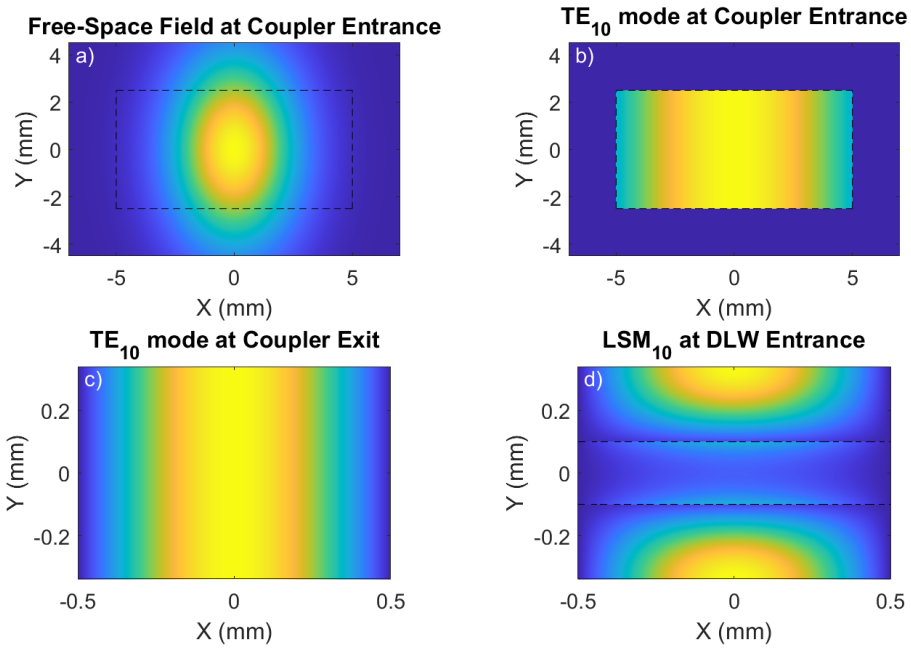

Figure 78: **a)** The assumed free-space E_y field profile at the coupler entrance. **b)** The E_y field profile in the TE_{10} mode at the coupler entrance at 0.47 THz. **c)-d)** The field profile at the coupler exit and in the LSM_{10} mode, respectively, at 0.47 THz. Free-space apertures are defined by black dotted lines.

Dispersion from the coupler was applied to the measured pulse spectrum by considering the coupler as a series of rectangular waveguides with decreasing dimensions along the coupler length, as depicted in figure 26a (page 80). Using equation 174, an effective propagation constant was defined for the coupler. The pulse spectrum was then propagated by multiplying by $e^{i\beta_{eff}L_c}$. Figure 79a shows the measured time profile and the time profile after the coupler dispersion was applied.

Coupling from the exit of the coupler to the LSM_{10} DLW mode was considered next. Since the TE_{10} mode at the exit of the coupler has a cutoff frequency of 0.15 THz, no frequency components below this were allowed to propagate into the waveguide. Mode matching was performed to estimate the energy efficiency of the coupling between the modes as a function of frequency, which is plotted in figure 79b. At the phase matched frequency, approximately 20 % of the energy at the coupler exit couples to the desired DLW mode. The transverse profiles of

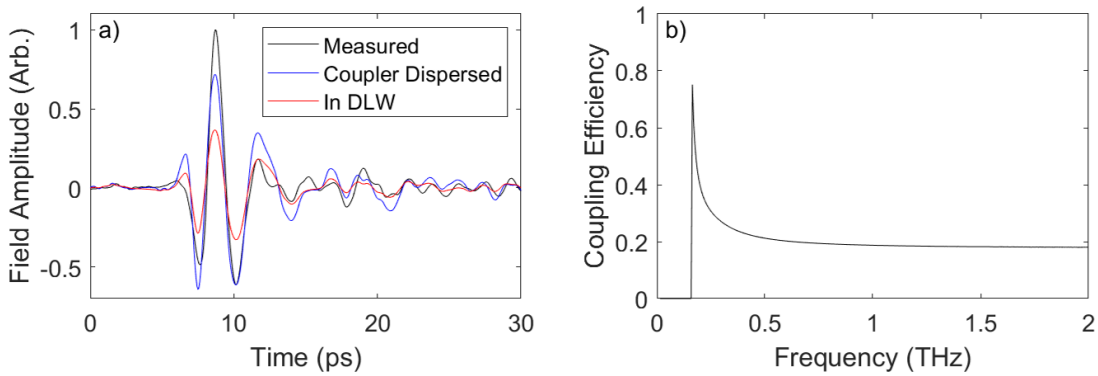

Figure 79: **a)** The measured pulse time profile against the estimated time profile of the pulse after being dispersed by the coupler and the estimated time profile of the pulse coupling into the waveguide, given the energy coupling efficiency in **b)**.

the E_y field in the TE_{10} mode at the coupler exit and in the LSM_{10} mode at the phase-matched frequency are shown in figures 78c and 78d, respectively. There is clearly a significant difference in the transverse field profile at the exit of the coupler compared to the DLW, which leads to the low energy coupling between them.

To find the coupled time domain profile of the electric field, the square root of the coupling energy efficiency was taken to reflect the field coupling. The field spectrum was then multiplied by the field coupling efficiency. The inverse Fourier transform of the coupled spectrum gives the time profile of the pulse in the LSM_{10} mode, as plotted in figure 79a. The time domain profile here takes into account the coupler dispersion, the cutoff frequency at the exit of the coupler and the frequency dependent coupling efficiency to the mode.

The sum over time of the intensity envelope gives a value proportional to energy. The ratio of the sum over the intensity envelope of the measured field and of the estimated field profile in the deflecting mode is 0.24. With the input pulse energy of 525 nJ, multiplying by 0.75 for clipping at the coupler entrance and by 0.24 for the coupling to the deflecting mode gives a maximum pulse energy in the DLW of approximately 95 nJ. The overall energy coupling efficiency from free-space to the deflecting mode in the DLW is 18 %.

The peak on-axis field in the deflecting mode can be calculated given the coupled time profile and the calculated pulse energy in the mode. Firstly, the LSM_{10} mode E_y and H_x field transverse profiles were defined for frequencies across the

pulse spectrum. At each frequency, the energy flux over the mode cross-section was normalised. The transverse profile was then projected over the spectrum coupled into the DLW mode to give $\widetilde{\mathrm{E}}_\mathrm{y}(\mathrm{x},\mathrm{y},\omega)$ and $\widetilde{\mathrm{H}}_\mathrm{x}(\mathrm{x},\mathrm{y},\omega)$. The inverse Fourier transform gave $\mathrm{E}_\mathrm{y}(\mathrm{x},\mathrm{y},\mathrm{t})$ and $\mathrm{H}_\mathrm{x}(\mathrm{x},\mathrm{y},\mathrm{t})$. The time axis is assumed to be the z axis multiplied by the speed of light. The same assumption is made in the measured pulse energy where a detector is placed at a given z position and gives a signal which is proportional to the time sum of the intensity profile. The energy in an electromagnetic wave is the volume integral of the energy density

$$\mathrm{W} = \frac{1}{2} \iiint \left(\epsilon_0\, \epsilon_\mathrm{r}\, \mathrm{E}_\mathrm{y}^2 + \mu_0\, \mathrm{H}_\mathrm{x}^2\right) \mathrm{dV}\ , \tag{216}$$

where electric and magnetic field envelopes are used here. It is clear that in the DLW, the integral in equation 216 needs to be calculated separately over the dielectric and vacuum regions. The LSM_{10} mode fields are symmetrical around y = 0 so the integral over the full cross-section is twice the integral over one half. If the electric field is given by a constant, E_0, multiplied the spatial profile and the magnetic field is the electric field divided by the impedance, the constant E_0 can be calculated as

$$\mathrm{E}_0 = \sqrt{\frac{\mathrm{W}}{\int_{-\infty}^{\infty}\int_0^\mathrm{a}\int_{-\mathrm{w}/2}^{\mathrm{w}/2}\left(\epsilon_0 + \frac{\mu_0}{\mathrm{Z_a}}\right)\mathrm{E}_\mathrm{y}^2\,\mathrm{dxdydz} + \int_{-\infty}^{\infty}\int_\mathrm{a}^\mathrm{b}\int_{-\mathrm{w}/2}^{\mathrm{w}/2}\left(\epsilon_0\epsilon_\mathrm{r} + \frac{\mu_0}{\mathrm{Z_d}}\right)\mathrm{E}_\mathrm{y}^2\,\mathrm{dxdydz}}}\ , \tag{217}$$

where $\mathrm{Z_a}$ and $\mathrm{Z_d}$ are impedances in the vacuum aperture and in the dielectric respectively. E_0 is then multiplied by the electric field on-axis in the mode, $\mathrm{E}_\mathrm{y}(0,0,\mathrm{t})$, to give the axial field in SI units. With $\mathrm{W} = 95\,\mathrm{nJ}$ coupled into the LSM_{10} mode, the peak axial field in the mode is $2.2\,\mathrm{MV/m}$.

5.3.3 Deflection Interaction

For simulation of the deflection interaction, the transverse, on-axis electric and magnetic fields were propagated in the Fourier domain by

$$\widetilde{\mathrm{E_y}}(\omega,\mathrm{z}) = \widetilde{\mathrm{E_y}}(\omega,\mathrm{z_0})\,\mathrm{e}^{\mathrm{i}\,(\beta_{10}-\mathrm{k}/\beta_\mathrm{e})\,\mathrm{z}} \tag{218}$$

$$\widetilde{\mathrm{H_x}}(\omega,\mathrm{z}) = \widetilde{\mathrm{H_x}}(\omega,\mathrm{z_0})\,\mathrm{e}^{\mathrm{i}\,(\beta_{10}-\mathrm{k}/\beta_\mathrm{e})\,\mathrm{z}} \tag{219}$$

where $\mathrm{e}^{\mathrm{ikz}/\beta_\mathrm{e}}$ gives the time delayed fields synchronised with the electron beam. The initial spectrum used for the simulation was the calculated spectrum within the DLW mode. The inverse Fourier transform gives the time domain field and tracking the field at a set time within the 5 mm long DLW gives the field experienced by a particle at that injection time. The fields $\mathrm{E_y}(\mathrm{t_e},\mathrm{z})$ and $\mathrm{H_x}(\mathrm{t_e},\mathrm{z})$ were calculated in MATLAB from the exit of the coupler. It was assumed that the difference in

the electron transverse position over the waveguide length was small so effects of a varying transverse field profile could be neglected. With these fields as a function of position along the waveguide for a given electron injection time, a fourth order Runge-Kutta solver was used to numerically propagate the electrons through the waveguide. The position of the beam on the screen was calculated after a free-space drift using the electron velocities at the end of the simulation

$$y_{MCP} = L_d \frac{v_y}{v_z} , \tag{220}$$

where the drift length, $L_d = 0.75\,\mathrm{m}$.

5.3.4 Deflection Experiment

Experimental deflection data were taken to verify the model of the interaction. The electrons were aligned through the waveguide structure onto the MCP, as described in section 5.1.5. The camera viewing the MCP was orientated to maximise the field of view of the MCP in the vertical direction for viewing of the streaked beam. The electron focusing was chosen such that the beam focus was close to the interaction point to maximise charge throughput of the waveguide. An ND 1 filter was placed in the light used for photocathode excitation giving an estimated bunch charge of $< 1\,\mathrm{fC}$. The charge was kept to these low levels in an attempt to minimise the bunch duration at the interaction point. The THz pulse energy was given continuously adjustable attenuation by a pair of wire grid polarisers. Synchronisation between THz and electrons was achieved by first matching path durations taken by the THz and the electrons to the interaction point, taking into account the sub-luminal electron velocity. The time-delay stage on the THz line was then adjusted until the electron beam size in vertical direction visibly changed.

Figures 80a and 80b show the beam without and with the THz interaction, respectively. The THz pulse energy here incident on the coupler was 225 nJ, which, according to the coupling efficiency derived earlier, corresponded to 41 nJ in the deflecting mode. The simulated peak transverse deflecting electric field on-axis with this energy in the mode and the calculated coupled time profile was $1.5\,\mathrm{MV/m}$. The time-delay between the THz and the electron was varied until an approximately vertical symmetrical deflection was seen. The timing corresponds to the THz pulse zero crossing, where the greatest field gradient is seen. The total electron vertical beam size increases from approximately 5 mm to 26 mm on the MCP.

The centre of the electron bunch in the horizontal direction appears to be deflected more than the edges. The disparity is likely due to the transverse field

profile of the LSM_{10} mode in the horizontal direction, which has a maximum in the centre and falls to zero at the metal walls. The fact that the centre is visibly deflected more suggests that the electron bunch width within the DLW is significant in comparison with the waveguide width.

Some charge is clipped by the vertical dimension of the waveguide which is why the beam without deflection is rectangular. The clipping could partly be due to misalignment of the electron beam pointing or it could be an indicator that the electron bunch focus is not quite at the waveguide plane. Clipping by the dielectric lining leads to the electron beam charging the dielectric material. The static charge above and below the electron beam path provides a focusing effect, leading to a larger beam at the MCP plane than if the waveguide is moved out of the beam path. A 100 keV beam is also very sensitive to small, stray magnetic fields, which are thought to have contributed to the peculiar bunch shape.

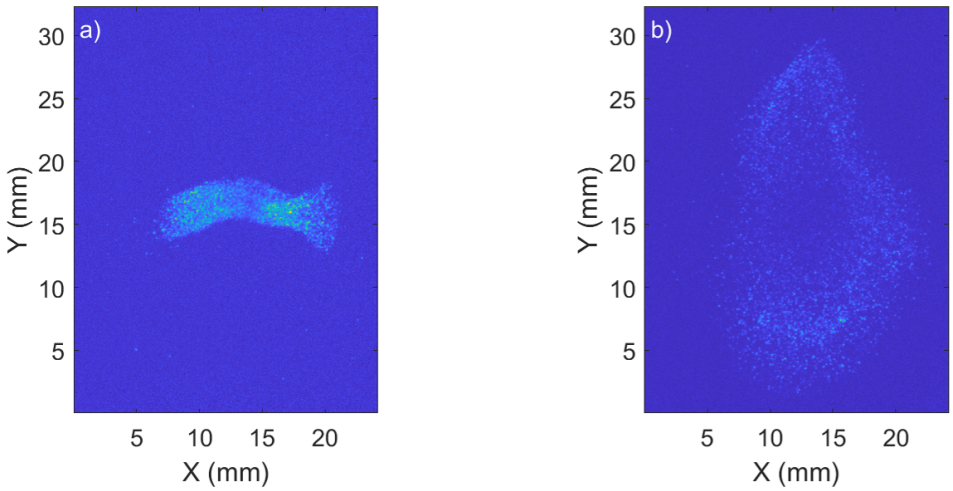

Figure 80: The measured electron beam transverse profile on the MCP without THz, **a)**, and with a THz-driven interaction, **b)**.

An accurate measurement of the electron bunch duration was difficult to achieve in this experiment as the duration was predicted to span over more than half the THz period. The vertical profiles of the electron bunches in figure 80 are shown in figure 81. The signal is higher at the edges of the bunch vertically than at the centre which suggests that the bunch duration is long enough to span over peaks of the sinusoidal THz field, where the field gradient with respect to time falls to zero. A bunch that spanned over more than two peaks of the THz field would dis-

play further charge spikes. Since these are not visible, a tentative estimate of the electron bunch duration is on the order of half the deflection period. As described later, the deflection period is approximately 4 ps, so a electron bunch duration of approximately 2 ps is estimated.

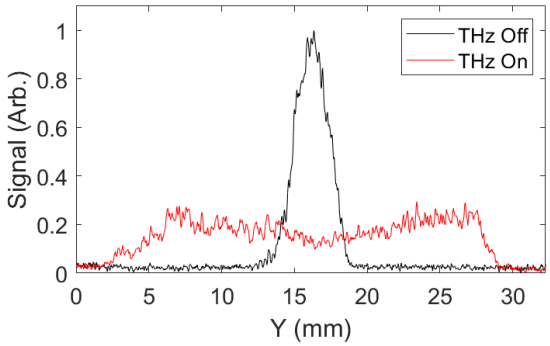

Figure 81: The electron beam profile in the vertical direction with and without THz streaking.

A time delay scan was taken by moving the THz delay stage, in figure 51, in increments of 20 μm, which corresponded to a pump laser time delay of 133 fs. At each stage position, 4 images were averaged, each with an exposure time of 0.8 s. With the laser rep rate set to 1 kHz, this meant 3200 shots were averaged to generate an image at each delay stage position. The averaged image at each time delay was summed in the horizontal direction to give the vertical profile. These vertical profiles were plotted as a function of time delay to generate a 2D plot dubbed a 'deflectogram'. Deflectograms with 10 %, 30 % and 43 % of the maximum available THz pulse energy are plotted in 82a, 82b and 82c respectively.

The 1D model described in section 5.3.3 was implemented to generate the trend line overlaid on these figures. The initial electric and magnetic field spectra, $\widetilde{E_y}(\omega, z_0)$ and $\widetilde{H_x}(\omega, z_0)$, were taken from the Fourier transform of the simulated field in the DLW in figure 79. Particle velocity in the propagation direction and the vertical direction for a number of injection times, t_e, was found after interaction in the DLW. Given the known drift length to the MCP, the expected beam centroid position in the vertical direction could be calculated by equation 220. The measured energy incident on the coupler entrance experimentally was 53 nJ, 158 nJ and 225 nJ, respectively, in figure 82. From the simulated 18 % coupling efficiency of energy at coupler entrance to the waveguide deflecting mode, the LSM_{11} mode was modelled

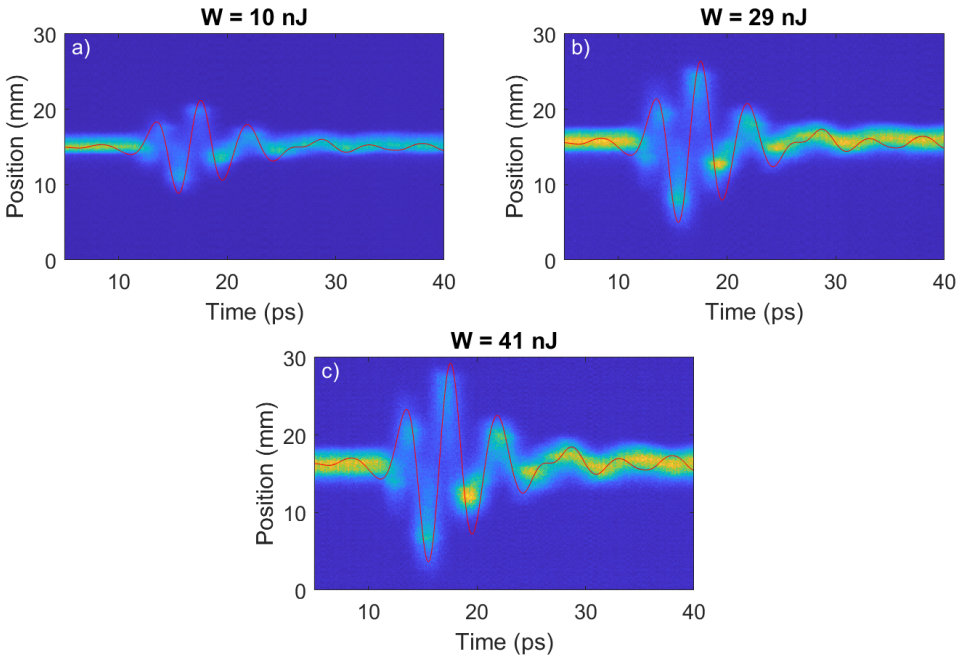

Figure 82: The vertical electron beam profile is shown as a function electron-THz time delay with THz pulse energies of 53 nJ, **a)**, 158 nJ, **b)**, and 225 nJ, **c)**, at the coupler entrance.

to have 10 nJ, 29 nJ and 41 nJ coupled, respectively, which corresponded to peak field strengths in the simulation of 0.7 MV/m, 1.2 MV/m and 1.5 MV/m.

The model appears to match the features displayed in the interaction with the main pulse. Both model and experiment appear to show a deflection period of approximately 4 ps, which is equal to the reciprocal of the phase matched frequency divided by β_e. The peak field estimation seems to be an overestimate of the experimental field. This is to be expected as the model did not account for material losses or any misalignment of the THz onto the coupler entrance. Oscillations can be seen in the modelled electron beam centroid far from the main pulse, which are not evident in the experimental data. It could be that these oscillation in the model come from error in the assumed THz spectra due to noise in the initial EO measurement. If the oscillations are a physical phenomenon, they could feasibly be washed out by the transverse electron beam size in the experimental deflectograms. Deflection data with the maximum pulse energy is not shown here. Clipping of the electron beam at the MCP position in the dataset limited the information that could be extracted. Electrons in this case are also deflected close to the charged dielectric within the DLW length. The model described above is no longer valid in this regime.

An important parameter in assessing an interaction such as this for measuring the electron bunch duration is the streaking speed. It can be stated in μrad/fs to characterise the interaction strength or μm/fs to help characterise the temporal resolution of the full system. To calculate the maximum streaking speed here, the derivative of the modelled centroid position for the highest energy deflectogram was taken with respect to time delay. From this, a streaking speed of $\approx 20\,\mu$m/fs was calculated. The limit on the temporal resolution of the bunch duration measurement is given by a mixture of this and the bunch vertical size. The streaking speed was calculated in terms of the deflected angle at the end of the waveguide by dividing the previously stated streaking speed by the drift length to the MCP, which gave a value of $26\,\mu$rad/fs. A greater number could be achieved by increasing the THz field strength, which would allow the THz-electron interaction to be closer to the MCP whilst achieving the same temporal resolution in the bunch duration measurement. For an electron bunch with a duration on the order of the THz period, increasing the THz field strength limits the charge reaching the MCP due to vertical clipping in the waveguide. An estimate of the required peak field for on-axis electrons phase-matched to the THz peak to reach the edge of the vertical aperture before the end of the waveguide length was calculated by outputting the electron y position at the end of the DLW from the deflection model. A peak electric field of 3.2 MV/m would be required for central electrons to be clipped before the end of the 5 mm waveguide length in the absence of charged dielectric. Off-axis electrons may still be clipped with a lower peak on-axis electric field.

5.3.5 Accelerating Mode Dispersion Properties

The LSM_{11} mode was exploited for acceleration of 100 keV electron bunches because it has a significant longitudinal electric field on-axis. To find the dispersion relation for this mode in the DLW, equation 116 was solved numerically in MATLAB, as in section 4.1.1 (page 69). Figure 83a plots the dispersion relation for the LSM_{11} mode. For the waveguide dimensions discussed previously (table 3), the cutoff frequency of the accelerating mode is 0.16 THz. Phase and group velocities are plotted as a function of frequency in figures 83b and 83c, respectively. The operating frequency for the accelerating mode, where the phase velocity of the accelerating field is equal to β_ec for 100 keV electrons, is 0.47 THz, and at this frequency, the group velocity is 0.48 c.

At the phase-matched frequency for this waveguide, the field components in the

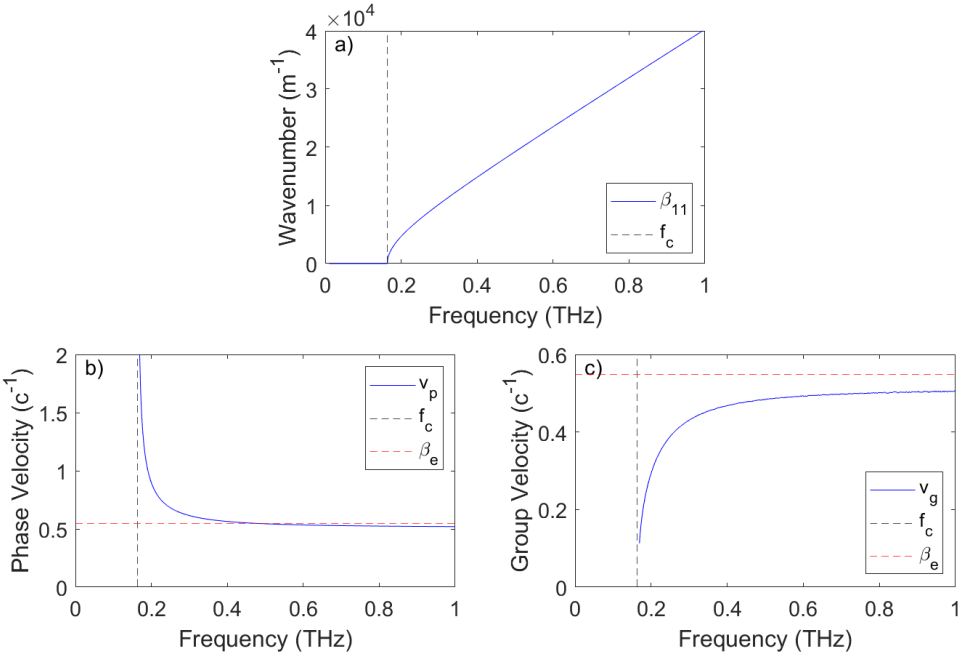

Figure 83: **a)** The propagation constant for the LSM_{11} mode in the DLW with properties given in table 3. **b)** and **c)** plot the phase and group velocity, respectively, as a function of frequency.

LSM_{11} mode, given by equations 110-114, in the DLW cross-section are shown in figure 84. The electric field in these figures is normalised to the maximum E_y and the magnetic field is normalised to the maximum H_x value. With this DLW geometry, only a small portion of the longitudinal field energy is contained in the waveguide aperture - the majority of the mode's longitudinal field energy is in the dielectric lining.

5.3.6 Coupling to the Accelerating Mode

To model the acceleration interaction, a Gaussian-Hermite TEM_{01} mode pulse transverse profile was assumed at the coupler entrance. The spot size in both the vertical and horizontal direction was kept the same as the THz camera image in figure 56b with $1/e^2$ intensity width of 5.5 mm and height of 8.4 mm. The time profile of the input pulse was again taken from the measured EO signal in figure 57 and used to define the pulse spectrum. An initial pulse energy of 525 nJ was chosen to reflect to the experimental source. Only 30 % of the initial energy in this pulse is contained within the coupler entrance aperture dimensions.

The coupling from free-space to the TM_{11} waveguide mode was calculated by the transverse profile matching calculation in section 4.1.2. The coupling efficiency

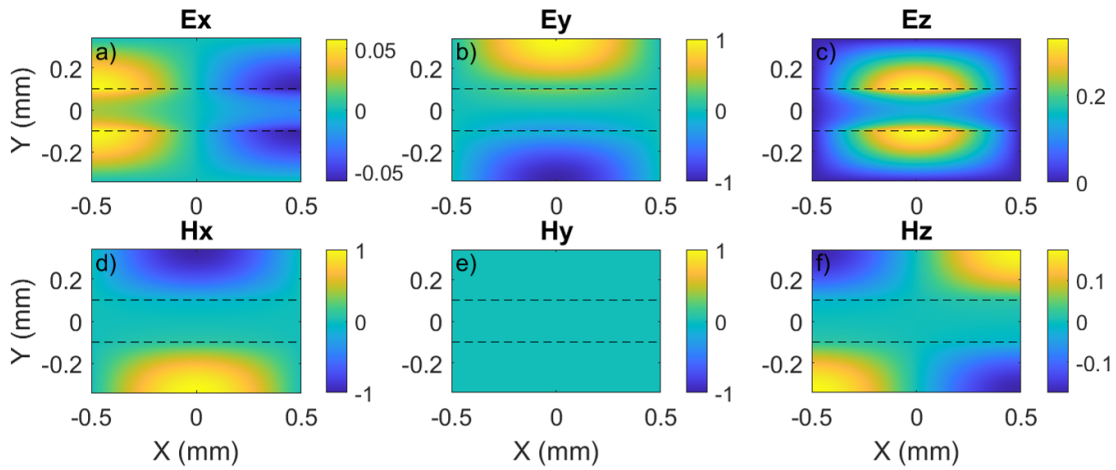

Figure 84: **a)-f)** The transverse profile of the electric and magnetic field components in the LSM_{11} mode at 0.47 THz of a DLW with dimensions given by table 3 .

is approximately constant with frequency, and allows 95 % of the energy at the coupler into the mode. The spatial profiles of the E_y field in free-space and in TM_{11} at the coupler entrance are shown in figures 85a and 85b respectively. The coupling efficiency from the TM_{11} mode to the LSM_{11} mode is also approximately constant with frequency, allowing approximately 100 % of the energy at the coupler exit in the TM_{11} into the LSM_{11} mode. The spatial profiles of the E_y field in the TM_{11} at the coupler exit and in the LSM_{11} mode are plotted figures 85c and 85d respectively. The cut-off frequency in the TM_{11} mode at the exit of the coupler is 0.27 THz which leads to a loss of approximately 19 % of the energy at the coupler exit. The measured time profile at the coupler entrance is shown alongside the time profile of the pulse after propagation through the 44 mm long coupler in figure 86, including cutoff losses. The strong dispersion of the TM_{11} mode in the coupler leads to a pulse with significant chirp and a smaller bandwidth at the beginning of the DLW.

Including clipping losses at the coupler entrance, the coupling losses and the cutoff losses, approximately 120 nJ of energy is coupled into the LSM_{11} mode from the initial 525 nJ pulse energy, which is approximately 23 %. With the coupled time profile in figure 86 and the LSM_{11} mode spatial profile, equation 217 gives the peak longitudinal field on-axis when there is 120 nJ in the accelerating mode, which is 0.89 MV/m.

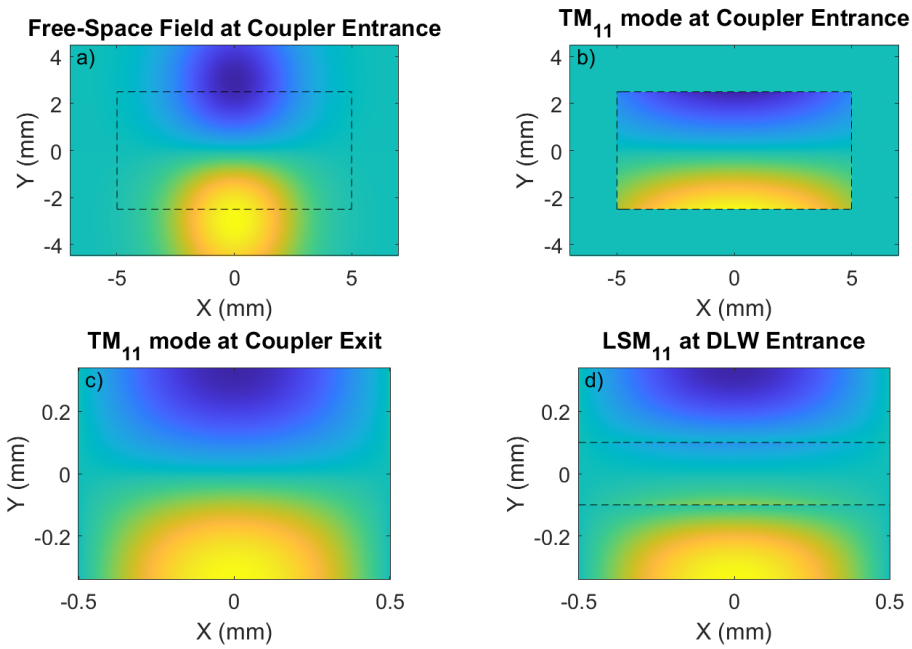

Figure 85: **a)** The assumed free-space E_y field profile at the coupler entrance. **b)** The E_y field profile in the TM_{11} mode at the coupler entrance at 0.47 THz. **c)-d)** The field profile at the coupler exit and in the LSM_{11} mode, respectively, at 0.47 THz. Free-space apertures are defined by black dotted lines.

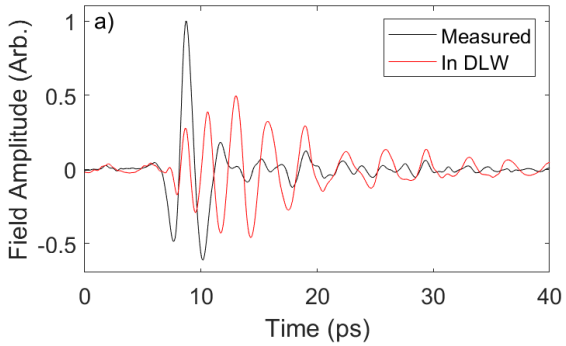

Figure 86: The measured transverse field time profile against the simulated time profile of the longitudinal field coupled into the waveguide accelerating mode, given the coupler dispersion and cutoff frequency.

5.3.7 Phase-matched Electron Beam Acceleration

The simulation of the acceleration interaction was performed using the same method as in section 4.1.3 for the acceleration of the CLARA electron beam. The initial spectrum, $\widetilde{E_z}(\omega, z_0)$, is the Fourier transform of the simulated time profile of the coupled field into LSM_{11} mode, as shown in figure 86. The propagated

spectrum at a distance, z, within the 5 mm long waveguide is given by

$$\widetilde{\mathrm{E}}_{\mathrm{z}}(\omega, \mathrm{z}) = \widetilde{\mathrm{E}}_{\mathrm{z}}(\omega, \mathrm{z}_0)\, \mathrm{e}^{\mathrm{i}\,(\beta_{11} - \mathrm{k}/\beta_{\mathrm{e}})\,\mathrm{z}}\,. \tag{221}$$

The inverse Fourier transform of equation 221 gives the longitudinal field as a function of time and z position. Tracking the field at a single time, $\mathrm{t_e}$ in this delayed frame gives the field experienced by a particle at that injection time. Integrating the field $\mathrm{E_z}(\mathrm{t_e}, \mathrm{z})$ with respect to z gives the energy gain, W, in electron volts at that electron injection time.

The peak field amplitude in the simulation was set to 0.89 MV/m to reflect the experimentally achievable field and the coupled longitudinal field time profile in figure 86 was used. A 5 mm long waveguide was simulated in MATLAB and the energy gain as a function of time is shown in figure 87a. The maximum electron energy gain is approximately 3.1 keV for the input THz pulse energy of 525 nJ. The FWHM interaction length is 3.2 mm, over which electrons at the injection time at which maximum energy gain occurs experience an average accelerating field of 0.76 MV/m. Since a smaller injection time in figure 87a is earlier in time, a positive slope is capable of imparting a negative chirp on an ultrashort electron bunch, which is required for velocity bunching. The maximum chirp simulated in this setup is 5.1 keV/ps.

The proposed design for concurrent bunching and streaking leaves a 0.6 m drift between the stages. From equation 122 (page 51), a space charge free estimate of the required chirp to achieve a minimum bunch length at 0.6 m is 130 eV/ps. A field strength approximately a factor of ≈ 40 lower than the predicted achievable gradient is required for this, which corresponds to a pulse energy that is a factor of 1600 lower than the 525 nJ available. Figure 87b shows the drift length at which compression is achieved as a function of THz pulse energy at the coupler entrance. An energy of 0.34 nJ is seen to be sufficient for a 0.6 m compression length. Having the chirp to achieve compression over a shorter drift length leads to a shorter electron bunch duration at the longitudinal focus. This is because, with an electron bunch with finite slice energy spread, a larger chirp leads to a larger energy difference compared to the slice energy spread so the slice energy spread limited minimum electron bunch duration will be smaller. Given the available THz energy for the interaction and the simulation results, it would be beneficial to shorten the proposed drift length between the stages. Required space for the second interaction imposes a minimum, practically achievable drift space between stages on the order of 0.2 m.

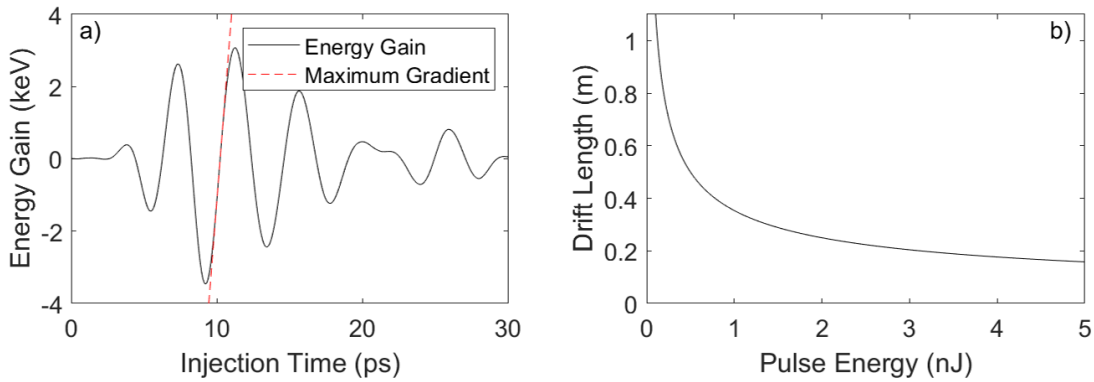

Figure 87: **a)** The simulated electron energy gain as a function of electron injection time. The point at which the largest gradient is observed is labelled. **b)** The drift length required for electron bunch compression with pulse energy assuming a short electron bunch is centred at the point at which the largest energy change gradient is observed.

The effect of spatial asymmetry in the input pulse transverse profile, as may be generated by the phase shifter, was explored by calculating the coupling efficiency into the coupler with a TEM_{01} transverse profile, where one vertical half was multiplied by 2. Figures 88a and 88b depict the coupling factor, A, into the TM_{11} modes at the coupler entrance for a symmetrical input profile and the asymmetrical one respectively. Here the coupling factor is normalised to unity in both plots and the mode definitions are normalised such that they each contain the same energy in the cross-section. The energy coupled into the TM_{11} mode is 86 % of the input for the asymmetrical profile rather than 95 % for the symmetrical one. The main discrepancy in the coupling appears to be the coupling into the TM_{12} mode. The cutoff frequency for this mode at the exit of the coupler is 0.47 THz which would clip a significant portion of the pulse coupled to this mode at the coupler entrance. It could nevertheless be detrimental to the accelerator performance if coupled into the deflecting mode. The average energy coupling efficiency over the frequency range of 0.47 THz to 1 THz between the TM_{12} mode at the coupler exit and the LSM_{10} is $\approx 2\,\%$. Combined with the $\approx 2\,\%$ of the energy incident on the coupler to the TM_{12} mode, $< 0.04\,\%$ of the input pulse is coupled to the deflecting mode in the DLW in this extreme case. Hence, the effect of a spatially asymmetrical input field should be negligible to the accelerator performance.

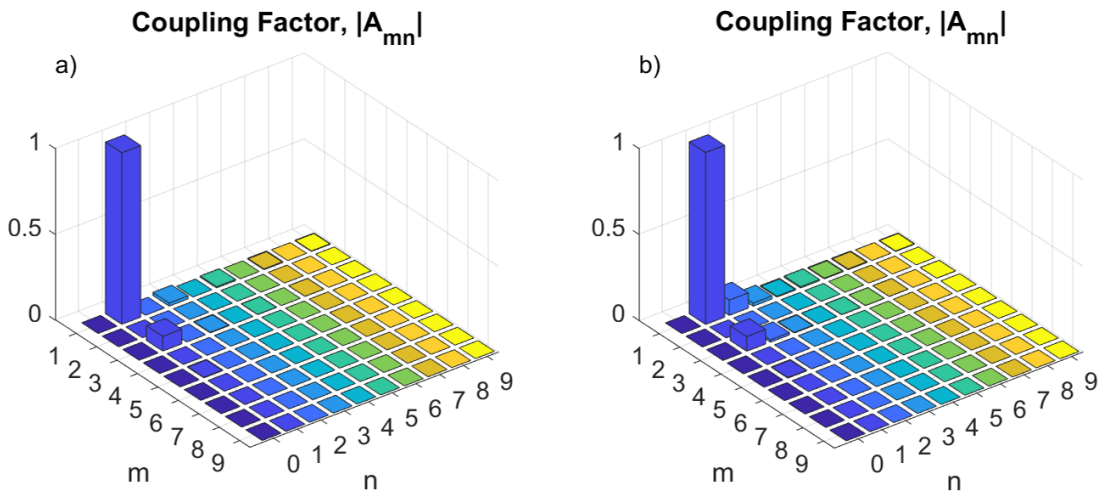

Figure 88: **a)** The magnitude of the normalised coupling factor into different TM coupler modes for a TEM_{01} mode pulse input profile. **b)** The magnitude of the normalised coupling factor into different TM_{11} coupler modes for the same TEM_{01} mode pulse input profile but with one half of the pulse in the vertical direction multiplied by 2.

5.4 Electron Interaction with a THz-Driven Sub-Wavelength Dimension Metallic Slit

A sub-wavelength slit in a thin metal foil can mediate an interaction between an electro-magnetic field and an electron to allow energy transfer. Electrons pass through the aperture undisturbed while the free-space laser propagation is perturbed by the slit. Significant perturbation of the electromagnetic field can be achieved with an aperture that is sub-wavelength in height. With a pulse in the THz frequency range, the spatial scale of such a structure can be large enough for significant charge throughput. A rectangular slit structure such as the one depicted in figure 89 is considered here. Slit structures have been used for THz-driven beam manipulation in [71, 80, 140]. The slit geometry dictates the mechanism by which the structure allows energy transfer between the THz and the electron beam. Enhancement of the field within the slit can lead to an effective confinement of the interaction to within the slit dimensions. Field enhancement can occur due to a waveguide cutoff resonance where the transverse dimension of the slit perpendicular to the laser polarisation is equal to half the incident radiation wavelength and the height is much less than the width [79, 143]. The waveguide cutoff resonance, exploited by [71, 80], is most effective with a narrow-bandwidth input THz source and leads to a field which falls to zero at the horizontal edges of the aperture - limiting the spatial region over which an electron bunch will see an approximately

uniform field. Field enhancement can also be seen in a metallic slit with a small size in the direction of the laser polarisation due to charge build up at the edge of the aperture [144]. Enhancement factors on the order of 10^3 have been reported using this mechanism [145] with nm-scale aperture sizes but transmission of significant electron beam charge would not be possible in such structures.

The metallic slit used here resembles the one reported in [140], where the height is less than the THz wavelength but the width is much larger. The energy transfer is not facilitated by field enhancement, but by breaking the symmetry between the electric and magnetic field within the slit dimensions. The mechanism described is non-resonant and allows a more uniform field over the electron beam dimensions than a structure optimised for waveguide cutoff enhancement. The aperture can also be 10s-100s μm in height to allow transmission of electron bunches with significant transverse size.

Slit structures such as this have a number of advantages over waveguides. Firstly, non-resonant slit structures do not have to be designed for a particular frequency as they do not rely on phase matching. They are much easier to manufacture and can be bought as stock components from a number of suppliers. They are shorter, hence easier to align to the electron beam, and do not contain dielectric material, which means charging up of the dielectric is not an issue.

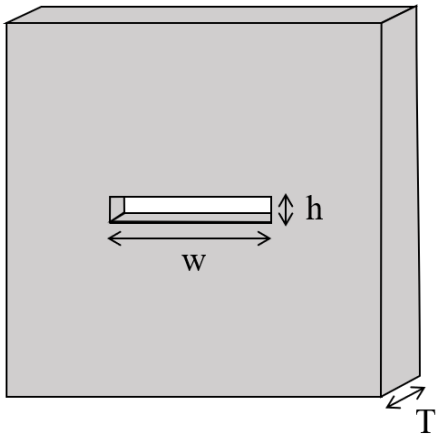

Figure 89: Geometry of a rectangular slit in a metal foil considered in this section.

This section will first simulate the deflection interaction and then describe the experimental results achieved with a slit of height, h = 200 μm. Simulation results will then be presented for acceleration of the 100 keV electron in the context of

achieving electron bunch compression.

5.4.1 Electron Beam Deflection in a Metallic Slit

At sub-relativistic electron velocities, the deflecting force from the free-space transverse electric field is larger than the force from the magnetic field. A net deflection though will not be achieved if the electron is allowed to pass through positive and negative phases of the deflecting field. The mechanism by which an electron beam can be efficiently deflected by THz radiation in the vicinity of a sub-wavelength is dependent on the slit geometry. The slits considered here are rectangular, as in figure 89, where the width is equal to 3 mm and the thickness is 130 μm. Apertures with heights of 50 μm, 100 μm and 200 μm were available experimentally made from stainless steel foil.

2D FDTD was implemented in MATLAB to explore the mechanism by which a slit with the dimensions discussed above allowed THz-electron energy transfer. In the FDTD model, a single-cycle pulse was initiated with a spectrum similar to the experimental source on a simulation grid of size 12 mm by 8 mm. The THz pulse was initialised 6.5 mm from the position of the slit centre where it reached a minimum free-space waist size of 4 mm $1/e^2$ intensity diameter. The simulated spot size was smaller than the measure spot with height of 8.4 mm and a width of 5.5 mm in order to limit the simulation box size, hence simulation time. The spatial step size was 5 μm and the temporal step size was $\simeq$ 12 fs. The slit material was implemented as a region of thickness 130 μm with very high electrical conductivity. As this calculation was performed in 2D, the slit width was essentially assumed to be infinite. This can be justified where the electron beam is significantly smaller than the aperture width and the THz transverse size in that dimension. However, the 2D approximation does exclude examination of effects arising from the waveguide cutoff resonance discussed earlier. The width of the slit though was not chosen to be in a regime in which the cutoff resonance should appear. Effects due to charge collection at the slit boundaries are accessible via this model. Figure 90 shows the initial transverse and longitudinal electric field simulated on the grid. The maximum electric field of the pulse envelope at the free-space focal position was equal to the experimental peak field estimate of 2.3 MV/m, found from the measured pulse energy and the time profile.

The electrons initially had $\beta_z = 0.55$ with no transverse velocity and were propagated on the grid using a 4th order Runge-Kutta solver. Space charge effects were

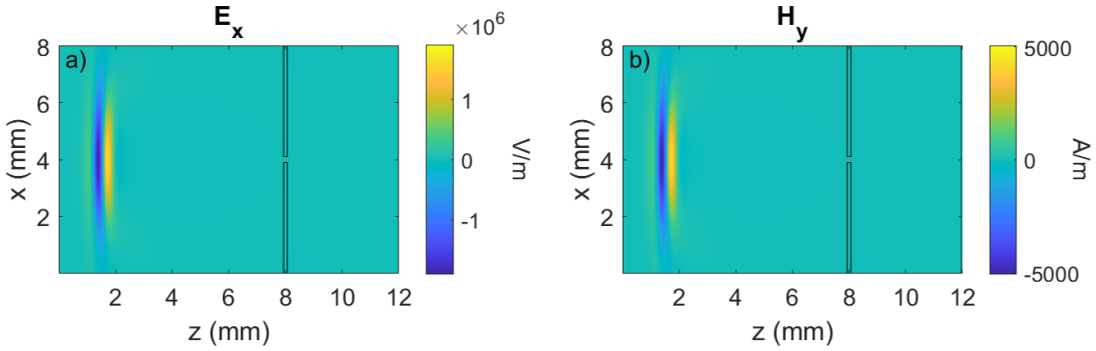

Figure 90: The initial transverse electric field, **a)**, and the initial transverse magnetic field, **b)**, for 2D FDTD calculations.

not considered. The initial electron bunch was aligned with the centre of the THz pulse and the slit in the x direction and had no transverse extent. Injection time was scanned by considering electrons with different initial positions in the laser propagation direction. Since the THz pulse was initialised 6.5 mm away from the slit, there was a region of approximately 6 mm before the slit in which electrons could begin the simulation without being injected into significant laser field at t = 0. A distance of 6 mm when travelling with $\beta_z = 0.55$c corresponds to an injection time window of approximately 36 ps.

At the injection time at which the maximum deflection was observed with a slit in place, figures 91a-91c show the electric field and $v_z \times B_y$ without the slit, with a 50 μm slit height and a 200 μm slit height respectively. The slit introduces a phase shift between the electric and magnetic field such that the peak magnetic field is at the slit entrance and the peak electric field is at the slit exit. This is due to reflection at the entrance and at the exit of the foil. At the entrance interface, the pulse is propagating from free-space to a medium with larger impedance so the reflected electric field undergoes a π phase shift. At the exit, the reflected magnetic field undergoes a π phase shift and the reflected electric field is in phase with the electric field propagating forward, so there is an effective enhancement. The enhancement is more pronounced for the 50 μm slit height compared to the 200 μm slit height since the impedance in the slit is greater, hence the reflection coefficient is larger. The increased reflection at the exit surface of the slit is also beneficial for suppression of the interaction after the slit which is π out of phase. From the integrated forces plotted in figures 91d-91f, the electric field at the slit exit is the driver for net deflection of electrons. A slit of height 50 μm provides this deflection approximately a factor of 2 more efficiently than the slit of height

200 μm. The simulated results can be explained without consideration of the field enhancement due to charge build up at the slit. The peak electric field in the slit is less than twice the peak field in free-space, so could feasibly be solely caused by the reflection at the exit surface of the slit.

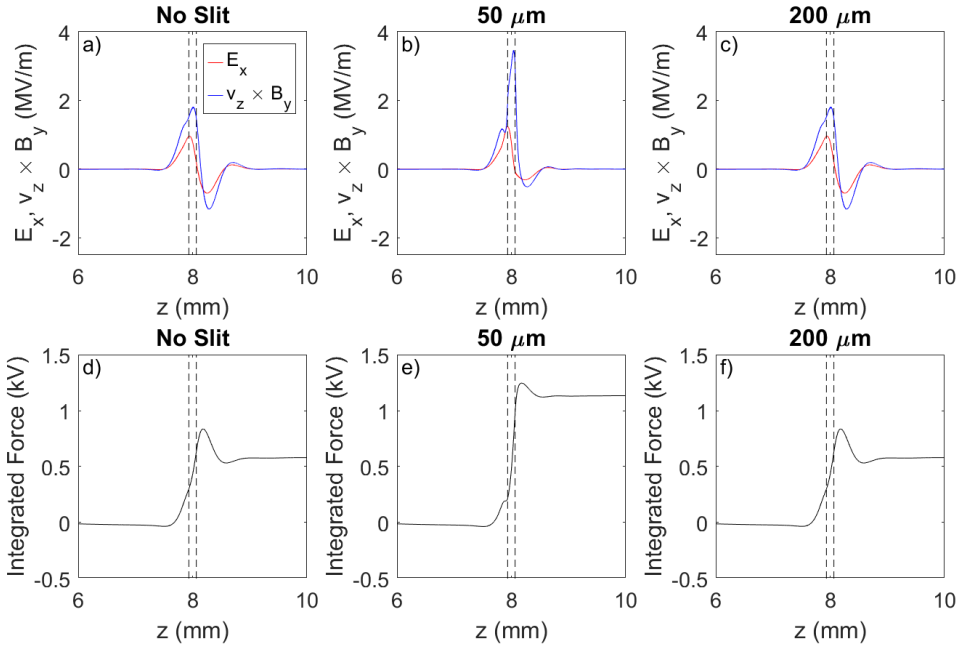

Figure 91: **a)-c)** Considering a single particle at the injection time where the maximum deflection is seen, E_x and v_z multiplied by B_y are shown without the slit, with a 50 μm slit height and with a 200 μm slit height. **d)-f)** The integrated force on the electron in the x direction due to electric and magnetic fields is plotted without the slit, with a 50 μm slit height and with a 200 μm slit height. The slit's front and back surface are denoted by dashed lines.

Experimental deflection data were taken to validate these simulations. The slit height used was 200 μm as that gave an electron aperture the same height as the waveguide for fair comparison of structures. The apparatus was setup as described in section 5.3.4, with the slit at the interaction point in figure 62 instead of the waveguide. The camera imaging the MCP was chosen to have smaller field of view than in the previous section since the expected deflection was lower. Figures 92a and 92b show the beam without and with the THz interaction respectively, where the injection time was chosen such that the electron bunch experienced the largest gradient in deflection with respect to injection time. The electron beam was once again focused at the structure, but it was not vertically clipped significantly as it

was in the waveguide case. The clipping on the waveguide was likely due to the length of the DLW making it more difficult to align. The beam size on the MCP is also much smaller in the absence of charged dielectric lining the electron aperture, as in the waveguide case. A time delay scan was taken by moving the THz delay stage in increments of 10 μm, which corresponded to a time delay of 67 fs. Again, at each stage position, 4 images were averaged, each with an exposure time of 0.8 s and the laser rep rate was 1 kHz. The averaged image at each time delay was projected along the horizontal direction to give the vertical profile for the deflectogram measurements. A deflectogram with the maximum available THz pulse energy is shown in figure 93. Simulation of the deflection interaction was performed in FDTD, as above, and the electron position on the MCP screen was inferred from the final velocities in the laser direction and the deflection axis by equation 220, with a 0.8 m drift length to the MCP. The simulated deflection from FDTD simulations is overlaid on the experimental data, where the THz carrier-envelope phase was chosen to best fit the experimental deflection. The FDTD model with electrons on-axis, denoted by the solid line, appears to underestimate the interaction. Field enhancement at the vertical boundaries of the slit could explain the discrepancy between FDTD and the experiment. Although charge collection at the slit edge due to the THz-induced surface current does not lead to significant enhancement of the field at the centre of the slit, the field close to the aperture edge is increased compared to on-axis. The FDTD simulation was repeated with electrons at an initial vertical position of 90 μm from the central axis to see how the edge field increased the deflection. The off-axis simulation, denoted by a dashed red line in figure 93, shows that larger deflection is observed when the electron beam travels close the slit vertical boundary. In reality, the transverse size of the experimental electron means that the bunch samples field from the entire vertical extent of the slit, so the experimental deflection is a combination of these two modelled regimes.

Both model and experiment exhibit a deflection period of ~ 3.2 ps. The deflection period is defined by the velocity mismatch between the electron bunch and the free-space THz propagation and the THz period. The period of the deflection is approximately equal to the THz period multiplied by the 1 - β_e.

The FDTD simulation had a peak electric field of 2.3 MV/m, given by the estimation from the THz transverse profile, the time profile and the pulse energy. The measured peak field strength from a calibrated EO measurement was 80 kV/m. A discrepancy between the EO measured field and the estimated field from the pulse energy is often observed. Here, with the electron beam deflection, we have a

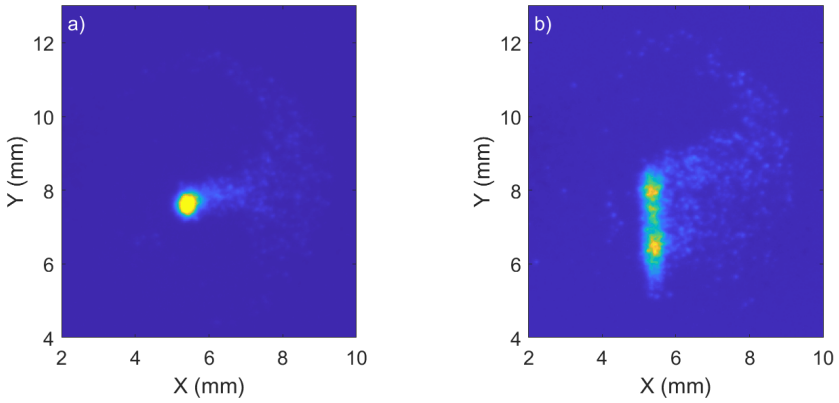

Figure 92: The measured electron beam transverse profile on the MCP without THz, **a)**, and with a THz-driven interaction, **b)**.

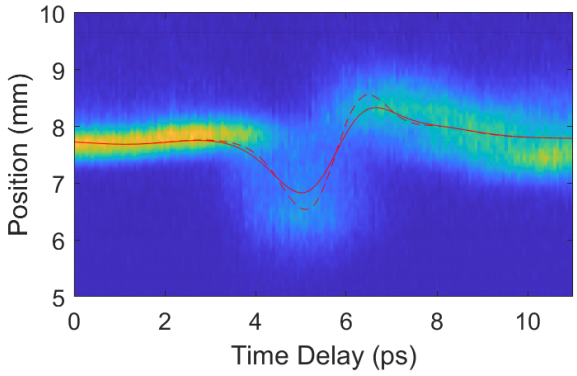

Figure 93: The vertical electron beam profile is plotted as a function electron-THz time delay. The solid line denotes the on-axis FDTD simulation, whereas the dashed line is the result of an FDTD simulation where electrons are initialised 90 μm from the central axis.

third, independent method of measuring the THz electric field strength. As seen in figure 93, this measure of the electric field strength corroborates the electric field estimation from the pulse energy.

The streaking speed was calculated from the modelled deflection to assess the temporal resolution of this system and compare the structure's effectiveness compared to the waveguide. A maximum value from the on-axis model of 1.6 μm/fs or 2 μrad/fs was calculated given a 0.8 m drift length to the MCP. The off-axis model gave a streaking speed of 2.5 μm/fs, or 3.1 μrad/fs. The DLW gave a streaking speed that was 8 times greater than the off-axis slit model and with only 43 % percentage of the THz pulse energy. Although tighter focusing at the slit interaction point would lessen this gap in structure efficiency, the waveguide has the

fundamental advantage of having a few millimetre long interaction, rather than a few hundred micron one.

A bunch duration measurement was difficult to achieve with the electron beam settings in the above plots in the same way as it was in section 5.3.4 with the waveguide deflection. It can be seen in the deflected electron bunch shown in figure 92b that two peaks are visible, suggesting the bunch duration was greater than half of the deflection period. The greater visibility on the MCP of the electron bunch through the slit compared to the waveguide allowed exploration of a lower charge electron beam, hence smaller bunch duration. The UV light onto the photocathode was attenuated by roughly a factor of 3. The electron bunch at this setting is shown in figure 94 without deflection and with deflection, where the injection time was chosen such that it gave the maximum increase in electron beam vertical size. The vertical profile of the deflected beam here does not appear to show significant interaction between regions of the bunch with the maximum and minimum of the sinusoidal field, so a bunch duration estimate could be made.

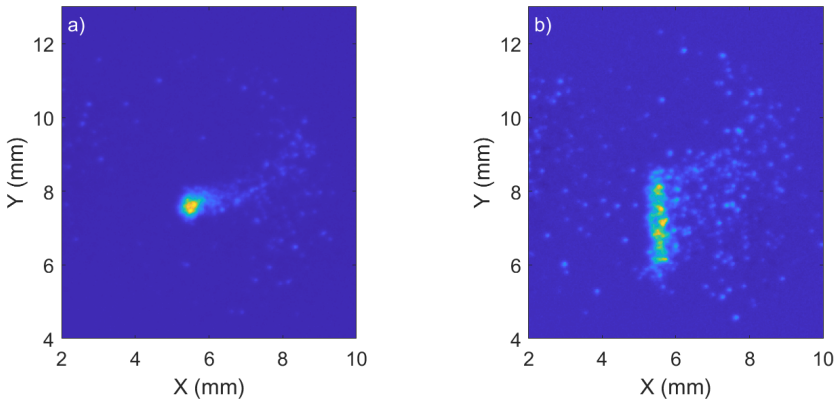

Figure 94: The measured electron beam transverse profile on the MCP without THz, **a)**, and with a THz-driven interaction, **b)**, with reduced electron beam charge.

The electron bunch length was estimated with the two measured streaking speeds, $\alpha = 1.6\,\mu$m/fs and $\alpha = 2.5\,\mu$m/fs, and assuming that the streak had a linear gradient along the bunch duration. The streak was applied to an electron bunch which was Gaussian in time and in vertical position. The signal measured on the screen, S(y), was assumed to be given by

$$S(y) = A \int_{-\infty}^{\infty} \exp\left(-\left(\frac{t - t_0}{\sigma_t}\right)^2\right) \exp\left(-\left(\frac{y - y_s(t)}{\sigma_y}\right)^2\right) dt \,, \qquad (222)$$

where A is a constant amplitude factor and the change in y position due to the deflection is $y_s(t) = y_0 + \alpha(t - t_0)$. The signal, S(y), will be a Gaussian distribution in y since the time profile and vertical position are both Gaussian. The projection of the images in figure 94 along the vertical axis is shown in figure 95. A Gaussian fit was performed on the unstreaked profile to find a value for the initial beam width σ_y. A least squares fit was then performed to calculate the parameters t_0, A and σ_t required to emulate the measured streaked profile. The fitted streaked profile from equation 222 is plotted as a dotted red line in figure 95. The FWHM bunch duration is 1.8 ps for the α calculated from the on-axis model, and 1.2 ps for the α calculated from the off-axis model. Although a bunch duration between 1.2 ps and 1.8 ps would lead to regions of the bunch outside the linear region of the THz field, the quality of the Gaussian fit to the streaked beam suggests that the linear field assumption gives a good approximation to the experimental data.

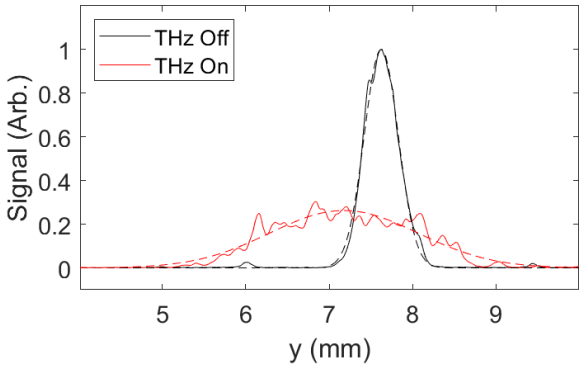

Figure 95: The vertical electron beam profile with and without THz streaking. The solid lines represent measured data, the black dashed line is a Gaussian fit and the red dashed line is a result of a fit using equation 222.

5.4.2 Electron Beam Acceleration using a Metallic Slit

Acceleration at the surface of a sub-wavelength slit has been explored with a co-linearly propagating electron bunch and Gaussian-Hermite TEM_{01} THz pulse. Considering the lowest order rectangular waveguide mode in the slit, the TM_{11} mode, for $w \gg h$, the cutoff frequency of this mode is given by $f_c \simeq \frac{c}{2h}$. Given the peak frequency in the measured THz pulse spectrum, $f_0 = 0.3$ THz, a slit of height $< 500\,\mu$m, will not allow transmission of the THz radiation. To confirm this applied to our structure, a 2D FDTD simulation was performed in MATLAB.

A single cycle, TEM_{01} Gaussian-Hermite pulse with a waist of 4 mm $1/e^2$ diameter was initiated with a spectrum similar to the experimental source on a grid of size 5 mm by 12 mm. The spatial step size was 10 μm and the temporal step size was 24 fs. The slit material was implemented as region of high conductivity, as in the previous section, and had an aperture height of 50 μm. Figure 96 shows a number of snapshots of the longitudinal electric field, where in figure 96a the pulse is propagating in the z direction. In figures 96b and 96c the field is at the slit interface but no longitudinal electric field enters the slit. Figure 96d shows the back propagating pulse. Given the reflection witnessed here, the mechanisms discussed for the transverse field interaction which allow energy transfer are not relevant for acceleration. However, energy transfer between a THz frequency accelerating field and a particle bunch can occur at the entrance surface of a sub-wavelength slit as the interaction is effectively truncated by the reflection.

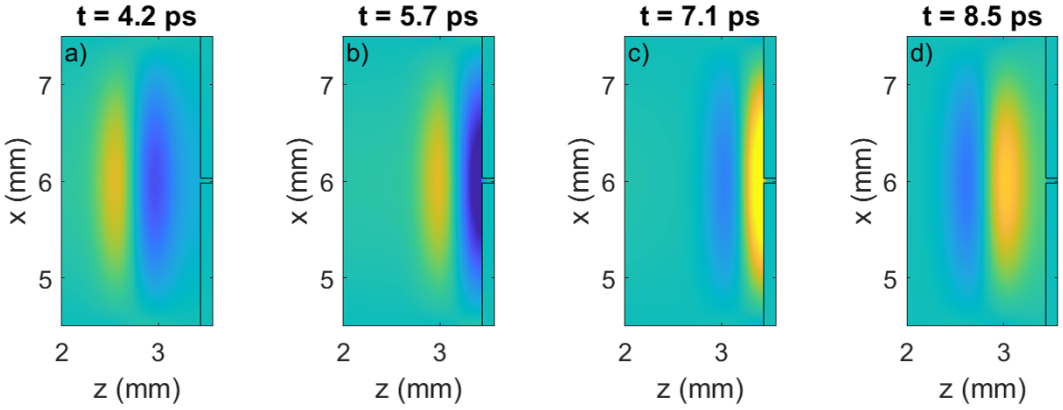

Figure 96: FDTD simulation of the longitudinal electric field of a TEM_{01} Gaussian pulse incident on a metallic slit of height 50 μm as a function of time. The incident field does not propagate into the slit and is entirely reflected.

Interaction between a THz pulse and an electron at the entrance surface to an aperture in a metallic foil was simulated to verify that the reflection could facilitate electron energy gain. A single cycle, TEM_{01} Gaussian-Hermite pulse was again initiated with a spectrum similar to the experimental source on a grid of size 10 mm by 12 mm. The spatial step size was 5 μm and the temporal step size was 12 fs. The maximum longitudinal electric field of the pulse envelope at the focus was 1 MV/m for this calculation. Figure 97 plots the initial transverse and longitudinal electric field on the grid. The field experienced by an on-axis electron was calculated by tracking the field at a point $z = z_0 + v_e t$, where at $v_e = 0.55c$.

Space charge effects were not considered and electron injection time was varied by changing the initial position of the particle at the beginning of the simulation.

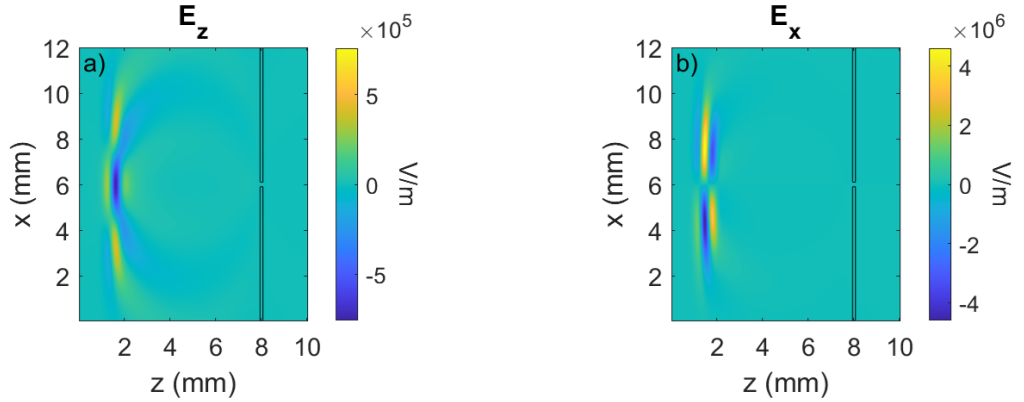

Figure 97: The initial longitudinal electric field, **a)**, and the initial transverse electric field, **b)**, for 2D FDTD calculations.

Figures 98a, 98b and 98c show the electron energy gain as a function of z with no slit, a slit of aperture height 50 μm and a slit of aperture height 400 μm, respectively. The injection time in these plots was chosen such that the maximum energy gain occurred with the slit in place. In a free-space interaction without the slit structure, electrons gain energy as they interaction with the positive THz phase and then lose it through interaction with the negative phase. Some net energy change can be seen as the THz phase velocity changes throughout the interaction since the pulse is focusing and then defocusing. The 50 μm slit effectively truncates the interaction at the slit entrance so no further electron energy is gained or lost afterwards. The 400 μm slit still truncates the interaction enough to facilitate energy transfer, but not as sharply as the smaller slit height so further interaction occurs after the slit entrance. The interaction after the slit entrance is detrimental to the electron acceleration.

Assuming the THz pulse is entirely reflected by the slit surface, a simple analytical model for this interaction can be derived assuming a plane wave that is entirely reflected by a slit placed at $z = 0$. The accelerating field can be written as

$$E_z = \begin{cases} E_0\ [\cos(\omega t - k z + \phi_0) + \cos(\omega t + k z + \phi_0)], & \text{for } z < 0\ , \\ 0\ , & \text{for } z > 0\ . \end{cases} \tag{223}$$

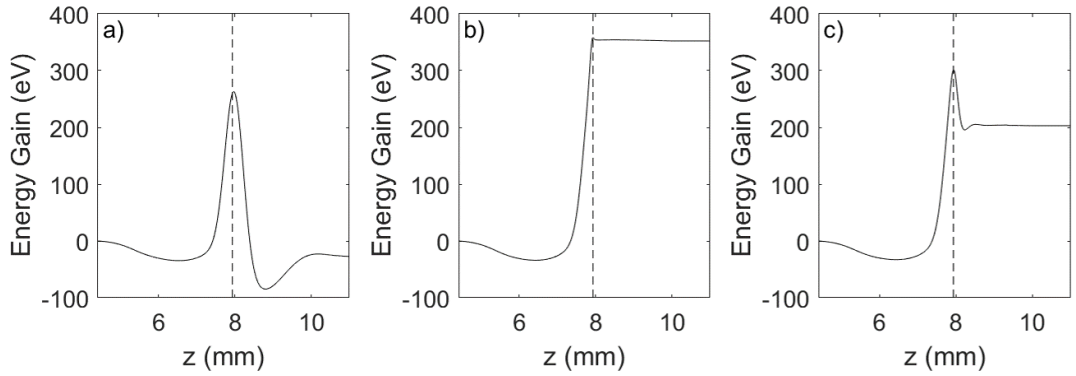

Figure 98: The simulated energy gain as a function of electron position with no slit, **a)**, a 50 μm slit height, **b)**, and a 400 μm slit height, **c)**.

The field at the position of an electron travelling at a velocity of β_ec is given by the field at z = β_ec(t - t_0), where t_0 is the time which the electron reaches the slit surface. The momentum gain can then be calculated by integrating the force exerted by this field with respect to t

$$\Delta p_z = q\,E_0 \int_{-\infty}^{\infty} \cos(\omega\,t - \omega\,\beta_e(t - t_0) + \phi_0) + \cos(\omega\,t + \omega\,\beta_e(t - t_0) + \phi_0)\,dt\ , \tag{224}$$

where it is assumed that ω = kc. The integral can be evaluated with the upper limit of t_0 since after that time the field at the particle position is equal to 0. With the assumption of a slowly varying field envelope, it follows that there is no interaction taking place at t = -∞. The integral then gives

$$\Delta p_z = q\,E_0 \cos(\omega\,t_0 + \phi_0) \left(\frac{1}{\omega\,(1 - \beta_e)} + \frac{1}{\omega\,(1 + \beta_e)} \right)\ , \tag{225}$$

At the injection time at which the maximum momentum gain occurs, the peak energy gain is

$$\Delta W = \frac{q\,E_0\,\beta_e\,c}{\omega} \left(\frac{1}{1 - \beta_e} + \frac{1}{1 + \beta_e} \right)\ . \tag{226}$$

Although this is for a single frequency, it gives an approximate energy gain for the stated interaction geometry.

To quantify how this simple estimate compares to the simulated energy gain for slits of different dimensions, 2D FDTD simulations were performed. The field was initialised in the same way as above but only the final energy gain was outputted for each slit height. Figure 99 shows that, as the slit height decreases, the net energy gain appears to tend towards the estimate given by equation 226, where the

frequency was chosen to be the weighted mean frequency in the longitudinal field spectrum. The discrepancy between equation 226 and the numerical simulation is large for the larger slit heights used, so the assumption of 100 % reflection and 0 % transmission is clearly not suitable.

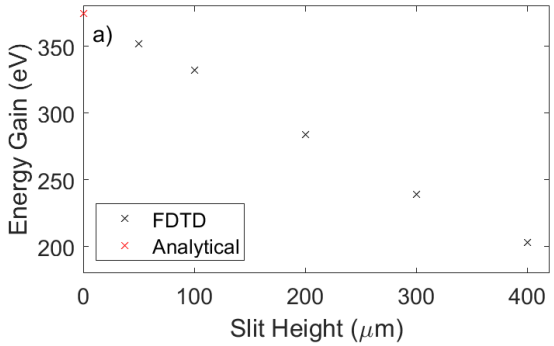

Figure 99: The final energy gain after interaction with slits of different height. The THz pulse's peak field at the focus was kept constant. The calculated energy gain from equation 226 is plotted in red at a slit height of 0.

The peak free-space transverse field for deflection measurements was calculated to be 2.3 MV/m from the pulse energy and time profile. Assuming 100 % conversion efficiency between a fundamental Gaussian pulse and the TEM_{01} Gaussian pulse, the peak longitudinal field achievable with the experimental pulse is 145 kV/m with the current pulse energy and waist size. With this peak field, the simulated energy gain as a function of injection time is plotted for a 50 μm slit height in figure 100a, where the same single cycle pulse input was used as in figure 97. The largest gradient which would lead to a negative bunch chirp is marked in red. The time between the peak energy gain and when the energy gain drops to zero is $\sim$ 2 ps, which is the region of an electron bunch which would be compressed. The maximum simulated energy gain is proportional to the peak longitudinal field, and the longitudinal field scales with the square root of the pulse energy. Given this, the drift length required for compression after the interaction (equation 122) as a function of energy is plotted in 100b. The solid lines depict the required drift length in the current setup. Due to the large THz focal spot, the conversion between transverse field and longitudinal field is poor. This is reflected in the small chirp imparted onto the bunch, and hence long drift length required to compress the bunch for both slits. The length of the interaction chamber places the constraint on the compression that it needs to be $\lesssim$ 1 m, which can not be achieved with the current setup. Replacing the final, f = 100 mm OAP with a f = 50 mm OAP would

half the spot size and give a longitudinal field that is 4 times greater, since $E_z \propto w_0^2$. The corresponding affect this would have on the compression length scaling is shown as dotted lines in figure 100b. A pulse energy >100 nJ would lead to a compression drift length <1 m for the 50 μm slit and an energy >200 nJ is required for the same result using the 200 μm slit. Even with the smaller focal spot, the energy efficiency of this structure is significantly lower than the waveguide due to the sub-millimetre interaction length and the diffraction-limited free-space focusing which imposes a limit on the peak achievable longitudinal field.

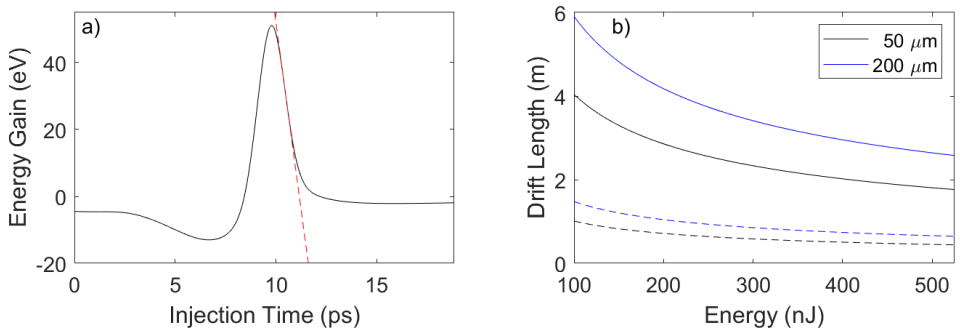

Figure 100: **a)** Electron energy gain as a function of injection time from an FDTD simulation. **b)** Drift length required for compression after interaction against THz energy for two different slit heights. Solid lines depict the current setup, dashed lines depict the drift length if the final, f = 100 mm OAP is replaced by an f = 50 mm OAP.

5.5 Discussion

Work has begun on commissioning a setup for THz-driven compression and deflection of a sub-relativistic electron beam. Initial measurements for deflection of an uncompressed bunch have been performed and design work towards the bunching interaction has been presented here.

An energy spectrometer has been designed and manufactured for high resolution electron energy measurements. This will be helpful when attempting to diagnose the electron bunch chirp after the velocity bunch interaction. The minimum energy resolution of the setup is approximately 16 eV, which was estimated from particle tracking simulations. This spectrometer is yet to be tested experimentally.

The physics of the THz-electron deflection interaction have been considered in a DLW and in a sub-wavelength slit in a metal foil. Coupling simulations using the experimentally measured THz spectra and transverse field profile predicted a peak field inside the waveguide of 2.2 MV/m, with approximately 18 % of the free-space THz pulse energy coupling to the deflecting mode. The period of the deflection was predicted to be the THz period multiplied by the electron velocity, which was approximately 4 ps. The deflection interaction in a sub-wavelength slit was modelled in 2D FDTD, with a maximum free-space peak field of 2.3 MV/m. The period of the deflection here predicted to be approximately 3.2 ps, which was related to the velocity mismatch between the THz phase and the electrons. The phase-matched interaction in the waveguide allows a significantly larger deflection for a given input THz pulse energy.

Deflection of the 100 keV beam has been performed experimentally using a dielectric waveguide and a small slit in a metal foil. The electron bunch duration used with the DLW was too large to decipher through streaking measurements, but the duration of a lower charge bunch was estimated using the slit interaction. Lower and upper bounds were calculated to be 1.2 ps and 1.8 ps from simulated upper and lower bounds on the streaking speed.

The efficiency of the interaction structures has been quantified by measuring the streaking speed. The waveguide interaction produced a streaking speed approximately 8 times larger than the largest calculated with the slit, with only 43 % of the THz pulse energy. The 26 μrad/fs streaking speed achieved with the DLW is larger than in all but one reported demonstration of THz streaking to the author's knowledge. In [66], a streaking speed of $>$140 μrad/fs was achieved. This device required two separate THz pulses, each with an energy of 6 μJ, whereas in the results presented here, a single THz pulse with a modest energy of 225 nJ was used. The streaking speed scales linearly with the peak field, hence square root of the energy. Taking this into account, our structure was $\sim$ 30 % more energy efficient for electron beam streaking. It is also worth noting that the electron beam energy was lower in the cited result, at 55 keV, so a smaller transverse velocity gain was required to give the same angle of deflection.

The experimentally measured deflectograms for the two structures are in agreement with simulation results in both peak deflection and in deflection period. For the waveguide, the agreement gives confidence in the coupling calculations performed to infer the field within the waveguide from the field at the coupler entrance. Only 18 % of the free-space THz pulse energy was simulated to couple

to the deflecting mode. These simulations give the framework to predicting how the free-space transverse field at the coupler entrance can be modified to enhance the energy coupling efficiency into the desired waveguide mode. Such calculations will inform future experimentation.

The deflection of the electron beam mediated by the slit structure gave an insight into the THz peak field. The magnitude of the deflection was consistent with a simulated peak field of 2.3 MV/m. An estimate of the peak field given the pulse energy and measured 3D profile corroborated this value, but a direct, electro-optic measurement of the field gave a much lower value of 80 kV/m. This result has given confidence in the estimated field from the pulse energy for future THz experimentation.

Sub-relativistic electron acceleration has been simulated with a waveguide and with a small slit in a metal foil mediating the interaction. The field coupled into the accelerating mode of the DLW was calculated given an assumed TEM_{01} mode Gaussian pulse at the coupler entrance with the waist and spectra of the experimentally measured THz pulse. The simulated peak coupled longitudinal field on-axis was 0.89 MV/m and approximately 23 % of the free-space THz energy coupled to the accelerating mode. The longitudinal field in the mode was propagated in the waveguide with the calculated propagation constant. The interaction in a small aperture in a metal foil was simulated in 2D FDTD with a TEM_{01} mode Gaussian pulse. The aperture was found to reflect the longitudinal field whilst allowing electrons to pass through, which effectively truncates the interaction.

The waveguide provides phase-matched acceleration of the electron beam, with a peak energy gain of 3.1 keV predicted with our current source. A maximum achievable negative chirp would be 5.1 keV/ps, which is significantly more than is required for compression over a drift length in the 10s of centimetre scale. Only a fraction of the experimentally available THz pulse energy is required to achieve compression within the interaction chamber, which is promising for future experimentation where multiple THz interaction stages may need to share this pulse energy. The slit interaction is much less efficient than the waveguide acceleration because of the shorter interaction length and the limited achievable peak field in free space. Due to the large THz focal spot in the current setup, a longitudinal slit interaction would not be able to compress the bunch within the length of the interaction chamber. The quadratic scaling of longitudinal field with spot size means achieving a smaller focal spot would dramatically increase the efficiency of this interaction and would make it a viable option for future velocity bunching

experiments. Using a slit with a smaller height is advantageous as it has a higher reflection coefficient, which leads to a sharper truncation in the THz-electron interaction.

6 Conclusion

The work detailed in this thesis has focused on the efforts in the Cockcroft Institute THz Acceleration Group to manipulate electron beams using THz-driven devices. Acceleration and deflection have been performed in separate experiments by interaction with optically generated THz radiation. Acceleration of fully relativistic 35 MeV electron bunches has been demonstrated in a dielectric-lined waveguide, and the temporal streaking of 100 keV electron bunches has been demonstrated in a dielectric-lined waveguide and in an interaction mediated by a metallic slit.

In chapter 4, acceleration of up to 10 keV was measured on the relativistic CLARA electron beam using a THz-driven dielectric-lined waveguide. These results [1] were the first demonstration of linear THz-driven acceleration of a fully relativistic electron beam. The THz source was a lithium niobate crystal pumped by a beat wave with a tilted pulse front, which allowed generation of tunable, narrow-bandwidth pulses. The waveguide accelerating mode was excited by delaying half of the pulse by half of the THz period in order to match the relevant coupler mode transverse profile. The waveguide design ensured the achievement of phase-matching between the relativistic electron beam and the accelerating field. Phase-matching is important as it allows longer interaction lengths and more efficient electron energy gain. The interaction length is limited by the THz group velocity to electron velocity mismatch and the bandwidth of the THz pulse in a structure such as this. Interaction efficiency with THz pulse bandwidth was calculated to be effectively constant when the pulse energy is kept constant. For this reason, it is advantageous to use narrow-bandwidth THz, as a higher optical pump pulse energy can be used without exceeding the crystal damage threshold when the pump pulse is stretched. Using a higher pump energy allows a higher THz pulse energy to be generated. For the specific waveguide and THz source used here, a full width at half maximum interaction length between 2.8 mm and 3.8 mm was estimated when the THz source was optimised. The average accelerating gradient of $\sim 3\,\mathrm{MeV/m}$ was observed with a 2.1 μJ THz pulse.

Confirmation that phase-matching was achieved in this experiment was inferred from the data where the THz central frequency was varied. This data was taken with a linearly chirped electron bunch of duration on the order of 10 ps. The measured scaling of modulation strength gave good agreement with the modelled interaction efficiency from the calculated waveguide dispersion relation. The peak interaction strength came when the THz central frequency matched the waveguide operating frequency. At frequencies close to the waveguide operating frequency,

the interaction efficiency was dictated by the strength of that frequency component in the THz pulse bandwidth. Far from the waveguide operating frequency, the model underestimated the interaction efficiency if the electron was allowed to experience the field from the whole pulse envelope. This indicated that a truncated, non-phase-matched interaction dominates when the THz pulse bandwidth contained sufficiently small amounts of the phase-matched component. Further evidence of the phase-matched interaction was the observed dependence of the modulation frequency with central frequency of the driving THz pulse. The modulation frequency was independent of driving frequency and set by the structure's phase-matched frequency. When the central drive frequency was offset from the structure frequency by more than the THz source bandwidth, weak THz frequency dependent interaction was observed. At these points, the truncated interaction dominated.

The multi-cycle THz interaction also enabled the diagnosis of the longitudinal phase space of chirped electron bunches with durations spanning multiple periods of the accelerating field. With an approximately linear bunch chirp, and the fixed and known THz modulation frequency, measurements of the energy separation between adjacent peaks in the electron energy spectra determined the local bunch chirp. This method circumvents the need for a dedicated deflecting cavity as in conventional RF diagnostics. Two electron bunch settings were diagnosed. Measurements from this diagnostic were consistent with the understanding of the CLARA beam dynamics in terms of longitudinal phase space.

The most significant improvement required to go from 10 keV energy gain to 1 MeV is in the THz source. Millijoule level THz pulse energy rather the 2.1 μJ measured here can be achieved by optimisation of the generation process and making full use of the 100s mJ pump energy available with the CLARA laser. Further gains can be made in the THz transport to the waveguide. As the experiment discussed here took place before the THz camera (section 3.3.2) was purchased, alignment of the THz radiation was very challenging. The THz camera should allow more precise parabola alignment in the transport and tuning of the transverse profile at the coupler entrance for optimal coupling efficiency. Finally, a 100 mm focal length TPX lens was used as the final THz focusing optic. Around 40 % of the THz energy was lost due to absorption in this optic, so only parabolic mirrors will be used in future beam runs. Very recent work undertaken at the CLARA facility around the time of this thesis completion (not included in this thesis) observed a 0.2 MeV energy gain and an acceleration gradient of 20 MeV/m using the techniques described here.

Chapter 5 describes the experiments in transverse streaking of a 100 keV electron bunch. Approximately fC level charge bunches were generated from a photocathode excited by frequency doubled light from a Titanium:Sapphire laser. Broad-bandwidth THz pulses were generated by tilted-pulse-front pumping of a lithium-niobate crystal using the same laser. A number of different interactions between the electron beam and the THz have been explored.

Deflection of the electron beam was observed using a dielectric-lined waveguide which provided a phase-matched interaction at approximately 0.5 THz. Measured deflection of a ~ 1 fC electron beam as a function of THz to electron time delay matched well with 1D simulations. The streaking speed of 26 μrad/fs achieved with 225 nJ of THz energy compares favourable against the literature. Although the bunch duration could not be characterised accurately in this case, the measured streaking speed suggests a high temporal resolution of our streaking setup.

A metallic slit structure was also used to mediate the deflection interaction, as in [140]. The streaking speed achieved was approximately a factor of 8 lower with this structure compared to the waveguide using a 2.5 times larger pulse energy. The shorter interaction length than the one available with the waveguide was compounded by the large THz focal spot, which meant the THz pulse energy was not efficiently used. The bunch duration of an electron bunch at a low charge was diagnosed with the slit streaking interaction. Upper and lower bounds for the measured streaking speed place an estimate on the FWHM electron duration between 1.2 ps and 1.8 ps. This interaction also gave vindication of the peak field measurement. Before streaking was performed with the slit, an EO field measurement was performed and a separate field calibration was done using the EO profile and the measured pulse energy. These estimations gave wildly different results for the peak field. When the slit interaction was simulated in 2D FDTD, the field estimate from the pulse energy gave a much better agreement to experimental results.

Both slit and waveguide structures have been simulated for an acceleration interaction - using a thin piece of plastic to convert the fundamental Gaussian laser mode to a quasi-TEM_{01} mode. The slit structure works by truncating the electron-THz interaction at a point where net energy transfer has been achieved. It requires a significantly smaller focal spot compared to the one currently used experimentally to achieve a longitudinal focus of the 100 keV electron beam within the interaction chamber, which is required in order to diagnose or use the compressed bunch. The dielectric-lined waveguide interaction on the otherhand only requires a small fraction of the available pulse energy in order to compress the bunch within the

chamber length. A maximum modelled energy gain with the THz source used for deflection was 3.1 keV.

The next stage in this experimental regime is confirmation of a compression interaction with both the energy spectrometer and with a THz-driven bunch duration measurement. A high resolution energy measurement diagnostic has been designed and manufactured for confirmation of the applied bunch energy chirp required for bunch compression. Particle tracking simulations suggest that this spectrometer will give a minimum energy resolution of approximately 16 eV. The spectrometer could not be commissioned before submission of this thesis due to facility operation schedules. Once an ultra-short electron bunch is measured at the second THz-driven interaction, the deflection stage will be replaced by an acceleration stage which will accelerate the electron bunch to MeV energies so it can retain its duration over a distance. An all-optical, MeV-level electron gun capable of producing few femtosecond, fC charge bunches would be an incredible step forward in electron bunch injector and ultra-fast electron diffraction technology.

7 Appendix

7.1 6D Magnet Transfer Matrices

The 6D transfer matrix to find a particle's 6D phase space with an initial Lorentz factor, γ, after a drift length, L, is given by

$$\mathrm{R}_{\mathrm{drift}} = \begin{pmatrix} 1 & \mathrm{L} & 0 & 0 & 0 & 0 \\ 0 & 1 & 0 & 0 & 0 & 0 \\ 0 & 0 & 1 & \mathrm{L} & 0 & 0 \\ 0 & 0 & 0 & 1 & 0 & 0 \\ 0 & 0 & 0 & 0 & 1 & \mathrm{L}/\gamma^2 \\ 0 & 0 & 0 & 0 & 0 & 1 \end{pmatrix} . \tag{227}$$

For a magnet with an exit face which is not normal to the exiting particle beam trajectory, the evolution of x, x' and δ is given by equation 202. The evolution of y, y' are given by a combination of 201 and a drift matrix with L equal to the length of the central trajectory through the magnet. The 6D magnet transfer matrix is

$$\mathrm{R}_{\mathrm{angled}} = \begin{pmatrix} \cos\theta & \rho\sin\theta & 0 & 0 & 0 & \rho\left(1-\cos\theta\right) \\ \frac{1}{\rho}\left(\cos\theta\tan\alpha - \sin\theta\right) & \sin\theta\tan\alpha + \cos\theta & 0 & 0 & 0 & \tan\alpha\left(1-\cos\theta\right) + \sin\theta \\ 0 & 0 & 1 & 0 & 0 & 0 \\ 0 & 0 & -\frac{\tan\alpha}{\rho} & 1 - \frac{\mathrm{L}\tan\alpha}{\rho} & 0 & 0 \\ 0 & 0 & 0 & 0 & 1 & 0 \\ 0 & 0 & 0 & 0 & 0 & 1 \end{pmatrix} . \tag{228}$$

References

[1] Morgan T. Hibberd et al. Acceleration of relativistic beams using laser-generated terahertz pulses. *Nature Photonics* **14,** 12 (2020), pp. 755–759. eprint: 1908.04055.

[2] Oliver Sim Brüning et al. *LHC Design Report*. CERN Yellow Reports: Monographs. Geneva: CERN, 2004.

[3] G. Aad et al. Observation of a new particle in the search for the Standard Model Higgs boson with the ATLAS detector at the LHC. *Physics Letters B* **716,** 1 (2012), pp. 1–29.

[4] S. Chatrchyan et al. Observation of a new boson at a mass of 125 GeV with the CMS experiment at the LHC. *Physics Letters B* **716,** 1 (2012), pp. 30–61.

[5] S. Webb. *The Physics of Medical Imaging*. Medical science series The Physics of medical imaging. CRC Press, 1988.

[6] Olive Emil Wetter. Imaging in airport security: Past, present, future, and the link to forensic and clinical radiology. *Journal of Forensic Radiology and Imaging* **1,** 4 (2013), pp. 152–160.

[7] K. Wells and D.A. Bradley. A review of X-ray explosives detection techniques for checked baggage. *Applied Radiation and Isotopes* **70,** 8 (2012), pp. 1729–1746.

[8] Randolf Hanke, Theobald Fuchs, and Norman Uhlmann. X-ray based methods for non-destructive testing and material characterization. *Nuclear Instruments and Methods in Physics Research Section A: Accelerators, Spectrometers, Detectors and Associated Equipment* **591,** 1 (2008). Radiation Imaging Detectors 2007, pp. 14–18.

[9] Ronald P Haff and Natsuko Toyofuku. X-ray detection of defects and contaminants in the food industry. *Sensing and Instrumentation for Food Quality and Safety* **2,** 4 (2008), pp. 262–273.

[10] A Thompson, I Maskery, and R K Leach. X-ray computed tomography for additive manufacturing: a review. *Measurement Science and Technology* **27,** 7 (2016), p. 072001.

[11] Min Yang, Gao Wang, and Yongzhan Liu. New reconstruction method for x-ray testing of multilayer printed circuit board. *Optical Engineering* **49,** 5 (2010), pp. 1 –6.

[12] The evolution of proton beam therapy: Current and future status (Review). *Mol Clin Oncol* **8,** 1 (2018), pp. 15–21.

[13] W. D. Kilpatrick. Criterion for Vacuum Sparking Designed to Include Both rf and dc. *Review of Scientific Instruments* **28,** 10 (1957), pp. 824–826.

[14] M Aicheler et al. *A Multi-TeV Linear Collider Based on CLIC Technology: CLIC Conceptual Design Report*. CERN Yellow Reports: Monographs. Geneva: CERN, 2012.

[15] D Broemmelsiek et al. Record high-gradient SRF beam acceleration at Fermilab. *New Journal of Physics* **20,** 11 (2018), p. 113018.

[16] Germán Sciaini and R J Dwayne Miller. Femtosecond electron diffraction: heralding the era of atomically resolved dynamics. *Reports on Progress in Physics* **74,** 9 (2011), p. 096101.

[17] Eric Esarey, Phillip Sprangle, and Jonathan Krall. Laser acceleration of electrons in vacuum. *Phys. Rev. E* **52,** 5 (1995), pp. 5443–5453.

[18] Pierre-Louis Fortin, Michel Piché, and Charles Varin. Direct-field electron acceleration with ultrafast radially polarized laser beams: scaling laws and optimization. *Journal of Physics B: Atomic, Molecular and Optical Physics* **43,** 2 (2009), p. 025401.

[19] R. Joel England et al. Dielectric laser accelerators. *Rev. Mod. Phys.* **86,** 4 (2014), pp. 1337–1389.

[20] T. Tajima and J. M. Dawson. Laser Electron Accelerator. *Phys. Rev. Lett.* **43,** 4 (1979), pp. 267–270.

[21] E. Esarey, C. B. Schroeder, and W. P. Leemans. Physics of laser-driven plasma-based electron accelerators. *Rev. Mod. Phys.* **81,** 3 (2009), pp. 1229–1285.

[22] SPD Mangles et al. Monoenergetic beams of relativistic electrons from intense laser-plasma interactions. *Nature* **431,** (2004), pp. 535–538.

[23] C. G. R. Geddes et al. High-quality electron beams from a laser wakefield accelerator using plasma-channel guiding. *Nature* **431,** (Sept. 2004), 538 EP –.

[24] J. Faure et al. A laser–plasma accelerator producing monoenergetic electron beams. *Nature* **431,** (Sept. 2004), 541 EP –.

[25] W. P. Leemans et al. GeV electron beams from a centimetre-scale accelerator. *Nature Physics* **2,** (Sept. 2006), 696 EP –.

[26] Xiaoming Wang et al. Quasi-monoenergetic laser-plasma acceleration of electrons to 2 GeV. *Nature Communications* **4,** (June 2013), 1988 EP –.

[27] Andreas R. Maier et al. Decoding Sources of Energy Variability in a Laser-Plasma Accelerator. *Phys. Rev. X* **10,** 3 (2020), p. 031039.

[28] Sören Jalas et al. Bayesian Optimization of a Laser-Plasma Accelerator. *Phys. Rev. Lett.* **126,** 10 (2021), p. 104801.

[29] E. Svystun et al. Beam quality preservation studies in a laser-plasma accelerator with external injection for EuPRAXIA. *NIM-A* **909,** (2018). 3rd European Advanced Accelerator Concepts workshop (EAAC2017), pp. 90–94.

[30] Yipeng Wu et al. High-throughput injection–acceleration of electron bunches from a linear accelerator to a laser wakefield accelerator. *Nature Physics* **17,** 7 (2021), pp. 801–806.

[31] K. H. Yang, P. L. Richards, and Y. R. Shen. Generation of Far-Infrared Radiation by Picosecond Light Pulses in LiNbO3. *Applied Physics Letters* **19,** 9 (1971), pp. 320–323.

[32] J. Valdmanis, G. Mourou, and C. Gabel. Subpicosecond electrical sampling. *IEEE Journal of Quantum Electronics* **19,** 4 (1983), pp. 664–667.

[33] Matthias C Hoffmann and József András Fülöp. Intense ultrashort terahertz pulses: generation and applications. *Journal of Physics D: Applied Physics* **44,** 8 (2011), p. 083001.

[34] H A Hafez et al. Intense terahertz radiation and their applications. *Journal of Optics* **18,** 9 (2016), p. 093004.

[35] Jason B. Baxter and Glenn W. Guglietta. Terahertz Spectroscopy. *Analytical Chemistry* **83,** 12 (2011), pp. 4342–4368.

[36] K Humphreys et al. Medical applications of terahertz imaging: A review of current technology and potential applications in biomedical engineering. *Conference proceedings : ... Annual International Conference of the IEEE Engineering in Medicine and Biology Society. IEEE Engineering in Medicine and Biology Society. Conference* **2,** (2004), pp. 1302–5.

[37] S. Koenig et al. Wireless sub-THz communication system with high data rate. *Nature Photonics* **7,** (2013), 977 EP –.

[38] G. Mourou et al. Picosecond microwave pulses generated with a subpicosecond laser-driven semiconductor switch. *Applied Physics Letters* **39,** 4 (1981), pp. 295–296.

[39] M. J. Cliffe et al. Generation of longitudinally polarized terahertz pulses with field amplitudes exceeding 2 kV/cm. *Applied Physics Letters* **105,** 19 (2014), p. 191112.

[40] E. Beaurepaire et al. Ultrafast Spin Dynamics in Ferromagnetic Nickel. *Phys. Rev. Lett.* **76,** 22 (1996), pp. 4250–4253.

[41] T. Seifert et al. Efficient metallic spintronic emitters of ultrabroadband terahertz radiation. *Nature Photonics* **10,** (2016), 483 EP –.

[42] Guo-Qian Liao et al. Demonstration of Coherent Terahertz Transition Radiation from Relativistic Laser-Solid Interactions. *Phys. Rev. Lett.* **116,** 20 (2016), p. 205003.

[43] W. J. Ding and Z. M. Sheng. Sub GV/cm terahertz radiation from relativistic laser-solid interactions via coherent transition radiation. *Phys. Rev. E* **93,** 6 (2016), p. 063204.

[44] M. Bass et al. Optical Rectification. *Phys. Rev. Lett.* **9,** 11 (1962), pp. 446–448.

[45] K. H. Yang, P. L. Richards, and Y. R. Shen. Generation of Far-Infrared Radiation by Picosecond Light Pulses in LiNbO3. *Applied Physics Letters* **19,** 9 (1971), pp. 320–323.

[46] J. A. Fülöp et al. Design of high-energy terahertz sources based on optical rectification. *Opt. Express* **18,** 12 (2010), pp. 12311–12327.

[47] D. H. Auston et al. Cherenkov Radiation from Femtosecond Optical Pulses in Electro-Optic Media. *Phys. Rev. Lett.* **53,** 16 (1984), pp. 1555–1558.

[48] J. Hebling et al. Velocity matching by pulse front tilting for large-area THz-pulse generation. *Opt. Express* **10,** 21 (2002), pp. 1161–1166.

[49] Xiao jun Wu et al. Highly efficient generation of 0.2 mJ terahertz pulses in lithium niobate at room temperature with sub-50 fs chirped Ti:sapphire laser pulses. *Opt. Express* **26,** 6 (2018), pp. 7107–7116.

[50] J.S. Fraser et al. Photocathodes in accelerator applications. *PAC 87, Washington, DC, USA* (Mar. 1987), p. 1705.

[51] J. G. Power. Overview of Photoinjectors. *AIP Conference Proceedings* **1299,** 1 (2010), pp. 20–28.

[52] C P Barty and F V Hartemann. T-REX: Thomson-Radiated Extreme X-rays Moving X-Ray Science into the "Nuclear" Applications Space with Thompson Scattered Photons (Sept. 2004).

[53] W.S. Graves et al. MIT inverse Compton source concept. *Nuclear Instruments and Methods in Physics Research Section A: Accelerators, Spectrometers, Detectors and Associated Equipment* **608,** 1, Supplement (2009). Compton sources for X/γ rays: Physics and applications, S103–S105.

[54] Heewon Yang et al. 10-fs-level synchronization of photocathode laser with RF-oscillator for ultrafast electron and X-ray sources. *Scientific Reports* **7,** 1 (2017), p. 39966.

[55] Umit Demirbas et al. "Attosecond resolution timing jitter characterization of diode pumped femtosecond Cr:LiSAF lasers". Optical Society of America, 2010, CTuDD6.

[56] Andrew J. Benedick et al. "CLEO:2011 - Laser Applications to Photonic Applications". Optical Society of America, 2011, CFK4.

[57] Liang Jie Wong, Arya Fallahi, and Franz X. Kärtner. Compact electron acceleration and bunch compression in THz waveguides. *Opt. Express* **21,** 8 (2013), pp. 9792–9806.

[58] Emilio A. Nanni et al. Terahertz-driven linear electron acceleration. *Nature Communications* **6,** (2015), pp. 1–8. eprint: 1411.4709.

[59] Dongfang Zhang et al. Cascaded Multicycle Terahertz-Driven Ultrafast Electron Acceleration and Manipulation. *Phys. Rev. X* **10,** 1 (2020), p. 011067.

[60] Hanxun Xu et al. Cascaded high-gradient terahertz-driven acceleration of relativistic electron beams. *Nature Photonics* **15,** 6 (2021), pp. 426–430.

[61] Heng Tang et al. Stable and Scalable Multistage Terahertz-Driven Particle Accelerator. *Phys. Rev. Lett.* **127,** 7 (2021), p. 074801.

[62] Acceleration of free electrons in a symmetric evanescent wave. *Laser Physics* **16,** 9 (2006), pp. 1311–1314.

[63] L. Pálfalvi et al. Evanescent-wave proton postaccelerator driven by intense THz pulse. *Phys. Rev. ST Accel. Beams* **17,** 3 (2014), p. 031301.

[64] D A Walsh et al. Demonstration of sub-luminal propagation of single-cycle terahertz pulses for particle acceleration. *Nature Communications* **8,** 1 (2017), p. 421.

[65] E. Curry et al. Meter-Scale Terahertz-Driven Acceleration of a Relativistic Beam. *Phys. Rev. Lett.* **120,** 9 (2018), p. 094801.

[66] Dongfang Zhang et al. Segmented terahertz electron accelerator and manipulator (STEAM). *Nature Photonics* **12,** 6 (2018), pp. 336–342. arXiv: 1711.03024.

[67] L. Serafini and M. Ferrario. Velocity bunching in photo-injectors. *AIP Conference Proceedings* **581,** 1 (2001), pp. 87–106.

[68] S. G. Anderson et al. Velocity bunching of high-brightness electron beams. *Phys. Rev. ST Accel. Beams* **8,** 1 (2005), p. 014401.

[69] M. Ferrario et al. Experimental Demonstration of Emittance Compensation with Velocity Bunching. *Phys. Rev. Lett.* **104,** 5 (2010), p. 054801.

[70] A Gliserin et al. Sub-phonon-period compression of electron pulses for atomic diffraction. *Nature Communications* **6,** 1 (2015), p. 8723.

[71] C. Kealhofer et al. All-optical control and metrology of electron pulses. *Science* **352,** 6284 (2016), pp. 429–433.

[72] Dominik Ehberger et al. Terahertz Compression of Electron Pulses at a Planar Mirror Membrane. *Physical Review Applied* **11,** 2 (2019), p. 1.

[73] E. C. Snively et al. Femtosecond Compression Dynamics and Timing Jitter Suppression in a THz-driven Electron Bunch Compressor. *Physical Review Letters* **124,** 5 (2020), pp. 1–6. arXiv: 1906.03358.

[74] Lingrong Zhao et al. Femtosecond Relativistic Electron Beam with Reduced Timing Jitter from THz Driven Beam Compression. *Physical Review Letters* **124,** 5 (2020), p. 54802. arXiv: 1906.06900.

[75] D. X. Wang, G. A. Krafft, and C. K. Sinclair. Measurement of femtosecond electron bunches using a rf zero-phasing method. *Phys. Rev. E* **57,** 2 (1998), pp. 2283–2286.

[76] David Alesini et al. RF deflector design and measurements for the longitudinal and transverse phase space characterization at SPARC. *Nuclear Instruments and Methods in Physics Research Section A: Accelerators, Spectrometers, Detectors and Associated Equipment* **568,** 2 (2006), pp. 488–502.

[77] Jared Maxson et al. Direct Measurement of Sub-10 fs Relativistic Electron Beams with Ultralow Emittance. *Phys. Rev. Lett.* **118,** 15 (2017), p. 154802.

[78] J. B. Pendry et al. Magnetism from conductors and enhanced nonlinear phenomena. *IEEE Transactions on Microwave Theory and Techniques* **47,** 11 (1999), pp. 2075–2084.

[79] F. J. Garcia-Vidal et al. Light passing through subwavelength apertures. *Rev. Mod. Phys.* **82,** 1 (2010), pp. 729–787.

[80] Lingrong Zhao et al. Terahertz Streaking of Few-Femtosecond Relativistic Electron Beams. *Phys. Rev. X* **8,** 2 (2018), p. 021061.

[81] X. L. Shen et al. A THz driven split-ring resonator based ultrafast relativistic electron streak camera. *AIP Advances* **9,** 8 (2019), p. 085209.

[82] V. Georgiadis et al. Dispersion in dielectric-lined waveguides designed for terahertz-driven deflection of electron beams. *Applied Physics Letters* **118,** 14 (2021), p. 144102.

[83] J A Clarke et al. CLARA conceptual design report. *Journal of Instrumentation* **9,** 05 (2014), T05001–T05001.

[84] Robert W. Boyd. *Nonlinear Optics, Third Edition.* 3rd. USA: Academic Press, Inc., 2008.

[85] R. Trebino. *Frequency-Resolved Optical Gating: The Measurement of Ultrashort Laser Pulses: The Measurement of Ultrashort Laser Pulses.* Springer US, 2000.

[86] Andrea Buzády et al. Temperature-dependent terahertz time-domain spectroscopy study of Mg-doped stoichiometric lithium niobate. *Opt. Mater. Express* **10,** 4 (2020), pp. 998–1006.

[87] G. Pretzler, A. Kasper, and K.J. Witte. Angular chirp and tilted light pulses in CPA lasers. *Applied Physics B: Lasers and Optics* **70,** (2000), pp. 1–9.

[88] Daniel Kreier and Peter Baum. Avoiding temporal distortions in tilted pulses. *Opt. Lett.* **37,** 12 (2012), pp. 2373–2375.

[89] Q Wu and X C Zhang. Electrooptic sampling of freely propagating terahertz fields. *Optical and Quantum Electronics* **28,** 7 (1996), pp. 945–951.

[90] Sang-Gyu Park, M. R. Melloch, and A. M. Weiner. Comparison of terahertz waveforms measured by electro-optic and photoconductive sampling. *Applied Physics Letters* **73,** 22 (1998), pp. 3184–3186.

[91] A. Leitenstorfer et al. Detectors and sources for ultrabroadband electro-optic sampling: Experiment and theory. *Applied Physics Letters* **74,** 11 (1999), pp. 1516–1518.

[92] G. Gallot and D. Grischkowsky. Electro-optic detection of terahertz radiation. *J. Opt. Soc. Am. B* **16,** 8 (1999), pp. 1204–1212.

[93] P.W. Milonni and J.H. Eberly. *Laser physics*. Wiley, 2010.

[94] Artur Carnicer et al. On the longitudinal component of paraxial fields. *European Journal of Physics* **33,** 5 (2012), pp. 1235–1247.

[95] E. Esarey et al. Theory and group velocity of ultrashort, tightly focused laser pulses. *J. Opt. Soc. Am. B* **12,** 9 (1995), pp. 1695–1703.

[96] H. Hirori et al. Single-cycle terahertz pulses with amplitudes exceeding 1 MV/cm generated by optical rectification in LiNbO3. *Applied Physics Letters* **98,** 9 (2011), p. 091106. eprint: `https://doi.org/10.1063/1.3560062`.

[97] S. P. Jamison, R. W. McGowan, and D. Grischkowsky. Single-mode waveguide propagation and reshaping of sub-ps terahertz pulses in sapphire fibers. *Applied Physics Letters* **76,** 15 (2000), pp. 1987–1989.

[98] R. Mendis and D. Grischkowsky. Undistorted guided-wave propagation of subpicosecond terahertz pulses. *Opt. Lett.* **26,** 11 (2001), pp. 846–848.

[99] Rajind Mendis and Daniel M. Mittleman. Comparison of the lowest-order transverse-electric (TE1) and transverse-magnetic (TEM) modes of the parallel-plate waveguide for terahertz pulse applications. *Opt. Express* **17,** 17 (2009), pp. 14839–14850.

[100] Kanglin Wang and Daniel M Mittleman. Metal wires for terahertz wave guiding. *Nature* **432,** 7015 (2004), pp. 376–379.

[101] Tae-In Jeon, Jiangquan Zhang, and D. Grischkowsky. THz Sommerfeld wave propagation on a single metal wire. *Applied Physics Letters* **86,** 16 (2005), p. 161904.

[102] Markus Wächter, Michael Nagel, and Heinrich Kurz. Metallic slit waveguide for dispersion-free low-loss terahertz signal transmission. *Applied Physics Letters* **90,** 6 (2007), p. 061111.

[103] John David Jackson. *Classical electrodynamics; 2nd ed.* New York, NY: Wiley, 1975.

[104] Shaghik Atakaramians et al. Terahertz dielectric waveguides. *Adv. Opt. Photon.* **5,** 2 (2013), pp. 169–215.

[105] A.L. Healy, G. Burt, and S.P. Jamison. Electron-terahertz interaction in dielectric-lined waveguide structures for electron manipulation. *Nuclear Instruments and Methods in Physics Research Section A: Accelerators, Spectrometers, Detectors and Associated Equipment* **909,** (2018). 3rd European Advanced Accelerator Concepts workshop (EAAC2017), pp. 199–203.

[106] Liling Xiao, Wei Gai, and Xiang Sun. Field analysis of a dielectric-loaded rectangular waveguide accelerating structure. *Phys. Rev. E* **65,** 1 (2002), pp. 1–9.

[107] Alisa L. Healy. Energy modulation of electron bunches using a terahertz-driven dielectric-lined waveguide. PhD thesis. Lancaster University, 2020.

[108] K. Floettmann. Generation of sub-fs electron beams at few-MeV energies. *NIM-A* **740,** (2014). Proceedings of the first European Advanced Accelerator Concepts Workshop 2013, pp. 34 –38.

[109] Jared Maxson et al. Direct Measurement of Sub-10 fs Relativistic Electron Beams with Ultralow Emittance. *Phys. Rev. Lett.* **118,** 15 (2017), p. 154802.

[110] G. Kirchhoff. Zur Theorie der Lichtstrahlen. *Annalen der Physik* **254,** 4 (1883), pp. 663–695. eprint: https://onlinelibrary.wiley.com/doi/pdf/10.1002/andp.18832540409.

[111] Max Born and Emil Wolf. *Principles of Optics: Electromagnetic Theory of Propagation, Interference and Diffraction of Light*. 7th ed. Cambridge University Press, 1999.

[112] H.J. Pain. *The Physics of Vibrations and Waves*. Wiley, Jan. 2005.

[113] Kane Yee. Numerical solution of initial boundary value problems involving maxwell's equations in isotropic media. *IEEE Transactions on Antennas and Propagation* **14,** 3 (1966), pp. 302–307.

[114] J.B Schneider. *Understanding the FDTD Method*. https://eecs.wsu.edu/~schneidj/ufdtd/. 2010.

[115] Donna Strickland and Gerard Mourou. Compression of amplified chirped optical pulses. *Optics Communications* **56,** 3 (1985), pp. 219 –221.

[116] RP Photonics. *Regenerative Amplifiers*. https://www.rp-photonics.com/regenerative_amplifiers.html.

[117] RP Photonics. *Multipass Amplifiers*. https://www.rp-photonics.com/multipass_amplifiers.html.

[118] Spectra-Physics. https://www.spectra-physics.com/f/spitfire-ace-regenerative-amplifier.

[119] Spectra-Physics. https://www.spectra-physics.com/f/synergy-femtosecond-oscillator.

[120] Spectra-Physics. https://www.spectra-physics.com/f/ascend-green-pump-laser.

[121] Spectra-Physics. https://www.spectra-physics.com/f/mai-tai-sp-ultrafast-oscillator.

[122] Kimball Physics. *EGH-8121A Electron Gun Technical Manual*. 2017.

[123] Torr Scientific Ltd. https://torrscientific.co.uk.

[124] John H. Scofield. Frequency-domain description of a lock-in amplifier. *American Journal of Physics* **62,** 2 (1994), pp. 129–133.

[125] Gentec-EO. https://www.gentec-eo.com/products/thz5i-bl-bnc.

[126] Yun-Shik Lee. *Principles of Terahertz Science and Technology*. Jan. 2009, pp. –.

[127] INO. https://www.ino.ca/en/solutions/thz/microxcam-384i-thz.

[128] Terahertz. http://www.terahertz.co.uk/index.php?option=com_content&view=article&id=140&Itemid=443.

[129] E. Curry et al. Meter-Scale Terahertz-Driven Acceleration of a Relativistic Beam. *Phys. Rev. Lett.* **120,** 9 (2018), p. 094801.

[130] C. M. Randall and R. D. Rawcliffe. Refractive Indices of Germanium, Silicon, and Fused Quartz in the Far Infrared. *Appl. Opt.* **6,** 11 (1967), pp. 1889–1895.

[131] WC Chew. *Lectures on theory of microwave and optical waveguides*. 2012.

[132] L.V. White and B. Boashash. On estimating the instantaneous frequency of a Gaussian random signal by use of the Wigner-Ville distribution. *IEEE Transactions on Acoustics, Speech, and Signal Processing* **36,** 3 (1988), pp. 417–420.

[133] Aniruddha S. Weling and David H. Auston. Novel sources and detectors for coherent tunable narrow-band terahertz radiation in free space. *Journal of the Optical Society of America B* **13,** 12 (1996), p. 2783.

[134] Zhao Chen et al. Generation of high power tunable multicycle teraherz pulses. *Applied Physics Letters* **99,** 7 (2011), p. 071102.

[135] Patrick O'Shea et al. Highly simplified device for ultrashort-pulse measurement. *Opt. Lett.* **26,** 12 (2001), pp. 932–934.

[136] Saroj R. Tripathi et al. Accurate Complex Refractive Index with Standard Deviation of ZnTe Measured by Terahertz Time Domain Spectroscopy. *Japanese Journal of Applied Physics* **52,** 4R (2013), p. 042401.

[137] Tianying Chang et al. Measurement of complex terahertz dielectric properties of polymers using an improved free-space technique. *Measurement Science and Technology* **28,** 4 (2017), p. 045002.

[138] Thomas H. Pacey. Development of Novel Applications of Dielectric Wakefield Structures for Electron Accelerators. PhD thesis. University of Manchester, 2019.

[139] S. Antipov et al. Experimental Observation of Energy Modulation in Electron Beams Passing through Terahertz Dielectric Wakefield Structures. *Phys. Rev. Lett.* **108,** 14 (2012), p. 144801.

[140] R. K. Li et al. Terahertz-based subfemtosecond metrology of relativistic electron beams. *Physical Review Accelerators and Beams* **22,** 1 (2019), pp. 1–7. arXiv: 1805.01979.

[141] Maksim Kunitski et al. Optimization of single-cycle terahertz generation in LiNbO3 for sub-50 femtosecond pump pulses. *Opt. Express* **21,** 6 (2013), pp. 6826–6836.

[142] M. J. Cliffe et al. Generation of longitudinally polarized terahertz pulses with field amplitudes exceeding 2 kV/cm. *Applied Physics Letters* **105,** 19 (2014), p. 191112.

[143] Jong-Ho Choe et al. Slot antenna as a bound charge oscillator. *Opt. Express* **20,** 6 (2012), pp. 6521–6526.

[144] J. H. Kang, D. S. Kim, and Q-Han Park. Local Capacitor Model for Plasmonic Electric Field Enhancement. *Phys. Rev. Lett.* **102,** 9 (2009), p. 093906.

[145] Young-Mi Bahk et al. Ultimate terahertz field enhancement of single nanoslits. *Phys. Rev. B* **95,** 7 (2017), p. 075424.